UNIVERSIDAD AUTÓNOMA DE NUEVO LEÓN
FACULTAD DE INGENIERÍA MECÁNICA Y ELÉCTRICA

TESIS

“SYNTHESIS AND CHARACTERIZATION OF TIN SULFIDE NANOMATERIALS AND THIN FILMS BY PULSED LASER ABLATION IN LIQUID”

PRESENTADA POR:
JACOB JOHNY

COMO REQUISITO PARCIAL PARA OBTENER EL GRADO DE
DOCTORADO EN INGENIERÍA DE MATERIALES

AGOSTO 2019

UNIVERSIDAD AUTÓNOMA DE NUEVO LEÓN

FACULTAD DE INGENIERÍA MECÁNICA Y ELÉCTRICA

“SYNTHESIS AND CHARACTERIZATION OF TIN SULFIDE NANOMATERIALS AND THIN FILMS BY PULSED LASER ABLATION IN LIQUID”

Submitted in partial fulfillment of the requirements for the doctoral degree in
Materials Engineering

By:

M.Sc. JACOB JOHNY

Supervised by

Dr. SADASIVAN SHAJI

SAN NICOLÁS DE LOS GARZA, NUEVO LEÓN, MÉXICO AUGUST 2019

UANL
UNIVERSIDAD AUTÓNOMA DE NUEVO LEÓN
FACULTAD DE INGENIERÍA MECÁNICA Y ELÉCTRICA

UNIVERSIDAD AUTÓNOMA DE NUEVO LEÓN
FACULTAD DE INGENIERÍA MECÁNICA Y ELÉCTRICA
SUBDIRECCIÓN DE ESTUDIOS DE POSGRADO

"SYNTHESIS AND CHARACTERIZATION OF TIN SULFIDE NANOMATERIALS AND THIN FILMS BY PULSED LASER ABLATION IN LIQUID"

Submitted in partial fulfillment of the requirements for the doctoral degree in
Materials Engineering

By:

M.Sc. JACOB JOHNY

Supervised by

Dr. SADASIVAN SHAJI

SAN NICOLÁS DE LOS GARZA, NUEVO LEÓN, MÉXICO AUGUST 2019

UANL
UNIVERSIDAD AUTÓNOMA DE NUEVO LEÓN
FACULTAD DE INGENIERÍA MECÁNICA Y ELÉCTRICA

UNIVERSIDAD AUTÓNOMA DE NUEVO LEÓN
FACULTAD DE INGENIERÍA MECÁNICA Y ELÉCTRICA
SUBDIRECCIÓN DE ESTUDIOS DE POSGRADO

The thesis committee members recommended that the thesis "**Synthesis and characterization of tin sulfide nanomaterials and thin films by pulsed laser ablation in liquid**" by student **M.Sc. Jacob Johny** with registration number **1831367** be accepted as an option for its defense to the degree of Doctor of Engineering in Materials.

Thesis Committee members

Dr. Sadasivan Shaji
Research guide

Dr. Selene Sepulveda Guzmán
Reviewer

Dr. David Avellaneda Avellaneda
Reviewer

Dr. Eduardo Martínez Guerra
Reviewer

Dr. Miguel Angel Gracia- Pinilla
Reviewer

Dr. Simon Martínez Martínez
Sub-director, Post-Graduate studies

San Nicolás de Los Garza, Nuevo León, 21st June 2019

ACKNOWLEDGEMENTS

To the almighty for all his grace.

To **CONACYT** for the financial assistance through research fellowship during the entire course of the program including a short research stay at Germany.

To **FIME**, UANL for providing all the experimental and characterization facilities as well as for the travel support to research stay at Germany.

To **CIIDIT**, UANL for the laboratory facilities provided.

To **Dr. Sadasivan Shaji** for the scientific supervision of my thesis, for all his comments, corrections and for the inspirational words.

To CEMIE-sol-CONACYT for the financial assistance for an international conference.

To **Dr. Selene Sepulveda Guzmán** for the strong collaboration, for the comments and corrections to the thesis work and for the nice friendly and motivational words.

To **Dr. Bindu Krishnan** and **Dr. David Avellaneda Avellanada** for their help in corrections and improvement of the thesis during the entire period of Ph.D.

To my thesis revisers Dr. Eduardo Martínez Guerra and Dr. Miguel Angel Gracia-Pinilla for their comments and corrections on the thesis.

To Dr. Marco Antonio Loudovic Hernández Rodríguez and Dr. Simón Martínez Martínez for their supports.

To the University of Duisburg-Essen and Dr. Stephan Barcikowski, Dr. Christoph Rehbock and the whole Barcikowski group for providing a platform for an exchange program. Special thanks to Anna Tymoczko and Ruksan Nadarajah.

To Dr. Manju T., for her continuous motivation and for connecting me to FIME, UANL.

To Dr. E.I. Anila, Dr. Anitha Abraham, Dr. Aijo John K., Dr. T.A. Safeera, V.N. Archana and Prof. M.R. Anantharaman for their support and collaborations.

To my beloved parents for their strong support during my entire academic career and for being with me at every single moment of my life.

To all my family relatives, cousins and especially to my grandmother who showed their support and love.

To all my friends and colleagues from Mexico as well as from India for their help and support. I would like to thank especially Vineetha, Dani, Sreed, Anjali, Anahi, Franco,

Eleazer, Ilse, Paloma, Isabel and Ernesto for their assistances during the entire period of the thesis. Sincere thanks to Jobish for his friendship and motivations.

To my dear Mary teacher and her family for all the care and love and for considering me as a member of her family.

To all the Mexicans I know for their friendly and polite approach and making me comfortable everywhere I went and to the Malayali community in Monterrey for the support.

Dedicated to my loving Pappa and Amma

- *M.C. Johny*
- *Celine Johny*

Abbreviations

(0-3) D	(0-3) Dimension
AFM	Atomic Force Microscopy
ALD	Atomic Layer Deposition
BE	Binding Energy
CBD	Chemical Bath Deposition
CIGS	Copper Indium Gallium Selenide
CV	Cyclic Voltammetry
CVD	Chemical Vapor Deposition
DMF	Dimethyl Formamide
EDX	Energy Dispersive X-Ray
EPD	Electrophoretic Deposition
FESEM	Field Emission SEM
FET	Field Effect Transistors
FF	Fill Factor
GIXRD	Grazing Incidence XRD
GO	Graphene Oxide
HER	Hydrogen Evolution Reaction
HRTEM	High-Resolution TEM
IA	Isopropyl Alcohol
ITO	Indium Tin Oxide
I-V	Current-Voltage
JCPDS	Joint Committee on Powder Diffraction Standards
LALs	Laser Ablation in Liquids
LED	Light Emitting Diode
LFL	Liquid Fragmentation in Liquid
LVCC	Laser Vaporization Controlled Condensation
MBE	Molecular Beam Epitaxy
Nd:YAG	Neodymium-Doped Yttrium Aluminum Garnet
NIR	Near Infrared
NPs	Nanoparticles
PIGE	Paraffin Impregnated Graphite Electrode
PL	Photoluminescence
PLAL	Pulsed Laser Ablation in Liquid
PLD	Pulsed Laser Deposition
PV	Photovoltaic
PVD	Physical Vapor Deposition
QDs	Quantum Dots
rGO	Reduced Graphene Oxide
SAED	Selected Area Electron Diffraction
SDS	Sodium Dodecyl Sulphate

SEM	Scanning Electron Microscopy	SERS	Surface Enhanced Raman Scattering
SILAR	Successive Ionic Layer Adsorption and Reaction	UV-Vis-NIR	Ultraviolet-Visible-Near Infrared
TEM	Transmission Electron Microscopy	XPS	X-Ray Photoelectron Spectroscopy
		XRD	X-Ray Diffraction

Contents

Summary

Tin monosulfide (SnS) and tin disulfide (SnS_2) nanoparticles were synthesized by employing pulsed laser ablation in liquid (PLAL) technique in various organic solvents where the influence of different laser parameters and solvents were investigated. Spray deposition technique has been implemented as a method to fabricate thin films of these materials where the spray parameters were optimized depending on the solvent and material. Combination of pulsed laser ablation in liquid with spray technique was used for the first time in the work. In the case of SnS nanoparticles, they were first prepared by laser ablation in isopropanol and N,N-dimethyl formamide and thin films of the same were deposited by spraying the laser generated nanocolloids onto heated substrates where the films fabricated were characterized for their structure, morphology and opto-electronic and electrochemical properties. Moreover, colloidal graphene oxide was mixed with SnS nanocolloids at different volume concentrations (0.1%, 0.5% and 1%) to obtain SnS: GO or SnS: rGO thin films where the nanocomposite films showed enhanced opto-electronic and electrochemical properties compared to the pristine SnS thin films. A solar cell configuration of glass/ CdS/ Sb_2S_3/ SnS:rGO was also fabricated using the SnS: rGO layer as the absorber and photoconversion efficiency of 2.3% was achieved. In the case of SnS_2 nanoparticles, effect of four different solvents (acetone, isopropanol, ethanol and DMF) and two different laser wavelengths (1064 nm and 532 nm) on the morphologies and properties of SnS_2 particles were studied in detail. Furthermore, influence of ablation fluence, liquid medium temperature and post irradiation on the SnS_2 nanoparticles were investigated in detail and the hydrogen evolution activity of these nanoparticles were tested in acidic medium. Electrochemical properties of the SnS_2 thin films deposited from SnS_2 nanoparticles in ethanol and isopropanol and after different post annealing treatments (200, 250 and 300 °C) were analyzed and the results were compared. For majority of the cases, the prepared nanoparticles and thin films were analyzed for their structure, crystalline nature, composition and morphology by XRD, Raman, XPS, TEM and SEM whereas the optical, opto-electronic and electrochemical properties were elucidated using the UV-Visible spectroscopy, I-V measurements under dark and illumination and electrochemical measurements respectively.

Chapter 1

Introduction to nanomaterials, pulsed laser ablation in liquid and spray deposition

1.1 Introduction to nanomaterials

1.1.1 Introduction

The ability to manipulate individual molecules and atoms for producing nanostructured and sub-micron materials that find real world applications can be defined as nanotechnology. Nanotechnology deals with small-sized materials or small structures where the typical dimension ranges from sub-nanometer to several hundred nanometers (a nanometer is 10^{-9} m). Nanomaterials find potential applications in various fields due to the versatile properties they exhibit at these low dimensions in contrary to their corresponding bulk materials. The main application fields include opto-electronics, nanomedicine, photovoltaics, optics, nano and molecular electronics and nanomechanics[3, 4]. Among many top-down and bottom-up approaches to fabricate nanometrials, pulsed laser ablation in liquid (hereafter referred as PLAL) is an experimentally simple and fast route to produce a variety of nanomaterials with high purity through a single step process. The resulted nanomaterials are typically free from surface impurities and thus can be directly used for the intended applications without further processing. Absence of expensive vacuum systems, availability of large variety of solvents and materials, easiness of the experimental setups and production of less or no chemical wastages make this nanomaterial fabrication technique notable among the researchers. In this thesis, we report synthesis and characterization of tin sulfide (SnS and SnS_2) nanomaterials by PLAL and their conversion to thin films by spray deposition for electrochemical, opto-electronic and photovoltaic applications.

1.1.2 Nanomaterials synthesis

There are two approaches towards the synthesis of nanomaterials: top-down and bottom-up and each individual synthesis method can be categorized as either of the two approaches. Top-down approach uses the bulk material as the starting component and the fragment it to the small dimensions whereas bottom-up approach refers to the build-up of a material from the bottom: atom-by-atom, molecule-by-molecule or cluster-by-cluster. Both approaches play important roles in nanotechnology as well as in modern industry. There are a variety of synthesis methods available up to date for synthesizing nanomaterials with desired morphologies and properties. Selection of the synthesis method also depends on the final properties and applications of the resulted nanomaterial products. Both top-down and bottom-up approaches have their own advantages as well as a few disadvantages. For instance, biggest problem with the top-down approach is the surface structure imperfection. Conventional top-down techniques like lithography can cause potential crystallographic damage to the processed patterns and during the etching steps, additional defects may be introduced. On the other hand, bottom-up approach provides a better chance to obtain nanostructures with more homogeneous composition, less defects and better short- and long-range ordering since this approach is mainly driven by the reduction of Gibb's free energy. Hence, nanomaterials produced in this way retain a state closer to the thermodynamic equilibrium state[4-7]. Explaining each synthesis method in detail will be out of the context of the thesis and therefore only the most important nanomaterials synthesis techniques are briefly described in the following part.

Photolithography is an important top-down approach for nanomaterial synthesis since almost all top-down manufacturing involves one or more photolithography fabrication steps. In a typical photolithography process, light from a source is directed to the substrate wafer covered with a photo-sensitive film though a mask containing the circuit design. The photo-sensitive film, called the photoresist can be partly removed by a chemical developer leaving well-defined substrate parts exposed to etching or metal deposition. To obtain better resolutions than a few micrometers of photolithography, either electron beam lithography or X-ray lithography is used[8]. Other variants of lithography such as focused ion beam lithography[9], extreme UV lithography[10], dip-pen lithography[11] and scanning probe lithography[12] are also useful top-down nanofabrication methods. However, photolithography is the most widely used fabrication technique used in fabrication of microelectronic devices. **Milling** or **attrition** is another example of top-down nanofabrication technique which can be used to produce nanoparticles of tens to several hundred nanometers in diameter. Due to the disadvantages discussed before and limited choice of methods of top-down techniques, majority of the nanomaterial fabrication is based on bottom-up approach.

There are several different bottom-up approaches available to date, which can be generally classified into either chemical or physical methods. Chemical methods usually include a chemical reaction step of two or more precursors during the process to obtain the final product whereas the physical process does not include this reaction step and directly form the nanomaterial from the precursor or target. One of the most used chemical synthesis methods is **Sol-gel** process which involves the use of liquid solutions as raw materials. Homogenization at a molecular level can be achieved in a short time since low viscosity liquids are mixed. On heating the gel, chemical reactions will be easy and requires lower temperatures[13]. **Chemical vapor deposition (CVD)** is defined as the deposition of a solid by chemical reaction in the vapor phase onto a heated surface. The deposition species are atoms or molecules or a combination of these. CVD can be used for the manufacturing of coatings, fibers, powders and monolithic components where metals, carbides, nitrides and intermetallics can be synthesized. Advantages of CVD include high deposition rate and wide range of suitable substrates of different geometries[14]. In **Physical vapor deposition (PVD)** processes, material is vaporized from a solid or liquid source in the form of atoms or molecules and transported in the form of a vapor through a low pressure gaseous or vacuum environment to the substrate and condenses. PVD processes are usually used to deposit films of thicknesses in the range of a few nanometers to thousands of nanometers. The main categories of PVD processing includes sputter deposition, vacuum deposition, arc deposition and ion plating[15]. **Laser ablation** is another important nanomaterial processing technique where a solid target is ablated by employing a high-power laser. Lasers are utilized not only in the nanostructures processing but also to modify the size, shape, phase, morphology and hence the properties of the nanostructures. Laser processing methods are almost simple, green, fast and one-step and produce materials with contamination free surfaces and thus important in biological and medical applications where purity of materials is of highest impact. Nanostructures of 0D, 1D, 2D and 3D can be synthesized using laser-based processing methods in gaseous as well as in liquid phases[16]. Laser-based approaches for generating nanoscale materials include Pulsed laser deposition (PLD)[17-19], laser vaporization controlled condensation

(LVCC)[20, 21], laser chemical vapor deposition[22-24], laser pyrolysis[25], laser ablation in liquids (LALs)[26, 27] and so on. **Pulsed laser deposition (PLD)** is an experimentally simple but highly versatile tool for multilayer and thin film research. Stoichiometric transfer, reactive deposition, growth from an energetic beam and inherent simplicity for the growth of multilayered structures are advantages of PLD in growing films of oxides and other chemically complex materials. Artificially layered materials and metastable phases have been created by PLD where the properties were varied by control of the layer thickness. During the laser pulse several events occur such as quick heating and vaporization of the target material, absorption increase by the vapor until breakdown occurs for a hot dense plasma, absorption of the remaining laser pulse for heating and accelerating the plasma containing neutral atoms, molecules and ions in both ground and excited states as well as energetic electrons. Simple oxide molecules are also formed in the ablation beam if ablation is carried out in a low-pressure reactive gas such as oxygen[28]. Even though experimentally simple and produces uniformly thick films, the need for a vacuum or gas filled chamber makes PLD costlier. Here is the important difference between PLD and pulsed laser ablation in liquid (PLAL) where the nanomaterials produced are directly dispersed into a given liquid in PLAL and thus rules out the need for costly vacuum systems. PLAL is described in more detail in section 1.2 since it is the nanoparticle synthesis method used for this thesis work. The nanoparticles produced by various methods possess various properties that are different from their bulk counterparts and are applied in a number of fields. The general properties of nanomaterials and their main application areas are briefly described in the following sections.

1.1.3 Properties of nanomaterials

Nanomaterials in general possess some novel remarkable properties that are significantly different from their corresponding bulk counterparts. Origin of these unique properties can be attributed to the spatial confinement, large fraction of surface atoms, less imperfections and large surface energy compared to the bulk[4]. For instance, mechanical properties of nanomaterials may reach one or two orders of magnitude higher than that of bulk single crystals due to the reduced probability of defects. Optical properties of nanomaterials, especially that of semiconductors, can be significantly different due to the shift in energy band gap towards higher values. On the other hand, absorption properties of metallic nanoparticles significantly change with their size which leads to different color of the particles[29, 30]. Melting points of nanomaterials are far lower than their bulk due to the high surface to bulk atom ratio. Electrical and magnetic properties of nanomaterials may also differ from that of the bulk due to the different behavior that can be expected at the confined nanometer scale[31]. Ferromagnetic bulk materials may transform into superparamagnetic materials when the dimensions are reduced to the nanoscale due to the huge surface energy whereas the electrical conductivity can be either reduced or enhanced owing to the higher surface scattering at the reduced dimensions or due to the better microstructure ordering[4]. These are just a few examples of the different properties exhibited by materials at the nanoscale compared to the bulk, however there are many more other properties as well that nanomaterials possess. Exploitation of one or more of these properties would lead to fabrication of devices based on nanomaterials with enhanced functionality and performance. Moreover, most of the properties may also depend on the synthesis method and post processing techniques which would open a way to tune them as desired.

1.1.4 Applications of nanomaterials

Since the nanomaterials possess enhanced and different properties than their bulk form, they find applications in a number of fields. These broad range of applications extend from electronics through biological systems to optical communications. Main applications of nanomaterials are based on the high surface area, versatile physical properties and small size offering more space for multiple functionalities. All the applications that are reported to date cannot be summarized here, and hence the most important ones are briefly described as following. One of the main application fields of nanomaterials is medicine, which is often denoted as nanomedicine. In nanomedicine, nanoscale devices are used for diagnostics and enhanced therapy and such devices are called nanorobots or nanobots[4]. The important advantage of using nanomaterials in medicine is the capability to carry out specific functions within a very short area without affecting the surrounding parts. Biocompatibility of nanomaterials is therefore a must requirement if the application involves direct contact between the used nanomaterial and the treated body part. Controlled drug delivery, diagnosis and therapy are some of the main biomedical applications consisting nanomaterials[32-34]. Another important application field is biology which is termed as nanobiotechnology which includes the use of biological molecules for assembling nanoscale structures and the use of nanostructures as highly sophisticated scopes, machines or materials in medicine and/or biology[35]. Many progress and efforts were also made in the nanoelectronics and molecular electronics[36-38]. Single molecules are expected to control the electron transport in molecular electronics which would explore the molecular functions for electronic devices. Nanomaterials based field effect transistors (FET)[39], tunneling junctions[40], electrically configurable switches[41], carbon nanotube transistors[42] and single molecular transistors[43] are some of the examples where nanomaterials are applied. Photoelectrochemical cells[44], carbon nanotube emitters[45], nanomechanics[46], quantum dot devices[47], catalysis by gold nanoparticles[48], plasmon waveguides[49] and photonic crystals[50] are some of the other important application areas of nanomaterials.

1.2 Pulsed laser ablation in liquid

1.2.1 Introduction

Pulsed laser ablation in liquid (PLAL) is an emerging green synthesis method for obtaining colloidal nanoparticles (NPs) of various kinds with tunable morphology and properties. In PLAL, the NPs are often obtained through a single stage process where the corresponding bulk target immersed in a liquid medium is irradiated by a pulsed laser. Even though the mechanism behind the NP generation by PLAL is complex, the experimental set-up employed is rather simple and relatively fast. Interactions between laser pulses and matter became the interest of many researchers after the invention of first pulsed laser by Maiman in 1960[51]. A similar or comparable method to PLAL is pulsed laser deposition (PLD), in which the role of liquid medium is replaced by vacuum or a gas environment. PLD is widely used for synthesizing quality thin films[17, 18, 28], however, the need of vacuum systems makes this method relatively expensive than PLAL. Another important aspect is that in PLAL, during the generation of the NPs, the formed plasma is confined by the surrounding liquid medium and thus different morphologies and properties can be expected in comparison with PLD[52]. Henglein and Cotton ablated pure metal targets in various solvents[53, 54] and thereafter PLAL was widely used to produce NPs of metals, semiconductors and polymers[27, 55, 56]. Variation of different lasing parameters such as laser wavelength, frequency (repetition rate), fluence (energy per unit area), pulse width (femto, pico, nano and micro) and wide range of solvents allow one to control the morphology of the generated NPs by PLAL and thereby tune the properties as desired.

1.2.2 Fundamentals and mechanisms

PLAL is a suitable choice for producing pure colloidal NPs often through a one step process and exhibit some characteristic advantages among other physical and chemical NP synthetic approaches. Some of the advantages are as follows:

(i) Since the NPs in PLAL are dispersed directly into the surrounding liquid media, expensive vacuum systems are not required and thus reduce the cost of the overall experimental set-up significantly in comparison with PLD.

(ii) Stabilizers or capping agents are often excluded in PLAL and therefore the NPs obtained by PLAL possess ligand-free pure surface which is highly beneficial for applications that require surface modifications as well as in biomedicine.

(iii) PLAL generated NPs usually acquire sufficient surface charge and hence are normally electrostatically stabilized which keeps the synthesized colloids stable for several days, months or even years.

(iv) The experimental set-up of PLAL is simple with fast NPs synthesis and allow use of a wide range of target materials from metals through semiconductors to bi-metals.

(v) Use of aqueous solutions and organic solvents allow one to control the confinement through the liquid and hence to vary the properties of the generated NPs.

(vi) The lasing parameters such as wavelength, repetition rate, energy fluence and pulse width affect significantly the final morphology and properties of the synthesized particles and thus can be used for tuning one or more of the NP properties in PLAL.

(vii) Very high pressure and temperature inside the plasma due to the liquid confinement and fast quenching leads to formation of even metastable phases in PLAL.

NP generation by PLAL can be classified into three stages such as the plasma stage, the cavitation bubble phase and a final phase where the particles are dispersed into the liquid. When laser pulses having an irradiance between 0.1 and 1 GW cm^{-2} interact with a solid target material, ejection of seed electrons occur due to multiphoton ionization and the ablated species form a hot atomic plasma as a consequence of photon absorption by inverse Bremsstrahlung[57]. The generated plasma contains highly ionized or atomic species with an initial density of about 10^{20} cm^{-3} depending on the pulse energy of the laser[58]. Duration of such a laser generated plasma is usually of the order of tens of nanoseconds to a few microseconds for each laser pulse and strongly depends on the laser parameters and surrounding liquid environment[55, 59, 60] and the pressure and temperature inside the plasma can be as high as hundreds of pascals and thousands of Kelvin[61]. The plasma expands supersonically by driving a shock wave in the surrounding liquid and thereafter slows down compressing the liquid until the plasma is completely disappeared. Plasma generated in a liquid environment during PLAL is essentially the same as that generated in air[62, 63], with the main difference being the distinct energy transfers during the plasma cooling. Low compressibility of the liquid leads to sudden confinement of the plasma in PLAL and hence the plasma holds a very high density of the ablated species inside. When the plasma cools down, due to the high thermal capacity of the liquid surrounding the plasma, the energy exchange is extremely fast. The trapped species inside plasma cools down first by reducing ions into neutral species by recombination and then by generating NPs which occurs very fast within the first tens of nanoseconds after the laser pulse and until the plasma disappears completely[61]. Due to the high energy transfer during the plasma cooling, the liquid layer that is in contact with the plasma plume undergoes a phase transition which leads to the formation of a thin vapor layer around the plasma volume[64-69] and this thin vapor layer is the early cavitation bubble.

The vapor layer generates at very high temperature and owing to its high pressure it expands in all directions, generating the cavitation bubble due to its expansion towards the liquid and causing plasma confinement due to the expansion towards the plasma. Lifetime of such a cavitation bubble is usually on the order of hundreds of microseconds which is 2 order of magnitude higher than the plasma lifetime and strongly depends on the characteristics of the incident laser pulse such as focusing conditions, external pressure, pulse duration and wavelength[70]. Ablated species (atoms, ions and clusters) can interact with the surrounding liquid and may undergo chemical reactions even inside the cavitation bubble. During this time, rapid plasma quenching occurs and then the cavitation bubble expands which has an initial size comparable to that of the laser focus[55]. Liquid matter is the primary content inside the vapor and it is assumed that solid crystallization occurs in this region leading to atom clusters and primary particles but droplets are also formed which lead to the secondary particles[71-73]. The cavitation bubble then immediately undergoes periodic evolution and further expansion and the shrink until it collapses completely. Pressure inside the cavitation bubble reaches the saturation pressure in between the expansion and collapse stages where the bubble equilibrates with the surrounding liquid. The bubble acquires its maximum radius at this condition and continues in the quasi-equilibrium status longer than in the compression and collapse stages. Therefore, the NPs have a larger volume to diffuse and longer time thereby decreasing their local concentration[61]. Since the bubble formation occurs at the plasma front, during the bubble expansion stage the produced material is sucked inside the cavitation bubble. After the maximum expansion, while the bubble starts to collapse, the NPs filling the bubble volume are pushed against the target, but due to the inability to drag the NPs while shrinking towards the target and passing through the NPs cloud, the NPs themselves are released and dispersed into the surrounding liquid[61]. Since the plasma and bubble characteristics strongly depends on the final products in PLAL, it is worth to mention briefly the impact of different lasing parameters and the role of liquid medium in PLAL. For instance, wavelength of most of the commonly used pulsed lasers are suitable for ablating materials but however it plays crucial roles when morphology modifications through laser post irradiations is desired since the laser energy has to be absorbed by the generated NPs in this case. Hence lasers with wavelengths corresponding to the plasmonic absorption of metals or that corresponds to the energy band gaps of semiconducting NPs are the best choices in this aspect.

For metals, ablation threshold is proportional to laser wavelength and hence higher wavelengths have higher threshold fluences[74]. Moreover, ablated mass per pulse may increase with wavelength since shorter wavelengths penetrate less in comparison with longer wavelengths in the target material. Generally, PLAL using higher wavelengths will lead to generation of bigger nanoparticles compared to the particles generated by lower wavelengths mainly attributed to liquid fragmentation in liquid (LFL)[75-80]. Laser fluence is another important parameter which affects the PLAL efficiency where the productivity increases with fluence above threshold fluence until optical breakdown is reached[81, 82]. Generally, life time of the cavitation bubble increases with fluence and as a result when the interval between laser pulses is faster than lifetime of the cavitation bubble, the incoming laser pulses are shielded by the bubble which reduce the ablation rate. On the other hand, focusing conditions of the laser beam on the target also plays important roles in determining the final morphology of the generated particles in PLAL. For example, when the focus is below, above or just on the target, the ionization degree of the surrounding medium and strength of the shock wave and laser fluence reaching at the target vary thus creating an opportunity to alter the morphology and phase of the particles[83-87]. Repetition rate, number of output pulses per second, has physical-chemical and technical effects on the PLAL process. At a particular laser power, decreasing the repetition rate will increase the pulse energy and thereby yielding a higher rate of ablation per pulse. Zamiri et al. reported that an optimal repetition rate is present in terms of NP stability depending on the liquid for Ag NPs produced in water[88]. On the other hand, repetition rate can also influence the particle size in PLAL as shown for Ag and Au NPs by different authors[89, 90]. Pulse duration, which is another important parameter that control the PLAL process, determines both efficiency of PLAL and degree of self-focusing during laser propagation[83]. Pulse duration effects depend on the cooling time of electrons (electron-phonon coupling constant) of the material. For lasers having femto second pulses, the electron cooling time is higher than the pulse duration and hence solid-vapor transitions is considered as the ablation process[91]. In contrast, the ablation mechanism using nanosecond lasers involve laser heating and melting of the target[55]. Above mentioned parameters are the ones that influence significantly the NP morphology in PLAL. However, in addition to these lasing parameters, different properties of the liquid medium also affect the generated NPs. Refractive index, polarity and viscosity are some of the important one among these properties associated with the surrounding liquid medium in PLAL where they modify the lifetime of the cavitation bubble and thereby the final morphology of the particles[2, 61, 92]. After the plasma production in PLAL, it is confined by the surrounding liquid media. Hence, as the liquid properties are changed, the plasma properties and its cooling can be significantly affected[79]. Therefore, tuning of the NP properties in PLAL can be done by adjusting both the parameters of the laser as well as by proper selection of the liquid medium. Even though majority of the laser ablation mechanisms were proposed for metallic NPs by PLAL, the same are applicable for generation of semiconducting particles as well. One probable difference could be the absorption of the laser beam by the semiconductor targets depending on the laser wavelength and the energy band gap of the semiconductor. However, synthesis of different semiconducting NPs by PLAL were shown previously and is described in detail in a later section in the thesis.

1.2.3 Experimental set-up

As already mentioned, the experimental set-up of PLAL is relatively simple. In a typical laser ablation experiment, the target material which is immersed in the chosen liquid medium is irradiated by a pulsed laser and after sufficient time of ablation the produced colloid is collected and characterized. However, depending on the variety of laser machines, optical components and other available instruments, one can set-up their own experimental set-up for the desired NP generation. Basically, the PLAL set-up includes two different kinds of methodologies *viz.* horizontal and vertical laser configurations. As their name indicates, in the horizontal configuration, the target is ablated horizontally using the laser whereas in case of the vertical configuration the laser beam interacts with the target vertically. Schematic representations of both configurations are presented in Fig.1.1. Usually, the vertical laser configuration is accompanied by a high reflective convex lens (99% reflective) since the lasers are usually emitting the radiation in the horizontal direction. A convex lens is usually placed in between the target and the laser beam to adjust the focus of the beam on the target surface and thereby vary the ablation fluence.

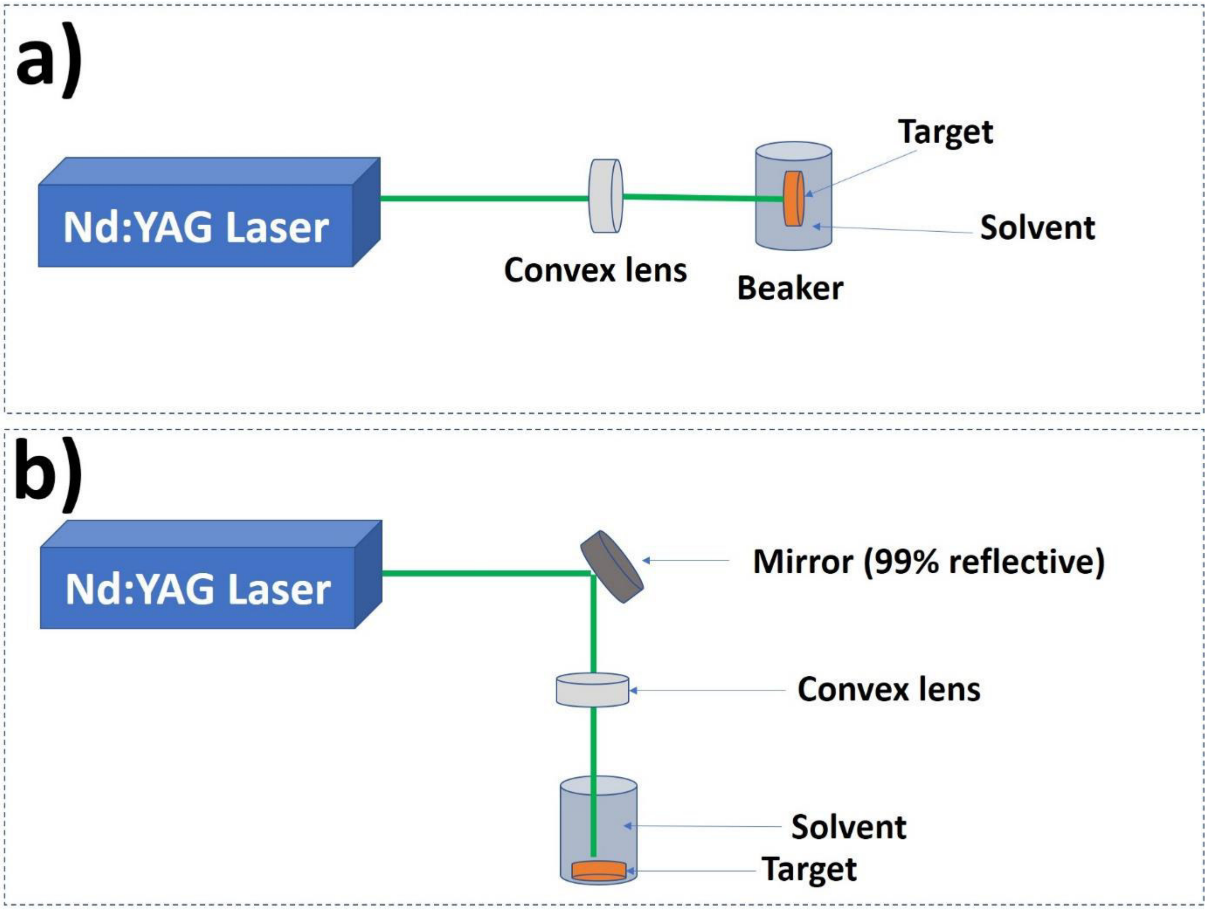

Fig.1.1. Experimental set-up for laser ablation (a) horizontal and (b) vertical configuration

To improve the NP productivity and to minimize post irradiation effects, target translation, liquid flow or beam scanning are often used. Two Nd: YAG pulsed lasers were used during the entire course of the present thesis work, both having 10 ns pulse width. Where one laser can be operated at a fixed frequency of 10 Hz and maximum power of around 1 J at 1064 nm and 500 mJ at 532 nm (solar laser systems, LQ929), the other one can be operated at repetition rates ranging from 10 to 100 Hz with a maximum power of around 90 mJ (solar laser systems, LQ629). Both lasers were employed for the generation of SnS and SnS_2 NPs depending on the desired NP productivity and properties. To avoid deep ablation craters on the target, a translation system (designed by mechatronics students of FIME, UANL) was employed for linear movement of the target during laser ablation with velocity ranging from 20 to 3000 µm/s. An optical power meter (Thorlabs Inc. PM100D) was used for measuring the output energy of the Nd:YAG pulsed lasers.

1.2.4 Variety of materials and applications

A wide variety of target materials have been used to synthesize their corresponding NPs by PLAL including metals, semiconductors, alloys and ceramics[93]. However, up to date most of the PLAL studies were carried out for metallic NPs in comparison with the other categories due to the less complications involved in the synthesis and applicability of these particles in various fields. In more detail, PLAL have been successfully applied to generated NPs of noble metals, metal oxides, hydroxides, carbides, nitrides, organic/inorganic NPs[16, 26, 27, 52, 94-100]. Oxide NPs by PLAL are usually produced by ablating the corresponding metal targets in aqueous solution where the ablated species interact with the molecules in the liquid medium and form oxides. NPs of TiO_2, SnO_2, ZnO, AlOOH, GaOOH, $Mg(OH)_2$, Co_3O_4 are some examples for this[99]. In such a case, where there is a reaction between the laser ablated species and the liquid medium occurs, it is called as reactive pulsed laser ablation or in short reactive laser ablation. However, in most of the ablation experiments, the surrounding liquid just provides an environment for the dispersion of laser generated NPs and thus are non-reactive in nature. Even though solid spheres having dimension in the nanometer scale are the common products of PLAL, other structures such as cubes, hollow particles, plates/sheets/disks, spindles, rods/tubes and core-shell NPs have also been reported. But it should be noted that some of these structures were generated using the help of some external factors such as electrical field and templates[93, 101]. Moreover, NPs based on carbon by PLAL has been also investigated by researchers. Carbon based composites, nanostructures and nanodiamonds are some of the examples[102-104].

Synthesis of a wide variety of nanomaterials by PLAL makes it a suitable technique for a number of different applications. Nanomaterials synthesized by PLAL are being used in distinct areas owing to their special morphologies and unique properties or both. These applications cover many areas including magnetism, optics, biology, plasmonics and catalysis. For biological applications, purity, ligand-free surface and facile nanointegration capability of the laser generated NPs are exploited. Especially for nanobioresponse, purity of the NPs is of particular interest[105]. Bioconjugation of the NPs is another field in the biological applications since laser generated noble metal NPs can be easily conjugated by the biomolecules in the liquid medium through one-step without any limitation on the biomolecule type[106-109]. PLAL synthesized Ag, Cu, TiO_2 and Ag-TiO_2 NPs have also shown their ability to be good antibacterial agents primarily attributed to the absence of surface ligands which helps in enhancing the antibacterial activity[55, 110-113]. Laser generated NPs are also suitable candidates as biofunctional NPs for various in vitro biomedical applications[55]. In magnetism, PLAL generated elemental, oxide, carbide and alloy magnetic particles are used where one can obtain different kinds of magnetic nanoparticles simply by adjusting the liquid composition[114-117]. NPs having a core-shell morphology where a magnetic core is protected by a thin shell (usually of a noble metal) is of great importance in this aspect. Elemental metallic NPs, alloys and composites can be used for surface enhanced Raman spectroscopy (SERS) as well owing to their high purity surface. Neddersen et al. showed that PLAL synthesized Au, Ag, Cu, Pd and Pt NPs have comparable SERS activity in comparison with their chemically prepared alternative colloidal particles[54]. PLAL generated plasmonic negatively charged NPs can be mixed with magnetic particles to assemble aggregates with both SERS and superparamagnetic properties[118]. On the other hand, semiconducting NPs generated by PLAL are often used for their luminescent properties. NPs of Si, Se, Ge, SnO_2, ZnO, TiO_2, CdS, PbS, SnS, SnS_2 are some of the examples[2, 79, 119-126]. PLAL synthesized Si- QDs (quantum dots) hybrid inorganic/ organic light emitting diode (LED) displayed excellent performance with optical power densities of around 700 nW/cm^2 and current 280 mA/cm. Catalysis is another field of application where laser generated NPs can be effectively used due to the one step synthesis and non-requirement of any post-synthesis cleaning procedures and ligands[127]. So far, highest performance reported for laser synthesized heterogeneous catalysts are by Pt/rGO (reduced graphene oxide) for methanol oxidation with 333.3 mA/mg[128], Au/CeO_2 for 4-nitrophenol reduction with 1.40×10^{-2} s^{-1} (μmol Au)$^{-1}$[129] and water oxidation with a high turn-over frequency and mass activity by Co_3O_4 NPs[130]. NPs obtained by PLAL have also shown their potential in other catalysis applications such as hydrogen fuel cells, photocatalysis, water oxidation (splitting) and glucose oxidation and biofuel cells. On the other hand, laser generated Cu(In,Ga)Se_2 NPs were effectively used for solar cell fabrication by Guo and Liu where a reliable photo conversion efficiency of 7.37 % was achieved[131]. However, device applications using PLAL NPs are still limited mostly due to the complications accompanied with integration of colloidal NPs in to thin films and devices.

1.3 Semiconductor nanoparticles by PLAL

1.3.1 Introduction

As previously mentioned, semiconducting NPs generated by PLAL is a less investigated area so far in comparison with metallic NPs. However, using PLAL for synthesizing semiconductor NPs may have big impact in the scientific society due to the extended range of applications where different semiconductors are applied. Among different NP types, semiconductor particles have attracted much attention due to their significant roles in nano-electronics, nano-optics and nano-optoelectronics[27]. Even when, semiconducting NPs are prepared by PLAL, the investigation is mostly limited to just their synthesis and characterization and hence probably not extended to the application aspects of the generated particles. Synthesis methods such as chemical deposition, sol-gel method, metal-organic chemical vapor deposition (CVD) or vapor phase transport are often chosen for fabricating nanomaterials of semiconductors. But most of these methods include tedious procedures or less control on the parameters required for device applications such as opto-electronics, spintronics and optics[27]. Laser ablation in this case provides an efficient way to control the properties and composition of the generated semiconducting NPs which is highly beneficial for device applications. Tuning of the properties can be achieved by modifying the target, changing the lasing parameters or by varying the liquid medium in PLAL. Moreover, compared to the chemical synthesis alternatives, PLAL is relatively fast and produces very less contamination. The main semiconductor categories that are investigated up to date by PLAL includes oxides, sulfides and single element semiconductors such as Si and Ge. Hence, this section of the thesis will provide an overview of these different semiconductor NPs generated by PLAL and their applications in some cases.

1.3.2 Oxide nanoparticles by PLAL

Oxide semiconductor NPs can be easily prepared by pulsed laser ablation of metal targets in liquid media (usually in water). Takeshi Sasaki et. al summarizes some research developments in the fabrication of metal oxide-based nanoparticles by PLAL[99]. The ablated species of the target react with the molecules of the surrounding media to form the desired oxide particles since the laser ablated species are electronically excited and therefore highly reactive[132]. Zinc oxide NPs is one of the mostly fabricated oxide semiconductor by PLAL due to its structural and optical properties[133]. In particular, ZnO NPs find applications in solar cells, transparent conductors, opto-electronics, and photovoltaics. Guillen et al. reported effect of liquid medium temperature and ablation fluence on the morphology of ZnO NPs synthesized by PLAL[134]. It was observed that formation of $Zn(OH)_2$ was favored for higher temperature of the liquid medium and spherical, nearly spherical and flake like nanostructures were observed by varying the liquid temperature. In a comparable work carried out by Fazio et al., effect of laser fluence on ZnO NP size was evaluated and a blue shift in the bad gap was identified for higher laser fluence indicating the possibility of particle size tuning by adjusting the lasing parameters[133]. Effects of liquid medium temperature and different surfactants on ZnO NPs were reported by Ishikawa et al. ZnO nanorods were obtained for NPs synthesized in deionized water and surfactant solution by increasing liquid medium temperature or by post annealing of colloids prepared at room temperature[135]. They also suggested that a temperature not less than 60 °C is required for transformation of spherical ZnO particles into rods. Another mostly studied oxide nanomaterial by PLAL is TiO_2 due to its versatile applications such as photocatalysis, solar cells and chemical stabilities[136, 137]. Liquid phase laser ablation was effectively used to synthesize TiO_2 NPs by a number of researchers where, in most of the studies photocatalytic application of these particles were explored. Zimbone et al. synthesized TiO_2 NPs by PLAL which displayed both antibacterial and photocatalytic properties[112]. Discoloration rates in methylene blue test using TiO_2 NPs were found to be 0.7, 0.8, 4.8 and 10^{-4} min^{-1} for MB (without catalyst), α-TiO_2(commercial amorphous), laser generated-NPs and c-TiO_2(commercial polycrystalline) respectively where the high discoloration rate for the laser ablated NPs was attributed to the higher number of hydroxyl group. Hydrogen in these hydroxyl groups when bonded to oxygen acts as a trap for the holes and the MB particles are adsorbed to these centers[138]. Antibacterial activity of laser generated TiO_2 NPs was tested against E.Coli bacteria where the survival of them was dropped from 80% to 15% upon using the TiO_2 NPs[112]. When TiO_2 NPs were prepared in different SDS (sodium dodecyl sulfate) concentration, most stable TiO_2 colloid with high crystallinity and abundance was observed for a near micelle concentration (0.01 M)[136]. In addition to the synthesis of pure TiO_2 NPs, laser irradiation can also be used as a technique to transform white TiO_2 NPs to black-TiO_2, which possess improved optical properties for enhanced photocatalytic activity. A recent work demonstrates the laser irradiation strategy for white TiO_2 and their successful transformation into black TiO_2 employing a pulsed laser[139]. So far, synthesis and applications of ZnO and TiO_2 NPs were discussed since these are two of the mostly studied oxide NPs by PLAL. However, other oxides such as Al_2O_3, NiO and Mn_3O_4 were also reported by PLAL by various authors[140-142]. For instance, laser generated Al_2O_3 NPs showed photoluminescence attributing to the oxygen vacancy defects and defects formed in the non-equilibrium phases due to the laser ablation synthesis in a liquid confined ambient[142]. On the other hand, NiO and Mn_3O_4 NPs having diameter less than 10 nm were synthesized by PLAL where Mn_3O_4 particles were effectively used for removing pentachlorophenol from aqueous solution[140, 141]. In addition to the above-mentioned oxides, oxide quantum dots have been also reported by PLAL. For example, SnO_2 quantum dots having diameter in the range 1-5 nm were prepared by a single step laser ablation process[143]. As generated SnO_2 quantum dots exhibited emission in the blue-green region due to the recombination of the trapped charges and electrons generated during photon absorption as well as due to the oxygen vacancies present in the synthesized dots. Antimony oxide (Sb_2O_3) is another example of oxide NP obtained through PLAL by ablating an antimony target in liquid media. In this case, when ablation was carried out in distilled water yielded nanofiber-like morphology, while in SDS solution, powder-like sample was resulted.

1.3.3 Sulfide and selenide nanoparticles by PLAL

Different sulfide and selenide NPs have also been reported so far by PLAL, but in contrast to the oxides where ablation of metallic targets in liquid leads to reactive ablation forming the oxide particles, in this case, usually targets of the desired compound itself (sulfide/ selenide) is ablated in organic solvents. Water is often excluded from the choice of solvents to reduce the possibility of oxide formations due to the reactions between hot ablated plasma with the molecules in the liquid media since water contains free oxygen and thus is highly reactive. The generated NPs usually possess similar structure and composition as that of the ablation target where the major role of the liquid medium is providing a platform for the dispersion of the laser generated particles like in the case of noble metal ablations. Tin sulfide (SnS)[144], cadmium sulfide (CdS)[80, 145, 146], molybdenum disulfide (MoS_2)[147-149], tin disulfide (SnS_2)[79], molybdenum selenide ($MoSe_2$)[150], antimony sulfide (Sb_2S_3)[151, 152], copper antimony sulfide ($CuSbS_2$)[153] and copper indium gallium selenide (CIGS)[131, 154] are some of the examples of sulfide NPs prepared so far by PLAL. In a most recent work, $CuSbS_2$ NPs were prepared by irradiating a $CuSbS_2$ target in different organic solvents using 532 and 1064 nm Nd:YAG lasers. The nanoparticles obtained in general presented a spherical morphology with varying sizes as either the liquid medium or the ablation wavelength was varied resulting in a change in the optical band gap. These particles were finally applied as an absorber layer in solar cells of structure glass/ITO/CdS/$CuSbS_2$ or glass/ITO/CdS/Sb_2S_3/$CuSbS_2$ and a maximum photoconversion efficiency of 0.65% was achieved. Even though, the obtained efficiency was much lower compared to the commercial solar cells up to date, the form of the J-V curves showed a good interface between the n-type CdS and laser ablated p-type $CuSbS_2$ NPs[153]. Similar way, CdS NPs were also prepared in organic solvents by PLAL where the effects of ablation wavelengths and liquid medium on the particle morphology was investigated and these particles were later used for photocatalytic reduction of methylene blue[80]. A solar cell consisting an absorber layer of CIGS prepared by PLAL was previously reported by Guo et al. having a reliable conversion efficiency of 7.37%[131]. Inorganic fullerene like MoS_2 particles were prepared by laser ablation of a MoS_2 target in water. These particles were later applied in cell viability studies together with human cells where the laser generated MoS_2 particles were found to be non-toxic up to the stated concentrations. In particular, these particles displayed good biocompatibility and solubility which is highly beneficial for biomedical applications such as drug delivery, cancer therapy and friction-reduction coatings[147]. In another study, Compagnini et al. monitored the formation process of fullerene-like MoS_2 particles by PLAL and found that the generation of MoS_2 nanostructures was in competition with the oxidative atmosphere created by the laser induced plasma[148]. In a comparable report, highly biocompatible $MoSe_2$ NPs were synthesized by laser ablation of $MoSe_2$ target in 30 vol% ethanol/water mixture where the plasma quenching into planar $MoSe_2$ was facilitated by the solvent[150]. Guillen et al.

synthesized luminescent SnS NPs in aqueous and organic solvents by PLAL which showed emission in the blue-green region[144].

1.3.4 Other semiconducting nanoparticles by PLAL

In addition to the oxides, sulfides and selenides, other semiconducting materials such as single element semiconductors (such as Si, Ge), tellurides etc. have also been synthesized by PLAL. Silicon (Si) is one of the mostly studied pure semiconductor material due to its versatile properties and applications in various fields[92, 155-163]. Svrcek et al. reported synthesis of blue luminescent Si NPs by nanosecond pulsed laser ablation in a transparent polymer and water where crystalline Si target was used as the target for ablation[163]. In another study by Perminov et al., Si NPs were prepared in water, glycerol and liquid nitrogen where the mean size of the synthesized particles depended on the liquid composition[161]. Laser generated big (around 20-100 nm) Si composite polycrystals were transformed into small (3-5 nm) Si nanocrystal by a post ultrasonication process in the presence of hydrofluoric acid[157]. Purity of such Si NPs generated by PLAL make them suitable candidates for various applications. For instance, colloidal Si NPs prepared by laser ablation was used as a contamination-free photosensitizer with potential advantages such as low dark toxicity, easy removal and non-photobleaching $^1O_2$[155]. As another pure semiconducting material, Ge was also synthesized by PLAL by ablating Ge target in acetone[164]. In addition to the pure semiconducting materials, some other semiconductors have also been reported by PLAL. For example, NPs of CdTe was synthesized by Semaltianos et al. employing a femtosecond laser of pulse width 180 fs, wavelength 387 nm and pulse repetition rate of 1 kHz where the particles exhibited deep red photoluminescent properties[165].

1.4 SnS and SnS_2 nanomaterials

1.4.1 Introduction

SnS and SnS_2 are semiconducting materials having earth abundant, less expensive and less toxic constituents (tin and sulfur) and hence are becoming candidates for future multifunctional devices. While both materials consist only Sn and S, they differ in their crystal structures as well as in the corresponding properties. SnS is normally considered as a p-type semiconductor while SnS_2 is often reported as an n-type semiconductor. Bulk optical band gaps of both compounds also differ where SnS has a much lower band gap (1.3 eV)[166] compared to SnS_2 (2.2 eV)[167] for direct transitions. Since, the main focus of this thesis is on synthesizing and evaluating the properties of SnS and SnS_2 nanomaterials and thin films, it is worth to mention the most important features of these two compounds. Therefore, the most important properties, applications and common synthesis methods of SnS and SnS_2 are described in this section.

1.4.2 Properties

SnS is a semiconducting material belonging to the IV-VI group and having a stable low symmetric, double-layered orthorhombic crystal structure with lattice parameters a = 0.4329, b = 1.1192 and c = 0.3984 nm[168]. Due to the structural lattice arrangement with cations and anions, these layer-structured materials are of potential interest in different device applications. SnS exhibits strong anisotropic vibrational properties due to their layered structure and therefore significant variations in their physical properties are noticed when measured along the crystallographic axes[169, 170]. Different layers in SnS are held together by weak Van der Waals force which provides intrinsically a chemical inert surface without surface density states and dangling bonds which makes the SnS surface free from Fermi level pinning [171, 172]. Since each layer of SnS is attached to another through weak Van der Waals force, they can easily be separated perpendicular to the "c" axis. Orthorhombic disordered crystal structure is observed for SnS at ambient temperatures and pressures which belongs to the space group P_{bmn} $(D^{16}{}_{2h})^{12}$ with corresponding JCPDS number 39-0354. The SnS crystal structure can be viewed as a slightly disordered NaCl structure since the electron pairs from Sn are drawn by the highly electronegative S atoms and becomes [Ne] $3s^2$ $3p^6$ and [Kr] $4d^{10}$ $5S^2$ $5p^0$. The non-bonding lone pair electrons from the 5s level of Sn distort the lattice significantly to convert from the rock-salt structure to disordered orthorhombic layered structure[168]. In the orthorhombic structure, each Sn atom is coordinated by six S atoms with three short Sn-S bonds having average length 0.266 nm. Even though the normal crystal structure exhibited by SnS is orthorhombic, while increasing the temperature a structural transformation into tetragonal structure can be observed[173]. Work function and dissociation energies of SnS are ~4.2 and ~4.5 eV respectively at room temperature[174, 175]. Moreover, SnS exhibits high melting (880 °C) and boiling (1230 °C) points and chemical stability towards acidic solutions[176].

Proportionate Sn vacancy sites induced by the excess of non-metallic atoms introduce two positive holes per every anion which gives the p-type conductivity to SnS[175]. SnS possess direct and indirect band gaps under normal temperature and pressure conditions where the indirect band gap varies from 1.07 to 1.25 eV and direct band gap varies between 1.30 and 1.39 eV depending on the growth conditions[168]. SnS also possess a high absorption coefficient on the order of 10^4 cm^{-1}. Both the band gap and high absorption coefficient of SnS are suitable for visible light harvesting and hence SnS is a suitable candidate in photovoltaic and opto-electronic device applications. SnS single crystals exhibit p-type conductivity and the conductivity varies from 10^{-1} to 10^{-4} Ω^{-1} cm^{-1} with a hole concentration of ~10^{17} cm^{-3} at ambient temperature[177, 178]. Conductivity of SnS thin films grown by dipping methods found to increase significantly with the alkalinity of $SnCl_2$ solution and the films showed an acceptor activation energy of ~0.3 eV[179]. SnS thin films exhibited a broad PL band located around 625 nm attributed to the Sn-vacancies at the deeper levels for the films grown by SILAR (successive ionic layer adsorption and reaction) method[180].

On the other hand, SnS_2 exhibit a layered structure possessing high polytypism resulting from the different stacking sequences of identical S-Sn-S[181]. Depending on the growth conditions, SnS_2 can exhibit several polytypes consisting 2H, 4H and 18R[182]. Different stacking orders of the layers produce a unique crystal structure even though the atomic structure of SnS_2 is defined. As an intrinsic semiconductor, bulk SnS_2 possess an indirect band gap of 2.18 eV whereas few-layer or monolayer SnS_2 exhibit increased band gap of ~ 2.41 eV[181]. SnS_2 exhibit a CdI_2 type (a = 0.3648 nm, c = 0.5899 nm) layered structure where tin cations in an octahedral coordination are sandwiched between two layers of hexagonally close packed sulfur atoms[183]. While the sulfur atoms form densely packed hexagonal layers, tin atoms are arranged inside these layers to form a stacking sequence of S-Sn-S along the *c*-axis of the crystal. In such an arrangement, each Sn atom is surrounded by three S atoms of each layer to form an octahedron. The bonds between these layers are weak Van der Waals type and hence like SnS, SnS_2 layers can be cleaved easily through the (0001) basal plane[184]. SnS_2 can easily accommodate guest species into the matrix and adapt to volume changes owing to the two dimensional (2D) layered characteristics of this material with a large interlayer spacing (c = 0.5899 nm)[185].

Reported conductivities of SnS_2 vary from 10^{-7} to 0.07 Ω^{-1} cm^{-1} whereas electron mobilities range from 15 to 52 cm^2 V^{-1} s^{-1} with carrier concentrations between 10^{15} and 10^{18} cm^{-3}[186-188]. Carrier mobility in SnS_2 along the *c*-axis shows normal lattice scattering ($\mu_n \propto T^{-1.9}$) while the mobility parallel to the same axis is associated with a hopping mechanism showing an exponential temperature dependence and an activation energy of 0.18 eV[186]. Due to the wide interest on both SnS and SnS_2, their nanoparticles and thin films have been synthesized using various techniques up to date. Hence the following section briefly summarizes different synthetic approaches that have been employed so far to synthesize these materials.

1.4.3 Synthesis methods

Depending on the desired properties and applications, different physical and chemical synthesis methods are used for preparing both SnS and SnS_2 nanocrystals, nanoparticles and thin films. Many of these synthesis techniques are common for SnS and SnS_2 since these materials differ primarily just in their composition. SnS thin films have been prepared through a number of chemical methods. Most of these methods are economic and simple however, the poor control over chemical composition of the obtained films and less quality of the films (not device grade) are some disadvantages[168]. Chemical bath deposition (CBD) or chemical precipitation method was used for the deposition of SnS and SnS_2 thin films from the corresponding precursor solutions and at specific bath temperatures[189, 190]. Guneri et al. studied the effect of deposition time on the electrical, optical and structural properties of SnS thin films prepared by CBD technique and found that the resistivity values depend on the deposition time of the films[191]. Moreover, SnS thin films having different crystal structures have been also reported using CBD method[192]. Another simple approach to obtain SnS thin films is dipping. SnS films were prepared by dipping substrates into a mixed solution containing stannous chloride dihydrate (2.22 M) and thiourea (1.31 M) [$Sn(NH_2)_2$ and $SnCl_2$ $2H_2O$] at a pH of 3 followed by heating in a furnace at 300 °C for 5 minutes[193]. Electrochemical deposition is another method used where the film deposition is carried out by passing electric current through a conductive medium[168]. SnS and SnS_2 thin films/ nanocrystals were also prepared by means of chemical vapor deposition technique (CVD)[194, 195]. Price et al. fabricated SnS and SnS_2 thin films by CVD method by the reaction of $SnCl_4$ and H_2S where SnS_2 was formed for substrate temperatures up to 500 °C and orthorhombic SnS was obtained for reaction at 545 °C[195]. Amorphous SnS and polycrystalline SnS_2 thin films were also reported by spray pyrolysis method from the same chemical precursors but at different substrate temperatures[196]. In this case however, both films showed n-type conductivity as confirmed by the thermoelectric probe method. High quality thin films of tin sulfides (SnS and SnS_2) were fabricated by atomic layer deposition (ALD) method[197, 198]. In contrast to the other synthetic methods, ALD can provide depositions controlled in atomic scale and with better control over the film thickness. Physical deposition methods such as thermal evaporation, molecular beam epitaxy (MBE), sputtering and sulfurization are also widely employed techniques for SnS thin film fabrication[168]. However, different methods are used for fabricating other nanostructures of these materials. Wet chemical synthesis[199, 200], solid state reaction[201] and gas phase laser photolysis[202] are some examples. Guillen et al. synthesized SnS NPs using pulsed laser ablation in liquid by ablating SnS target in water and other organic solvents where the effect of laser wavelength and fluence on the particle morphology was evaluated[144].

1.4.4 Applications

Owing to the unique and versatile properties, SnS and SnS_2 are considered as promising candidates for wide range of applications. These applications may cover areas from opto-electronics through photovoltaics to photocatalysis and energy storage. Most of the applications of SnS and SnS_2 are based on the enhanced properties arise due to the layered structure of these materials together with their ability to harvest visible light due to the suitable optical band gaps. This section will provide an overview of the most important applications of these two materials reported by various researchers. In comparison with SnS_2, SnS has a smaller band gap with p-type conductivity and thus is more compatible for solar light harvesting applications. Hence, SnS is widely attracting attention as a stable, low cost and environment friendly absorber layer in solar cell devices. Even though the reported efficiency of SnS based solar cells are quite low in comparison with single crystal Si based solar cells or perovskite based solar cells, earth abundant low-cost constituent elements and less toxicity make SnS still a strong candidate in the photovoltaic (PV) applications. The highest efficiency reported so far for a SnS based solar cell is 4.4% by Sinsermsuksakul[203]. This efficiency was achieved by reducing the recombination at the grain boundaries by annealing the SnS thin films in presence of H_2S and thereby reducing grain boundaries by increasing the grain size of SnS. Moreover, a few SnO_2 monolayers were introduced to reduce the recombination near the p-SnS/n-Zn(O,S) junction. SnS based solar cells with an efficiency as high as 3.88% was also reported for the films prepared by congruent thermal evaporation[204]. Burton et al. pointed out a band misalignment with commonly used buffer layers and back contacts as a possible origin of the low conversion efficiency in comparison with other absorbers such as CdTe, $CuInSe_2$ and Cu_2ZnSnS_4[205]. Many other attempts have been also carried out to overcome the efficiency limitations of SnS based solar cells by different authors[206-208]. Gas sensing and light detection is another important field of application of SnS due to the high absorption coefficient and layered structure. For instance, Lu et al. studied gas dependent photoresponse properties of photodetectors based on SnS NPs and found that the adsorbed gas molecules play significant roles in photosensitive properties of SnS[209]. Ultrathin single crystalline nanoribbons of SnS obtained through a solution synthesis method were also effectively used for photodetection applications[210]. SnS based flexible photodetectors, photodetectors for visible and near infrared detection based on SnS thin crystals or SnS thin films were also reported[211, 212]. In addition to the PV and photodetector applications, SnS based nanomaterials have been also used for other applications such as visible light photocatalysis[213, 214], photo electrochemical cells[215, 216] and charge storage[217-219].

On the other hand, SnS_2 is widely exploited for charge storage, photodetection and photocatalytic applications due to its unusual properties originating from the 2D layered structure. Thin crystals of SnS_2 synthesized by chemical vapor deposition was used for fast photodetection by Su et al.[194]. In this case, thin crystal arrays of SnS_2 was grown at predefined locations on a chip with photocurrent response time as high as ~5μs. Xia et al. demonstrated large scale growth of 2D SnS_2 crystals driven by screw dislocations for photodetector application but the photoresponse time was ~42 ms[220]. Ultraviolet to near infrared photodetection capability of SnS_2 nanosheet microsphere film was also studied previously [221]. Due to the chemical stability in acid or neutral solutions and non-toxic nature, SnS_2 has the potential to be an efficient visible light photocatalyst[222]. Hence SnS_2 or SnS_2 based composites have been widely investigated for visible light photocatalytic applications. In a comparative study made by Li et al. to investigate photocatalytic activity of different dyes on SnS_2 and CdS, SnS_2 displayed much higher activity for the degradation of organic dyes containing N=N double bond[223]. Different morphologies of SnS_2 such as flower-like, nanosheets and nanoflakes were also synthesized by various synthetic approaches for photocatalysis[224-226]. For SnS_2 nanoflakes synthesized by heating the mixture of $SnCl_2 \cdot 2H_2O$ and excess sulfur powders at different temperatures in the range 200-240 °C, the one prepared at 200 °C outperformed the others by presenting a methyl orange degradation of nearly 100% and 86% for the first and fifth cycles respectively after 60 min. illumination[226]. 2D architecture of SnS_2 is highly beneficial for charge storage applications as well. Laterally confined (<150 nm) 2D SnS_2 nanoplates were used as an electrode material for Lithium ion (Li ion) battery with extraordinary high discharge capacity[227]. Discharge capacity of such an electrode during the first cycle was found to be 1311 $mAhg^{-1}$ which was close to the sum of theoretical irreversible capacity (587 $mAhg^{-1}$) and maximum theoretical reversible capacity (645 $mAhg^{-1}$). SnS_2 nanosheets having thickness ~2 nm synthesized by a one-step solvothermal process displayed excellent charge-capacity retention of ~95% even after 50 cycles[228]. Many researchers also investigated in enhancing the performance of SnS_2 based anode materials by combining them with other materials. Graphene is one of the commonly used material together with SnS_2 due to its unique properties. For instance, 2D graphene-SnS_2 and few-layer SnS_2-graphene hybrids were fabricated by different authors with enhanced Li ion performance[229, 230]. Even though not as widely investigated as SnS for solar cell applications, SnS_2 has been tested by some searchers for PV applications as well. For example, Tan et al. used SnS_2 colloidal quantum dots for organic/inorganic hybrid solar cell application[231]. SnS_2 was applied by different authors as counter electrodes in dye-sensitized solar cells[232-234]. Tin disulfide has been also used for a number of other applications including antibacterial activity[235], optical sensor[236], hydrogen generation[237], electrocatalysis[238] and supercapacitors[239].

1.5 Thin film fabrication from colloidal suspensions and spray deposition

1.5.1 Thin film deposition using nanocolloids

Thin films are usually deposited from their corresponding chemical precursors or from solid compounds. In such cases, the thin film properties and composition are controlled either by adjusting the molar ratios of the precursors or by varying the deposition conditions. But, when thin films with unique characteristics and predefined properties are needed to be fabricated, normal thin film deposition techniques are of less interest. One reliable alternative is direct thin film fabrication from the respective colloidal suspensions of NPs of the material. When thin films are fabricated from colloidal NPs, the film formation process is less complicated and thus one can achieve better control over the film morphology and properties since they are primarily ruled by the properties of the NPs in the suspension. Moreover, this method would significantly reduce thin film deposition time with the additional benefits of film deposition at ambient temperature and pressure conditions in contrast to the chemical synthesis methods which include tedious procedures or high temperature processing. Since the NPs of the desired material is used as the source material, film composition may remain exactly the same unless large variations in the deposition parameters are utilized. In this section of the thesis, thin film depositions using colloidal suspensions of various materials reported so far are summarized. Lee et al. reported fabrication of all-nanoparticle conformal thin film coatings by aqueous-based layer-by-layer processing in 2006[240]. TiO_2 and SiO_2 NP suspension were used for the film deposition process where the films exhibited a porous structure. These nanopores existed in the thin films resulted in antireflection, antifogging and superhydrophilic properties. CdTe thin films were deposited by spraying NP precursors by different authors[241, 242]. Schulz et al. prepared insoluble CdTe NPs by a metathesis approach and subsequent thin film deposition by spraying these NPs onto heated substrates[241]. Thin film deposition was carried out in one or two steps at elevated temperatures (280 – 440 °C) or lower temperatures (25-125 °C) respectively where the films prepared at lower temperatures were undergone a post annealing process. While the ones prepared by annealing low temperature synthesized films exhibited a pure cubic CdTe phase, the films obtained by one-step deposition at higher temperature resulted in the formation of some oxide besides the cubic CdTe phase. In another report, CdTe NPs having average size 3.9 ± 0.8 nm was used for film deposition by spray, while the films were fabricated at growth temperatures of ~200 °C lesser than conventional spray pyrolysis technique[242]. In normal spray pyrolysis, usually high substrate temperature is required since this thermal energy is supplied for carrying out the chemical reaction between the different precursors and thereby forming the final compound. But in case of thin film deposition from nanocolloidal suspensions, since the desired material is already present in the form of NPs, the films can be formed at temperatures significantly lower than normal spray pyrolysis or other chemical synthesis alternatives. Au/TiO_2 composite thin films were also prepared by spray deposition of NPs[243]. Surface plasmon absorption maximum of the films was varied from 544 nm to 600 nm while substrate temperature during spray deposition was deviated from 200 °C to 550 °C. Some authors used spin coating technique instead of spray deposition for fabricating thin films from NP suspensions[244, 245]. ZnO thin films obtained in such a way showed a resistivity of 1.89×10^5 Ω.cm when deposited on quartz substrates[244]. Toolan et al. studied the mechanisms of self-assembly and dependence on difference dispersion properties such as solvent viscosity, volatility and particle weight fraction for latex colloids[245].

1.5.2 Thin film deposition from laser generated nanocolloids

Laser generated nanocolloids can be effectively used for thin film deposition owing to the easiness of the NP synthesis and purity of the generated NPs in the colloidal form. Moreover, PLAL gives control over the morphology and properties of the nanoparticles produced by adjusting the lasing parameters or liquid composition. Hence the thin film properties are predetermined up to an extent by PLAL where the formed films can be used for further applications even without further processing. Fabrication of thin films from laser generated colloids is not totally new since some authors have already reported the same. For example, Guo et al. used electrophoretic deposition (EPD) technique to fabricate thin films of Cu(In,Ga)Se_2 (CIGS) from laser ablated colloids for solar cell application[131]. The fabricated solar cell showed a photoconversion efficiency of 7.37% for an active area of 0.132 cm^2 with open circuit voltage being 0.363 V, short-circuit current density of 34.58 mA/cm^2 and fill factor 58.76%. However, in this case, only Cu-In-Ga NPs were produced by PLAL and then after the EPD process the films were selenized to obtain CIGS. Surface charge of the NPs acquired by electrostatic stabilization during the PLAL process is exploited for depositing the films when an electric field is applied. In another study, Sun and Tsuji demonstrated thin film deposition of Sb_2S_3 by spin coating from laser generated colloids[152]. Sb_2S_3 NPs having stoichiometric composition were prepared in water by laser ablation while argon gas bubbling was used to remove the dissolved oxygen in the solvent. The obtained films displayed reliable semiconducting properties (density and carrier mobility) and good visible light absorption which are highly beneficial for PV application. Even though the as obtained films showed an amorphous structure, low temperature annealing (200 °C) led to the formation of crystalline thin films. Even though not many authors have shown interest in developing thin films from laser generated colloids, the above-mentioned works demonstrate that thin films obtained from laser processed colloids are suitable for device applications because of the special morphology, properties and low temperature processability.

1.5.3 Spray deposition

Spray deposition provides many advantages over other alternative thin film fabrication methods. This section of the thesis presents some of the important aspects of this technique. In a normal spray pyrolysis method, a precursor solution is pounded using a neutral gas so that very fine droplets arrive at the heated substrate. Due to the thermal energy provided by the substrate, the constituents react on it thereby forming the chemical compound. The chemical precursors are selected in such a way that all other byproducts than the desired compound are volatile at the temperature of deposition[246]. A normal spray pyrolysis unit consists of a spray nozzle, substrate heater, temperature controller and air compressor. Properties of the films deposited using this technique depends on the spray rate, anion to cation ratio, ambient atmosphere, substrate temperature, droplet size, carrier gas and cooling after deposition while the film thickness is primarily governed by the distance between the substrate and spray nozzle, substrate temperature and precursor solution concentration. Spray pyrolysis technique is widely employed for depositing thin films of metal oxides, binary, ternary and quaternary chalcogenides and superconducting oxides[246]. Schematic representation of a simple spray deposition system is presented in Fig.1.2. Spray technique can be used for thin film fabrication in a cost-effective manner for large area depositions. Moreover, this technique also possesses the advantage of depositing very thick films of high quality with practically no limitation on the film thickness.

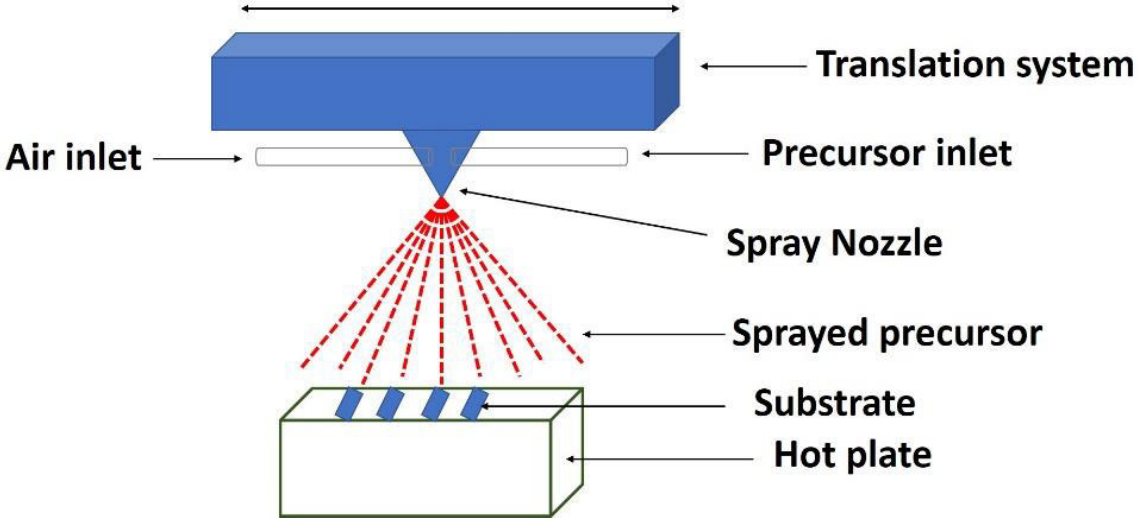

Fig.1.2. Schematic representation of a simple spray deposition system

1.5.4 Applications and advantages of combining PLAL with spray technique

Combining PLAL with spray deposition may have many advantages owing to the versatilities associated with both techniques. The term "spray deposition" is intentionally used instead of "spray pyrolysis" since no chemical reaction is expected to be carried out on the substrate. NP synthesis by PLAL is an emerging technique with many unique characteristics as mentioned in the previous sections. The main advantages of PLAL includes synthesis of a wide variety of materials including semiconductors and metals. Moreover, the nanocolloids obtained from PLAL do not usually require any post processing purification processes since the NPs are directly dispersed into the solvent and hence exhibit unique surface properties due to the absence of ligands or capping agents. Control of the lasing parameters and liquid composition in a good manner will lead to fine tuning of the morphology, composition and properties of the laser generated NPs. Even though normal spray pyrolysis is carried out at elevated temperatures to initiate the reaction between the supplied precursors, when spray deposition from laser ablated nanocolloids is carried out, in contrast, the film deposition can take place at relatively lower temperatures. Since the NPs of the desired material is already present in the colloid, they do not need to undergo any kind of reaction on the substrate surface while sprayed unless required.

However, in some cases, at higher temperatures oxide thin films can be prepared by spraying metallic NPs where they can react with the atmospheric oxygen leading to the formation of their corresponding oxides. The primary role of the substrate heating in spray when laser generated colloids are used is to evaporate the solvent and to provide sufficient kinetic energy to the NPs reaching on the substrate. Hence, when organic solvents with lower boiling points are used as the liquid medium in PLAL, in the later step for thin film deposition, substrate temperatures even below 100 °C can be used. Moreover, the NPs in the colloidal form already present a crystalline nature and therefore thin films prepared from them would also be crystalline as prepared without any further heat treatments which is highly beneficial for device applications. Morphology and properties of such fabricated thin films would be primarily ruled by the characteristics of the NPs produced by PLAL. However, the spray parameters such as spraying speed, distance between the nozzle and the substrates and substrate temperature also influence the final morphology of the films. By controlling the NP morphology by PLAL, thin films with special morphologies and unique properties can be generated. Spray deposition is widely known for large area depositions at relatively less cost and with no practical limitations over film thickness. In this case, the film thickness would primarily depend on the amount of the nanocolloidal suspension sprayed and the concentration of the suspension. Therefore, when PLAL is combined with spray deposition, thin films with special morphologies and properties can be fabricated easily which can be applied in opto-electronic and photovoltaic applications. High quality "nano" devices can be produced cost effectively without compromising the performance. Considering the above-mentioned advantages and high application possibilities, it is worth to combine PLAL with spray deposition technique for converting the colloidal NPs into solid thin films. This effective combination can also reduce the chemical contamination due to thin film fabrication in comparison with many chemical synthesis methods. Since the NPs are itself dispersed in contamination free solvents and thin films are fabricated by directly spraying these colloids onto heated substrates, no toxic or contaminated byproducts are generated either during the NP generation or the thin film deposition.

1.6 Hypothesis

Thin films can be synthesized using spray technique from nanocolloids obtained by pulsed laser ablation in liquid in which the ablation parameters (laser wavelength, fluence, repetition rate) and solvent properties (refractive index, polarity and viscosity) can influence the morphology and properties of the NPs as well as thin films.

1.7 Objectives

1. To synthesis binary chalcogenide (SnS and SnS_2) NPs by PLAL
2. To characterize laser generated SnS and SnS_2 NPs by TEM, XRD, XPS, Raman, UV-Vis spectroscopy and photoluminescence spectroscopy for their morphology, structure, elemental composition, chemical states and optical properties
3. To study the effect of different laser parameters (laser wavelength and ablation fluence) and liquid medium on the morphology and properties of the NPs
4. To deposit thin films of SnS and SnS_2 by spray technique using the laser ablated nanocolloids as corresponding precursors
5. To characterize the deposited thin films for their morphology, crystal structure, chemical states, optical properties, opto-electronic properties and electrochemical properties by employing various characterization techniques
6. To investigate the effects of lasing parameters, liquid medium, NP morphology and post annealing process on the thin film properties and morphology
7. To fabricate nanocomposite thin films of SnS and reduced graphene oxide by spray technique, their characterization and incorporation into PV devices

1.8 Justification

Pulsed laser ablation in liquid is an emerging technique for producing nanoparticles of semiconductors, metals and metal oxides by one-step method. Among other nanoparticle synthesis methods, PLAL possess the advantages as generating high purity nanocolloids in short time without the use of stabilizers/surfactants. Moreover, no toxic byproducts are generated after the PLAL process since the nanoparticles are dispersed into the surrounding liquid medium producing a concentrated colloidal suspension of the desired material. Morphology and properties of the nanoparticles can be tuned in an effective manner by accurately controlling the ablation parameters such as wavelength, repetition rate and fluence and the liquid composition. SnS and SnS_2 are binary chalcogenide semiconductors that find applications in a number of different areas including photovoltaics, opto-electronics, photocatalysis and charge storage. These materials attract wide attention due to their earth abundance, low cost of the constituents and versatile properties. Producing nanoparticles of these materials by PLAL can thus stimulate the application possibilities of them owing to the peculiarity of the synthesis method and characteristic features of these semiconductors. SnS and SnS_2 NPs are generated in different organic solvents by PLAL where effect of different lasing parameters on the particle morphology is investigated. However, since the NPs are generated in a colloidal form by PLAL, their application possibilities are limited. This study therefore focusses on combining the PLAL technique with spray deposition for converting the colloidal NPs by PLAL into thin films. Spray deposition is employed since it can be used for fabricating thin films on large areas cost-effectively. Such thin films will exhibit special morphologies and properties according to the properties of the synthesized NPs as well as the thin film deposition conditions. The special morphologies and promising properties would make these thin films suitable for applications in photovoltaics and opto-electronics. Moreover, the properties of the deposited thin films can be effectively controlled by adjusting the laser parameters, liquid properties or the deposition conditions. Effect of various lasing parameters (laser wavelength, fluence and repetition rate), solvent properties and deposition parameters were studied on SnS and SnS_2 NPs as well as thin films. Device performance of selected samples as photovoltaic prototypes is also verified including that of nanocomposite thin films consisting SnS and reduced graphene oxide.

Chapter 2

Experimental details of synthesis and characterization of nanoparticles, thin films and devices

2.1 Introduction

Nanoparticles of SnS and SnS_2 were synthesized by pulsed laser ablation of SnS and SnS_2 targets in different liquid media. Different parameters of the laser such as wavelength, laser fluence or repetition rate were varied to study the effect of these parameters on the NPs obtained in addition to the change of the liquid environment or solvent. Thin films of SnS and SnS_2 were fabricated using spray technique where the laser ablated nanocolloids were sprayed onto heated substrates. The laser ablation experimental configuration, parameters and spray deposition conditions were different depending on the desired properties of the generated particles or thin films. The NPs and their thin films were characterized for morphology, crystal structure, elemental composition and chemical states as well as optical, opto-electronic and electrochemical properties by different characterization techniques. Hence this chapter of the thesis deals with details of the experimental set-up used in each case of NP synthesis by PLAL and thin film deposition by spray as well as the characterization methods employed.

2.2 Laser generation of SnS and SnS_2 NPs

2.2.1 Laser synthesis of SnS NPs

SnS NPs were synthesized by irradiating a commercial SnS target (supplied by Beijing metals, China, 2” diameter and ¼” thickness) of purity 99.9% in isopropanol or DMF solvent (supplied by Fermont chemicals, Mexico) using the second harmonic output of an Nd:YAG pulsed laser (Solar laser systems, LQ-629) of frequency 100 Hz and pulse width 10 ns. The solvents were of analytical grade and used as supplied without any further purification steps in all experiments. The laser beam was focused horizontally onto the SnS target surface using a convex lens (focal length 15 cm) which was kept 10 cm away from the target. The measured laser spot size at this distance was 1.18 mm and the corresponding energy fluence calculated was 7.8 J/cm^2. During ablation, the liquid was continuously stirred using a magnetic stirrer to reduce the effect of NP post irradiation by the incoming laser pulses and a liquid layer thickness of 2 cm was maintained in each ablation experiment. Schematic of the laser synthesis of SnS NPs is given in fig.2.1. Photograph of the ablation set-up is presented in fig.2.2.

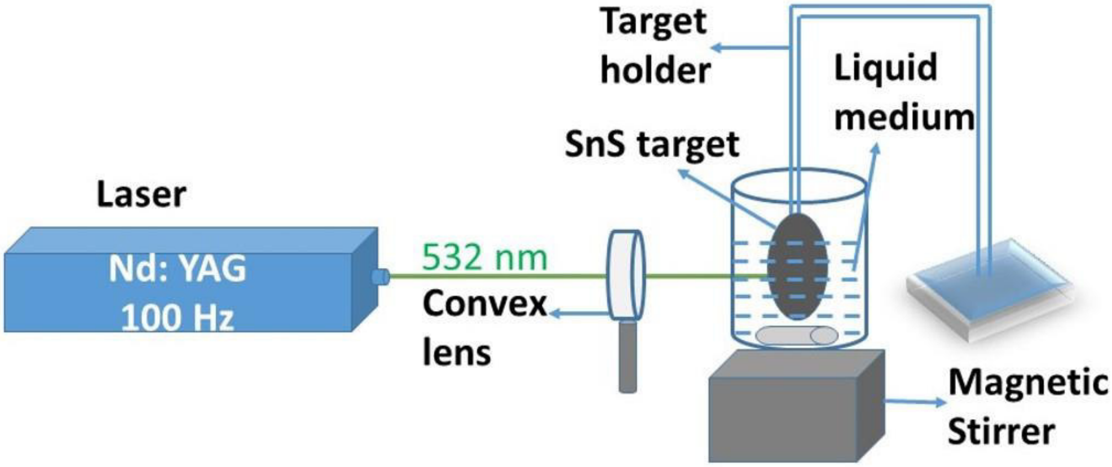

Fig.2.1. Schematic of the experimental set-up for SnS NPs synthesis by pulsed laser ablation in liquid

SnS NPs were also generated using a 1064 nm Nd:YAG pulsed laser (Solar laser systems, LQ-929) of frequency 10 Hz and pulse width 10 ns for preparing thin films of SnS and nanocomposites of SnS with reduced graphene oxide (rGO). Vertical laser configuration where the SnS target was irradiated from the top was employed in this case. During the ablation process, polished SnS target was immersed in a 250 ml Pyrex glass beaker containing an organic liquid (either dimethyl formamide or isopropyl alcohol). The target was kept at the bottom of the beaker maintaining a liquid layer thickness of 3 cm above the target. Disk shaped commercial SnS sputter target (purity 99.99%) was used for the ablation. Ablation was carried out for 5 minutes for each liquid medium. During ablation, the target was linearly translated at a speed of 100 mm/s using a microcontroller-based translation system to avoid deep ablation traces on the target as well as to reduce the effect of post irradiation on the produced NPs.

2.2.2 *Laser synthesis of SnS_2 NPs*

To study the effect of different liquid media and laser wavelength on the SnS_2 NP morphology, SnS_2 NPs were prepared in four different solvents using two different laser wavelengths. Disk-shaped SnS_2 target (2” *1/4”) of 99.9% purity was purchased from Beijing Metals, China. The target was polished with sand paper and rinsed gently with distilled water/isopropyl alcohol and dried at ambient conditions to remove any surface contaminants on the target. A pyrex glass beaker was filled with 50 ml of the respective solvent where the target was immersed in the solvent at the bottom of the beaker. The NPs were prepared by the LQ-929 Nd:YAG pulsed laser using the 1064 and 532 nm outputs. Measured laser fluence was 0.95 J/cm^2 for the 1064 nm output whereas 0.63 J/cm^2 for the 532 nm laser output.

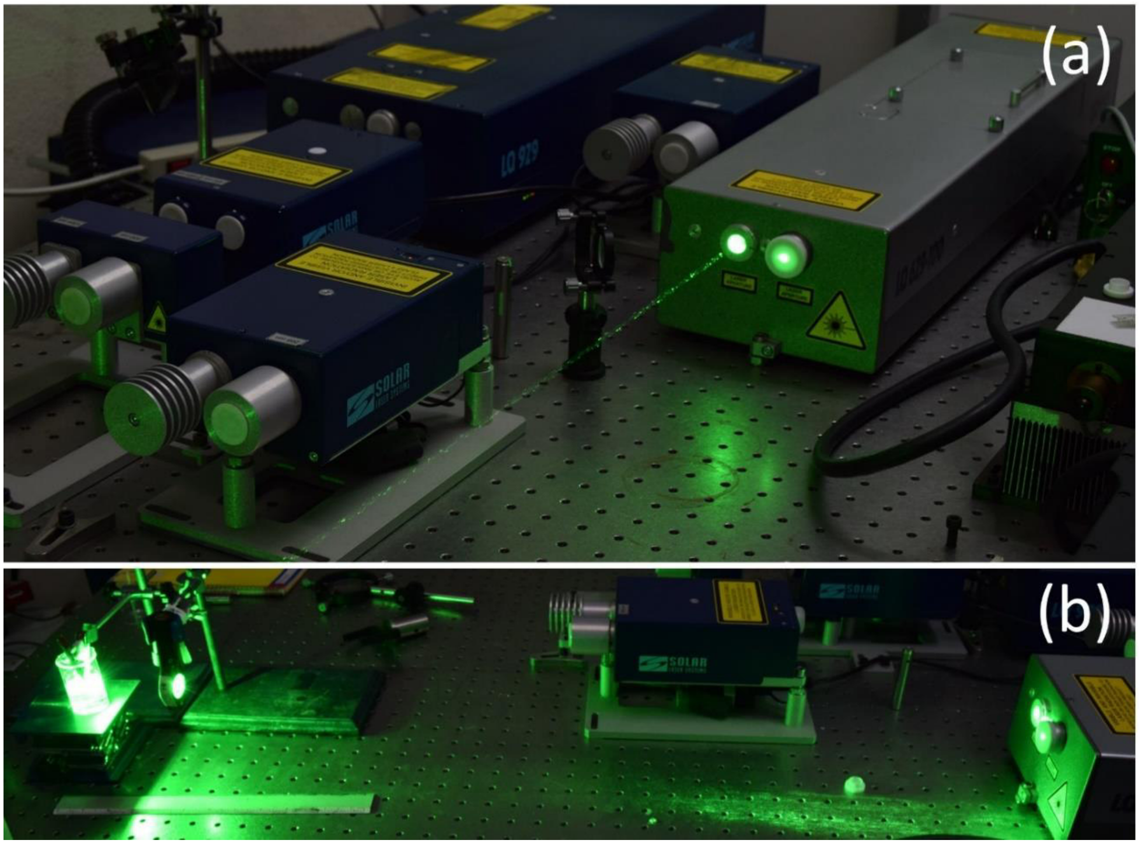

Fig.2.2 (a) Nd:YAG laser under operation (b) Experimental set-up for SnS NP synthesis by PLAL in horizontal configuration

During laser ablation, the target was scanned at a speed of 500 μm/s using a translational stage to avoid ablation craters on the surface of the target as well as to reduce the chance of post irradiation on the synthesized NPs by the incoming laser pulses. Acetone, isopropanol, ethanol and dimethyl formamide (DMF) were used as the solvents for ablation where the ablation time was only 30 sec. for all the solvents and both laser wavelengths.

To study the effect of laser fluence on particle morphology, SnS_2 NPs were generated in acetone, isopropanol and dimethyl formamide (30 ml in each case) using 532 nm output of the Nd: YAG pulsed laser (LQ-929). The laser spot was aligned to the surface of the target which was irradiated for 1min. Laser fluence studies were carried out by preparing NPs at four different fluences viz. 0.25, 0.37, 0.5 and 1.65 J/cm^2 in acetone and isopropanol. Ablation fluences of 0.25, 0.35 and 0.5 J/cm^2 were achieved by adjusting the laser parameters (YAG laser oscillator and amplifier energy parameters selected without affecting the pulse width and frequency). The output energy/pulse was measured using an energy meter (Thorlabs PM100D with ES245C pyroelectric energy sensor). The spot size was 10 mm (direct beam) for these fluences since no lens was used for ablation under these conditions. To obtain the laser fluence of 1.65 J/cm^2, a convex lens of focal distance 50 cm was fixed 20 cm away from the target (spot size of 5.5 mm, target above focus) where the laser was operated at the same conditions as that of 0.5 J/cm^2. SnS_2 NPs were synthesized in room temperature and 80 °C preheated DMF solutions to investigate the effect of liquid medium temperature on the nanoparticle morphology. But in this case the 100 Hz Nd:YAG laser was employed at a fluence of 2.9 J/cm^2. In this case also a convex lens of focal distance 50 cm was placed 40 cm away from the target to focus the laser beam (spot size 1.4 mm, target above focus). In addition to that, SnS_2 NPs generated in room temperature DMF was also post irradiated using the same laser (Nd:YAG, 532 nm, 100 Hz) for 5 min. using the direct laser beam at a fluence of 0.53 J/cm^2.

For deposition of SnS_2 thin films, PLAL was carried out using the second harmonic (532 nm) output of the 10 Hz q-switched Nd:YAG laser. Laser energy and fluence were respectively 450 mJ/pulse and 0.57 J/cm^2. The NPs were obtained in isopropanol and ethanol in this case. Each ablation experiment was for 30 seconds in 50 ml of each liquid medium after which the transparent solvent changed into golden yellow color due to the dispersion of the SnS_2 NPs.

2.3 Spray deposition of SnS, SnS:rGO and SnS_2 thin films

2.3.1 *Spray deposition of SnS thin films*

SnS thin film deposition was carried out using a homemade spray unit (designed by mechatronics students, FIME) with a hot plate and a spray nozzle (Spray Systems co., Mexico, Model: 1/4JCO-SS+SU11-SS) on well cleaned heated glass and ITO substrates from the corresponding SnS colloidal suspensions (SnS in DMF and SnS in isopropanol). The spray system was equipped with an automated movement in one direction and controlled air pressure. Photograph of the spray unit used is presented in fig.2.3. 100 °C and 200 °C were used as the substrate temperatures for isopropyl alcohol and DMF respectively and the spray pressure (compressed air) was 0.75 kg/cm^2 for both.

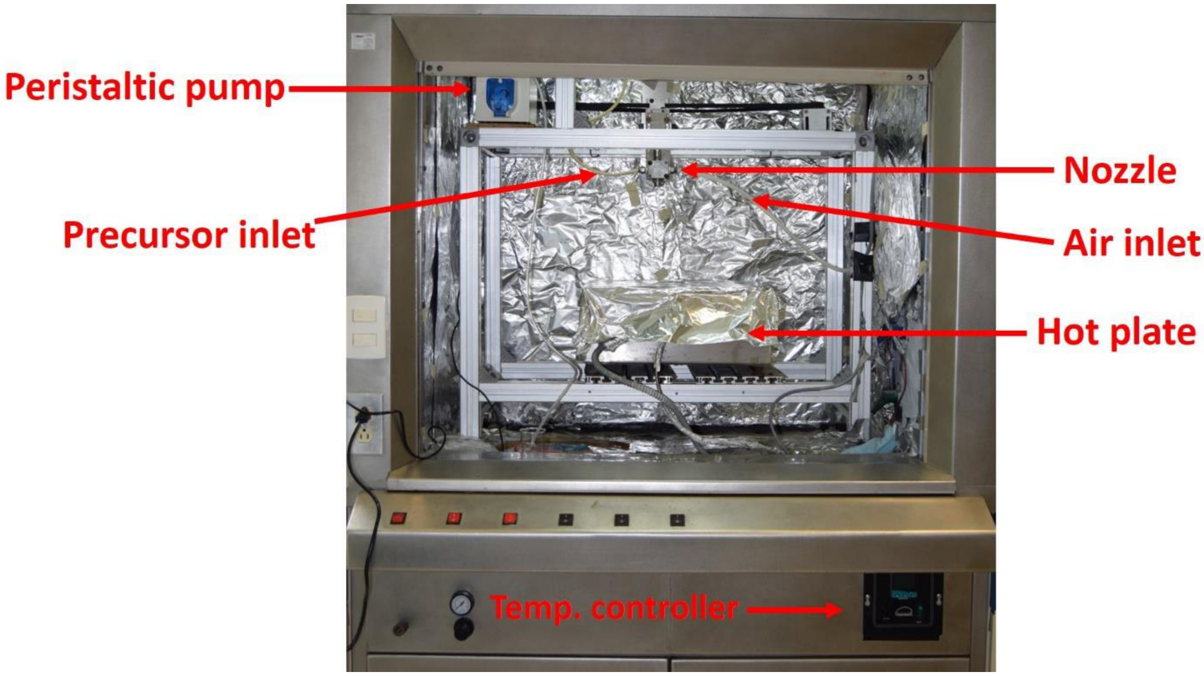

Fig.2.3. Photograph of the spray deposition unit used for SnS and SnS_2 thin film deposition

Vacuum annealing (380 °C for 1 hour) was employed for the as deposited films to improve the quality as well as crystalline properties of the SnS thin films.

2.3.2 *Spray deposition of SnS:rGO thin films*

For depositing SnS:GO nanocomposite thin films, SnS colloid prepared by PLAL in DMF or isopropanol was mixed with graphene oxide of concentration 4.3 g/l which was synthesized using Marcano´s method [247]. In a typical experiment of GO synthesis, 1g of graphite was placed in a mixture of concentrated H_2SO_4/H_3PO_4 (40:8 ml) and 5g of $KMnO_4$ was added into it. The mixture was heated to 40 °C and continuously stirred for 12 h. The reaction was cooled to room temperature and poured onto ice (150 ml) with 30% H_2O_2 (1 ml). The GO bright yellow dispersion was kept overnight to complete potassium permanganate neutralization and then GO was separated by centrifugation. The solid material was first washed with an acidic solution of 50 ml of water and 100 ml of 30% HCl. The GO dispersion was then finally washed by several centrifugation/re-dispersion cycles with deionized water until pH 6. The glass, ITO and Si wafer substrates for deposition were heated at temperatures 120 °C and 250 °C respectively for isopropyl alcohol and dimethyl formamide. Furthermore, the substrates were also preheated for 10 minutes at the specified temperatures to improve the film adhesion and quality. The substrate to nozzle distance was kept fixed (27 cm) and the spray pressure (compressed air) was 0.75 kg/m^2. SnS thin films were fabricated by spraying the pristine SnS nanocolloids and SnS:GO thin films by a mixture of SnS nanocolloid and graphene oxide. The deposition of SnS:GO thin film was as follows: Different concentrations of GO viz. 0.1%, 0.5% and 1% by volume were added to the SnS in IA as well as DMF nanocolloids and stirred well for 30 minutes at ambient temperature. The solution mixture was kept in an ultrasonic bath for 5 minutes for better dispersion and then sprayed onto heated substrates under the same spray conditions used for pristine SnS film depositions. The SnS:GO thin films obtained were darker than the bare SnS thin films due to the presence of GO. Pristine SnS and SnS: GO thin films were annealed at 380 °C for 1 hour in vacuum to improve their crystallinity as well as for the reduction of GO to rGO in the SnS:GO films.

2.3.3 Spray deposition of SnS_2 thin films

SnS_2 thin film deposition was carried out using the nanocolloids prepared by PLAL in ethanol and isopropanol. 1L of each nanocolloidal suspension was sprayed onto heated substrates (100 °C for both SnS_2 suspensions) to obtain thin films of SnS_2. The as prepared films were annealed in vacuum at different temperatures viz. 200, 250 and 300 °C to improve the crystallinity of the films and to study the changes in their morphology and properties.

2.4 Characterization of NPs and thin films

2.4.1 Morphology and crystal structure of the NPs by transmission electron microscopy (TEM)

TEM is considered as a premier and one of the most efficient method for characterizing materials at the nanometer scale[248]. As the name indicates, TEMs use electrons penetrating through a material for different kinds of information, specifically for the morphology of the very small particles. Electrons have the advantage over X-rays that they can be easily concentrated using electromagnetic lenses and therefore can be used for obtaining real-space images with resolutions on the order of a few tenths to a few nanometers[249]. In a typical TEM analysis, the electrons are accelerated at a very high potential (100 to 400 kV) and allowed to pass through a thin sample (usually less than 100 nm) and then viewed on a fluorescent screen. TEMs can be used for acquiring images at a very high resolution (called as high-resolution TEM or HRTEM) as well as for collecting electron diffraction patterns (Selected area electron diffraction or SAED) Due to the electronic excitations happen in the sample material upon interaction with the electrons, TEMs are usually equipped with EDX (energy dispersive X-ray) unit for identifying the elemental composition of the material being analyzed. The laser generated SnS and SnS_2 NPs were characterized by TEM (FEI Titan G2 80-300) for their morphology and crystal structure. Elemental composition of the SnS NPs was also determined by TEM-EDX. TEM samples were prepared by drying a small drop of the respective nanocolloidal suspension on Cu coated carbon grids at ambient conditions. Average size of the NPs was determined by counting the NPs in the TEM images and the HRTEM images and SAED patterns were utilized for information on their crystal structure.

2.4.2 Crystal structure analysis by X-ray diffraction (XRD)

Atomic structure of crystalline materials can be determined by X-ray powder diffraction analysis. The term powder refers to polycrystalline samples such as solid thin films grown on substrates. The principle behind the XRD technique is based on the reinforcement of the scattering wave in periodic array of atoms and cancellation of the wave in others while

X-rays interact with materials. A relationship between the incident X-ray wavelength λ, angle of incidence θ and the spacing between the lattice planes d can be written as follows:

$$\mathbf{n\lambda = 2d\sin\theta} \qquad (1)$$

where n is the order of diffraction. Such a relation is called Bragg's law based on which X-ray diffraction analysis works[249]. Crystal structure of the laser generated SnS_2 NPs as well as spray deposited thin films of SnS, SnS:rGO and SnS_2 were analyzed by XRD in grazing incidence mode (GIXRD). A Panalytical Empyrean X-ray diffractometer having Cu-Kα as the source was employed for recording the diffractograms of the samples. Samples prepared on glass or Si wafer were used for the XRD analysis. In most of the cases, the diffractograms were collected using an angle of incidence of 0.3° and by scanning in the two-theta range of 10-90 degrees. In the case of SnS samples, SnS thin films deposited from SnS in isopropanol and DMF as well as nanocomposite thin films of SnS and rGO with 1% GO concentration was analyzed by XRD whereas for SnS_2, the laser generated SnS_2 NPs in different liquid media and SnS_2 thin films obtained from SnS_2 in ethanol and isopropanol were analyzed. Moreover, in addition to the as prepared thin films, vacuum annealed samples were also studied to see the effect of thermal annealing on the crystallinity of the materials.

2.4.3 Elemental composition and chemical state analysis by X-ray photoelectron spectroscopy (XPS)

X-ray photoelectron spectroscopy is a surface analysis technique used for acquiring information on the elemental composition and chemical state of the materials. Interaction of high energy X-rays with the material results in ejection of photoelectrons from the core-levels of which the kinetic energy is measured and later estimated the binding energy (BE). Depending on the material and its chemical state, the BEs of each level differs and hence are used to identify each element present on the sample surface and the corresponding chemical state[250]. SnS and SnS:rGO thin films, SnS_2 NPs and thin films were analyzed by XPS employing an Al-Kα monochromatic radiation having energy 1486.68 eV (Thermo Scientific K-Alpha). In a typical XPS analysis, a low-resolution survey spectrum was used to identify the elements present whereas the chemical state analysis was done using a high-resolution photoelectron spectrum of each element (mostly Sn and S). The high-resolution spectra are deconvoluted into individual peaks if necessary by applying a Shirley-type background. All the survey spectra and high-resolution scans presented in the thesis are after applying an adventitious carbon correction at 284.6 eV. XPS was used to verify the presence of desired elements (Sn and S) and their oxidation states in the NPs as well as their thin films.

2.4.4 Crystalline phase analysis by Raman analysis

Raman analysis can probe the structure of both amorphous and crystalline solids, gases and liquids. It works based on the inelastic scattering of light by matter[249]. Raman analysis was carried out on NPs and thin films to identify the phases present. Raman active vibrational modes on each sample were identified using an excitation line of 532 nm (Thermo Scientific DXR Raman microscope). In majority of the cases, the thin films deposited, or NPs drop casted on Si wafer were used for Raman analysis to reduce the background noise in the recorded spectra.

2.4.5 Morphology by Scanning electron microscopy (SEM)

SEM provides information on morphology, topographical features, compositional differences and phase distribution of materials. After the interaction of the focused electron beam with matter, the outcoming secondary electrons or back scattered electrons or both are analyzed for different information regarding the sample. Field emission SEM (FESEM, Hitachi SU8020) was used for determining the surface morphology of SnS, SnS:rGO and SnS_2 thin films. Thin films deposited on ITO substrates were selected for the SEM measurements to have better charge compensation. Moreover, colloidal silver paint was applied between the sample and the metallic sample holder for improved charge transfer and thereby to acquire good quality images at high magnifications.

2.4.6 Optical absorption spectroscopy (UV-Visible spectroscopy)

After detailed studies on the structure and morphology, the optical properties of NPs and thin films were elucidated by means of UV-Vis spectroscopy. Measurement of attenuation of a beam of light after passing through a sample constitute the UV-Vis spectroscopy. Optical properties of the materials such as absorption, transmittance and reflectance can be evaluated using this technique[249]. A dual beam spectrometer (Jasco-V770) was employed to explore the optical properties of the laser synthesized nanocolloids as well as spray deposited thin films. In the case of NPs, the light beam was passed through the colloidal suspension kept in a 1 cm pathlength quartz cuvette keeping the respective solvent as the reference in the spectrometer whereas for thin films, glass substrates were used as the reference while scanning the light in the UV-Vis-NIR region. Later, from the absorption data, optical band gaps of the samples were estimated using the Tauc plot relation to study the effects of lasing parameters, liquid medium, spray conditions or post thin film treatments on the band gaps.

2.4.7 *Photoluminescence (PL) spectroscopy*

For investigating the electronic structure of semiconducting and semi-insulating materials, PL is a powerful characterization tool. It gives a clear picture of purity and overall crystal quality. Defect complexes and impurity concentrations in the samples can also be determined by this method. In this thesis work, PL spectroscopy was used to collect the emission spectra of the nanocolloids and thin film samples. The samples were excited using a wavelength in the range 345-350 nm depending on the material while the emission spectra were recorded in the range ~400 to 600 nm.

2.4.8 *I-V and photoconductivity measurements*

I-V and photoconductivity measurements were respectively used for evaluating the electronic conduction and opto-electronic properties of thin films. In the case of as prepared and annealed SnS_2 thin films, the I-V curves were measured in the voltage range 5-100 V at equal steps of 5 V in dark and under illumination from a blue LED light source (optical power 50 W, 450-460 nm). On the other hand, for the photoconductivity measurements, the current was measured under constant applied voltages in dark and light. For all I-V and photoresponse measurements, a pair of silver electrodes (colloidal silver) having equal dimensions were painted on the film surface and dried to which the terminals were connected. A Keithley Picoammeter-voltage source (model No. 6487) was used for the simultaneous application of voltage and measurement of the current. For annealed SnS thin films prepared from the 532 nm laser ablated nanocolloids, the photoconductivity measurements were done by illuminating the sample using a halogen lamp (100 W). The photoresponse switching of the same samples were tested employing a 532 nm diode pumped solid state laser for illumination. In the case of SnS:rGO samples, different wavelength LEDs (white, blue, green, red and yellow) of optical power 50 W were used at an applied voltage of 2 V whereas the opo-electronic properties of the SnS_2 thin films annealed at 300 °C in vacuum were evaluated by illuminating the samples using the 50 W blue LED.

2.4.9 Electrochemical analysis by cyclic voltammetry (CV)

Cyclic voltammetry uses currents induced by a triangular potential waveform to determine the electrochemical properties of materials such as diffusion coefficients, electron stoichiometry, mechanism of charge transfer and rate constants[249]. Electrochemical properties of the SnS, SnS:rGO and SnS_2 thin films were analyzed by means of CV using a 3 electrode cell in a potentiostat (BAS Epsilon). In all the measurements, annealed thin films deposited on ITO substrates were used as the working electrodes while platinum wire and Ag/AgCl were used as the counter and reference electrodes respectively. For SnS and SnS:rGO (with 1% GO) thin films, 0.1 M NaCl solution was used as the electrolyte for the experiments carried out at a scanning speed of 50 mV/s and 20 mV/s respectively. The CV of pure ITO is also measured as a reference in the case of SnS thin films. Prior to each measurement, the electrolyte was bubbled with nitrogen flow for 5 minutes and the measured scanning range was from -400 mV to 1200 mV for SnS thin films whereas it was from -400 to 600 mV for SnS:rGO thin films. To study the ability of SnS thin films to sense chemical reactions, the CV measurements were also carried out in 0.1 M potassium ferrocyanide[$K_4Fe(CN)_6$]. In all CV measurements, two cycles were measured, and all the results shown are from the second scan cycle to avoid any inherent electrochemistry interference effects.

Hydrogen evolution reaction on laser generated SnS_2 NPs were tested by CV measurements carried out in 1M H_2SO_4. SnS_2 nanoparticles dispersed in dimethyl formamide (DMF) mixed with carbon black and suspended on glassy carbon electrode was employed as the working electrode. 3 mg of carbon black was added to 200 μl of the nanocolloidal suspension (SnS_2 NPs obtained in DMF) and mixed well. In addition, 0.025% nafion was added as the binder. 50 μl of the such prepared mixture was then drop casted over well-polished glassy carbon electrode and dried in air using an oven. The potential window used for the cyclic voltammetric (CV) tests was 250 to -1000 mV at a scan speed of 100 mV/s. The working electrode was illuminated using a 50 W UV LED to study the light assisted hydrogen evolution. CVs were collected in dark and each 5-minute interval upon illumination for comparing the onset potential and current of the SnS_2 NP based electrodes.

In the case of SnS_2 thin films, the as prepared and 200, 250 and 300 °C annealed thin films synthesized from SnS_2 in isopropanol and ethanol were analyzed. 0.1M KCl was used as the electrolyte at scanning speed of 50 mV/s. Light assisted CV measurements were done by illuminating the working electrodes using the 50 W blue LED source.

2.5 Fabrication and characterization of the SnS:rGO based photovoltaic device

2.5.1 Fabrication of the photovoltaic device and characterization

A solar cell structure glass/ITO/CdS/Sb_2S_3/SnS (DMF):GO was fabricated and characterized to demonstrate the functionality of the synthesized SnS:GO nanocomposite thin film. CdS and Sb_2S_3 layers were successfully deposited on ITO coated glass substrate by chemical bath deposition (CBD) technique [251]. The glass/ITO/CdS/Sb_2S_3 structure was heat treated by rapid thermal processing (RTP) at 400 °C for 3 min. followed by the deposition of SnS (DMF): GO thin film by spray technique above glass/ITO/CdS/Sb_2S_3 as described earlier. After the deposition of SnS:GO, the cells were annealed at 380 °C in vacuum for 1h followed by a rapid thermal process at 425 °C for 10 s. for the effective reduction of GO. SnS (DMF):GO was selected over SnS (IA):GO due to the higher conductivity of SnS (DMF):GO thin films compared to the SnS (IA):GO films. The photovoltaic characterization was realized by isolating a 0.25 cm^2 active cell area on the structure and electrodes were painted using colloidal conductive carbon followed by silver. J-V characteristics of the solar cells were measured under illumination using a solar simulator of intensity 100 mW/cm^2 under AM 1.5 radiation as well as in dark.

2.5.2 Deposition of CdS and Sb_2S_3 by CBD for fabrication of the solar cell structure

CdS and Sb_2S_3 thin films were deposited on ITO coated glass substrate using CBD technique. A typical bath of CdS contained 10 ml cadmium chloride, 5 ml triethanolamine, 10 ml ammonium hydroxide, 10 ml thiourea and 65 ml deionized water preheated at 70 °C. The deposition was carried out for 20 minutes at 70 °C. As obtained CdS thin film was then annealed at 400 °C for 30 min. in air.

For the deposition of Sb_2S_3 layer above CdS, following bath composition was used. Initially, 650 mg of $SbCl_3$ was dissolved in acetone (2.5 ml) and 1M $Na_2S_2O_3.5H_2O$ (25 ml) and deionized water (72.5ml) were added one by one and stirred well. CdS deposited ITO samples were dipped in the bath and kept at 25 °C for 2 h. After 2 h, Sb_2S_3 layer of thickness about 200 nm was successfully deposited above the CdS layer.

Chapter 3

Thin films of tin monosulfide (SnS) using laser generated SnS nanocolloids

3.1 Introduction

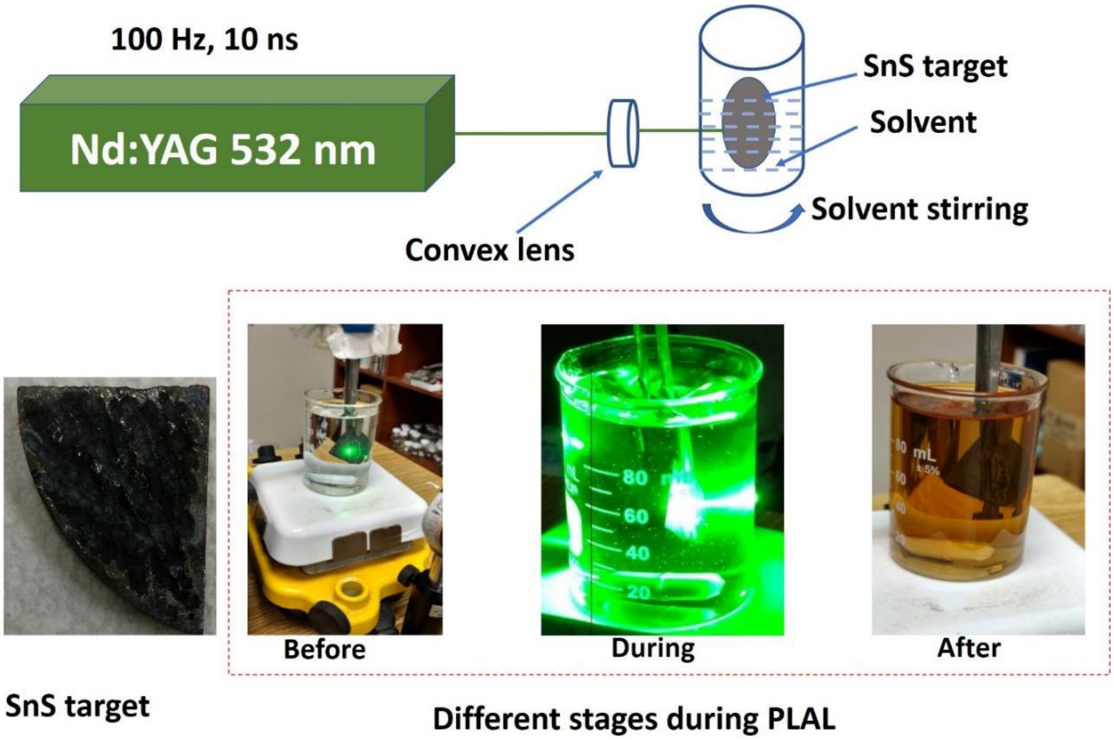

Fig.3.1. Schematic of the PLAL experimental set-up used for SnS NP synthesis and photographs of SnS target and different stages during the PLAL process

In this chapter, synthesis and characterization of nanostructured SnS thin films prepared by spraying the nanocolloid of SnS obtained by PLAL is reported. SnS nanocolloids were prepared in two different solvents viz. dimethyl formamide (DMF) and isopropyl alcohol (IA) by PLAL technique. SnS nanoparticles as well as their thin films formed by spray technique were characterized using different techniques for their structure, morphology and properties. A comparative study on the effect of liquid media on the properties of the SnS NPs and thin films is described. The results demonstrated in this chapter were published in reference [2].

3.2 SnS nanoparticles and their thin films: results and discussion

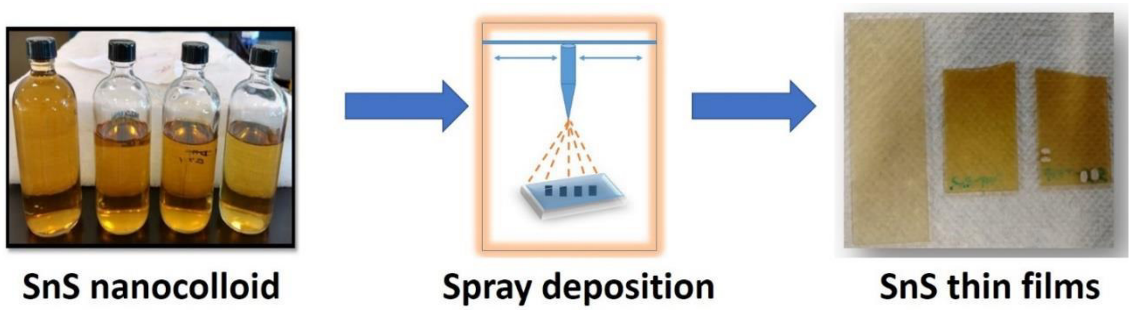

SnS nanocolloid **Spray deposition** **SnS thin films**

Fig.3.2. Photographs of SnS nanocolloid and thin films together with schematic of spray deposition. Reproduced with permission [2] © 2017, Wiley

Schematic of the experimental set-up used for SnS NP synthesis is shown in fig.3.1(top). The transparent liquid medium (DMF or isopropyl alcohol) turned into golden yellow in color after 20 minutes of ablation indicating the dispersion of the SnS NPs into the solvent and the resulted colloid was stable without any precipitates (see fig.3.1 (bottom)). Thin film deposition of SnS was carried out using an automated spray depostion system on different substrates kept on a temperature controlled hotplate. As deposited films were having yellow-brown color (fig.3.2) where the color of the films changed to black after the vacuum annealing. The resulted films were stable and uniform with good adhesion on the substrates. The deposited SnS thin films had an average thickness of around 1 μm by spraying one liter of nanocolloid, as estimated by cross-section SEM.

3.2.1 *Morphology and structure of SnS nanoparticles obtained by PLAL*

Morphology, crystalline structure and composition of the SnS nanoparticles were analyzed using a transmission electron microscope with Energy Dispersive X-ray analysis (EDX). TEM samples were prepared by drying a drop of SnS nanocolloid at ambient temperature on a carbon coated copper grid immediately after the PLAL experiment. The morphology, selected area electron diffraction (SAED) pattern and EDX spectrum of the SnS nanoparticles obtained in DMF and isopropyl alcohol are depicted in figures 3.3 and 3.4 respectively. A wide size distribution of the nanoparticles can be seen as in fig.3.3 and 3.4 as expected for PLAL synthesized nanoparticles. While some nanoparticles possess bigger size, most of them possess a size less than 10 nm. Agglomeration of smaller SnS nanoparticles might have led to the fomation of bigger particles. Individual SnS particles have a spherical morphology, but they appear like interconnected without definite boundaries which can probably be attributed to the higher concentration of the NPs in the liquid medium. In this case, higher repetition rate (100 Hz) of the pulsed laser could have also played an important role. The probability of NPs synthesized in solution being post irradiated by the incoming laser pulses and thereby changing the morphology due to laser induced heating/melting is higher when a laser of large repetition rate is used. But in contrast, stirring of the liquid medium during ablation process might reduce the post irradiation effects (similar to that of a liquid flow chamber) and thereby synthesizing highly concentrated and stable colloids. In figs. 3.3(a) and 3.4(a) morphologies of the nanoparticles are similar in both liquid media. Fig. 3.3 (c) and 3.4(b) show the HRTEM images of SnS nanoparticles in DMF and isopropyl alcohol respectively with the crystalline

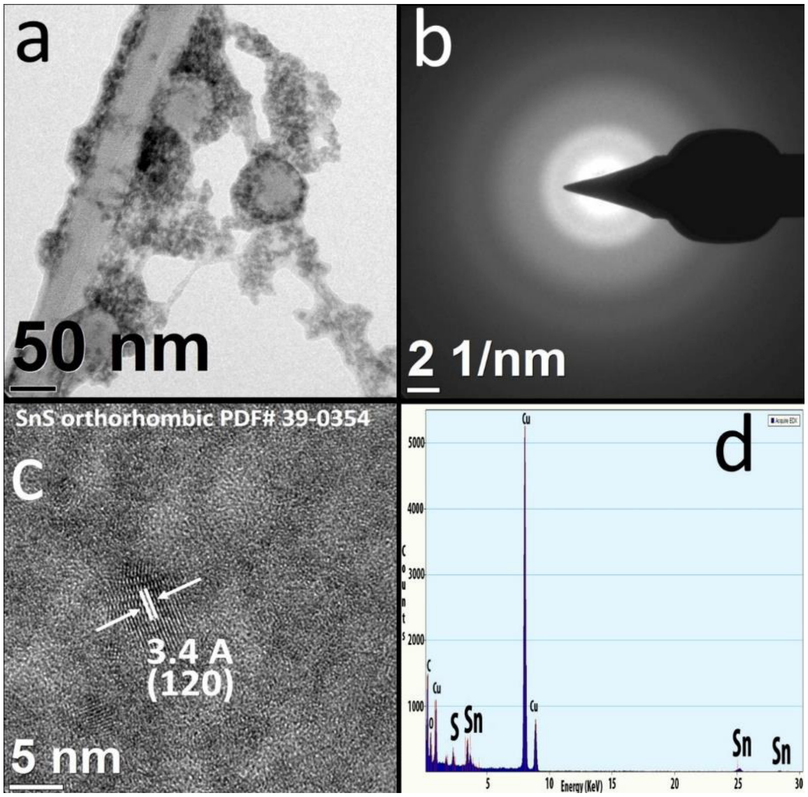

Fig.3.3. (a) TEM, (b) HRTEM, (c) SAED pattern and (d) EDX pattern of SnS nanoparticles synthesized in DMF. Reproduced with permission [2] © 2017, Wiley

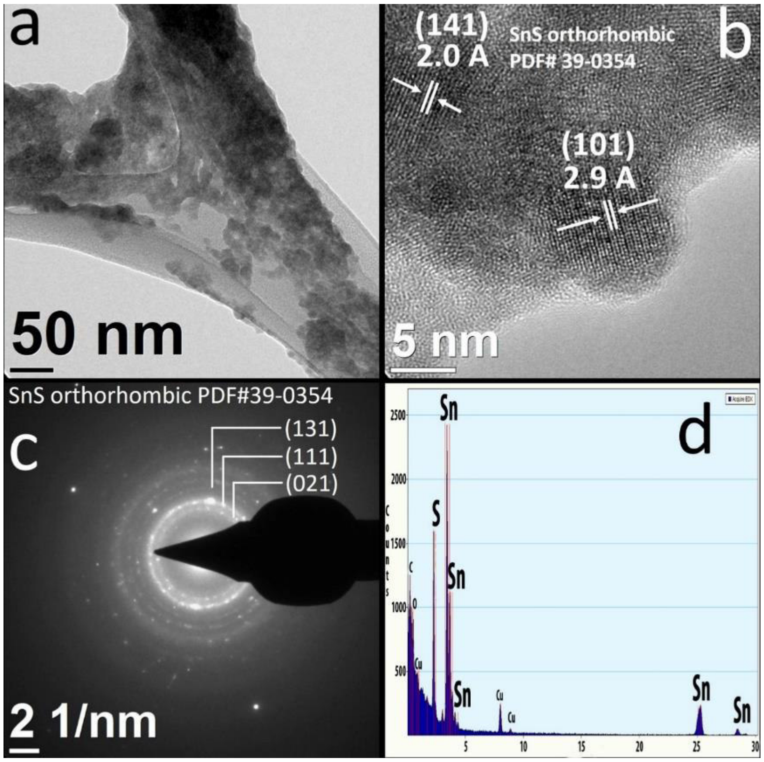

Fig.3.4. (a)TEM, (b) HRTEM, (c) SAED pattern and (d) EDX pattern of SnS nanoparticles synthesized in isopropyl alcohol. Reproduced with permission [2] © 2017, Wiley

planes corresponding to each visible particle marked. While DMF was used as the liquid medium, no bright spots were observed in the acquired SAED pattern of SnS nanoparticles (Fig. 3.3(b)) due to the solvent effect. The samples for TEM measurements were dried at ambient temperature where evaporation temperature of DMF is ~153 ℃. Most of the analyzed regions remain amorphous as seen from the HRTEM image of SnS nanoparticles obtained in DMF. On the other hand, the effect from the solvent was comparatively less in the case of the samples prepared in isopropanol since alcohol evaporates much faster. Thus, SAED pattern with many diffraction spots was resulted as shown in fig. 3.3(c) for the SnS colloid obtained in isopropanol. The measured interplanar spacings from the SAED pattern were in good agreement with the spacings for the (021), (111) and (131) planes for the orthorhombic SnS structure with JCPDS file No. 39-0354. The EDX analysis carried out on both samples showed tin and sulfur as major components. In addition to Sn and S, copper (Cu) and Carbon are also detected in the EDX measurements. The detected Cu is from the TEM grids since Cu coated carbon mesh was used for drying the SnS samples for TEM analysis. The detected carbon could be due to the carbon from the grid, carbon from the liquid medium (DMF or isopropyl alcohol) and adventitious carbon present on the sample surface. Guillen et al. reported laser generated SnS NPs using 532 and 1064 nm lasers and at different laser fluences in various liquid media where the particles were primarily having a spherical particle morphology.

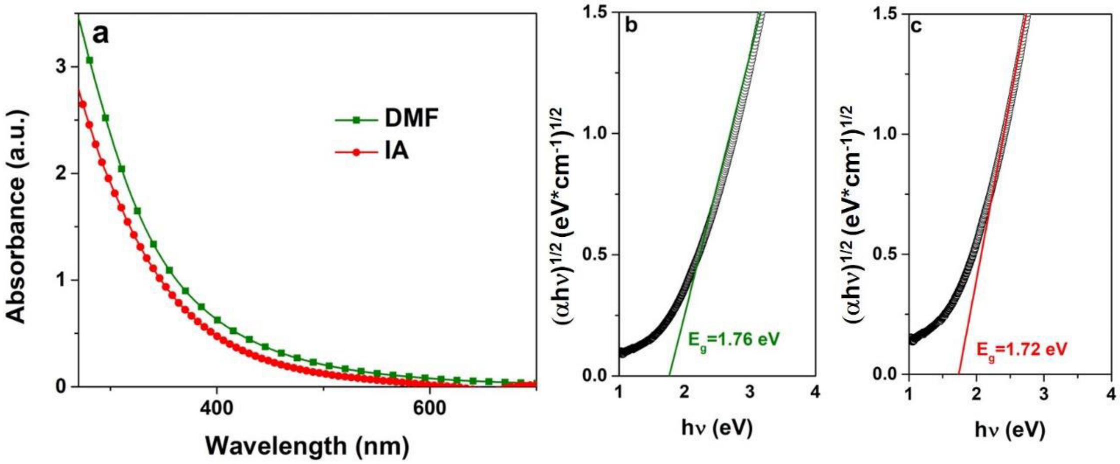

Fig.3.5. (a) Absorption spectra of SnS nanoparticles in isopropyl alcohol (IA) and dimethylformamide (DMF). Band gap of SnS nanocolloids in (b) dimethylformamide and (c) isopropyl alcohol. Reproduced with permission [2] © 2017, Wiley

However, the average size and size distribution of the particles were found to depend on the lasing parameters and nature of the solvent. The crystalline SnS particles in that case also exhibited an orthorhombic crystal structure. But in some liquids, the ablation also yielded oxides due to the reaction between the ablated species and the molecules in the liquid[144].

3.2.2 *Optical properties of SnS nanocolloids*

A UV-visible absorption spectrophotometer was employed to record the absorption spectra of the SnS nanocolloids in both liquid media soon after the laser synthesis of NPs. Fig.3.5 shows the absorption spectra of the SnS nanoparticles in DMF and isopropyl alcohol with the corresponding calculated optical band gaps. SnS nanocolloids obtained in both liquids show almost same range of absorption edges in the visible region. Band gaps of the nanoparticles in each liquid media were estimated using Tauc plot. The corresponding band gap plots are presented in fig. 3.5 (b,c). In isopropyl alcohol, the band gap of SnS nanoparticles was 1.72 eV whereas in DMF, it was 1.76 eV. The difference in bandgap evaluated in the two solvents is not very significant since it is very small and thus may fall in the range of calculation error. Increase in the band gap for the SnS NPs compared to the bulk SnS (1.3 eV) is due to the quantum confinement effect as well as the morphology effects. SnS NPs obtained through a wet chemical method showed band gaps of 1.78 and 1.2 eVs for direct and indirect transitions respectively[252].

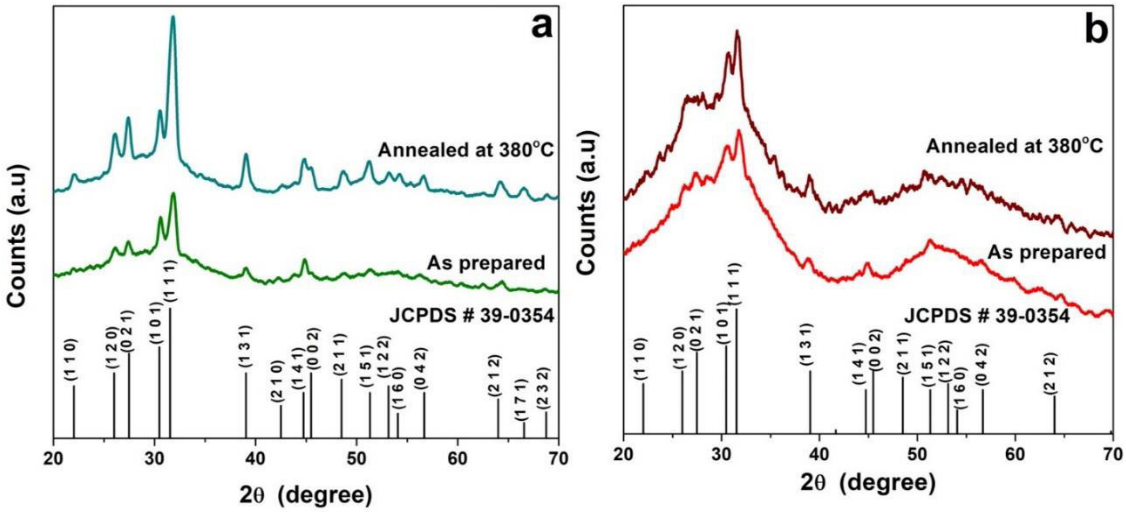

Fig.3.6. GIXRD patterns of as prepared and annealed SnS thin films synthesized by spray deposition of SnS in (a) dimethyl formamide and (b) isopropyl alcohol. Reproduced with permission [2] © 2017, Wiley

3.2.3 *Crystal structure of SnS thin films by GIXRD*

Fig.3.6. presents the GIXRD patterns of the as prepared and annealed SnS thin films synthesized by spray technique from the laser generated SnS nanocolloids. Both the GIXRD patterns agree with JCPDS # 39-0354 corresponding to the orthorhombic SnS. XRD pattern of the SnS target used for the laser ablation was also assigned to orthorhombic SnS[144]. Thin films synthesized from SnS in DMF show better crystallinity compared to the film synthesized from SnS in isopropyl alcohol as revealed by the XRD peak intensities. The DMF liquid medium might have enhanced the stability and crystallinity of the nanoparticles during the nanoparticles production by PLAL in comparison with the nanoparticles generated in isopropanol. Higher substrate temperature used while spraying

nanocolloid of SnS in DMF could be another reason. To study the effect of heat treatment on the film properties, the as deposited SnS thin films were annealed in vacuum for one hour at 380 °C. The intensities of the XRD peaks increased after the heat treatment in both liquids due to the improved crystallinity of the films. Moreover, a preferential orientation was observed along the (111) plane for all the samples. As evident from the XRD patterns, no other phases or impurities were detected in the analysis which could be attributed to the high purity of nanocolloids generated by the specific synthesis method (PLAL). The obtained results are in agreement with previously reported data for SnS films since SnS thin films deposited by conventional spray pyrolysis at a substrate temperature of 350 °C also showed orthorhombic structure where an increase in the preferred orientation along with enhanced grain size was noticed for higher substrate temperatures[253]. SnS thin films obtained by RF sputtering and electrophoresis also showed orthorhombic crystal structure [254, 255].

3.2.4 *Optical properties of SnS thin films*

Absorbance spectra and band gap plots of the annealed SnS thin films synthesized from SnS in DMF and isopropanol are presented in Fig.3.7. Both annealed SnS films show good absorption in the visible region which suggest that the films are better candidates for opto-electronic and photovoltaic applications. SnS thin films synthesized from SnS in DMF and IA showed band gaps 1.87 and 1.7 eV respectively. SnS thin films grown by spray pyrolysis showed an optical band gap of 1.32 eV whereas RF sputtered SnS films were having band gap values between 1.08 and 1.18 eV[253, 254]. The estimated band gaps of SnS films in the present work are slightly higher since the films were obtained directly from the SnS colloidal NPs.

The band gaps of the films were calculated using average thickness obtained from cross section SEM images (presented in section 2.2.6).

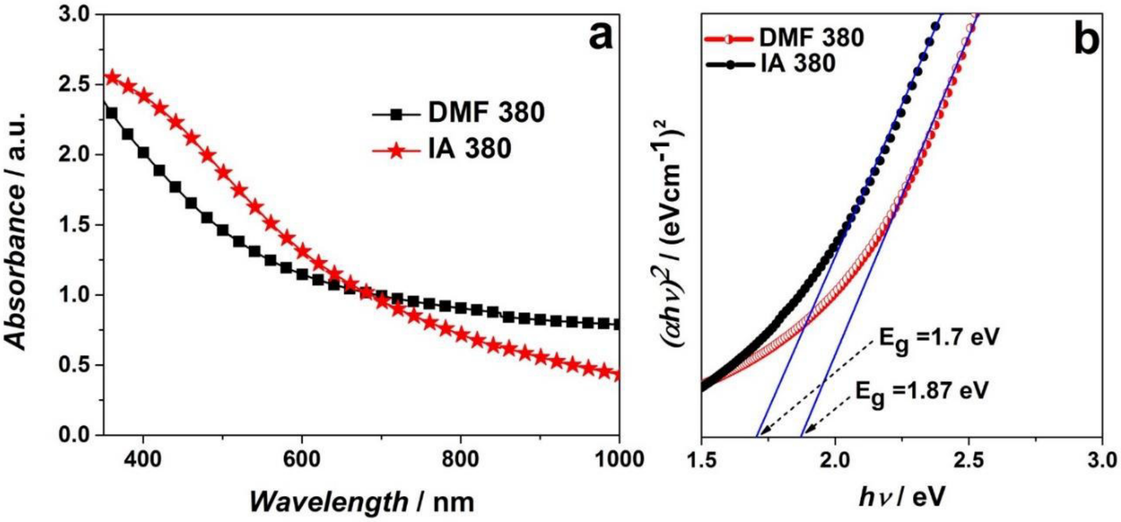

Fig.3.7. (a) Absorption spectra and (b) band gap plots of annealed SnS thin films synthesized from SnS nanoparticles in dimethylformamide (DMF) and isopropyl alcohol (IA). Reproduced with permission [2] © 2017, Wiley

3.2.5 *Elemental composition and chemical states of SnS thin films by XPS*

Elemental composition and chemical states of the annealed SnS thin films were identified from their binding energies measured by XPS. Fig.3.8. presents the XPS survey spectrum of SnS thin films synthesized from SnS in DMF and in isopropyl alcohol. The binding energy (B.E.) of adventitious carbon at 284.6 eV was used to correct all the XPS spectra and the high resolution scans shown were collected after a soft surface etching using argon ions to remove any contaminants present on the sample surface. In the XPS survey spectra, all the elements present on the surface of the samples are identified and marked as shown in fig.3.8 where the major photoelectron peaks are assigned to that of tin, sulfur, carbon and oxygen present on the surface. The high resolution spectral scans of Sn3d and S2p of the film synthesized from SnS in (a, b) dimethylformamide and (c, d) isopropyl alcohol is shown in Fig. 3.9. In the high resolution scan of Sn 3d (fig. 3.9(a)) for the film synthesized from SnS in DMF, the binding energies of $3d_{3/2}$ and $3d_{5/2}$ are 494.49 eV and 486.09 eV respectively. The splitted 3d peaks ($3d_{5/2}$ and $3d_{3/2}$) possess a binding energy difference of 8.42 eV. Both the binding energies and the energy separation for the spillted peaks are in exact match with the corresponding reported values of Sn 3d from SnS [256]. The narrow width of Sn 3d and S 2p peaks confirmed the presence of single phase SnS as supported by the XRD analysis. Fig. 3.9(b) shows the high resolution S 2p scan of the SnS sample

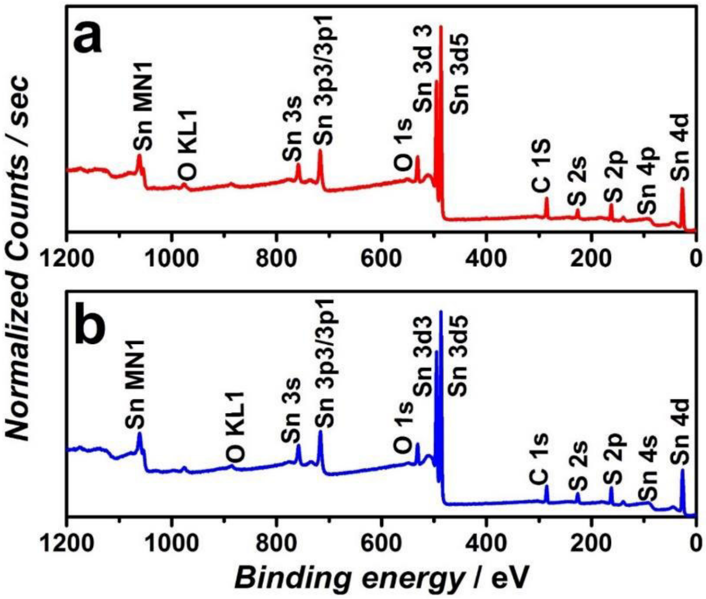

Fig.3.8. XPS survey spectrum of SnS thin films synthesized from SnS in (a) DMF and in (b) isopropyl alcohol with corresponding peaks marked. Reproduced with permission [2] © 2017, Wiley

synthesized from SnS in DMF. The binding energies of S2p$_{3/2}$ and S2p$_{1/2}$ levels are 161.29 eV and 162.46 respectively whereas the binding energy difference between the S2p$_{3/2}$ and S2p$_{1/2}$ levels is 1.17eV which are also in good agreement with the reported binding energies of sulfur in SnS[256]. For the films synthesized from SnS in isopropyl alcohol, the Sn3d peaks were observed at 485.95 eV and 494.36 eV. The small peaks appeared after deconvolution correspond to elemental tin (Sn) which originated due to the effect of argon ion etching of the sample surface. This might have occured because of the low substrate temperature used in spray deposition for SnS in isopropyl alcohol in comparison with that of DMF. The S2p$_{3/2}$ and 2p$_{1/2}$ peaks were observed at binding energy values 161.22 and 162.40 eV respectively which correspond to the sulfur from tin sulfide. The as prepared SnS thin films deposited from SnS in DMF and isopropanol also present similar XPS binding energies implying that the as prepared film itself is SnS wihout any other phases as shown in fig.3.10. SnS NPs synthesized by PLAL in different liquid media showed similar BEs where the Sn3d$_{5/2}$ and S2p$_{3/2}$ were showing BE values of ~486 eV and ~161.7 eV respectively.

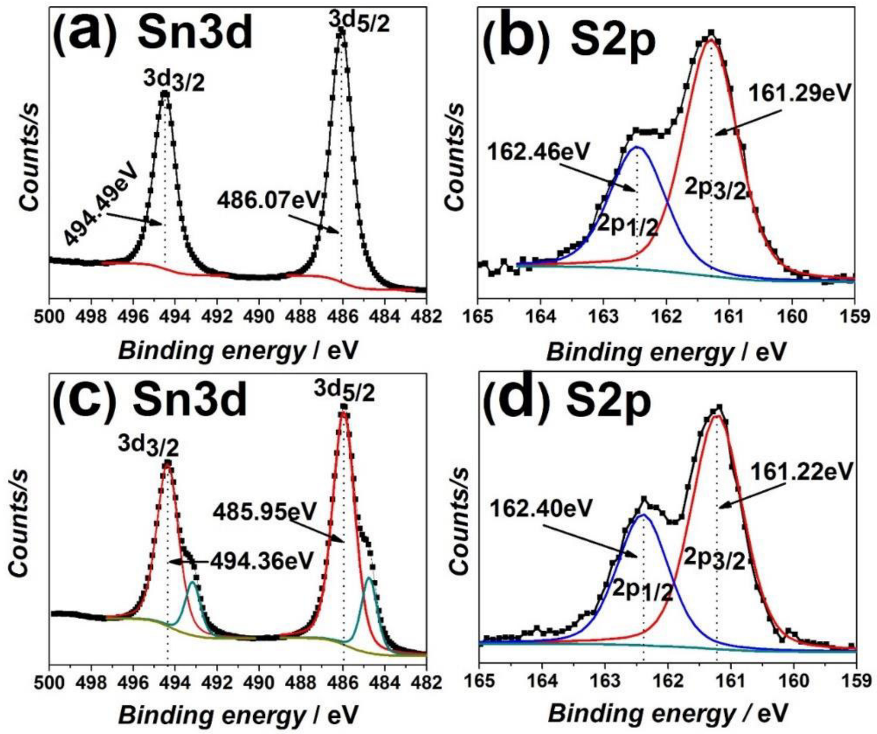

Fig.3.9. XPS high resolution scans of (a, c) Sn 3d and (b, d) S 2p of SnS thin films synthesized from SnS in (a, b) dimethylformamide and (c, d) isopropyl alcohol. Reproduced with permission [2] © 2017, Wiley

Furthermore, the SnS target used for ablation also presented close BEs to the values reported here[144]. The Sn $3d_{5/2}$ and $S2p_{3/2}$ were respectivley at 485.4 and 160.8 eVs for a SnS thin film obtained by thermal evaporation whereas the corresponding BEs were 486.4 and 161.1 eV for SnS thin films deposited by electrodeposition[257, 258].

XPS is a surface analysis technique with an average sampling depth of only 10 nm. Hence, depth profile analysis was carried out to study the distribution of the elements (Sn and S) along the entire film thickness (depth) and the corresponding graphs are depicted in Fig.3.11. Distribution of Sn and S through depth of the samples were analyzed using XPS depth profile. SnS was sputtered out from the film using Ar^+ ions of energy 2 keV as the sputtering source. Each etching cycle was 30 seconds corresponding to an approximate sputtering rate of 1.19 nm/s. Photoelectrons from different levels were collected for both samples.

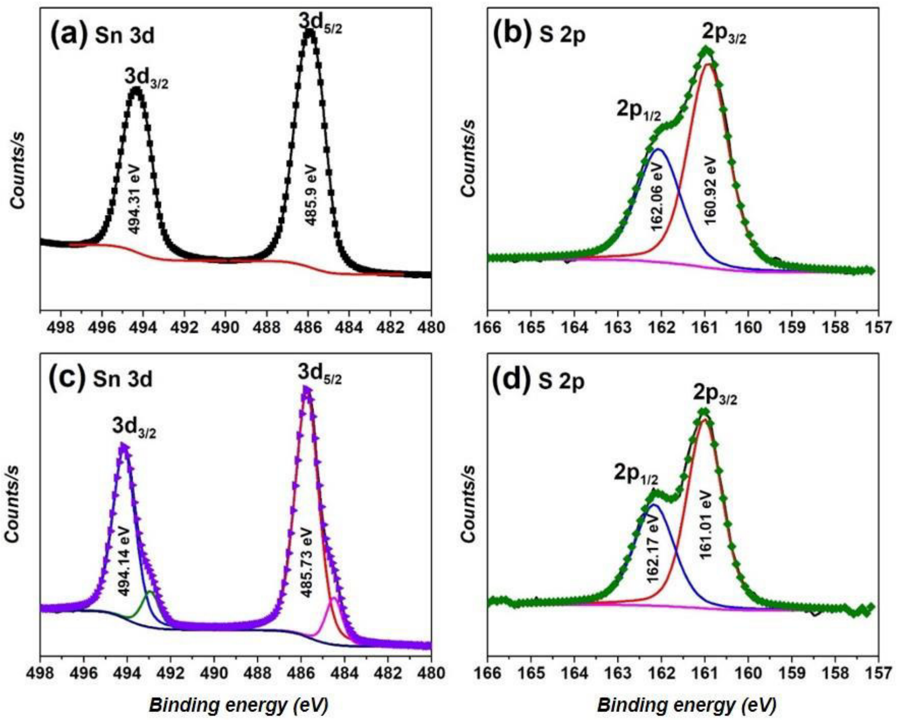

Fig.3.10. XPS high resolution scans of (a, c) Sn3d and (b, d) S2p of SnS thin films synthesized from SnS in (a, b) dimethylformamide and (c, d) isopropyl alcohol. Reproduced with permission [2] © 2017, Wiley

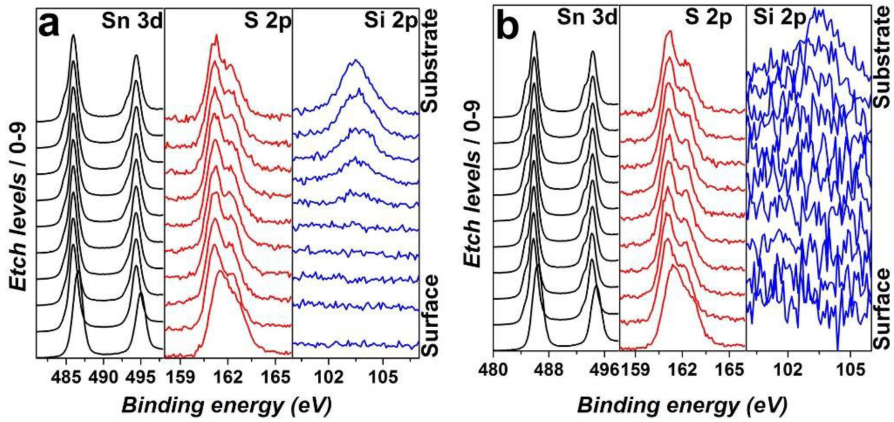

Fig.3.11. Depth profile analysis of annealed SnS thin films synthesized from SnS in (a) dimethylformamide (DMF) and (b) isopropyl alcohol (IA) . Reproduced with permission [2] © 2017, Wiley

A delay time of 45 seconds was applied before acquisition of data after each etch cycle.

Photoelectrons were collected from Sn, S and Si (from the substrate). Uniform distribution of SnS throughout the depth of the film is revealed from the depth profile analysis.

3.2.6 *Morphology of SnS thin films*

Morphology of the as deposited and annealed SnS thin films were analyzed using field emission scanning electron microscopy (FESEM). SnS films deposited on ITO substrates at the same conditions as on glass substrates were used for the SEM analysis. Figs.3.12 and 3.13 show the SEM images of the SnS thin films (a, b, c) as deposited and (d, e, f) annealed from SnS in DMF and SnS in isopropyl alcohol respectively. A porous layered surface morphology is identified on the sample synthesized from SnS in DMF. The layered morphology is clearly visible in the low magnification images whereas the high magnification image displays the porous surface of the films. SnS film with a different morphology was obtained when the films were prepared using SnS in isopropanol. The film surface is more porous in isopropanol compared to the films deposited using SnS in DMF. This indicates that the SnS thin film morphology depend on the liquid medium used in PLAL. One reason for the better compactness of SnS-DMF film could be the generation of more nanoparticles during the PLAL process when DMF was used as the solvent. The spray conditions could also have played a role in the final morphology since isopropyl alcohol is a medium with lower density and the substrate temperature used was low (100 °C) compared to that for DMF (200 °C). The two different substrate temperatures were chosen based on the boiling point of the liquid media to evaporate the solvents as they reach on the hot substrate. The porous like morphology of SnS is favourable in enhancing the photo and gas sensing properties as reported by Fangyuan Lu et al.[209]. Even though the substrate temperature was maintained above the boiling temperature of the corresponding liquid media used in PLAL, existence of small amount of the solvent on the film surface cannot be neglected. But use of higher substrate temperatures in spray may lead to oxidation of the deposited thin films. Annealing at a higher temperature in vacuum (380 °C) after the film deposition helped to remove any solvent present in the as prepared films and to improve the crystalline properties. After the annealing process, the films became more compact in both cases as seen from the SEM images. Average thickness of

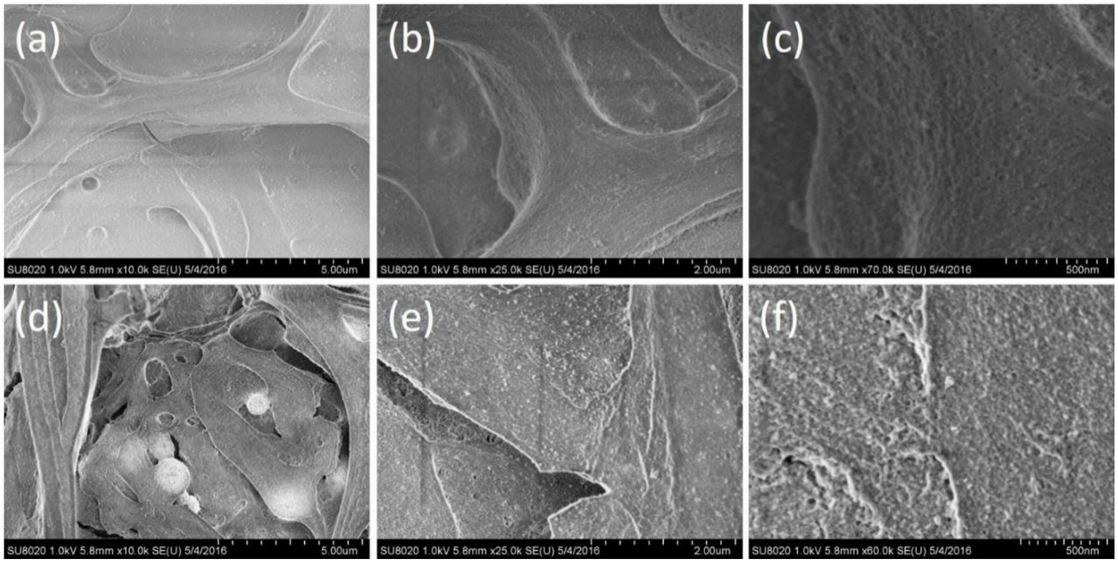

Fig.3.12. FESEM images of the (a, b, c) as prepared and (d, e, f) annealed SnS thin films synthesized from SnS nanocolloids in DMF at different magnifications.

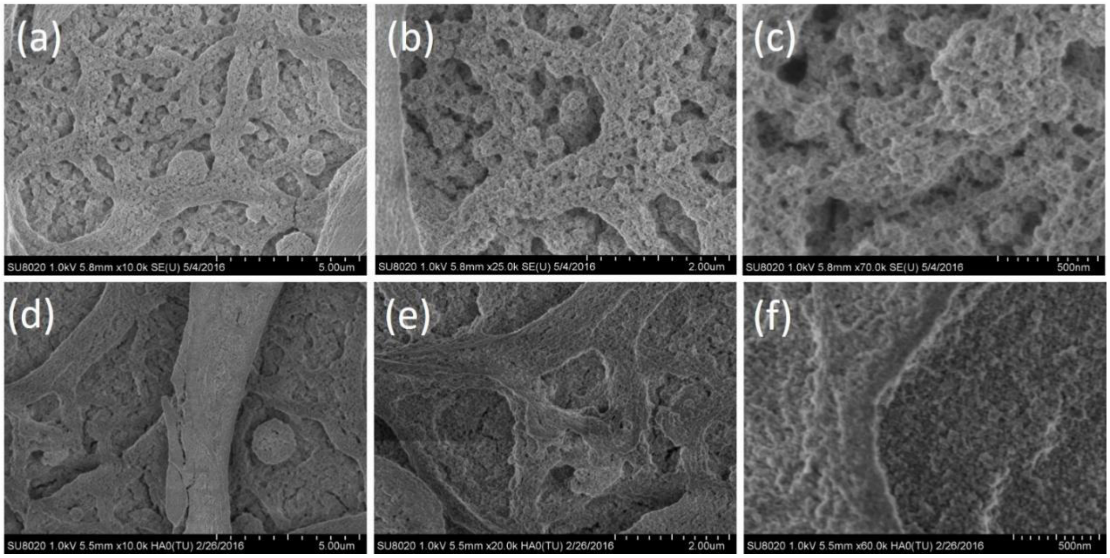

Fig.3.13. FESEM images of the (a, b, c) as deposited and (d, e, f) annealed SnS thin films synthesized from SnS nanocolloids in isopropanol at different magnifications.

the annealed SnS thin films was measured using cross-section scanning electron microscopy (Fig.3.14).

To calculate the thickness variation on the film surface, thickness was measured at two different regions on both samples. For SnS thin films synthesized from SnS in DMF, the measured film thickness was 1.3 μm and 1.1 μm at the two measured points as seen in the SEM image. On the other hand, SnS film deposited from SnS in isopropyl alcohol had thicknesses varying from 1.2 μm to 1.7 μm. From the cross-section SEM analysis, it was clear that both annealed SnS films have an average thickness greater than 1.2 μm which suggest that these films can be employed as absorber layer in solar cells. Thicknesses of the films were confirmed using stylus profilometer measurements. Film thickness measured by the profilometer was in good agreement with the cross-section SEM analysis (above 1 μm for both films).

For SnS thin films obtained by electrodeposition, a rough film surface having large grains and small crystal clusters was resulted[258]. On the other hand, SnS thin films grown by room temperature RF sputtering showed an elongated grain morphology with porosity and equiaxed surface with less porosity as the Ar pressure was altered during the film deposition[254]. This indicates that the morphology of SnS thin films strongly depend on the deposition technique and parameters of deposition. SnS thin films obtained in the present work show totally different surface morphology compared to the films synthesized by other conventional methods.

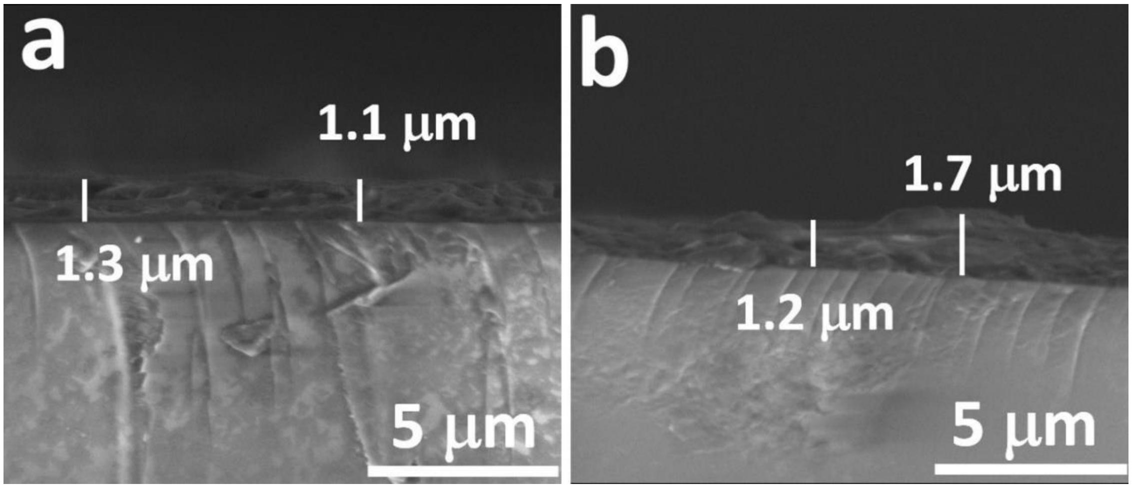

Fig.3.14. Cross section SEM images of annealed SnS thin films synthesized from SnS in dimethylformamide (DMF) and in (c, d) isopropyl alcohol (IA). Reproduced with permission [2] © 2017, Wiley

3.2.7 *Electrochemical properties of SnS thin films*

Cyclic voltammetry (CV) analysis of the films was carried out using a three electrode potentiostat. SnS thin films deposited on ITO (indium tin oxide) were used as the working electrodes in these measurements. Ag/AgCl was used as the reference electrode and the counter electrode was a platinum wire. 0.1 M NaCl solution was used as the electrolyte for the experiments carried out at a scanning speed of 50 mV/s. The CV of pure ITO is also included as a reference. Prior to each measurement, the electrolyte was bubbled with nitrogen flow for 5 minutes and the measured scanning range was from -400 mV to 1200 mV. SnS films used in the measurements were those after the heat treatment in vacuum and all the readings shown are from the second cycle of the measurement. The CVs of SnS thin films synthesized from SnS in DMF and isopropyl alcohol and that of ITO are presented in Fig. 3.15(a). Nanostructured SnS thin films showed improved capacitive nature than bare ITO electrode as seen from the CV measurements. The observed current for the SnS films is higher as compared to that of bare ITO. The increased surface area due to SnS nanoparticles might have enhanced the properties of the electrical double layer formed at the interface of the working electrode and the electrolyte. The SnS DMF film shows a higher current at potential of 1.2 V, suggesting that SnS DMF film has a great promise in electrolysis reactions. This might be explained based on the effects of morphology, crystallinity and layered structure of the films obtained using spray deposition of laser generated nanocolloids. These results are in correlation with that of XRD where enhanced crystallinity was observed for the films deposited from SnS in DMF. As explained earlier, more nanoparticles are obtained in DMF liquid medium (higher absorbance in fig.3.4) and/or morphology of the particles in DMF medium would be favorable for the film formation and its surface properties. To study the ability of these nanoparticles to sense chemical reactions, the same experiment was carried out in 0.1 M potassium ferrocyanide[$K_4Fe(CN)_6$]. The chemical reactions taken place at the surface of the working electrode during the scanning can be summarized as follows:

$$\mathbf{Fe(CN)_6^{-4} \longrightarrow Fe(CN)_6^{-3} + e} \text{ (Oxidation)} \qquad (2)$$

$$\mathbf{Fe(CN)_6^{-3} + e \longrightarrow Fe(CN)_6^{-4}} \text{ (Reduction)} \qquad (3)$$

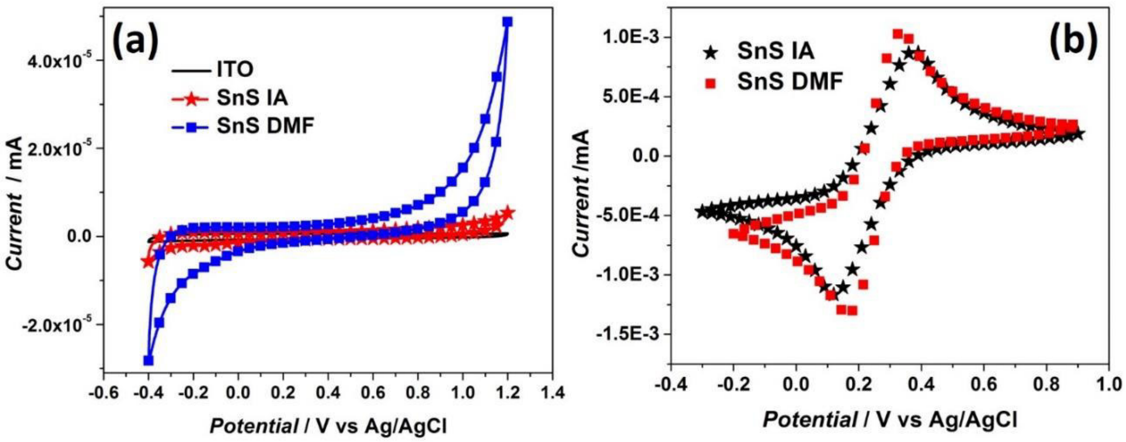

Fig.3.15.(a) Cyclic voltammograms of SnS thin films synthesized from SnS in DMF and isopropyl alcohol and of ITO. Electrolyte: 0.1M NaCl; Scanning speed: 50 mV/s ; Measured cycle: 2 (b) Cyclic voltammogram of SnS thin films synthesized from SnS in DMF and isopropyl alcohol in 0.1 M $K_4Fe(CN)_6$ electrolyte. Reproduced with permission [2] © 2017, Wiley

The anodic and cathodic peaks observed in the cyclic voltammogram represent one of the above reactions (2 and 3). The respective measurement using SnS thin film as the working electrode is shown in fig. 3.15(b). In the case of SnS thin film synthesized from SnS in DMF, the anodic and cathodic peak currents I_{pa} and I_{pc} were $1.04x10^{-3}$ mA and $1.01x10^{-3}$ mA respectively. The formal reduction potential E_0' obtained in the reaction was 0.25 V and the number of electrons involved in the reaction was estimated as 351. On the other hand, for the SnS films synthesized from SnS in isopropyl alcohol, the anodic and cathodic peak currents were $0.9x10^{-3}$ mA and $0.91x10^{-3}$ mA respectively. Formal reduction potential calculated in this case was 0.25 V with 229 electrons participated in the reaction. The number of electrons was calculated using the following expression:

$$n = \frac{59\,mV}{E_{pa} - E_{pc}} \tag{4}$$

for reversible couple in the redox reaction. More number of electrons involved in the reaction using SnS-DMF thin film also shows the enhanced electrochemical properties than the film synthesized from SnS in isopropanol arising from the improved microstructural features.

3.2.8 *Opto-electronic properties of SnS thin films*

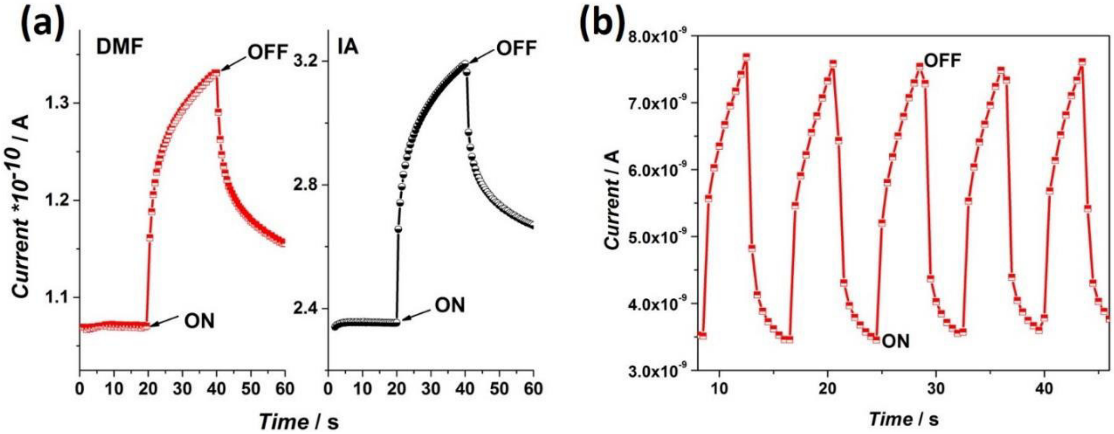

Fig.3.16.(a) Photoresponse of SnS thin films annealed at 380 °C at applied bias voltage of 10V. First 20 seconds in dark, then 20 to 40 seconds under light illumination and followed 20 seconds after illumination is turned off (b) Reversible photocurrent switching effect of SnS-DMF annealed film under illumination from 532 nm continuous wave (CW) laser. Reproduced with permission [2] © 2017, Wiley

Fig. 3.16(a) shows the photoresponse of SnS thin films fabricated from SnS in DMF and in isopropyl alcohol and annealed at 380 °C for an applied voltage of 10V. In fig.3.16(a), the first 20 seconds is in dark and from 20 to 40 seconds, the sample is illuminated (light) using a halogen lamp and next 20 seconds again in dark. For the film synthesized from SnS in DMF, the dark and light resisitivites were 1.1×10^5 and 0.9×10^5 Ω.m repectively whereas for the film deposited using SnS in isopropanol it was 6.2×10^4 and 4.5×10^4 Ω.m. During the illumination time, the photocurrent increased due to the additional charge carriers generated owing to light absorption by SnS. This behavior is beneficial for optoelectronic applications like photodetectors, solar cells and sensors. Photoresponse switching of the SnS thin films prepared from SnS in DMF and annealed at 380 °C was measured by illuminating the film using a 532 nm diode pumped solid state laser. The photocurrent measurement with respect to switching time is presented in fig. 3.16(b). The photocurrent of the SnS thin film was found to switch very fast according to the ON and OFF states of the illumination which denotes the photo response stability of the synthesized SnS thin films. In each cycle, the sample was kept ~4 seconds in dark and the next 4 seconds under illumination constituting a total time of 8 seconds for each measured cycle. 5 consecutive cycles were measured in the same manner in a total time of ~37 seconds. This kind of photoresponse and response stability makes SnS thin films a promising candidate in applications like photoelectric devices[259].

Refractive index, viscosity and polarity of the liquid medium affect the morphology of the nanoparticles[52, 61] in PLAL. If the nanoparticles produced react with the liquid medium (reactive PLAL), then the ablation can lead to new phases or compounds in the nanocolloids as well as thin films. Also, the solvent properties help with better dispersion for the nanoparticles in the colloid. In this work, SnS thin films were obtained using SnS nanoparticle colloids and the films had a different morphology with improved optoelectronic properties compared to those obtained by other methods described in references [189, 210, 252, 260, 261]. An increase in bandgap was also resulted from the nanostructured morphology. This morphological change of SnS films contributed to an increased surface area giving rise to better electrochemical properties.

3.3 Conclusions

Nanostructured thin films of tin monosulfide were successfully deposited using an effective spray technique from laser generated SnS nanocolloids. The influence of two different liquid media (an alcohol and another organic solvent) on the properties of the SnS NPs and the obtained thin films were studied. The crystalline structure and morphology of the NPs were identified by transmission electron microscopy. Crystallinity and chemical composition of SnS thin films were investigated using XRD and XPS. Films annealed at 380 °C showed improved crystallinity compared to the as-deposited films. FESEM images revealed the porous morphology of the SnS thin films. The SnS thin film preparation method also influenced its opto-electronic and electrochemical properties. In general, the films synthesized from SnS in DMF exhibited better crystallinity and improved electrochemical properties in comparison with the films deposited from SnS in isopropanol.

Chapter 4

Synthesis and properties of nanocomposite thin films of tin sulfide with reduced graphene oxide (SnS:rGO) by combinatorial PLAL- spray technique

4.1 Introduction

Owing to both the high absorption coefficient and suitable bulk band gap, SnS has been widely investigated for visible light harvesting applications such as PV devices. For instance, many attempts have been made by the researchers to employ SnS as an absorber material in solar cells[262-265]. Nevertheless, they lack noticeable efficiency and performance as required by the present scenario. SnS nanostructures are also widely applied as anode materials in storage devices and photodetectors[209-211, 216, 266]. Although the theoretical efficiency of SnS based solar cells is >25%[262, 263], the maximum reported value up to date is 4.4%[264] for a solar cell fabricated by atomic layer deposition (ALD). In that work, p-type SnS was combined with n-type zinc oxysulfide thereby blocking holes and selectively transmitting electrons simultaneously. Grain boundary recombination was also effectively reduced by annealing the SnS thin films in presence of H_2S to form bigger grains thereby reducing grain boundaries and the recombination near the p-n junction was reduced by placing a few monolayers of SnO_2 between the p-SnS and n-Zn(O,S). Hence the thin film processing followed to obtain such a conversion efficiency was very tedious and moreover ALD is a slow and expensive film fabrication technique compared to its alternatives and thus puts a barrier towards cost effective and large scale solar cell production[267]. Many research groups investigated the gas sensing properties of SnS [209, 211, 268, 269]. Majority of these properties originate from the band gap and layered orthorhombic structure of SnS chalcogenide. Single crystal SnS nanowires[270, 271] and SnS particles with morphologies like nanoflower[272], nanoribbons[210, 216] and nanobelts[259, 273] have been reported by different authors. SnS is a good p-type absorber having an exceptional interlayer spacing (c=0.4330 nm, space group Pnma). Nonetheless, the low dark conductivity of SnS limits its use in PV and other optoelectronic applications.

On the other hand, graphene is well known for its excellent optical[274], electronic[275] and mechanical[276] properties. But graphene itself is hard to disperse in solvents or to combine directly with other semiconducting materials. Graphene oxide in this context is better than graphene due to its better solubility. Oxygen defects are introduced into graphite to obtain graphene oxide (GO)[277]. Physicochemical properties of GO depend on factors such as dopants, microstructure, degree of oxidation/reduction and sheet size[278]. Removal of oxygen from GO would lead to the formation of Reduced graphene oxide (rGO) and thus rGO possesses higher electronic conductivity compared to GO. Nanocomposites based on GO or rGO and semiconductors have showed their suitability and functionality for different applications[279-283]. Dye sensitized solar cell having 7.47% conversion efficiency was reported using SnS-rGO nanocomposite as the counter electrode[284]. When nanocomposites of semiconductors and graphene related materials are formed, the abundance of delocalized electrons in the conjugated sp2-bonded network enhance the charge separation and their transport [120, 285]. Various properties such as porosity, conductivity and strength of the resulted material can be improved by introducing graphene in it[286]. P-type conductivity of SnS originating from the tin vacancies in the lattice which creates the acceptor levels[287], increases (transforming into a p+ layer) when nanocomposite of SnS and rGO is fabricated and the result is a composite material with high electronic conductivity and other enhanced properties due to the synergistic effects. When this p+ layer is incorporated in solar cells, it may probably help in enhancing the cell efficiency by improving the short-circuit current resulting from high and fast conduction through the SnS:rGO network. In most cases, rGO acts as a conductive layer which enhances the charge carrier transport in the semiconductor. Efficient charge carrier separation and high carrier life time are necessary for achieving high short circuit currents to improve cell conversion efficiencies when applied in solar cells[288].

This chapter describes synthesis of nanocomposite thin films of SnS with GO and rGO by spray deposition of tin sulfide nanocolloids mixed with GO and the results shown in this chapter were published [289]. SnS nanocolloids (obtained by PLAL) and GO (synthesized by Marcano’s method) were physically mixed in different ratios and sprayed onto heated substrates to obtain the SnS:GO thin films. As deposited SnS:GO thin films were converted into SnS:rGO by thermal reduction applying vacuum annealing to the films. A systematic study was carried out on SnS thin films synthesized using the colloids in different liquid media and on the properties of pristine SnS, SnS:GO and SnS:rGO thin films as a function of GO. SnS thin films having GO or rGO network exhibited better optoelectronic and electrochemical properties in comparison with pristine SnS films. Finally, a solar cell device having maximum photoconversion efficiency of 2.32% was fabricated using SnS:rGO thin film absorber, as a preliminary step towards the device fabrication employing the combinatorial PLAL - spray method.

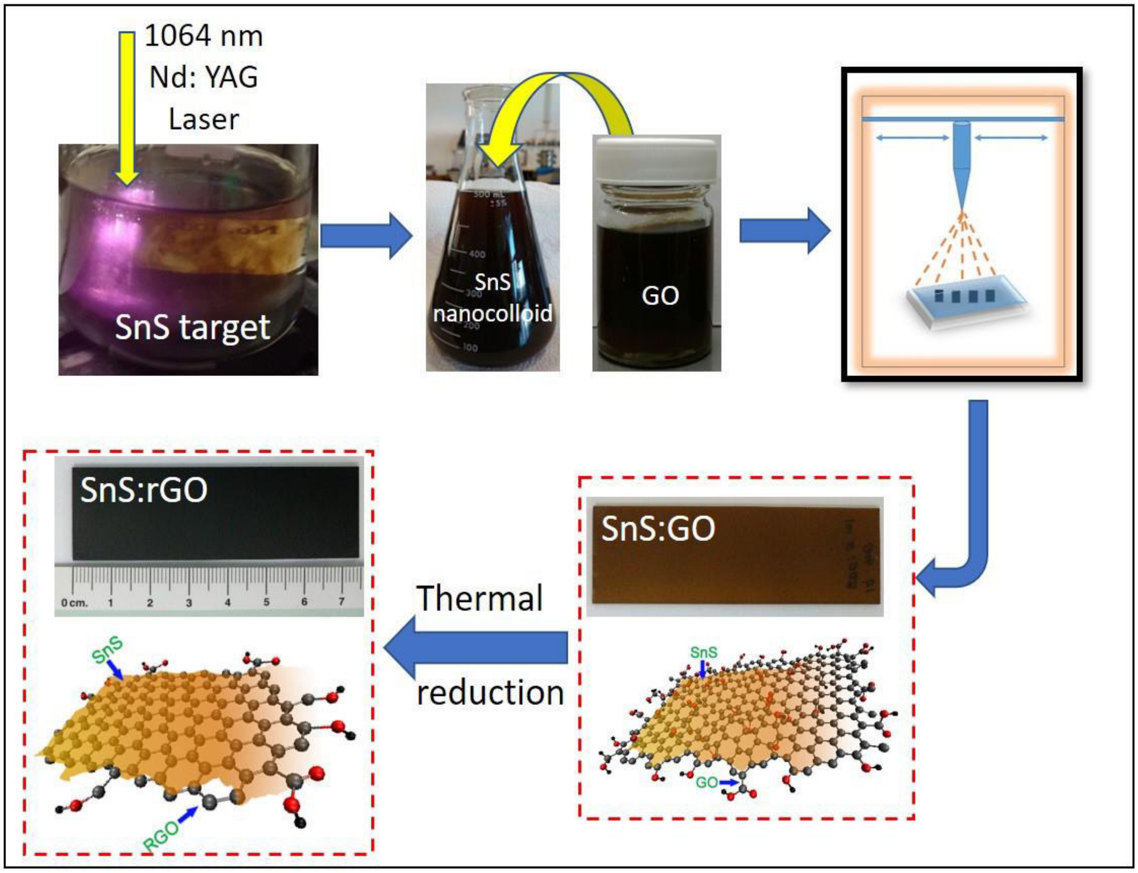

Fig.4.1. Experimental set-up used for pristine SnS and nanocomposite SnS:rGO thin film synthesis © 2019, Elsevier

4.2 SnS and SnS:rGO; Structure, morphology and properties

After 5 minutes of laser ablation, a dark brown highly concentrated colloidal suspension of SnS NPs is resulted in isopropyl alcohol and DMF (as shown in fig.4.1). Stability of SnS nanocolloids was determined by Zeta potential analysis. SnS NPs synthesized in both liquid media were stable as revealed by the average zeta potential values of -36 mV and -46.5

mV respectively for SnS in isopropyl alcohol and DMF. Zeta potential values showed that SnS NPs were more stable in DMF than in isopropyl alcohol. Thin films of SnS and SnS:GO were fabricated by spraying the nanocolloids. As prepared SnS thin films were brown in color whereas the films containing GO were darker. GO concentration was 4.3 g/l. Pristine SnS films were prepared by spraying 1L of the colloid whereas SnS:GO films were deposited by mixing 5, 2.5 or 0.5 ml of GO to 500 ml SnS colloid. The vacuum annealed films with 1% GO showed black color. In the case of SnS (DMF) with 1% GO both as-prepared and annealed films are black since the film deposition was carried out at higher temperature leading to in-situ reduction of the GO.

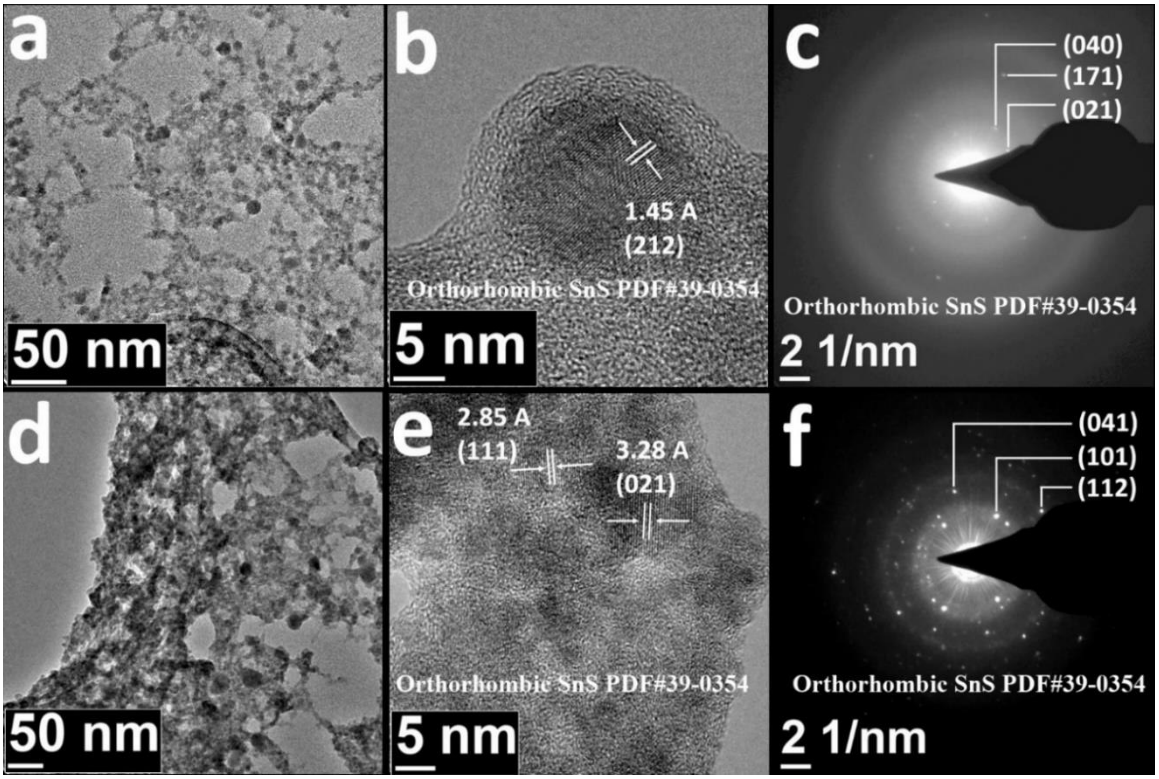

Fig.4.2. TEM, HRTEM and SAED pattern of SnS NPs in (a-c) DMF and (d-f) isopropyl alcohol respectively © 2019, Elsevier

4.2.1 Morphology and crystal structure of SnS NPs by TEM

Morphology of SnS NPs was determined by Transmission electron microscopy. TEM micrographs, high resolution TEM (HRTEM) and selected area electron diffraction (SAED) patterns of SnS NPs in both liquid media are presented in Fig. 4.2. As the TEM analysis shows, the SnS NPs present quite similar morphology in both liquid media (mostly spherical shaped SnS particles). One reason for the similar morphology of the particles in both liquids could be laser post irradiation of SnS particles. The synthesized NPs have undergone laser post- irradiation due to the longer ablation time (5 min) leading to changes in the initial particle morphology. Crystallinity of SnS NPs was verified using the HRTEM images. Interplanar spacing of a large particle in DMF (Fig. 4.2b) was evaluated as 1.45 Å corresponding to the (212) plane of orthorhombic SnS (JCPDS#39-0354). In isopropyl alcohol, two individual particles were identified with different spacings of 2.85 and 3.28 Å corresponding to (111) and (021) planes respectively. SAED analysis was also performed for further confirmation of the crystalline structures of SnS NPs. SnS NPs formed in both liquid media presented orthorhombic crystal structure, coinciding to that of the SnS target used for the laser ablation. For the particles generated in DMF, the identified crystal planes are (040), (171) and (021) corresponding to the orthorhombic SnS structure while the particles in isopropanol showed reflections from (041), (101) and (112) according to the JCPDS no. 39-0354 as marked in the respective SAED patterns.

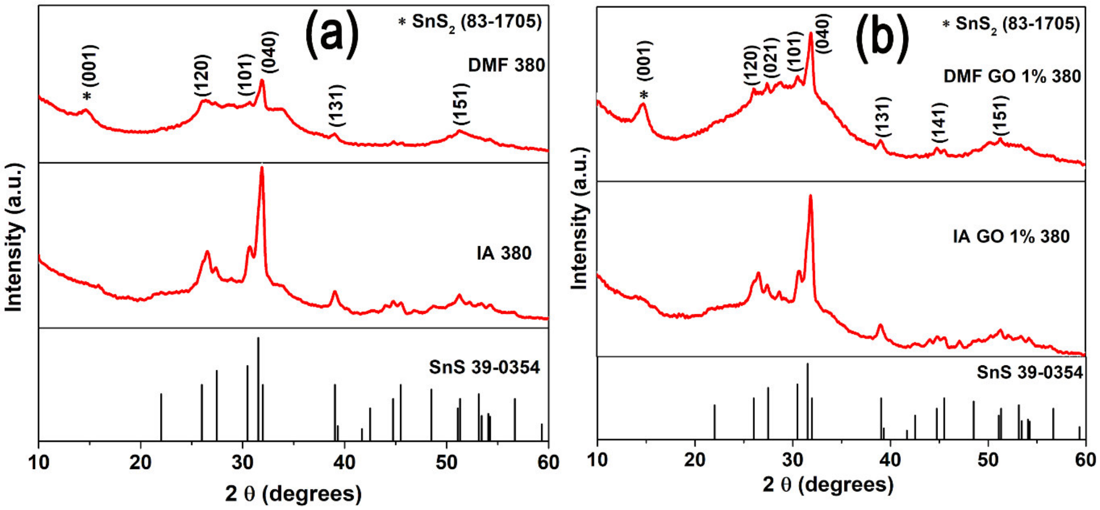

Fig.4.3. (a) GIXRD patterns of annealed pristine SnS and (b) SnS:rGO thin films with 1% GO along with the JCPDS reference data for orthorhombic SnS © 2019, Elsevier

4.2.2 Crystal structure of SnS and SnS:rGO thin films by GIXRD

Crystalline structures of SnS and SnS:rGO thin films were determined by grazing incidence X-ray diffraction (GIXRD) analysis. Annealed SnS thin films synthesized from SnS in DMF /isopropyl alcohol and SnS thin films with 1% graphene oxide were used for the

GIXRD analysis. Fig.4.3 (a, b) presents the GIXRD patterns of the samples on the same intensity scale together with the JCPDS data for orthorhombic SnS (PDF No. 39-0354). For SnS as well as SnS:rGO, all the major diffraction peaks were identified as reflections from the planes (120), (101), (040), (131), (151) and (141) of orthorhombic SnS in agreement with the JCPDS file no. 39-0354. In addition to this, a minor peak at 15° (marked with ∗) was observed in the films synthesized from DMF colloids which was assigned to the (001) crystal plane of SnS_2 (JCPDS file # 83-1705).

4.2.3 Phase structure of SnS and SnS:rGO thin films by Raman analysis

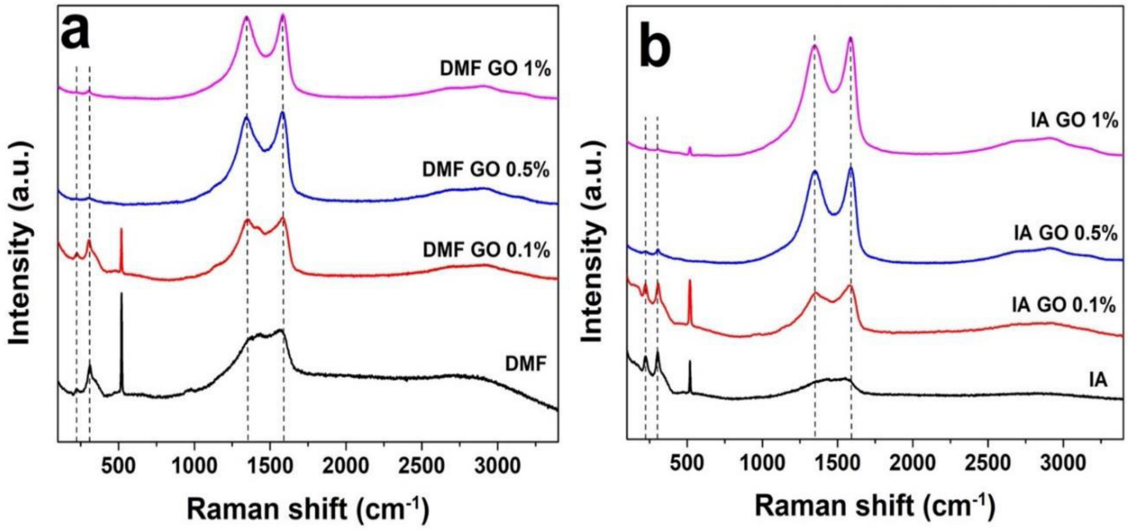

Fig.4.4. Raman spectra of pristine SnS and nanocomposite SnS:rGO thin films with different GO ratios for the films deposited from SnS in (a) DMF and (b) isopropanol © 2019, Elsevier

Raman spectra of the bare SnS and SnS:rGO thin films with various GO concentrations were collected using 532 nm laser excitation. Fig.4.4(a, b) depicts the recorded spectra for SnS and SnS:rGO samples with 0.1%, 0.5% and 1% GO concentrations synthesized from SnS in DMF as well as SnS in isopropanol. The D and G bands (corresponding to structural imperfections and the first order scattering of the E_{2g} mode) present at 1350 cm^{-1} and 1585 cm^{-1} in the SnS:rGO samples are characteristic peaks of GO, confirming the presence of GO in the samples along with SnS. The peak observed at 222 cm^{-1} corresponds to an SnS vibrational mode whereas the peak at 311 cm^{-1} is attributed to the vibrational mode of SnS_2. Hence the slight presence of SnS_2 phase is also detected in Raman analysis in addition to

XRD. The Raman band located at ~524 cm^{-1} is assigned to the vibrational mode of Si which is from the substrate used for the film deposition (samples deposited on Si wafer were used for Raman analysis for better background noise reduction).

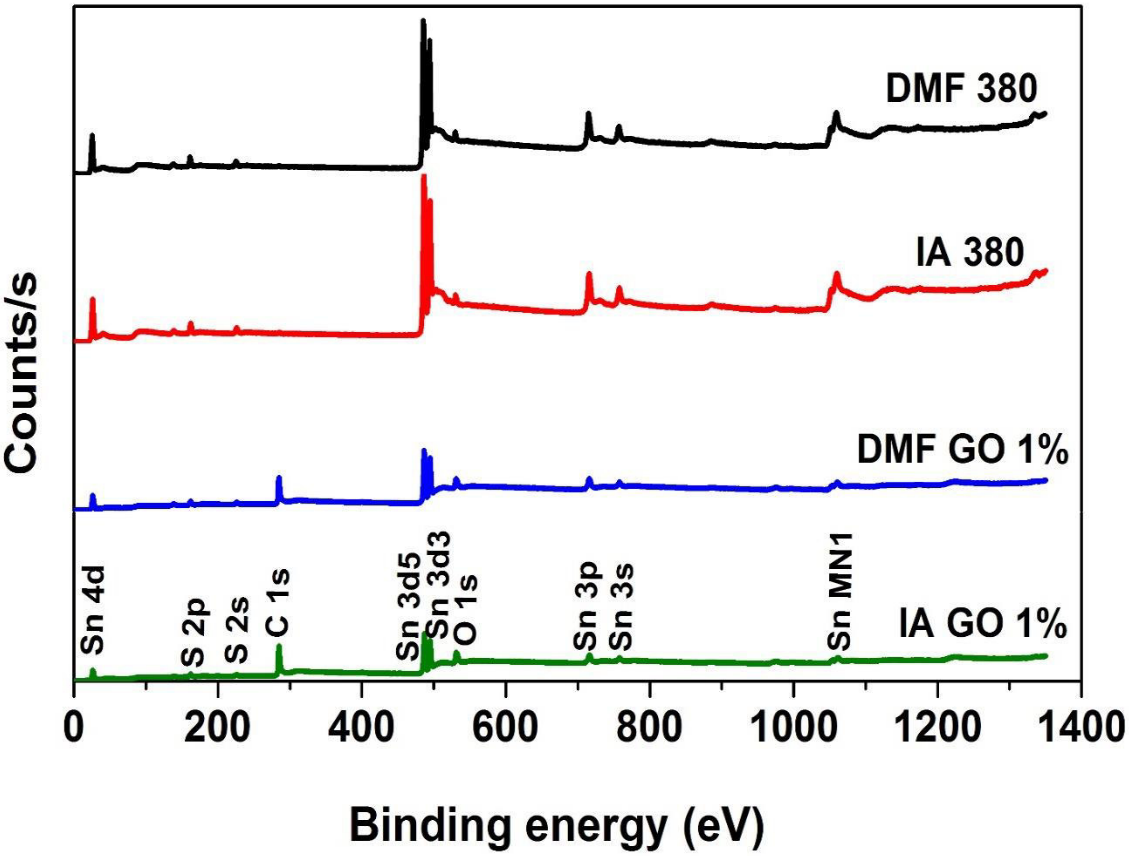

Fig.4.5. XPS Survey scan spectra of annealed pristine SnS thin films and SnS:rGO thin films having 1% GO © 2019, Elsevier

4.2.4 Elemental composition and Chemical state analysis of SnS and SnS:rGO thin films by XPS

Elemental composition and chemical states of the pristine and graphitic material incorporated SnS thin films were determined by X-ray photoelectron spectroscopy using survey (low resolution) and high-resolution spectral analyses. XPS survey scans of SnS and SnS:rGO thin films show the presence of all desired elements (Sn, S and C) on the sample surface (Fig. 4.5). Intensity of the carbon peak present at 284 eV in the samples with GO is much higher as compared to the pristine SnS films which again confirms the successful incorporation of GO into the SnS films thus making the SnS:GO composites.

Deconvolution of the high-resolution peaks were done by applying a Shirley type background to each individual peak. Charge compensation to the samples was provided by a flood gun attached to the XPS machine. Fig.4.6 (a-d) presents the high-resolution scans

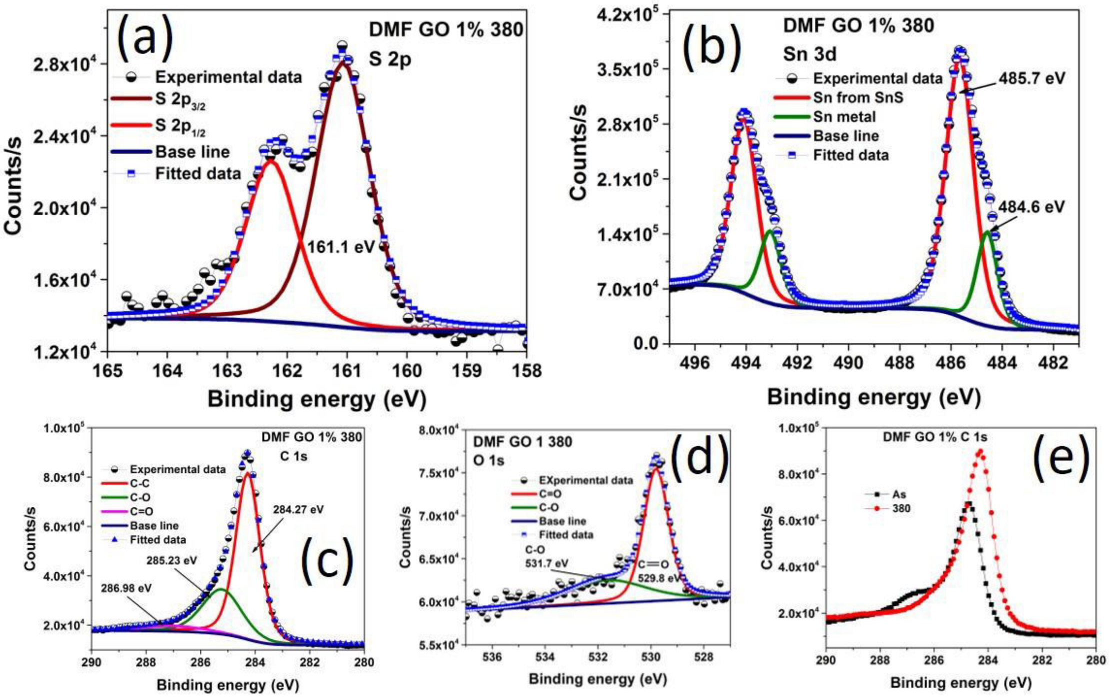

Fig.4.6. XPS high resolution scans of (a) S 2p (b) Sn 3d and (c) C 1s (d) O 1s of the SnS:GO thin film having 1% GO synthesized in DMF. (d) depicts the C1s scan after and before thermal treatment indicating the GO reduction © 2019, Elsevier

of Sn3d, S2p, C1s and O1s of SnS:rGO thin films synthesized from SnS in DMF with 1% GO and annealed at 380 °C. The spectra of C1s peak of the same sample before and after the heat treatments are also included to prove the reduction of GO due to the thermal treatment in vacuum (Fig.4.6e). The $Sn3d_{5/2}$ peak is constituted by two distinct peaks at binding energy values of 485.7 eV and 484.6 eV assigned to doubly ionized tin (Sn^{2+}) from SnS and elemental tin (Sn^0) respectively. Elemental tin appeared due to the preferential sputtering of sulfur over tin during Ar^+ etching. The S2p doublet was deconvoluted to corresponding $2p_{1/2}$ and $2p_{3/2}$ singlet peaks presenting S $2p_{3/2}$ peak binding energy of 161.1 eV that corresponds to the sulfur (S^{2-}) from SnS. Deconvolution of the C 1s peak of the DMF-SnS:GO sample resulted in three peaks where the major peak is assigned to C-C of binding energy 284.3 eV. Other two peaks of binding energies 285.2 eV and 287.0 eV are assigned to C-O and C=O respectively. However, among the three C 1s deconvoluted

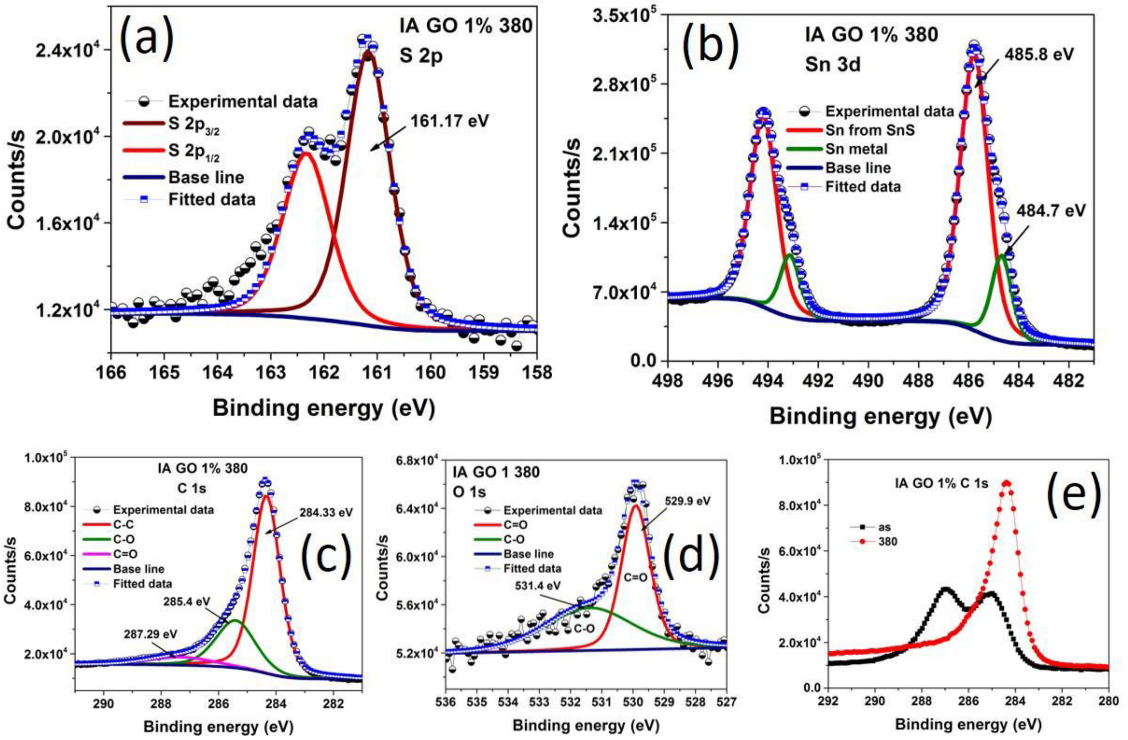

Fig.4.7. XPS high resolution scans of (a) S 2p (b) Sn 3d (c) C 1s and (d) O 1s of the SnS:GO thin film having 1% GO synthesized in isopropanol. (e) depicts the C1s scan after and before thermal treatment indicating GO reduction © 2019, Elsevier

peaks, the intensity of the C-C peak was much higher than that of the other two implying the successful reduction of graphene oxide due to the thermal treatment. The O 1s peak is deconvoluted into two peaks related to the C=O at 529.8 eV and C-O at 531.7 eV. As shown in Fig.4.6 (e), intensity of the C 1s peak is significantly increased along with a small peak shift towards lower binding energy after the annealing process. Fig.4.7 (a-d) presents the high-resolution spectra of Sn 3d, S 2p, C1s and O 1s scans of the sample synthesized from SnS in isopropyl alcohol having 1% GO after the annealing process. C 1s spectra of both as prepared and annealed samples are also given for comparison (Fig. 4.7 e). In this case, Sn $3d_{5/2}$ peaks located at 485.8 and 484.7 eVs are assigned respectively to the Sn from SnS and elemental Sn. S $2p_{3/2}$ peak with binding energy 161.2 eV is assigned to sulfur from

SnS.

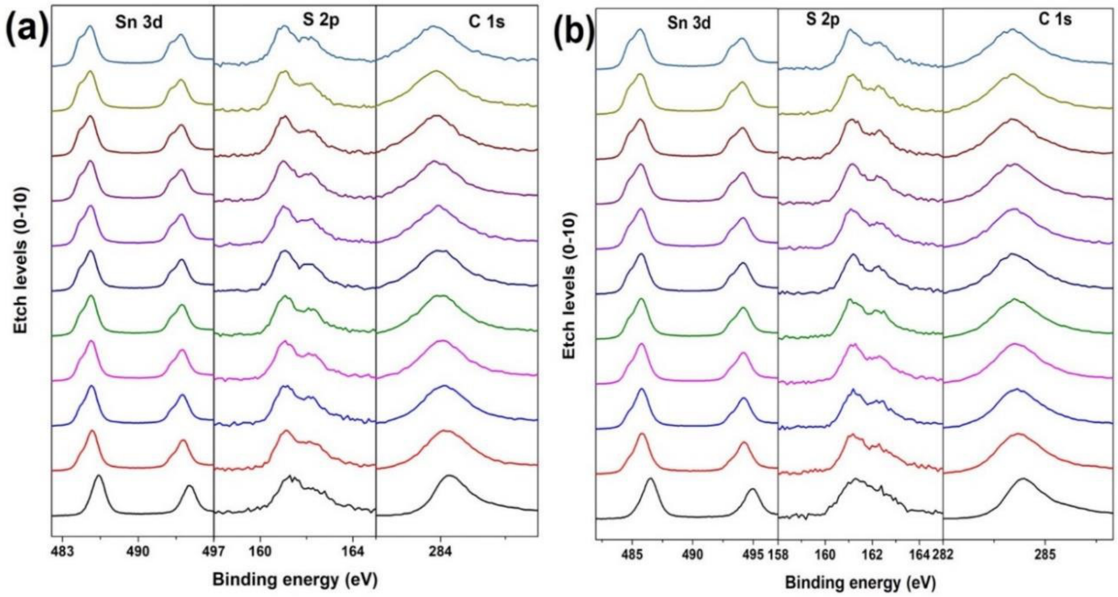

Fig.4.8. Depth profile spectra of Sn 3d, S 2p and C 1s of the SnS:rGO thin film synthesized from SnS in (a) DMF and (b) isopropyl alcohol having 1% GO. Spectra corresponding to each element show the distribution for first 10 etch levels through depth of the film © 2019, Elsevier

Table 4.1. XPS peak BEs of Sn, S, C and O of the present work and the values reported in the literature for comparison

XPS Peak	Values in the present work (eV)		Values reported in literature (eV)
	SnS-DMF	SnS-IA	
Sn $3d_{5/2}$	485.7	485.8	485.7[195]
S $2p_{3/2}$	161.1	161.17	161.0[195]
C 1s (C-C)	284.27	284.33	284.5[290]
O 1s (C=O)	529.8	529.9	529.6[290]

The peaks originated from C-C, C-O and C=O are located at binding energies of 284.3, 285.4 and 287.3 eV respectively. The C 1s spectrum of the as prepared sample composed of the C-O species with higher intensity than the C-C implies less reduction of GO due to the low deposition temperature of the film in isopropanol in comparison with the films synthesized from SnS in DMF. However, binding energies of Sn 3d, S 2p, C 1s and O 1s peaks for both samples (synthesized from SnS in DMF and isopropanol) confirm the existence of the SnS phase and GO/rGO in the films obtained by spraying laser ablated SnS nanocolloids.

The XPS results are summarized in table 4.1 and are in good agreement with previously reported values for SnS and graphene oxide as shown. C/O intensity ratio of the SnS:GO samples were calculated from the O 1s and C 1s high resolution spectra of the as prepared and annealed samples. The C/O ratio was increased from 3.8 to 6.1 after the heat treatment in vacuum for SnS(DMF):GO film, whereas for the film synthesized from isopropyl alcohol, the increment was from 0.38 to 11. The values of C/O ratio underlined that an extent of GO was already reduced during the film deposition in SnS(DMF): GO sample as mentioned earlier due to the higher deposition temperature. For SnS(IA):GO as prepared sample, even though the oxygen content was higher than that of carbon, effective reduction was achieved through the thermal annealing. Binding energy values of Sn and S for all the samples agree with the previously reported values for SnS and that of the SnS target used in PLAL experiment[144, 256, 291]. These results reveal that the samples prepared are composed of only the desired elements/phases and verified the successful reduction of GO by vacuum annealing. Depth profile analysis for composition of the samples were also acquired by Ar^+ etching of the samples. Depth profiles of SnS:rGO thin films with 1% GO synthesized from SnS in DMF and isopropanol showing the uniform elemental distribution are presented in Fig.4.8. Sn, S and C are present in all the given etch levels. A minor component of elemental tin is also identified which could be attributed to the effect of Ar^+ etching since the elemental tin is not detected on the sample surface and start to appear only from the first etch level. Presence of carbon in all etched levels indicate that the identified carbon is not adventitious carbon but originate due to the presence of graphene oxide. Depth profile shows that the film distribution towards the substrate is uniform and thus elemental homogeneity of the samples is confirmed.

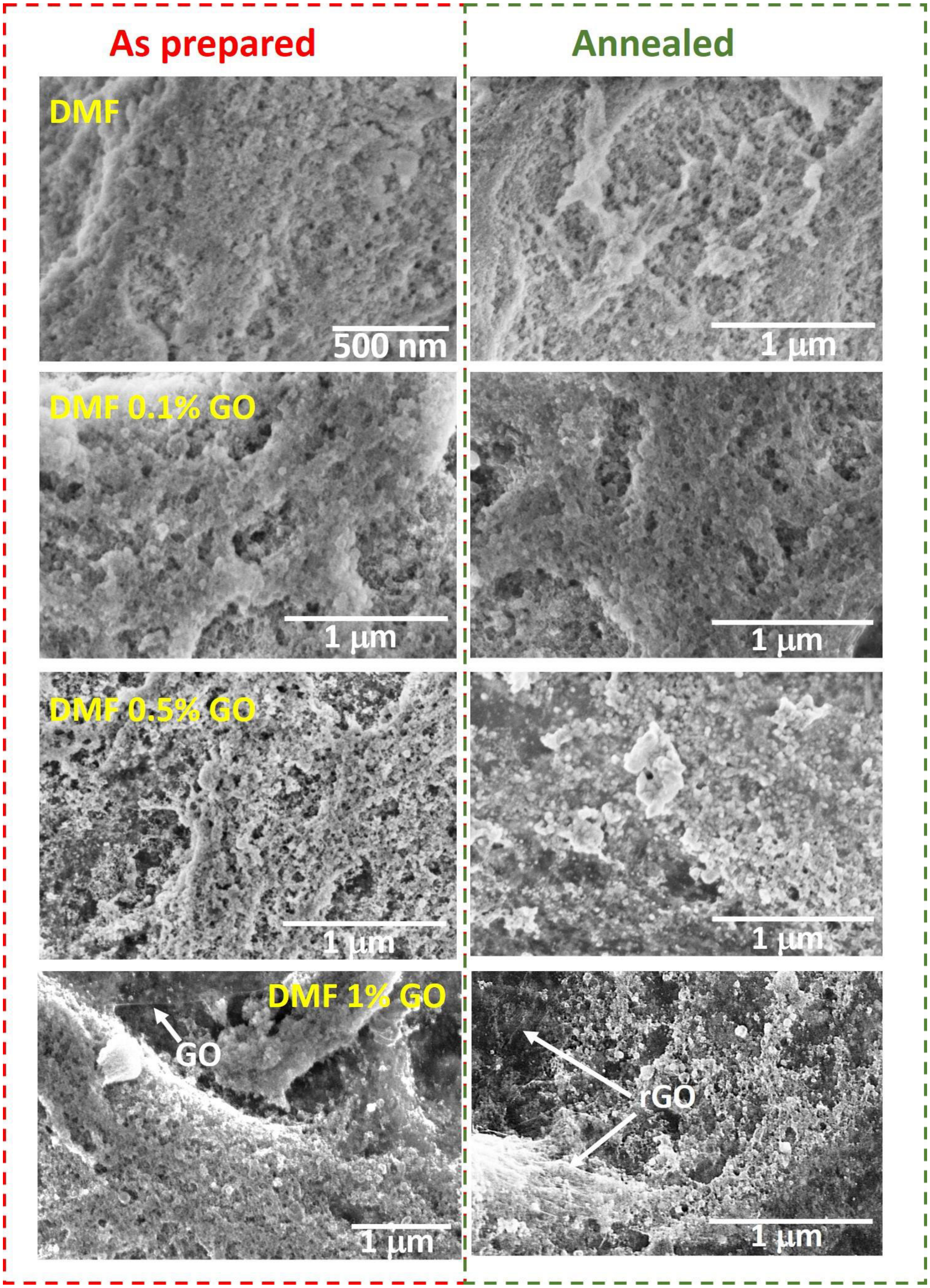

Fig.4.9. FESEM images of as prepared and annealed pristine SnS and SnS:GO thin films synthesized from SnS in DMF having different GO concentrations © 2019, Elsevier

4.2.5 Morphology of SnS and SnS:rGO thin films by SEM

Field emission scanning electron microscopy (FESEM) was employed to determine the surface morphology of the as prepared and annealed SnS and SnS:GO thin films synthesized from SnS in DMF as well as isopropanol. Fig. 4.9 depicts the surface topography of as prepared and annealed pristine SnS and SnS:rGO composite thin films synthesized from SnS in DMF. From the images, the surfaces of SnS and SnS:rGO thin films are of divergent morphologies. SnS layers of different heights are combined together to achieve the film formation as evident from the intensity contrast originated due to the height difference of the layers. The high magnification secondary electron images display a porous sponge-like surface morphology. The active surface area increases as the surface gets more porous which is beneficial for applications that require active surface modifications. For example, films with such a morphology would be highly beneficial for gas sensing applications where the gas molecule can be easily accommodated inside the available pores on the film surface. SnS thin films synthesized from SnS in isopropyl alcohol (fig.4.10) present a slightly different surface morphology from that of the films synthesized using SnS in DMF. This can be primarily attributed to the different substrate temperatures used while spray deposition of the films. Moreover, the in-situ reduction of GO during the deposition of SnS(DMF):GO thin films also contributes to the small difference in the morphology. The SnS film surface remains porous even after the addition of GO. GO or rGO incorporated into the as prepared or annealed SnS thin films can be seen as spider web or sheet like structures connected through the SnS particles. Surface morphologies of the SnS/ SnS:rGO films synthesized using the NPs in different liquid media show that they can be used for energy storage and gas sensing applications owing to the increased surface area originating from the porous structures. After the heat treatment in vacuum, the graphitic material is well embedded among the SnS particles compared to the as prepared films which can be attributed to the well reduction of GO above 250 °C.

SEM cross section images of the annealed SnS (DMF) and SnS (IA) thin films with 1% GO were recorded using electron beam incident at 45° to the sample (fig. 4.11). Film thicknesses calculated from the SEM images were 1.8 μm and 2.6 μm for SnS (DMF):rGO and SnS(IA):rGO thin films respectively. From the surface and cross section morphology seen in the images, not only the surface, but the entire film is growing in the spongy type

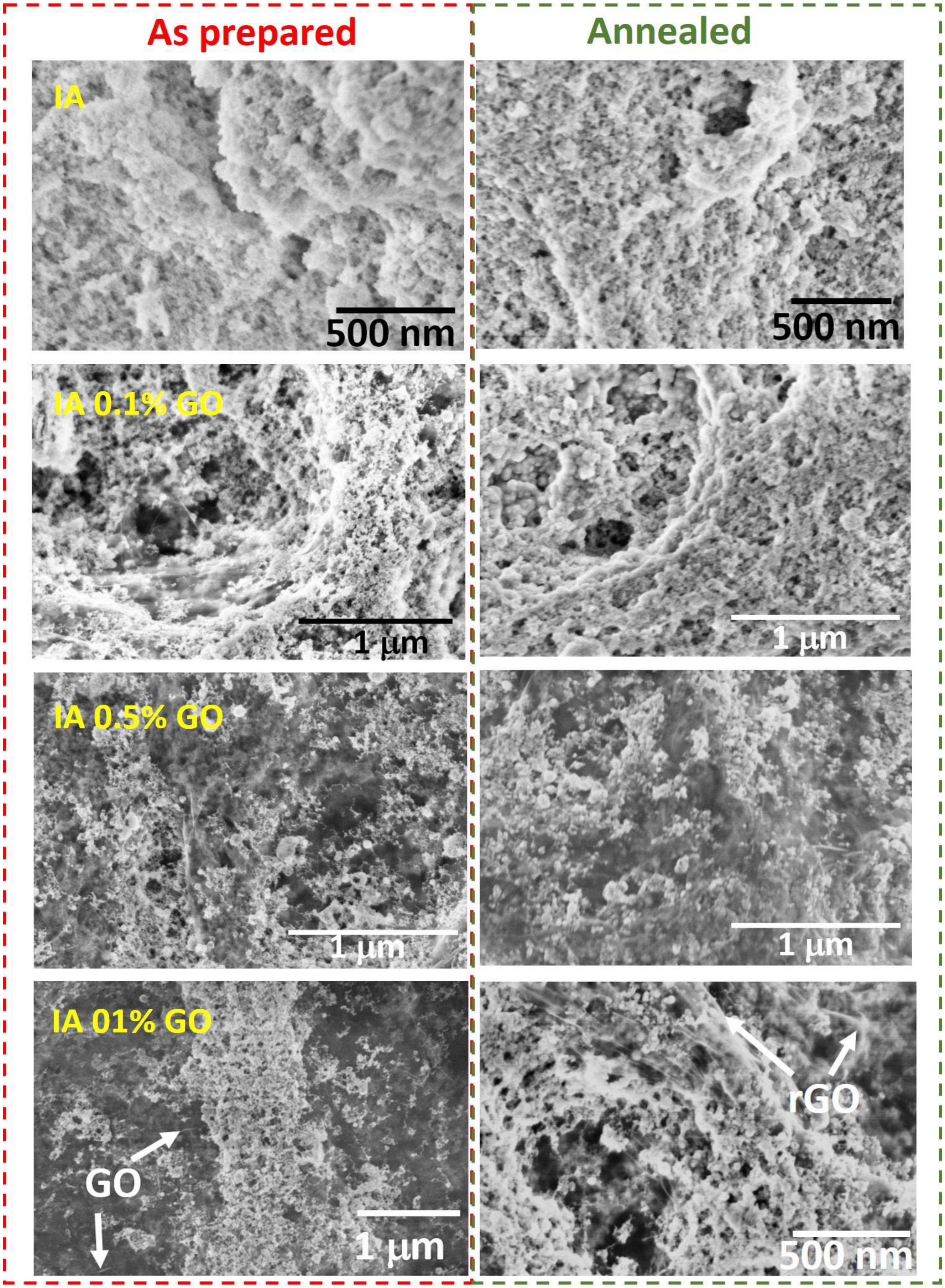

Fig.4.10. FESEM images of as prepared and annealed pristine SnS and SnS:GO thin films synthesized from SnS in isopropyl alcohol (IA) with different GO concentrations© 2019, Elsevier

structure. In addition to this, the films synthesized from SnS in DMF is more densely packed than the film synthesized from SnS in isopropanol (since the films in DMF has lower thickness compared to the films obtained from SnS in IA even though same quantity of both was sprayed). This can be attributed to both the well dispersion of SnS particles in DMF than IA as identified from the higher zeta potential of SnS in DMF as well as to the higher substrate temperature used during the spray deposition. Thickness obtained from the cross-section SEM images were in agreement with the thickness measured by profilometry technique. Thickness of all the films were measured by profilometry and it was observed that each of them has a thickness ~1.5μm or higher. This shows that the film deposition technique used in this work can pave the way towards fast synthesis of thick nanocomposite thin films with unique morphologies and enhanced properties.

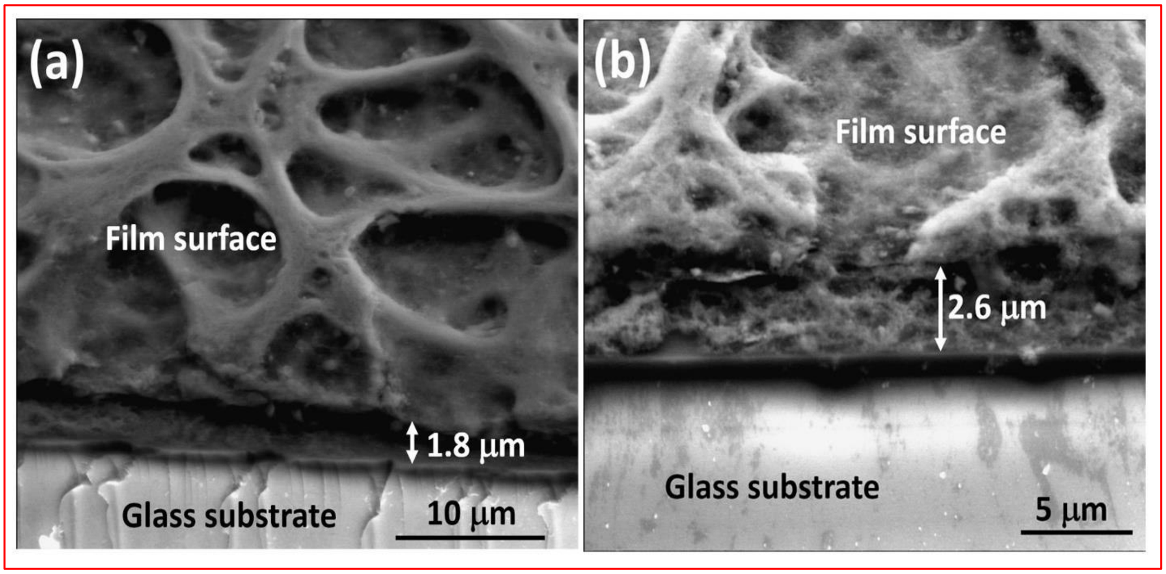

Fig.4.11. Cross section SEM images (taken at 45°) of (a) SnS (DMF):rGO and (b) SnS (IA):rGO having 1% GO. Cross section and surface show the spongy type morphology of the SnS:rGO thin films © 2019, Elsevier

Morphology of SnS thin films synthesized by combining spray technique with PLAL is different from typically reported morphologies of SnS thin films synthesized by conventional spray pyrolysis[265] or other methods[292, 293]. The surface topographies of the samples in the present work are highly porous compared to the other SnS surface structures reported by various synthesis methods. Peculiarity of the synthesis technique by combining PLAL to produce nanocolloids and spray deposition for the film formation plays important role in generating films with such a morphology. When the nanocolloid mixture is deposited at a higher substrate temperature, in-situ reduction of graphene oxide is achieved together with deposition of the film excluding the need of post thermal treatments for GO reduction. Degree of reduction of GO could be easily controlled by varying the substrate temperature which may lead to formation of nanocomposite thin films having various morphology and properties. NP synthesis by PLAL results in in-situ stable dispersions of SnS NPs in the given solvents (isopropanol and DMF) during the ablation as evident from their negative zeta potential values. This is one of the advantages of laser ablation in liquid technique so that the solubility problem of the components in the desired solvents is not affected. Spray process was carried out soon after the laser ablation synthesis of the colloids to exclude any possible chance of precipitation. Smaller size of the nanoparticles, homogeneity of their dispersion in solvents by ablation and stability of these nanocolloids account for the deposition of good quality thin films.

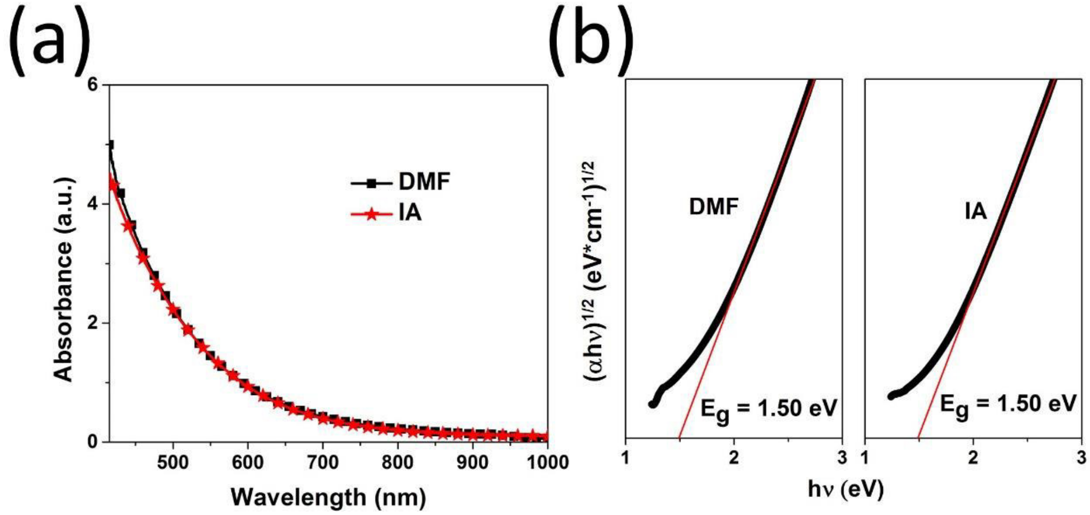

Fig.4.12. (a) Absorption spectra of SnS NPs in DMF and isopropyl alcohol (IA) and (b) the corresponding optical band gaps estimated from Tauc plots © 2019, Elsevier

4.2.6 Optical properties of SnS and SnS:rGO thin films

Optical absorption of the films and nanocolloids were measured using a UV-Vis-NIR spectrophotometer. For the absorption measurement of the nanocolloids, the respective solvent (DMF or isopropanol) was used as the reference in the dual beam spectrophotometer, in the measured wavelength range (400 to 1000 nm). The absorbance spectra of SnS NPs in DMF and isopropyl alcohol, and their corresponding band gaps evaluated from linear fit to the Tauc plots are presented in Fig. 4.12.

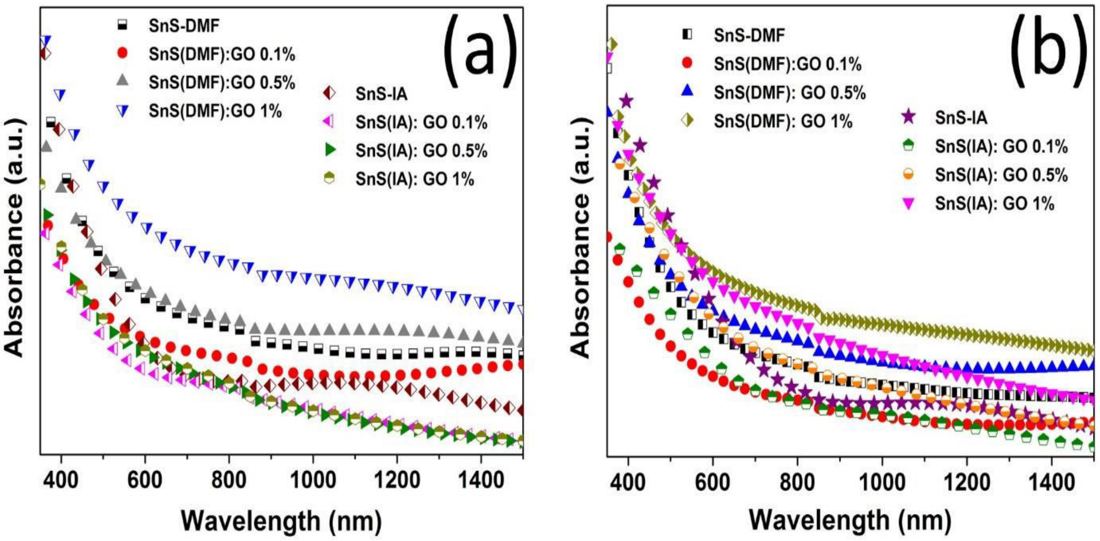

Fig.4.13. Absorption spectra of (a) as prepared and (b) annealed pristine SnS and SnS:GO thin films synthesized from SnS in isopropanol and DMF having different GO concentrations © 2019, Elsevier

SnS NPs synthesized by laser ablation show good optical absorption in the visible region irrespective of the solvent where the absorption spectra are quite similar in both liquids used. Band gaps of SnS NPs corresponding to indirect transition calculated using the Tauc plot as 1.5 eV for SnS in DMF as well as in IA. An increase in the band gap compared to the bulk SnS (1.1 eV) can be attributed to the quantum confinement effect in the nano scale which arose from the small size of the particles as well as their morphologies by PLAL. Properties of the liquid media such as polarity, density, refractive index, viscosity, number of carbon chains and functional groups play important roles on determining the final morphology of the NPs. Moreover, the band gap of SnS NPs falls in the range of optimum band gap required for photovoltaic applications covering almost the entire visible range.

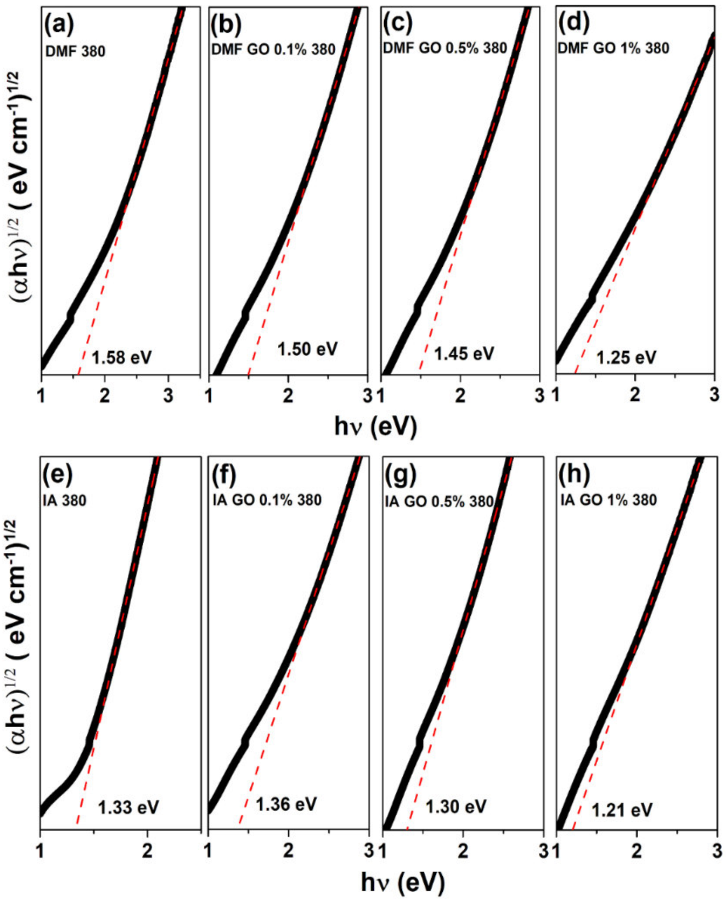

Fig.4.14. Estimated band gap of the annealed pristine SnS and SnS:rGO thin films having 0.1, 0.5 and 1% GO deposited from SnS in DMF and isopropanol © 2019, Elsevier

Absorption spectra of the as prepared and annealed SnS and SnS:rGO thin films with various GO concentrations were measured using the same UV-Vis-NIR spectrophotometer in the range of 350 nm to 1500 nm using a plain glass substrate as the reference (Fig.4.13). Both pristine SnS and SnS:GO/rGO films exhibited good absorption in the visible region. Pristine SnS thin films deposited using the laser ablated nanocolloids in isopropanol and DMF present optical band gaps of 1.33 and 1.58 eVs respectively (Fig.4.14). Different band gaps according to the change in liquid medium could be attributed mainly to the small differences in the nanoparticle morphology in one solvent compared to the other (as reveled by TEM analysis). Moreover, the solvent properties such as viscosity, refractive index and boiling point also play important roles in determining the final morphology of the spray deposited thin films which may then influence the band gap.

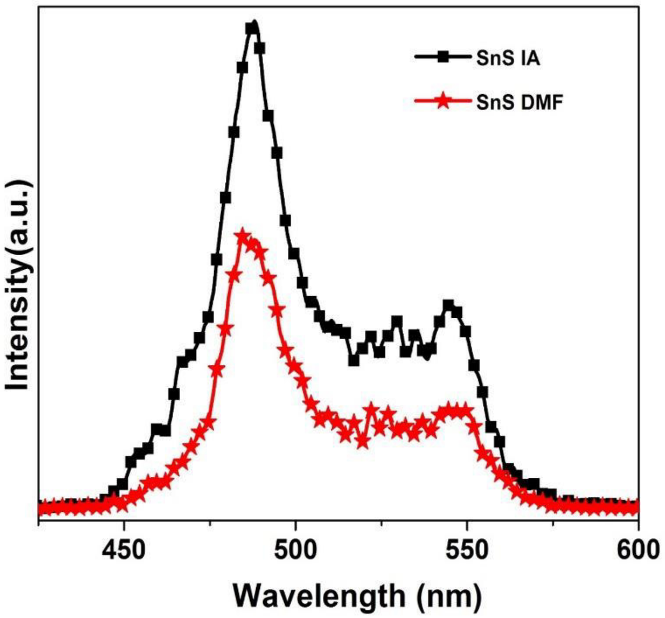

Fig.4.15. Photoluminescence (PL) spectra of SnS NPs synthesized in DMF and isopropanol showing strong emission at 487 nm. Excitation wavelength used was 350 nm © 2019, Elsevier

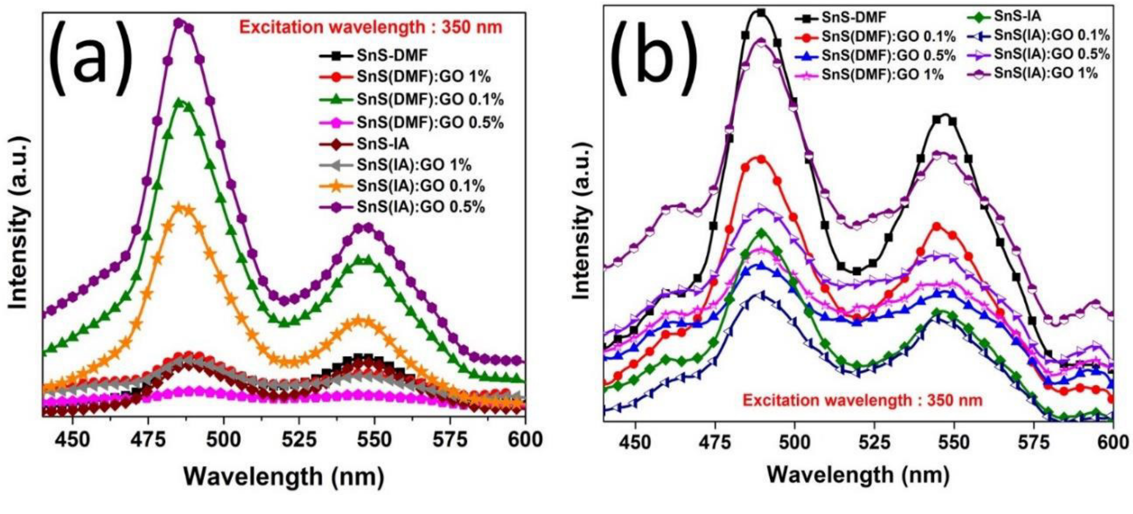

Fig.4.16. PL spectra of the (a) as prepared and (b) annealed pristine SnS and SnS:rGO thin films having different GO concentrations deposited from SnS in DMF and SnS in isopropanol. Excitation wavelength used was 350 nm © 2019, Elsevier

As the GO concentration is varied from 0.1 to 1%, a corresponding decrease in the band gap was observed irrespective of the liquid medium used in PLAL. The films possess band gaps of 1.5, 1.45 and 1.25 eV respectively for 0.1, 0.5 and 1% GO when DMF was used as the solvent whereas in isopropanol the estimated band gaps are 1.36, 1.3 and 1.21 eV for the corresponding GO concentrations (fig. 4.14). Band gaps of the SnS: rGO thin films are comparable with that of bulk SnS which suggest that the nanocomposite SnS:rGO films are suitable candidates for applications that require visible light harvesting. It can be seen that the optical band gap reduces as the GO concentration increases for both sets of samples. The change in band gap of the films can be attributed mainly to the small band gap of rGO compared to SnS thus after the band alignment forming a composite of lower band gap[294]. In addition to this, the morphological changes due to the GO addition can also contribute to the alteration in the film band gaps.

Photoluminescence (PL) spectra of the SnS nanocolloids were collected to identify the emission energy (fig. 4.15) using an excitation line of 350 nm. A strong blue emission with a peak centered at 487 nm is exhibited by the SnS NPs in both liquids. In addition to this, a low intense green emission around 545 nm is also observed. PL spectra of the as prepared and annealed SnS and SnS:GO thin films were also measured (Fig.4.16) using the same excitation wavelength as that of the SnS NPs. The PL spectra of as prepared and annealed SnS and SnS:GO thin films resembles that of the NPs with a strong emission peak centered at ~487 nm. No significant difference in the PL spectra between the annealed and as prepared SnS and SnS:GO thin films is observed as seen in Fig.4.16. More defect levels can be formed between the empty and occupied states of the SnS semiconductor NPs due to extreme conditions of the plasma and rapid cooling inherent to the pulsed laser ablation in liquid technique and hence the de-excitation from the excited to lower level may not be straight forward. SnS NPs synthesized by PLAL in different liquid media by 532 and 1064 nm pulsed lasers also showed similar emission properties as shown by Guillen et al.[144]

4.2.7 Comparison of opto-electronic properties of pristine SnS thin films with nanocomposite SnS:rGO thin films

Opto-electronic properties of the annealed SnS and SnS:rGO thin films were explored by photoconductivity measurements. Light emitting diodes (LEDs) of different wavelengths were used to illuminate the samples in order to measure the photoresponse. Optical power of the LEDs used for the sample illumination was 50 W. The thin films were illuminated either by white light or other selected wavelengths of the visible spectrum viz. yellow, red, green and blue. All the annealed pristine SnS and SnS:rGO thin films exhibited an increase in the current under illumination (photocurrent) compared to the current in the dark (fig.4.17).

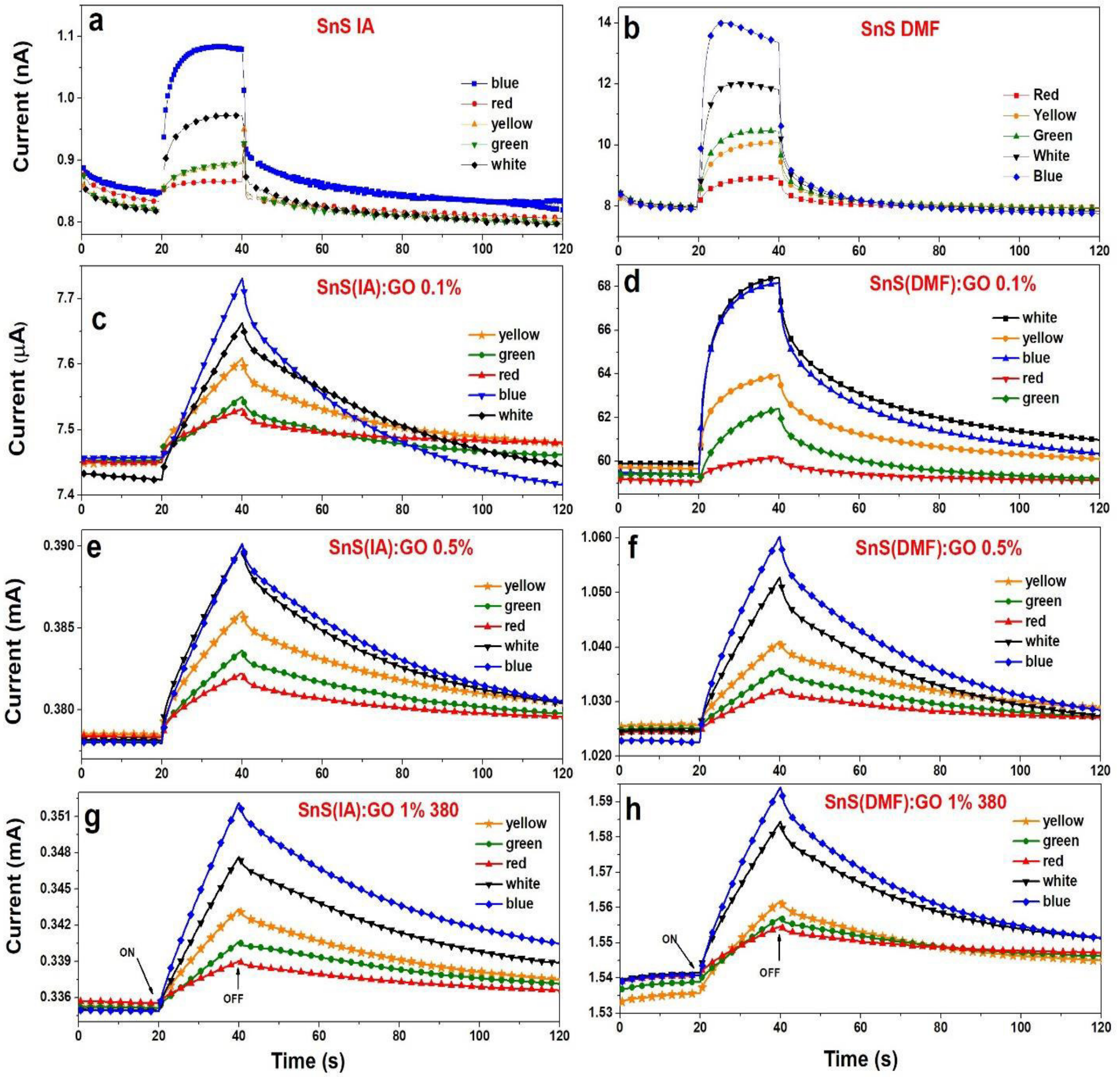

Fig.4.17. Photocurrent response of pristine SnS and SnS:rGO thin films with 0.1%, 0.5% and 1% GO concentrations deposited from (a,c,e,g) SnS in IA and (b,d,f,h) SnS in DMF © 2019, Elsevier

By adding 1% of GO into the samples, the dark current showed an increase of nearly 7 orders of magnitude compared with that of pristine SnS thin films. For the films synthesized with 0.1% GO, the measured photocurrent is in micro ampere range where as in films with 0.5%, the current is in milli ampere scale. The increase in the magnitude of photocurrent by 3 orders in this case is attributed to the higher concentration of GO thereby enhancing the electronic properties of the films. Even though pristine SnS thin films also show appreciable photoresponse to all wavelengths of illuminations used, the photocurrent is in the order of nano amperes. Hence it is clear from the presented graph that, conductivity of SnS thin films is enhanced several orders of magnitude with the addition of GO/rGO network into it. In the case of SnS:rGO, the photo-generated charge carriers can easily travel through the highly conductive rGO layer which is embedded between the SnS particles (refer to the morphology characterization by SEM in section 4.2.6). As evident from fig.4.17, SnS:rGO thin films show distinct behavior under different wavelength illumination. The thin films synthesized from DMF and isopropyl alcohol exhibit similar photocurrent response where the most absorbed wavelength is blue which can be correlated with the absorption spectra of the films (fig.4.13) due to the increased absorption at shorter wavelengths. By comparing the films synthesized from SnS in DMF and isopropyl alcohol, the photocurrent range is higher for the films synthesized from SnS in DMF. A few authors reported the photoresponse of SnS based photodetectors by excitation of different wavelengths[210, 211]. Study regarding the photoresponse behavior under different wavelength illuminations is a key factor in photodetector applications.

4.2.8 Comparison of electrochemcial properties of pristine SnS thin films with nanocomposite SnS:rGO thin films

Electrochemical properties of the SnS and SnS:rGO films were explored by cyclic voltammetry measurements. A three electrode potentiostat was employed to identify the capacitive nature and cyclic performance of the thin films. Pristine SnS or SnS:rGO thin films deposited on ITO were used as the working electrodes for the measurements while platinum wire and Ag/AgCl (silver/silver chloride) were employed as the counter and reference electrodes respectively. All the electrochemical tests were carried out in 0.1M NaCl (sodium chloride) solution. Prior to each measurement, the electrolyte was bubbled with nitrogen gas and continuously stirred for 5 minutes to remove the dissolved oxygen in the electrolyte. Fig. 4.18 (a, b) shows the CVs of pristine SnS and SnS:rGO thin films. As the GO concentration in the films increased, the capacitance also increased. Addition of GO modifies the surface of the electrodes which would modify the properties of the electrical double layer formed at the interface of the electrode and the solvent. From the figure, better electrochemical activity of the SnS:rGO in comparison with bare SnS is evident.

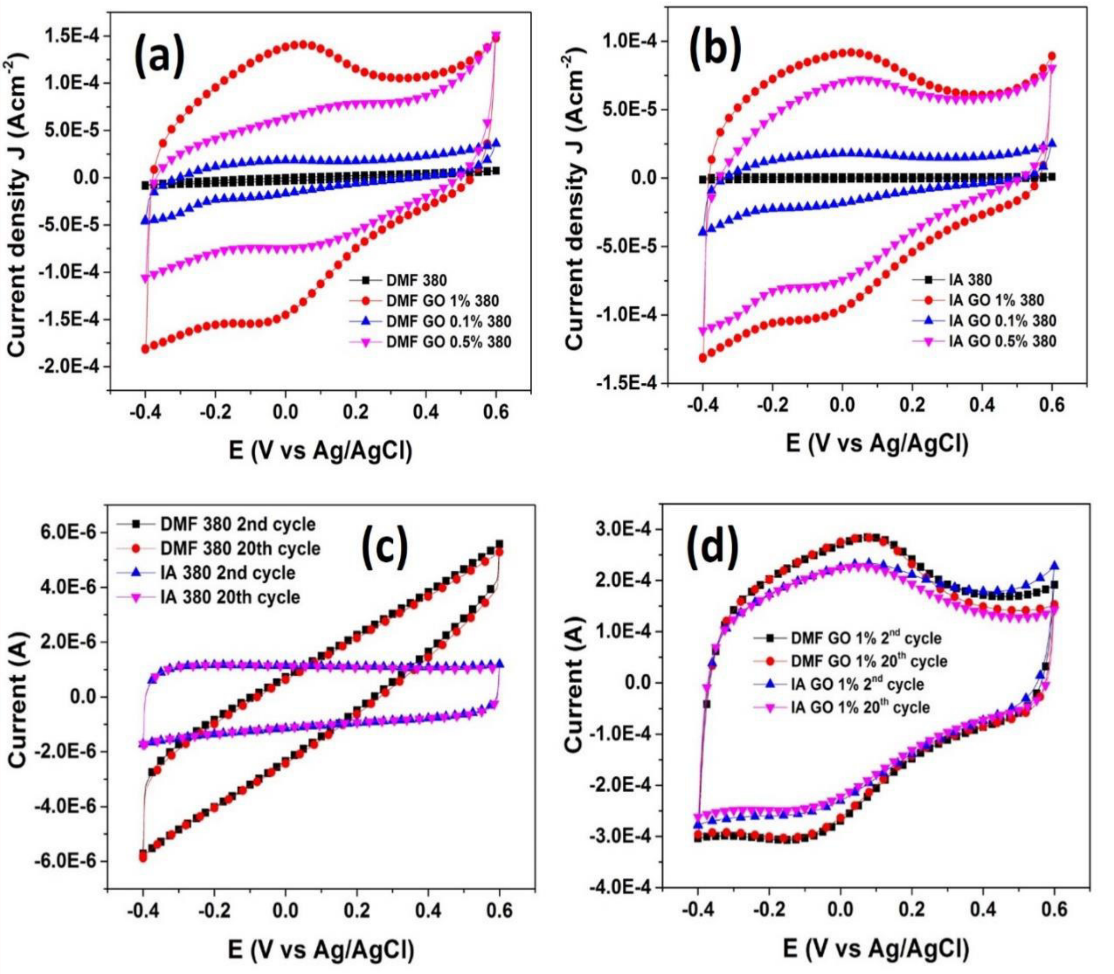

Fig.4.18. Cyclic voltammogram of (a) SnS(DMF) and (b) SnS(IA) thin films having different rGO concentrations in 0.1 M NaCl at 20mV/s Cyclic voltammetry stability test of (a) annealed pristine SnS thin films and (b) SnS: rGO thin films with 1% GO synthesized from SnS in DMF and isopropyl alcohol in 0.1M NaCl at scan speed 20 mV/s © 2019, Elsevier

The capacitance values estimated from CV analysis are summarized in Table 4.2.

Table.4.2: Capacitance of annealed bare SnS and SnS:rGO thin films for different concentrations of GO calculated from CV measurements

Sample	Capacitance (mF)	Sample	Capacitance (mF)
SnS-DMF	0.123	SnS-IA	0.012
SnS (DMF) rGO 0.1%	0.551	SnS (DMF) rGO 0.1%	0.405
SnS (DMF) rGO 0.5%	2.12	SnS (DMF) rGO 0.5%	1.16
SnS (DMF) rGO 1%	2.21	SnS (DMF) rGO 1%	1.98

The pristine SnS thin films synthesized using NPs in both liquids display lower capacitance compared to that of nanocomposite SnS:rGO films. Adsorption of some ions from the electrolyte on the electrode surface restrict the measured current and hence contribute to the slight deviations in the current at some specific potential values as seen from the fig. Moreover, this deviation increases with increase in the GO concentration in the films. The graphitic material incorporated in the films accounts for the adsorption of ions from the electrolyte on the electrode surface since no such deviation in current is noticed for pristine SnS electrodes. Hence the capacitance in the pristine SnS electrodes are purely double layer whereas in SnS:rGO, both double layer and pseudo capacitances are present. Graphitic material acts as more electro active species in the electrodes to improve the capacitance of SnS:rGO electrodes as the GO concentration is increased. The following equation (4) was employed to estimate the capacitance (C) of all the films

$$C = \frac{A}{2(E_2-E_1)V} \tag{4}$$

where A is the area under the CV curve, V is the scanning speed and E_1 and E_2 are the initial and final scan potentials. The capacitance values calculated using the above equation are summarized in Table.1. The highest capacitances calculated were 2.21 and 1.98 milli

Farads respectively for the electrodes of SnS:rGO in DMF and isopropyl alcohol with 1% rGO. Higher specific capacitance obtained for SnS:rGO in DMF could be originating from the improved electrode-solvent interface formation in these electrodes as well as better stability of SnS nanoparticles in DMF (as revealed by the zeta potential values). Cycle performance of the SnS and SnS:rGO electrodes (with 1% GO) was explored by measuring 20 continuous CV cycles in the potential range from -0.4 to 0.6 V and the corresponding cyclic voltammograms (CVs) are displayed in fig.4.18 (c,d). No significant deviation in the measured current is noticed for either the pristine SnS or SnS:rGO electrodes even after 18 continuous measurement cycles which in turn displays the stability of these electrodes in the given solvent. Voltammograms of pristine SnS thin films (Fig.4.18(c)) recorded at 2nd and 20th cycles coincide exactly with each other implies the stability of SnS electrodes even after 18 cycles. In the same way, stability of SnS:rGO electrodes with 1% GO in the given solvent (0.1 M NaCl) is also clearly seen from Fig.4.18(d).

Nano SnS was identified as an electrode for electrochemical capacitors by Jayalakshmi et al. SnS immobilized on paraffin impregnated graphite electrode (PIGE) showed specific capacitances of 6.29 Fg^{-1} and 4.19 Fg^{-1} in 0.1 M KOH and 0.1 M NaCl solutions respectively[295]. Some other efforts were also carried out to show the potential of SnS to be applied in supercapacitors due to its versatile electrochemical properties[296, 297]. Sponge-like b-$Ni(OH)_2$ NPs having surface area 56.4 m^2g^{-1} was reported by Dubal et al. where the films exhibited good specific capacitance attributing to the high surface area and effective distribution of the pores[298]. Sponge-type porous morphologies possess large surface area which is beneficial for optoelectronic, gas adsorption/sensing and electrochemical applications. The present results show that it is possible to enhance the electrochemical behavior of SnS electrodes by integrating GO/rGO into SnS matrix with sponge type morphology.

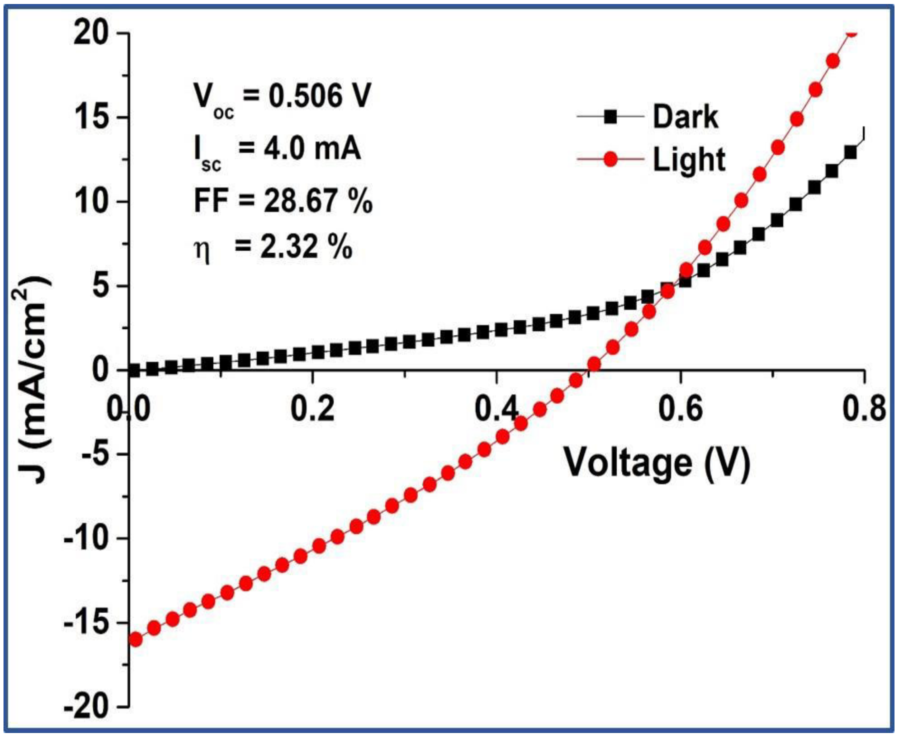

Fig.4.19. J-V curve of Solar cell structure ITO/CdS/Sb_2S_3/SnS(DMF):rGO in dark and illuminated states showing conversion efficiency of 2.32% © 2019, Elsevier

Quasi-single-dimensional ribbon like SnS structures exhibited better thermal transport and electronic properties compared to nanowires and nanotube materials[210]. Exceptional physical properties originating from their special geometries and ultrathin thicknesses make them materials of wide interest for applications like sensing, opto-electronic and nanoscale electronic devices.

4.2.9 SnS:rGO thin film absorber in photovoltaic device and J-V characterization

Photovoltaic application of SnS:rGO nanocomposite thin films was proved by fabricating a solar cell of structure glass/ITO/CdS/Sb_2S_3/SnS(DMF):rGO where the SnS(DMF):rGO layer acts as the absorber material. The cell structure consisted of a CdS layer (deposited by chemical bath deposition) as the n-type layer and Sb_2S_3 (deposited by CBD) as an intrinsic layer to constitute the p-i-n junction. J-V characteristics of the solar cell based on SnS:rGO under dark and illumination is presented in Fig.4.19.

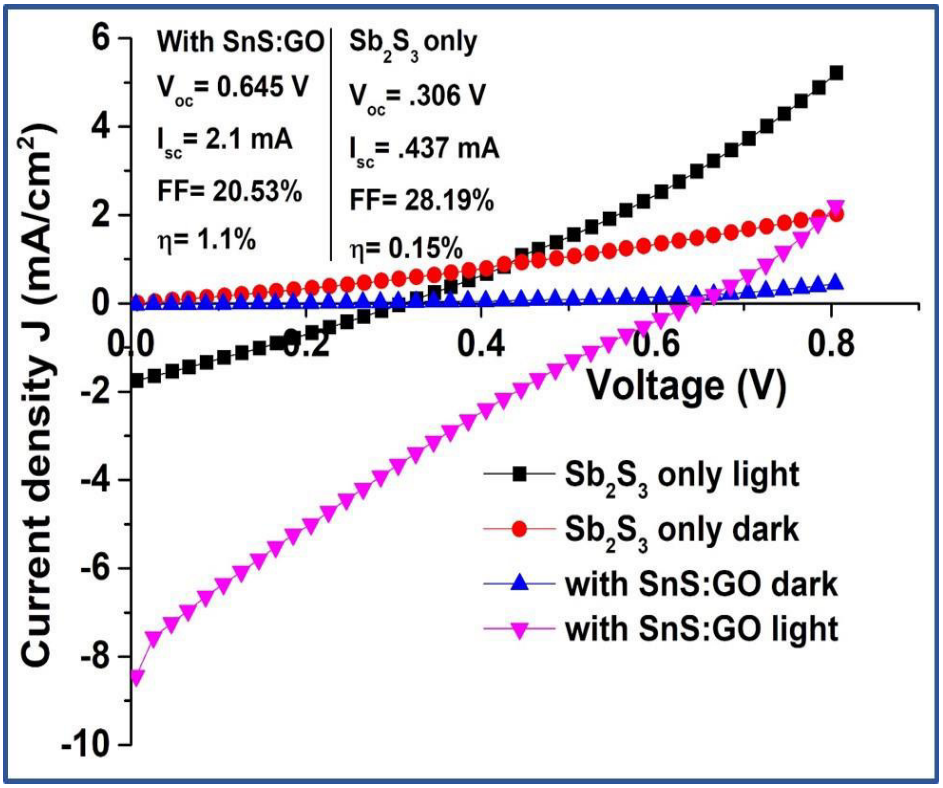

Fig.4.20. J-V characteristics of the solar cell structures ITO/CdS/Sb_2S_3 and ITO/CdS/Sb_2S_3/SnS (DMF):GO (before annealing) in light and dark conditions with the corresponding solar cell parameters © 2019, Elsevier

A maximum photo conversion efficiency of 2.32% was obtained for the SnS (DMF):rGO photovoltaic device. For comparison, a solar cell without the SnS(DMF):rGO layer was also tested under the same conditions keeping all the other layers the same and the obtained efficiency was only 0.15% (see fig.4.20). Difference in the efficiency of the cell with and without the SnS:rGO layer confirms that the increase in the conversion efficiency is solemnly due to the SnS:rGO layer. J-V curves of the cell with only Sb_2S_3 and with SnS(DMF):rGO before annealing (SnS:GO instead of SnS:rGO due to the absence of thermal reduction) are given in fig.4.20. Short circuit current of the cell with SnS(DMF):rGO layer (4 mA) was about 9 times greater than that of the cell with only Sb_2S_3 (0.437 mA) layer and the efficiency was increased about 15 times with the incorporation of the SnS(DMF):rGO layer. As seen from the Fig.4.19, short circuit current and open circuit voltage of the solar cell are increased remarkably with the incorporation of the SnS:GO layer into the cell. An increase of 7 mA in the short circuit current was observed in the cell with SnS:GO after the annealing process. These results demonstrate the potential applicability of the synthesized SnS:rGO nanocomposite thin films in the photovoltaics field.

4.3 Conclusions

SnS, SnS:GO and SnS:rGO nanocomposite thin films were synthesized by spraying SnS nanocolloids obtained by PLAL mixed with GO. Crystal structure, morphology, optical, opto-electronic and electrochemical properties of the films were determined using different characterization techniques. SEM images showed porous SnS film layers embedded with GO net-like structures (sponge-like morphology). Electrochemical and opto-electronic properties of SnS thin films were enhanced by incorporating rGO into the SnS matrix owing to the higher electronic conductivity of rGO. A solar cell was fabricated to demonstrate the potential of the synthesized thin films in the area of photovoltaics. A photovoltaic device with SnS:rGO nanocomposite thin film as the absorber layer showed photoconversion efficiency of 2.32%. The applied green synthesis technique (by combining PLAL and spray deposition) can fulfill the need of large area nanocomposite thin film deposition and the study can pave the way towards enhancement in the device performances and cost-effective production of photodetectors, gas sensors, charge storage devices and solar cells.

Chapter 5

Tin disulfide (SnS_2) nanoparticles by pulsed laser ablation in liquid: effects of wavelength, fluence, liquid, temperature and post irradiation

5.1 Introduction

Tin disulfide (SnS_2) is an important phase of the tin sulfide family due to its versatile properties and applications as explained in the first chapter of the thesis. Hence, the present and next chapter of the thesis describe the laser ablation synthesis of SnS_2 NPs and their deposition as thin films using the spray method. Details of the characterization results and properties of nanoparticles as well as some electrochemical applications of the NPs and thin films are included. Since SnS_2 NPs synthesis by PLAL was first reported by us, this chapter will focus on the synthesis and characterization of SnS_2 NPs by PLAL in different solvents. SnS_2 NPs were synthesized in four different liquids (DMF, isopropanol, ethanol and acetone) using two laser wavelengths (532 nm and 1064 nm). Moreover, effects of ablation fluence on SnS_2 nanoparticle morphology was studied for the particles obtained in acetone and isopropanol while the effects of liquid medium temperature and post irradiation were investigated for SnS_2 in DMF. The liquid medium temperature and post irradiation studies were also aiming to obtain different morphologies at these conditions to explore the hydrogen evolution studies since hydrogen evolution reaction (HER) is considered as one of the most important mechanism for the future renewable energy due to its applicability in conversion systems and energy storage[299]. Even though the best performing electrocatalyst for HER up to date is platinum (Pt), the high cost and low natural abundance of Pt led to the searching of HER catalysts from environment friendly, cost-effective materials including semiconductors. Transition metal dichalcogenides (TMDs) are one of the current research topics due to their flexibility in design and low cost to replace Pt electrodes. So far, only a few reports describe the electrochemical properties of tin based binary chalcogenides such as SnS and SnS_2[300]. Further, due to the layered structure, structure dependent optoelectronic properties and different morphologies, they can be utilized as electrocatalysts for different applications including HER. Results of this chapter were published in references [79] and [301].

5.2 Results and discussion

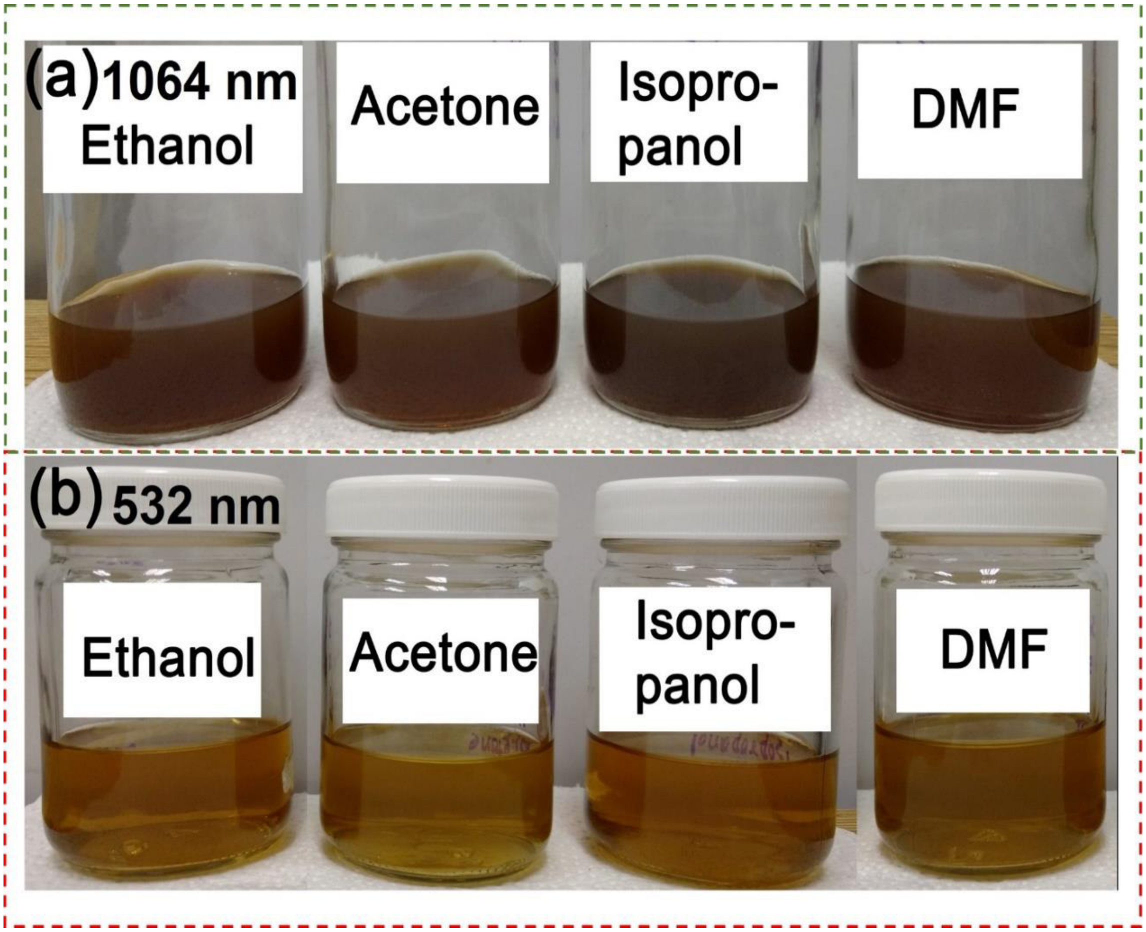

Fig.5.1. Photographs of SnS_2 nanocolloids in ethanol, acetone, isopropanol and DMF by (a) 1064 nm and (b) 532 nm pulsed laser outputs © 2018, Elsevier

Photographs of SnS_2 NPs synthesized in 4 different liquids using two different laser wavelengths are presented in fig.5.1. The nanocolloids were prepared by a very short time of laser ablation (30 seconds) in each solvent. As synthesized nanocolloids of SnS_2 were golden yellow colored for 532 nm ablation and brown color for 1064 nm irrespective of the liquid medium selected. The darker color of nanocolloids prepared by 1064 nm laser can be attributed to the increased concentration of the colloids due to the higher energy of infrared (IR) output (~900 mJ) in comparison with the second harmonic output (~450 mJ) as well as change in the morphology and band gap of the SnS_2 nanoparticles by ablation using different laser wavelengths. The particles were quite stable for several days without any surfactants (as no precipitates were found in the sample bottles) which could be attributed to the formation of an electrostatic potential on the surface of the particles (electrostatic stabilization) during laser ablation as reported for many laser generated NPs.

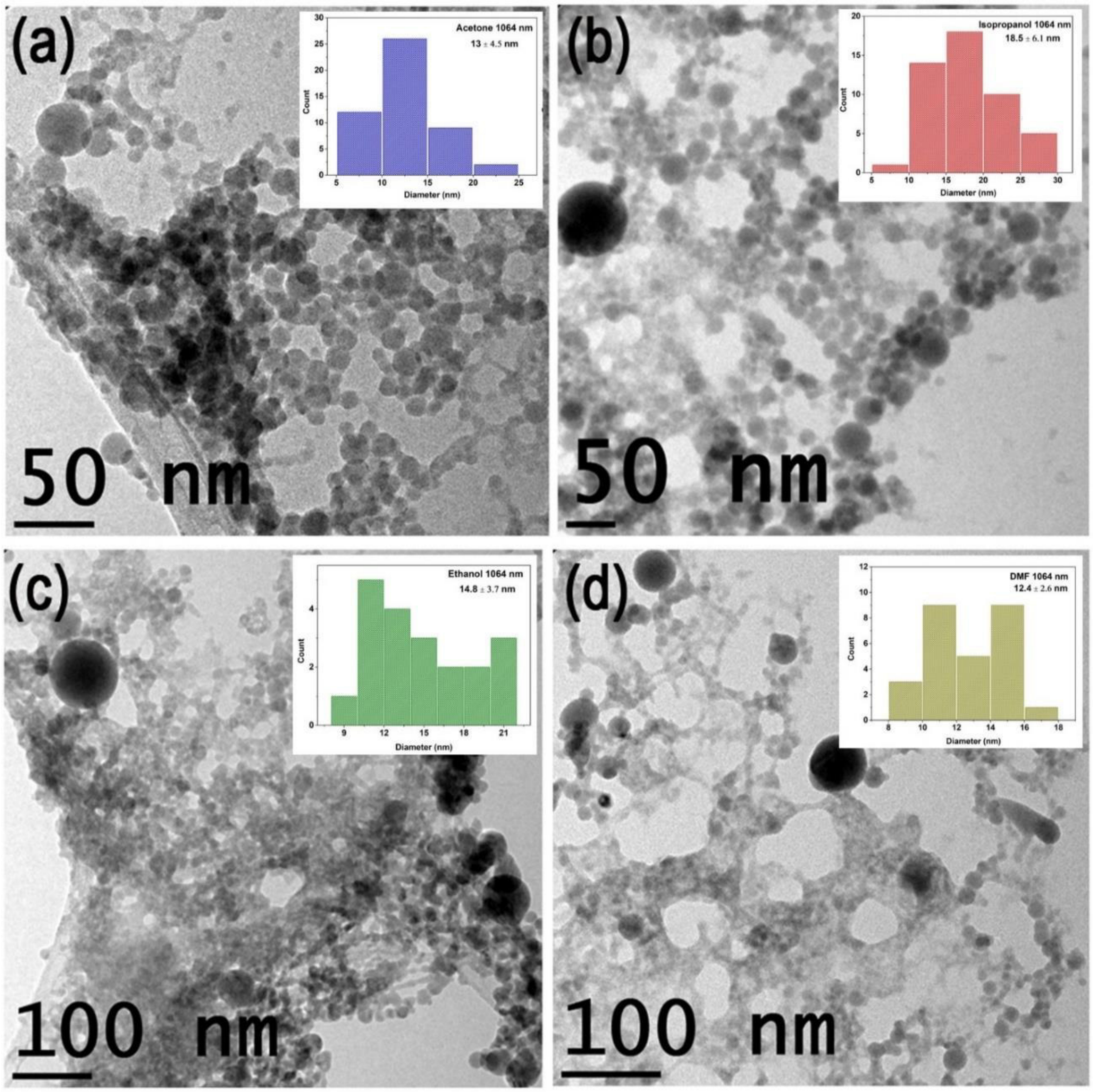

Fig.5.2. TEM images of SnS_2 NPs by 1064 nm laser in (a) acetone (b) isopropanol (c) Ethanol and (d) DMF solutions indicating the NP morphology in each liquid. The insets show average particle size in each solvent © 2018, Elsevier

5.2.1 Morphology of SnS_2 NPs: effects of liquid medium and ablation wavelength

Morphology of the NPs was identified using TEM analysis of the samples where HRTEM images and selected area electron diffraction patterns were used for identifying the crystalline microstructure of the laser generated particles. TEM images of SnS_2 NPs prepared by 1064 nm laser are presented in Fig.5.2. HRTEM images of all the samples are given in Fig.5.3 (a-d) where the interplanar distances were calculated and compared with JCPDS data to confirm the crystal structure corresponding to each sample as well as to compare with that of the SnS_2 target used for laser ablation.

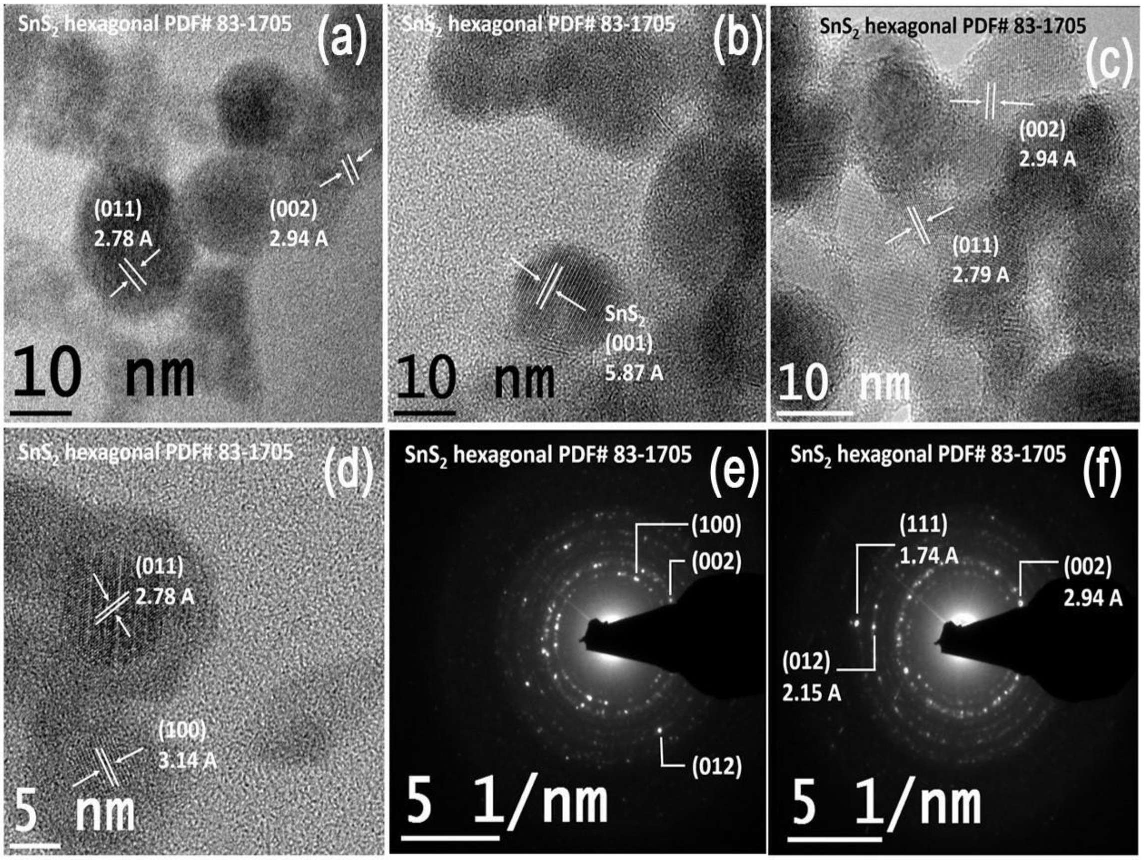

Fig.5.3. HRTEM images of SnS_2 NPs by 1064 nm laser in (a) acetone (b) isopropanol (c) Ethanol and (d) DMF solutions. SAED patterns of SnS_2 in (e) acetone and (f) ethanol © 2018, Elsevier

As depicted in fig. 5.2, 1064 nm laser ablation generated spherical NPs in all the four liquid media. In acetone and isopropanol, the nanoparticles have definite boundaries where individual particles are not easily distinguishable in case of the particles formed in DMF and ethanol. In addition to the smaller NPs, a few larger particles are also present in all the liquids which might have resulted due to the agglomeration of smaller nanoparticles.

Presence of irregular shaped particles can be seen in ethanol and DMF also. Images in figure. 5.3(a-d) present the HRTEM analysis of the SnS_2 NPs in each liquid medium. The crystalline SnS_2 particles can be easily identified from the HRTEM images. In all cases, the interplanar distance of the respective planes are identified and matched with JCPDS file No. 83-1705 corresponding to hexagonal SnS_2. In acetone, the interplanar distances identified are 2.78 Å and 2.94 Å which correspond to the (011) and (002) planes respectively of SnS_2. In isopropanol also, the analyzed particle is highly crystalline where

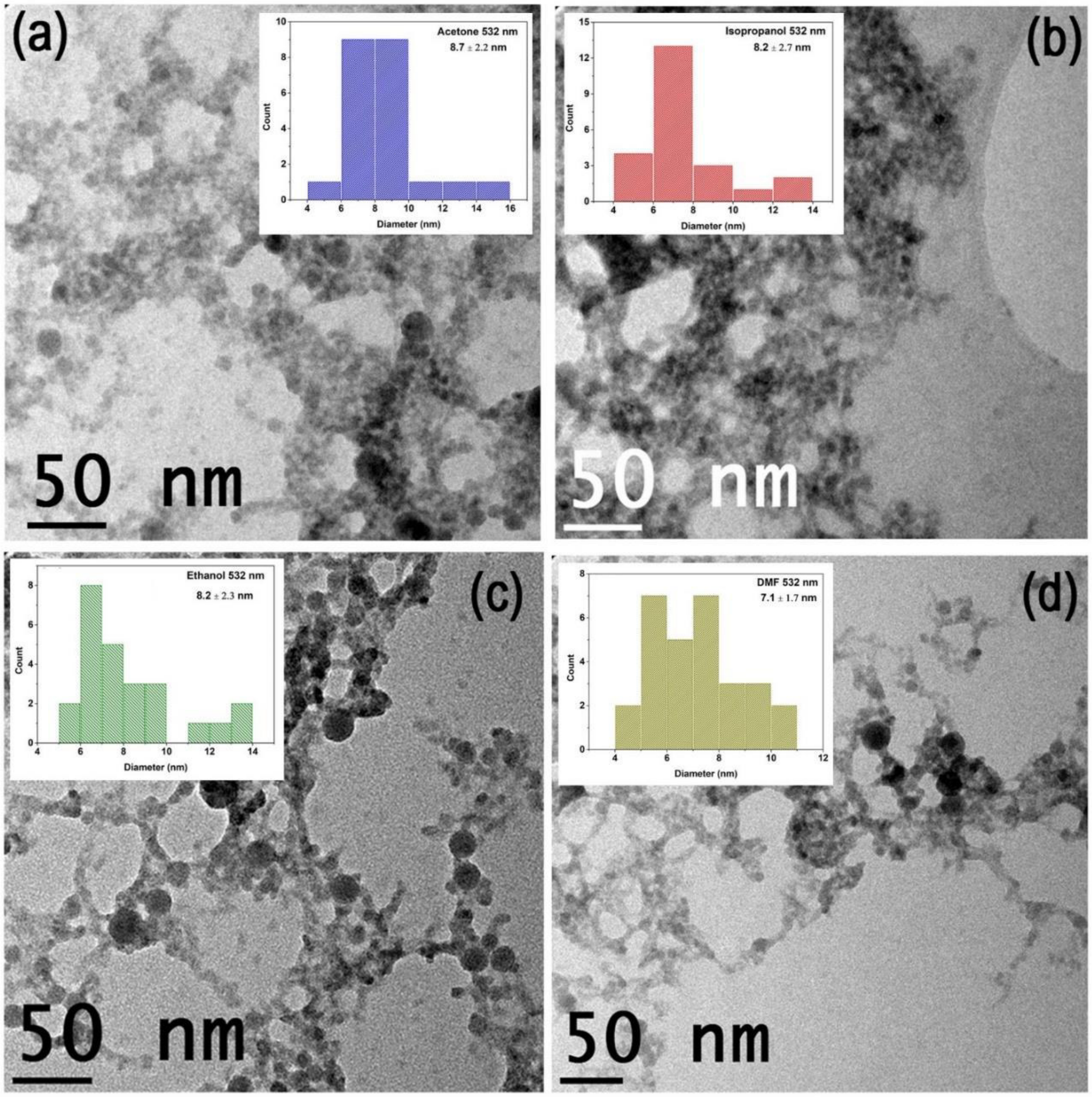

Fig.5.4. TEM images of SnS2 NPs by 532 nm laser in (a) acetone (b) isopropanol (c) Ethanol and (d) DMF solutions indicating the NP morphology. The insets show average particle size in each solvent © 2018, Elsevier

the estimated interplanar distance was 5.87 Å and match with the spacing of (001) set of planes which has the highest intensity according to the JCPDS data for hexagonal SnS_2. SAED patterns of SnS_2 NPs in acetone and ethanol are shown in figure. 5.3 (e,f). In both cases, the patterns contain many diffraction spots which again confirm the crystallinity of the SnS_2 particles produced by laser ablation of the SnS_2 target in various solvents. Reflections from (100), (002) and (012) crystal planes are identified for SnS_2 in acetone and (111), (012) and (002) planes for that in isopropyl alcohol. Average size of the SnS_2 NPs was elucidated from the TEM images by counting the NPs. The corresponding particle statistics are presented in insets of fig. 5.2. Average size of the NPs estimated were 13±4.5, 18.5±6.1, 12.4±2.6 and 14.8±3.7 nm respectively for the NPs prepared in acetone, isopropanol, DMF and ethanol by the 1064 nm laser output.

TEM images of SnS_2 NPs in different liquid media prepared by 532 nm laser are presented in Fig.5.4. SnS_2 nanoparticles synthesized by 532 nm laser also exhibit spherical morphology in acetone, ethanol and DMF whereas in isopropanol the particles are like connected each other without definite boundaries. Crystalline SnS_2 particles are produced upon using the 532 nm laser as revealed by the HRTEM images as in fig.5.5. The interplanar distances calculated and corresponding crystallographic planes according to the JCPDS data for hexagonal SnS_2 are marked in the respective HRTEM images. The (100) plane is identified for SnS_2 NPs synthesized in all liquid media. The SAED patterns shown are for the SnS_2 particles prepared in isopropanol and in DMF. Reflections from (002) and (100) planes are identified for SnS_2 in isopropanol where as in the case of DMF, the bright spots observed are from (012) plane.

It is clear from the TEM characterization of the SnS_2 NPs that the liquid medium and laser wavelength play significant roles on the morphology of the particles. When either the liquid medium or the laser wavelength is varied, the SnS_2 particles formed were of different morphologies (however, in general they all possess nearly spherical particle morphology as to reduce the overall surface energy of the particles). While using the 1064 nm laser, SnS_2 particles with defined spherical boundaries are obtained compared to the particles generated using the 532 nm laser. The NPs average size is also varied by changing the laser wavelength. NPs produced by 532 nm laser possess average particle sizes of 8.7±2.2, 8.2±2.7, 7.1±1.7 and 8.2±2.3 nm respectively for the particles generated in acetone, isopropanol, DMF and ethanol solvents (insets, fig.5.4). Hence, smaller NPs are generated while using the 532 nm laser compared to the particles obtained by 1064 nm laser ablation. Ablation fluence of the laser pulses also have played a role in changing the morphology of the SnS_2 particles since the 1064 nm output (0.95 J/cm^2) was having higher energy fluence compared to the 532 nm (0.63 J/cm^2) output. In the case of PLAL, once the plasma is formed, it is confined by the surrounding liquid medium and hence the cavitation bubble life time and properties of the plasma are different in different liquid media. Liquid properties such as polarity, refractive index and viscosity effectively influence the formation mechanism of the NPs and thereby the morphology of the synthesized particles[93]. The refractive index, polarity, viscosity, density and thermal conductivity of the solvents selected are listed (table 5.2). Acetone and DMF possess higher dipole moments compared to ethanol and isopropanol. Because of the higher dipole moment, density and

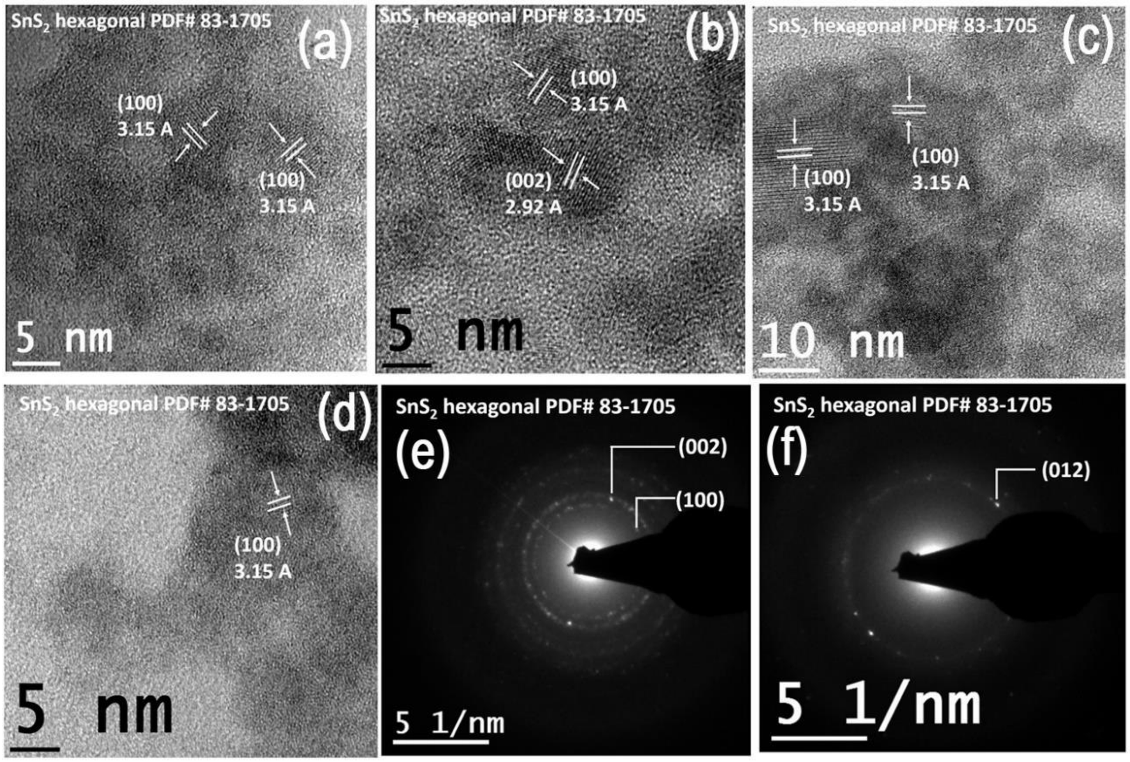

Fig.5.5. HRTEM images of SnS2 NPs by 532 nm laser in (a) acetone (b) isopropanol (c) Ethanol and (d) DMF solutions. SAED patterns of SnS_2 in (e) isopropanol and (f) DMF

thermal conductivity of DMF, smaller nanoparticles are obtained in DMF by ablation using 532 nm (7.1±1.7 nm) as well as 1064 nm (12.4±2.6 nm) compared to the other solvents used in the present study. Reports indicate that the PLAL process can be controlled by effectively adjusting the lasing parameters[302, 303]. Table 5.1 summarizes the average size of SnS_2 NPs synthesized at different conditions.

Table.5.1. Average particle size of SnS_2 NPs synthesized at different conditions in various liquids by PLAL

Laser wavelength (nm)	Liquid medium	Fluence (J/cm^2)	Average particle size from TEM (nm)
1064	Acetone	0.95	13±4.5
	Isopropanol		18.5±6.1
	Ethanol		14.8±3.7
	DMF		12.4±2.6
532	Acetone	0.63	8.7±2.2
	Isopropanol		8.2±2.7
	Ethanol		8.2±2.3
	DMF		7.1±1.7
532	acetone	0.25	13±5.9
		0.37	14±4
		0.5	16.3±6.1
		1.65	11±2.8
	Isopropanol	0.25	7.7±1.6
		0.37	13.7±6.9
		0.5	20.5±7.1
		1.65	8.4±4.6

Usually average NP size increases when longer laser wavelengths are applied[76, 78, 304] in PLAL. The higher photon energy for 532 nm (2.33 eV) can be more effectively absorbed by SnS_2 NPs during ablation leading to the laser fragmentation/melting of the synthesized particles[303, 305]. This may additionally contribute to the change in particle morphology. A higher laser fluence leads to increased cavitation bubble life time. Shock wave strength and degree of ionization of the liquid also strongly depend on the ablation fluence which can also contribute to a change in the particle morphology[302]. However, in the present work, changes in the morphology could have originated from an individual and combinational contribution of the laser wavelength as well as the ablation fluence since both parameters are varied simultaneously in the same liquid.

Table.5.2. summarizes various physical properties of the solvents used in the present work (acetone, isopropanol, DMF and ethanol). It has been previously reported that solvents with short chain length lead to the formation of unstable NPs by PLAL while chain lengths ranging from C3-C5 results in stable colloids [306]. Hence in isopropyl alcohol and acetone, the NPs formed are more stable compared to that in ethanol which has lesser number of carbon chains. Acetone and DMF possess higher dipole moments that help to create an electrical double layer around the particles to preserve the shape of the particles from changing further. In addition, boiling point of DMF is 153 °C whereas for all the other three solvents it is less than 85 °C. When the plasma cools down, it heats the liquid layer in contact by transferring the thermal energy into it forming a thin vapor layer and this is the early stage of cavitation bubble. Therefore, in the case of DMF, it requires more heat to transform it from liquid to vapor state. Higher density of DMF compared to other solvents can also be a reason for the formation of smaller particles as suggested by Tsuji et al.[307].

Table.5.2. Properties such as refractive index (for 532 and 1064 nm), viscosity, dipole moment, density and thermal conductivity of acetone, ethanol, isopropanol and DMF.

Liquid medium	Refractive index		Viscosity Pa S	Dipole moment D	Density Kg/m^3	Thermal conductivity W/m-K at 20 °C
	532 nm	1064 nm				
Acetone	1.3614	1.3487	0.000316	2.88	784	0.181
Ethanol	1.3637	1.3536	0.001095	1.69	786	0.179
Isopropanol	1.3851	1.3763	0.00192	1.66	789	0.1407

Dimethyl formamide	1.428	0.00092	3.86	944	0.1842

5.2.2 Morphology of SnS_2 NPs: effect of laser fluence

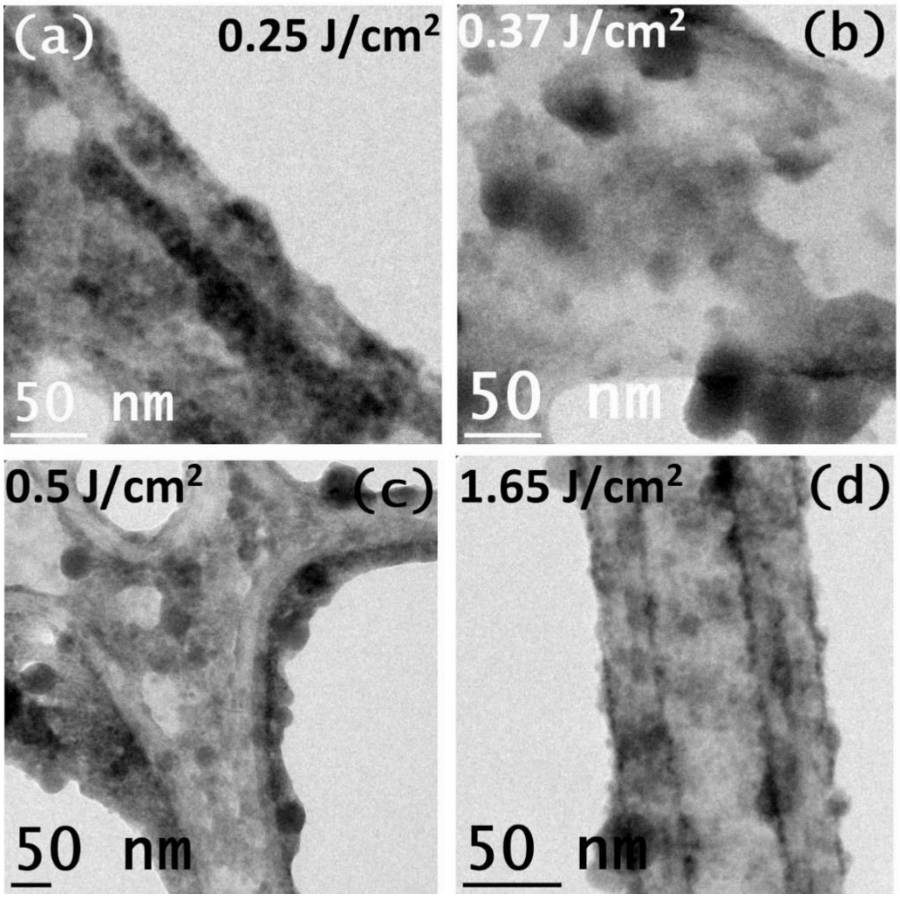

Fig.5.6. TEM images of SnS_2 NPs synthesized at laser fluences of 0.25, 0.37, 0.5 and 1.65 J/cm^2 in isopropanol © 2019, Elsevier

Effect of ablation fluence on the NPs morphology was investigated by analyzing SnS_2 nanocolloids prepared at three different laser fluences (0.25, 0.37, 0.5 and 1.65 J/cm^2) using transmission electron microscopy (TEM) where the crystal structure of the particles was determined using HRTEM images and SAED patterns. SnS_2 NPs were produced at above mentioned fluences in two different solvents viz. isopropyl alcohol and acetone using second harmonic (532 nm) laser output. TEM images, HRTEM and SAED patterns of

SnS_2 nanoparticles prepared at four different fluences in isopropyl alcohol are presented in fig. 5.6 and 5.7.

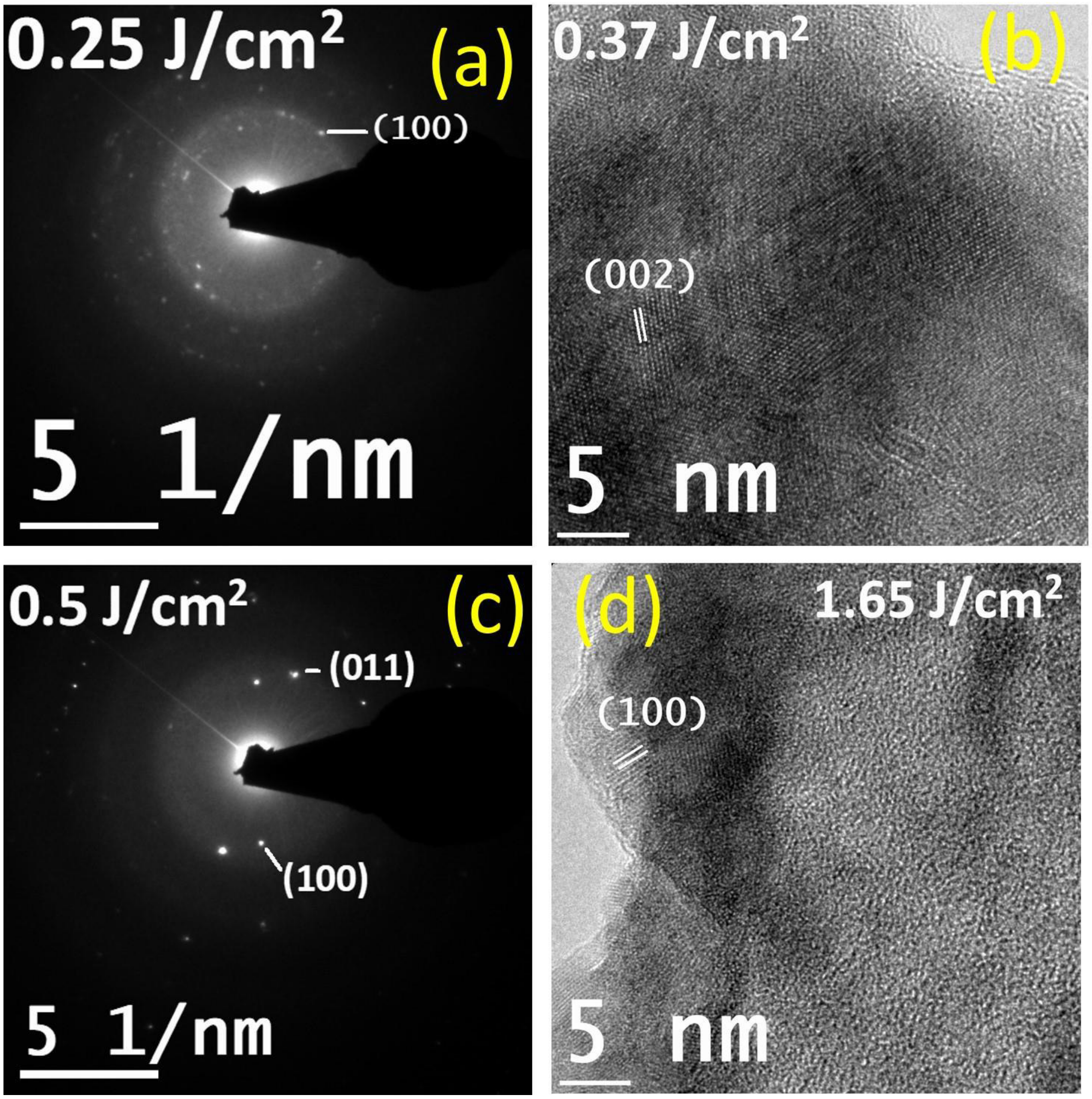

Fig.5.7. (a,c) SAED patterns and (b,d) HRTEM of SnS_2 NPs synthesized at laser fluences of 0.25, 0.37, 0.5 and 1.65 J/cm^2 in isopropanol © 2019, Elsevier

SnS_2 NPs possess spherical morphology (fig.5.6) with large size distribution (fig.5.8) in isopropyl alcohol regardless of the laser fluence used. Average sizes of the SnS_2 NPs were determined by counting the NPs in TEM images. The calculated average sizes were 7.7 ± 1.6, 13.7 ± 6.9, 20.5 ± 7.1 and 8.4±4.6 nm respectively for laser fluences 0.25, 0.37, 0.5 and 1.65 J/cm^2 where the average particle size increases with the laser fluence up to 0.5

J/cm^2 for the particles prepared in isopropanol. When the laser fluence was changed from 0.5 to 1.65 J/cm^2 (target above focus), the average size decreased with a broader size distribution. Non-linear effects of absorption resulted from the tight focusing condition used to obtain this higher laser fluence may account for this size variation. When the laser is focused at below or above the target surface, degree of ionization of the surrounding liquid medium, laser fluence arriving at the target and shockwave strength are altered and NPs of different composition, size and shape could be generated. In PLAL, the average particle size usually increases with the laser fluence due to the enhancement in the lifetime of the cavitation bubble. On the other hand, when the bubble's lifetime is shorter than the pulse interval, the incoming pulses are shielded and reflected by the bubbles thereby decreasing the ablation rate [302].

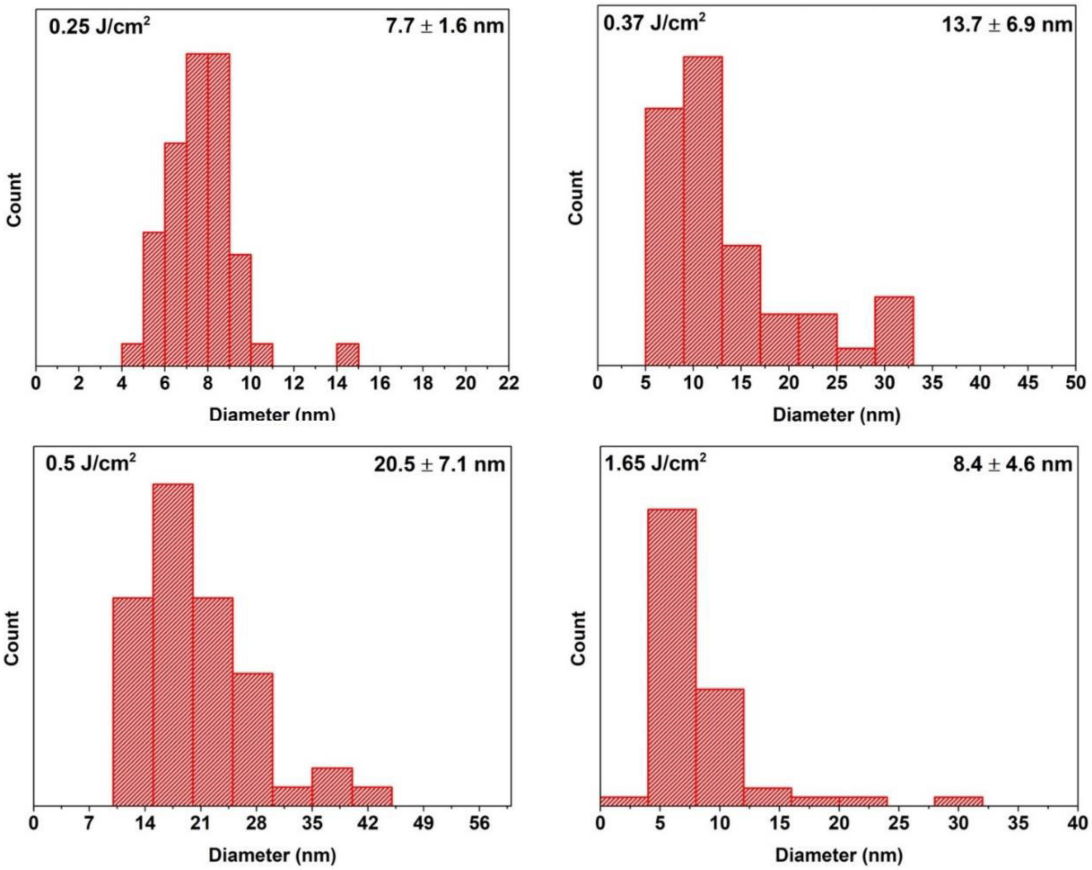

Fig.5.8. Particle size histograms of SnS_2 NPs synthesized at laser fluences of 0.25, 0.37, 0.5 and 1.65 J/cm^2 in isopropanol © 2019, Elsevier

Crystalline structure of the NPs was determined using HRTEM and SAED analyses. Fig.

5.7 (a,c) shows the SAED patterns of the SnS_2 NPs synthesized at 0.25 and 0.5 J/cm^2. In both diffraction patterns, spot corresponding to (100) crystal plane of hexagonal SnS_2 with an interplanar distance of 3.15 Å is identified whereas in the sample prepared at 0.5 J/cm^2 fluence (011) plane is also marked. In the HRTEM image of 0.37 J/cm^2 fluence, reflection from the (002) crystal plane of hexagonal SnS_2 is identified (JCPDS # 83-1705) corresponding to an interplanar distance of 2.94 Å whereas for 1.65 J/cm^2 fluence, the (100) plane is identified. During the irradiation of SnS_2 target, the generated plasma might contain molecules of SnS_2 as well as S and Sn ions.

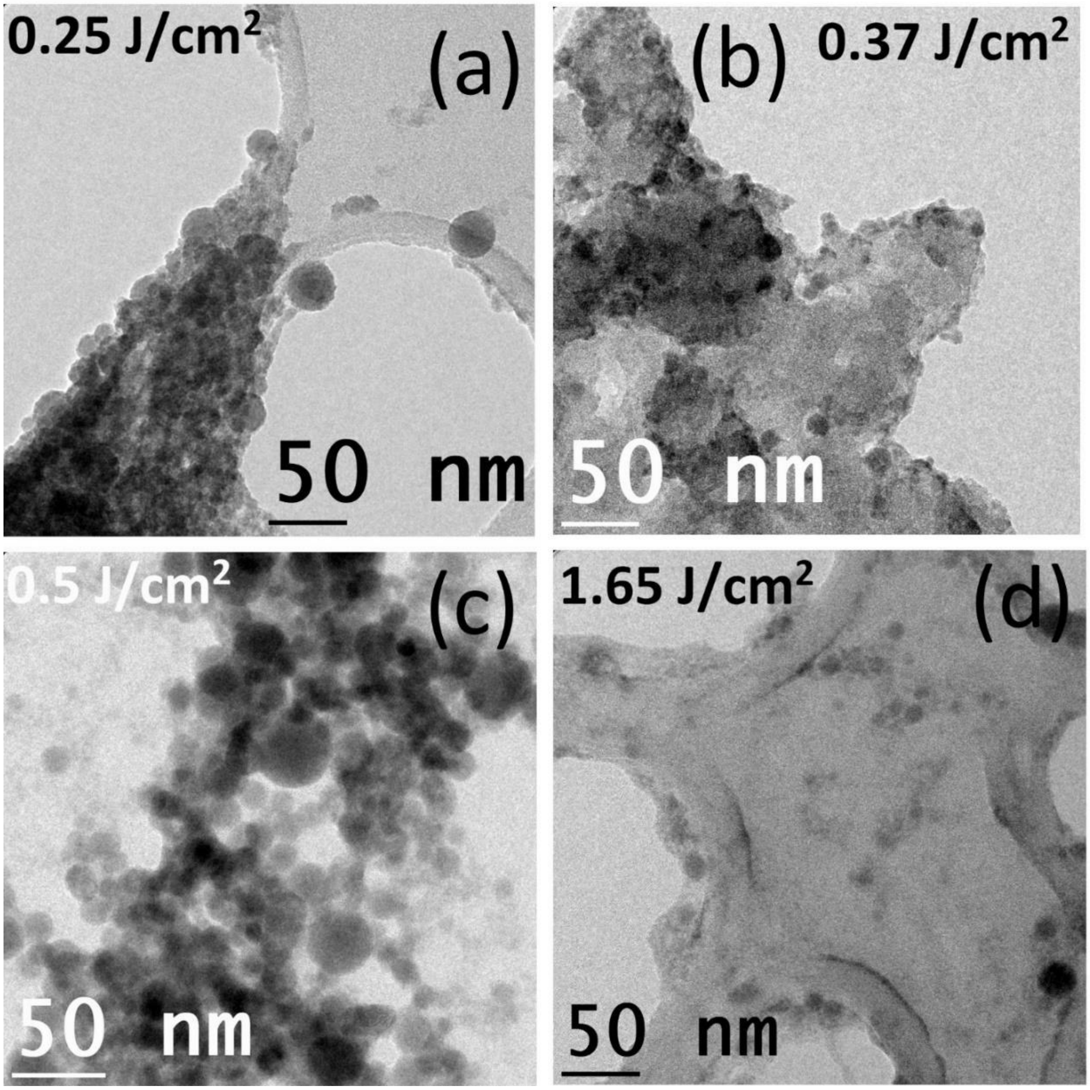

Fig.5.9. TEM images of SnS_2 NPs synthesized at laser fluences 0.25, 0.37, 0.5 and 1.65 J/cm^2 in acetone © 2019, Elsevier

Depending on the thermodynamic properties of the plasma, crystalline phases could be formed either by direct nucleation of droplets or by reaction between ions and atomic clusters inside the plasma[308]. Hence, the SnS_2 particles might have formed from direct nucleation of SnS_2 species or by reaction between S and Sn ions inside the laser induced plasma.

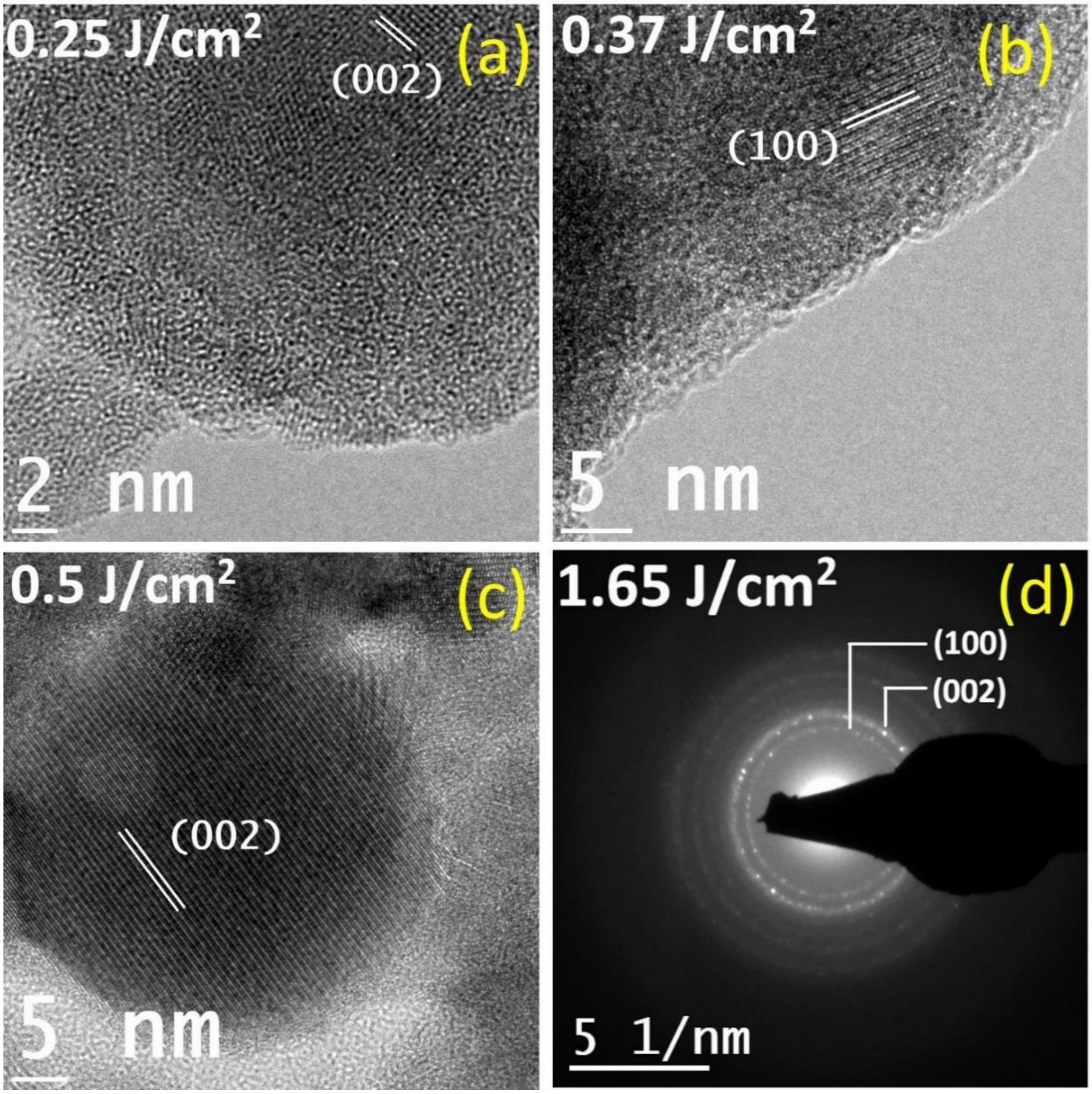

Fig.5.10. (a-c) HRTEM, (d) SAED pattern of SnS_2 NPs synthesized at laser fluences 0.25, 0.37, 0.5 and 1.65 J/cm^2 in acetone © 2019, Elsevier

TEM micrographs of SnS_2 NPs prepared in acetone are depicted in fig.5.9. The SnS_2 NPs present spherical morphology in acetone as well, but with better defined boundaries than the particles obtained in isopropanol.

For laser fluences 0.25, 0.37, 0.5 and 1.65 J/cm^2, the average sizes obtained were correspondingly 13 ± 5.9, 14 ± 4, 16.3 ± 6.1 nm and 11± 2.8 nm (Fig.5.11). In the case of NPs obtained in acetone also the particle size increased gradually with laser fluence up to 0.5 J/cm^2 while particle size was comparable for the lowest and highest laser fluences due to the focusing conditions applied (target above focus). Some bigger spherical particles are also observed in the TEM images together with the well dispersed nanoparticles, which might have formed due to agglomeration or heating/melting of smaller particles.

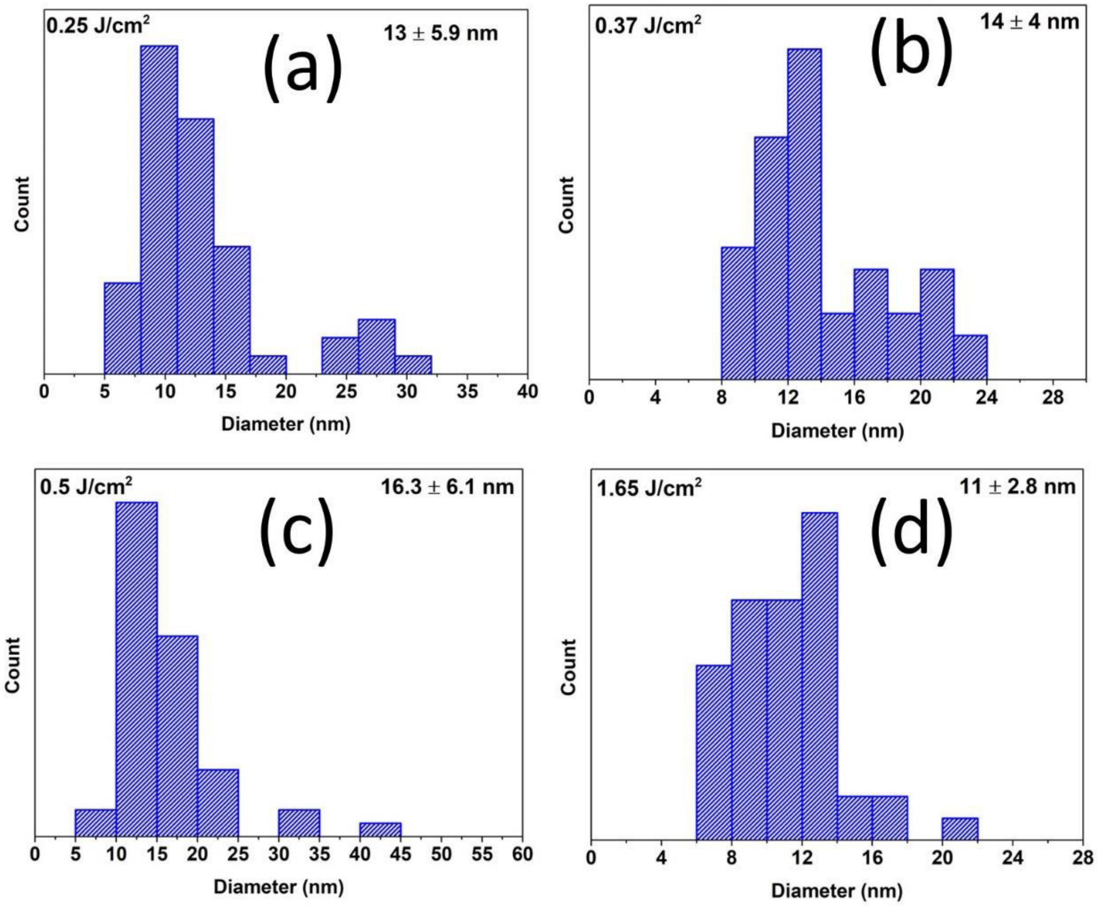

Fig.5.11. Particle size histograms of SnS_2 NPs synthesized at laser fluences 0.25, 0.37, 0.5 and 1.65 J/cm^2 in acetone © 2019, Elsevier

These bigger particles are also considered in calculating the average size. High resolution TEM images (Fig.5.10 a-c) show the (002) and (100) planes identified corresponding to interplanar spacings of 2.94 and 3.15 Å respectively of hexagonal SnS_2. SAED analysis of the particles synthesized at 1.65 J/cm^2 also shows diffraction spots for the same (002) and

(100) planes (Fig.5.10 d). Morphology characterization by TEM indicates that SnS_2 particles prepared by PLAL in acetone and isopropanol possess wide size distributions. Controlling the particle size in PLAL is a major challenge since the temperature profile and atomic density are varying inside the plasma[309]. However, studies show that by effective control of the laser parameters or by addition of small concentrations of surfactants to the liquid medium, the particle size can be effectively controlled in PLAL[302, 310-313]. The hydrodynamic diameters of the SnS_2 nanoparticles prepared in acetone and isopropanol at different laser fluences were measured by dynamic light scattering (DLS) and the results are summarized in Table 5.3.

Table.5.3. Hydrodynamic diameter of SnS_2 NPs prepared by PLAL at different laser fluences in acetone and isopropanol together with average size obtained from TEM

Liquid medium	**Fluence (J/cm^2)**	**Hydrodynamic diameter (nm)**	**TEM average NP size (nm)**	**Liquid medium**	**Fluence (J/cm^2)**	**Hydrodynamic diameter (nm)**	**TEM average NP size (nm)**
Acetone	0.25	219.5	13±5.9	**Isopropa-nol**	0.25	153.3	7.7±1.6
	0.37	278.6	14±4		0.37	123.1	13.7±6.9
	0.5	211	16.3±6.1		0.5	132.6	20.5±7.1
	1.65	201.8	11±2.8		1.65	227.8	8.4±4.6

The hydrodynamic diameters measured by DLS are much higher compared to the average Feret diameters calculated from the TEM images hence the ionic layer outside the particle is also considered in the DLS measurement. Moreover, DLS underestimates smaller particles in presence of bigger ones which leads to inaccurate particle size calculations. In this aspect, the Feret diameters obtained from TEM images provides more reliable information on the actual particle sizes of SnS_2 in the dispersions.

5.2.3 Influence of laser post irradiation and liquid medium temperature on morphology of SnS_2 NPs

To study the effect of liquid medium temperature on the morphology of SnS_2 NPs, they were synthesized in DMF solvent which was preheated and maintained at 80 °C using a 100 Hz, 10 ns Nd: YAG pulsed laser of 532 nm output. The laser fluence measured was

2.9 J/cm^2 with target above focus. For comparison, SnS_2 NPs were also prepared in room temperature DMF solution at the same laser parameters. Moreover, the SnS_2 NPs prepared in room temperature DMF solvent was post irradiated for 5min (without focusing, fluence of 0.53 J/cm^2) using the same Nd:YAG laser output. The TEM, HRTEM, SAED patterns and particle size histograms of SnS_2 NPs prepared in room temperature DMF, 80 °C preheated DMF and post irradiated for 5 min are shown in Fig.5.12 and 5.13.

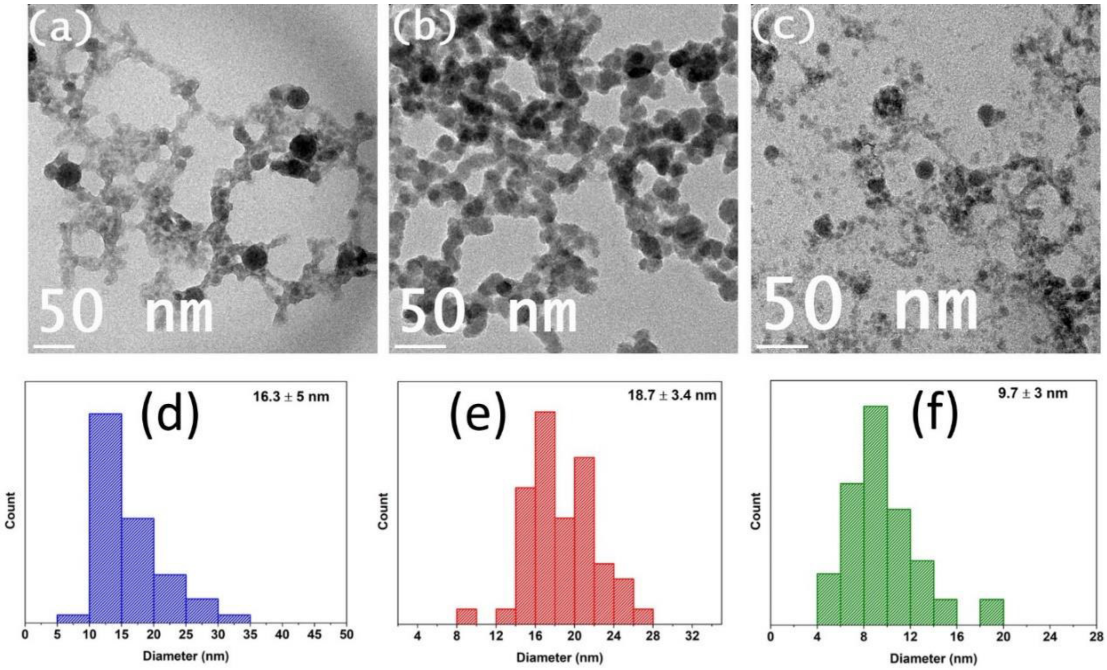

Fig.5.12. TEM images of SnS_2 nanoparticles synthesized in (a) room temperature DMF, (b) in 80 °C preheated DMF solution and (c) post irradiated colloid for 5min. respectively and (d-e) the corresponding particle size distributions © 2019, Elsevier

SnS_2 NP morphology is different in room temperature DMF solvent compared to that in the preheated solution (fig.5.12 a,b). The particles do not possess definite boundaries in room temperature solvent. They have a large size distribution with an average particles size of 16.3±5 nm. On the other hand, when the ablation was carried out in 80 °C preheated DMF solvent, bigger NPs with well-defined boundaries are generated. It is observed that the ablation in hot DMF liquid medium resulted more uniform NPs compared to the particles synthesized in room temperature DMF. Moreover, the average particle size of SnS_2, has increased to 18.7±3.4 nm when the liquid medium used for ablation was preheated (fig.5.12). When the nanocolloidal suspension (room temperature DMF) was post irradiated for 5 min using the laser, smaller NPs with average size 9.7 ±3 nm were obtained. The dispersed NPs in the suspension might have undergone fragmentation due to the incoming laser pulses which led to the formation of smaller spherical NPs. The HRTEM images (Fig.5.13 a-c) as well as SAED patterns (Fig.5.13 d-f) are indexed with corresponding crystal planes according to the JCPDS# 83-1705 for hexagonal SnS_2. Reflections from the planes (100), (011) and (012) are identified for different samples in the HRTEM image or SAED pattern.

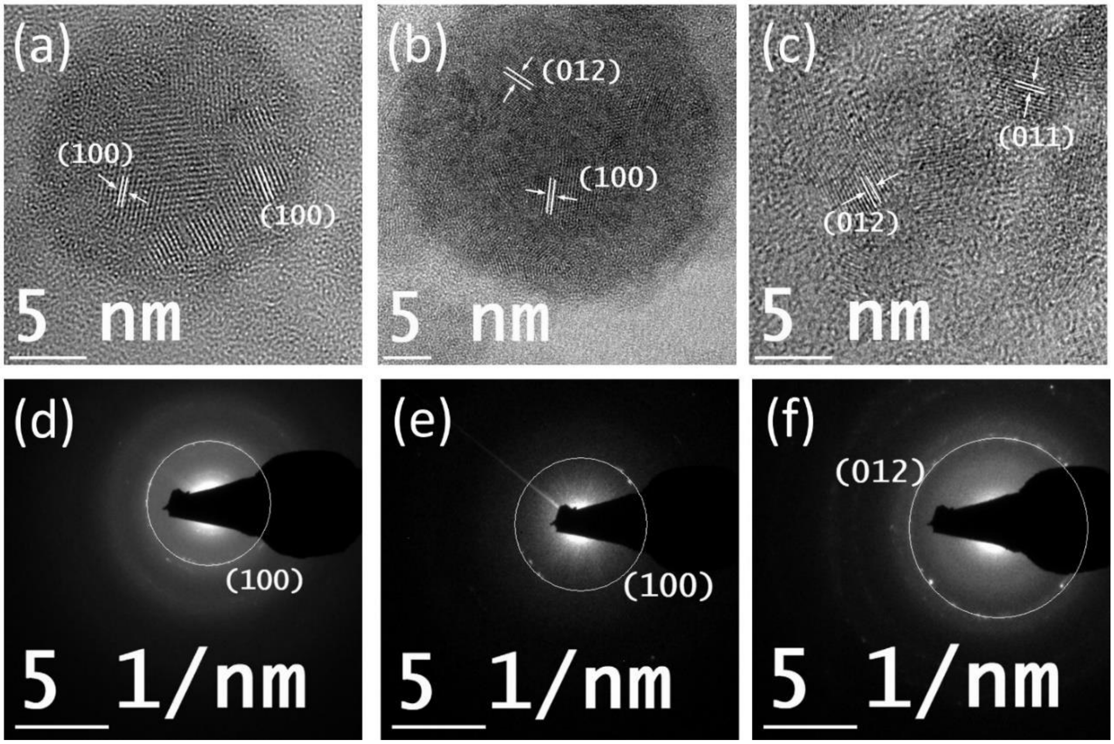

Fig.5.13. HRTEM and SAED patterns of SnS_2 nanoparticles synthesized in (a, d) room temperature DMF, (b, e) in 80 ºC preheated DMF solution and (c, f) post irradiated colloid for 5min. © 2019, Elsevier

According to previous studies, when nanocolloids are post-irradiated using lasers with compatible wavelengths, bigger NPs are formed. This happens due to the absorption of energy from the incoming laser pulses and thereby undergoing heating and melting which can lead to coagulation of the NPs[314, 315]. If the incoming laser energy is not absorbed by the particles, then the most likely phenomenon is the fragmentation of nanoparticles in the colloid where the individual particles break into much smaller ones[316-318]. In the present work, the SnS_2 NPs possess wide optical band gaps close to the UV region, and hence most of the green laser wavelength cannot be absorbed by them which leads to fragmentation instead of heating and coagulation. This would result in the formation of smaller particles instead of bigger ones. Bae et al. reported similar results for silver NPs prepared in NaCl solution by laser ablation where the fragmentation effect dominated over the enhanced van der Waals force. Average size of the Ag NPs was also reduced due to the irradiation using a UV source[318]. Instantaneous and localized high temperature and pressure at ablation shockwave edge can enhance crystallization of the particles. When the synthesized NPs in the optical pathway of laser above the laser spot(on target) are post-irradiated, laser heating leads to enhanced crystallinity of the produced NPs[99]. The liquid medium temperature is also a key parameter that can be used to tune the morphology, composition and structure of the NPs generated by PLAL. However, most of the reports which include study on the effect of solvent temperature are for reactive laser ablation where the final products are obtained by reacting the hot atomic plasma with the molecules in the surrounding liquid medium. For instance, Ishikawa et al. reported formation of rod-like and flower-like ZnO nanostructures by laser ablation of Zn plate in 60 °C and 80 °C heated deionized water[135]. It is reported that a transient temperature gradient is present between the laser induced plasma plume and the surrounding liquid. The liquid medium temperature may strongly affect the cooling of the plasma which may lead to the formation of NPs having different morphologies[319]. Normally, during the plasma cooling in PLAL, it exchanges heat energy to the surrounding liquid medium very fast and due to this fast energy transfer, a thin vapor layer is formed at the interface which is called as the early cavitation bubble. If the liquid medium temperature is high, then this heat transfer from the plasma to the surrounding liquid might be slow which may result in the formation of NPs with different size or shape. When cold liquids are employed, during the NP formation, they are quenched rapidly which would not occur if the surrounding medium is hot.

5.2.4 Crystal structure of SnS_2 target and NPs by XRD

X-ray diffraction analysis was carried out for further confirmation of the crystalline structure of laser generated SnS_2 NPs. NPs synthesized in two different liquid media (ethanol and acetone) obtained by 532 nm laser and in other two solvents (isopropanol and DMF) by 1064 nm were analyzed by XRD in the grazing incidence mode and the respective diffractograms are presented in Fig.5.14. All the analyzed SnS_2 nanoparticle samples present XRD patterns similar to the SnS_2 target (fig.5.15) used in PLAL with a preferential orientation along the (001) crystal plane. Reflections from the (001), (100), (002), (011), (003), (110), (111), (004), (113)/ (014), (005) and (114) crystal planes are identified from the hexagonal crystal structure of SnS_2 (JCPDS file # 83-1705) with a preferential orientation along the plane (001) for the SnS_2 target.

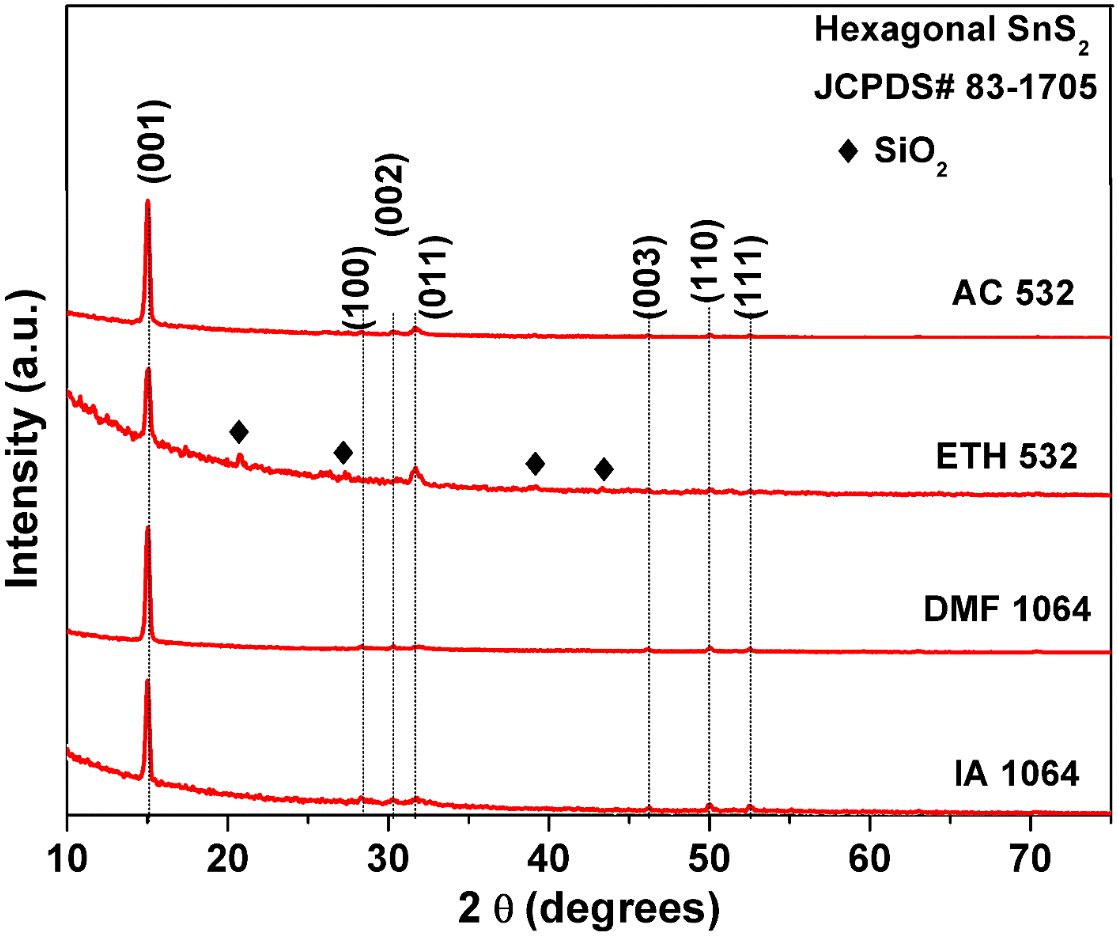

Fig.5.14. GIXRD patterns of SnS_2 particles synthesized by two different lasers in two liquid media each showing the crystallinity of the particles © 2018, Elsevier

XRD analysis confirms the high order of crystallinity and phase purity of the SnS_2 target as revealed by the intensity of the XRD peaks as well as detection of XRD peaks corresponding to only SnS_2 phase. Diffractograms of the samples are also matched with the same JCPDS data for hexagonal SnS_2. Reflections from (100), (002), (011), (003), (110) and (111) are also identified in the diffraction patterns of SnS_2 NPs in different solvents. Additional peaks observed in the sample synthesized in ethanol are attributed to SiO_2 which is from the substrate used to drop cast the nanocolloids for XRD analysis.

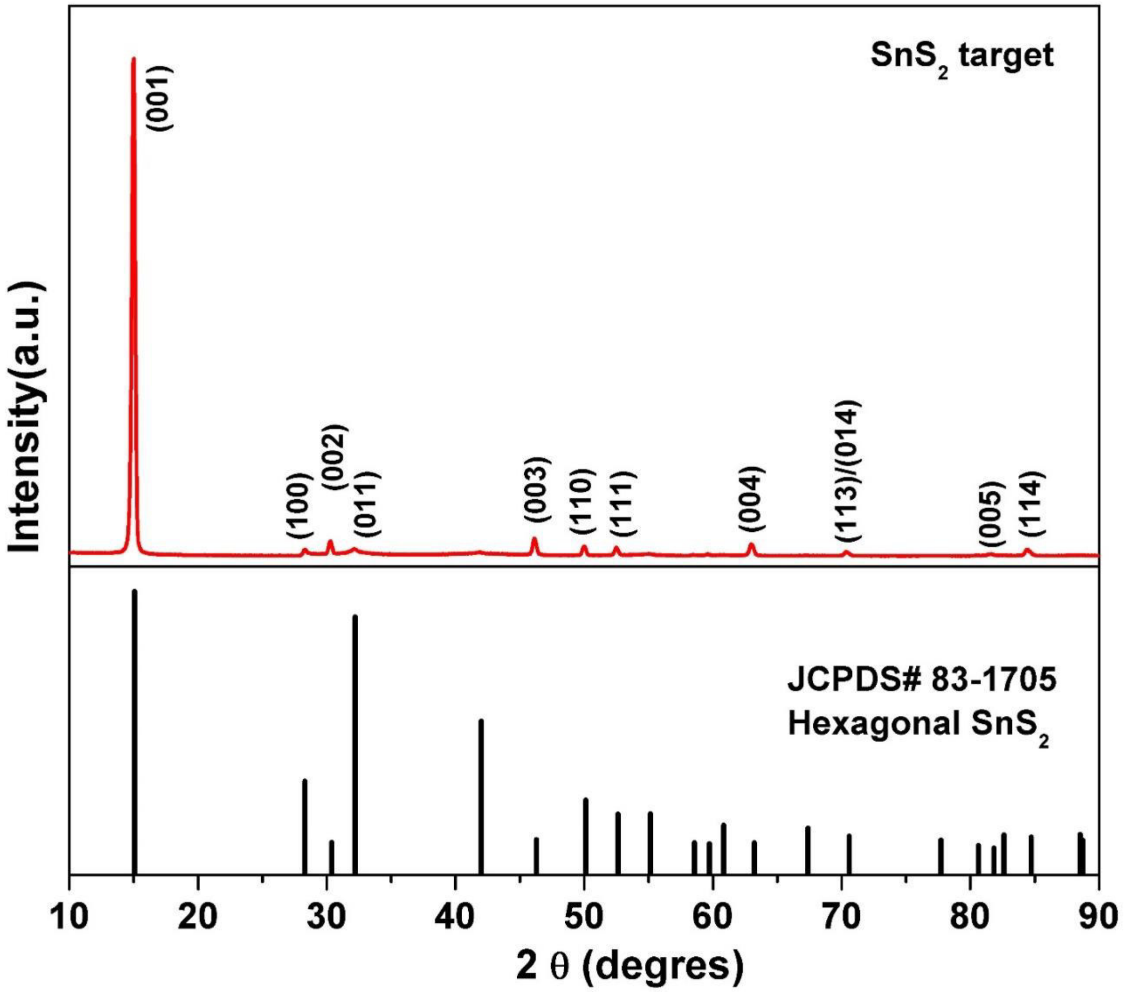

Fig.5.15. XRD pattern of the SnS_2 target used for laser ablation along with the corresponding JCPDS data for hexagonal SnS_2 © 2018, Elsevier

In the case of the samples prepared for fluence studies, the NPs synthesized in isopropanol and acetone at 0.5 J/cm^2 laser fluence and the particles generated in room temperature DMF were analyzed by grazing incidence X-ray diffraction (GIXRD) for the confirmation of their crystal structure. The XRD patterns were collected at an incident angle of 0.3° and scanning from 10 to 80 degrees two-theta (2θ) range. Fig.5.16 presents the XRD patterns of the SnS_2 NPs in isopropanol, acetone and DMF with their crystalline planes marked.

XRD patterns of SnS_2 NPs synthesized by laser ablation in acetone, isopropanol and DMF are characterized by a high intensity peak at 15.05° corresponding to the (001) crystal plane of hexagonal SnS_2 (JCPDS No. 83-1705). In addition to this, reflections at 2θ values 32.2, 30.38 and 46.28 degrees are also identified in the XRD patterns corresponding to the (011), (002) and (003) planes respectively for hexagonal SnS_2, indicating formation of pure crystalline SnS_2 phase. SnS_2 thin films synthesized from laser ablated SnS_2 nanocolloids in ethanol and isopropanol present resembling XRD patterns where the major peak is assigned to the (001) plane of hexagonal SnS_2[320].

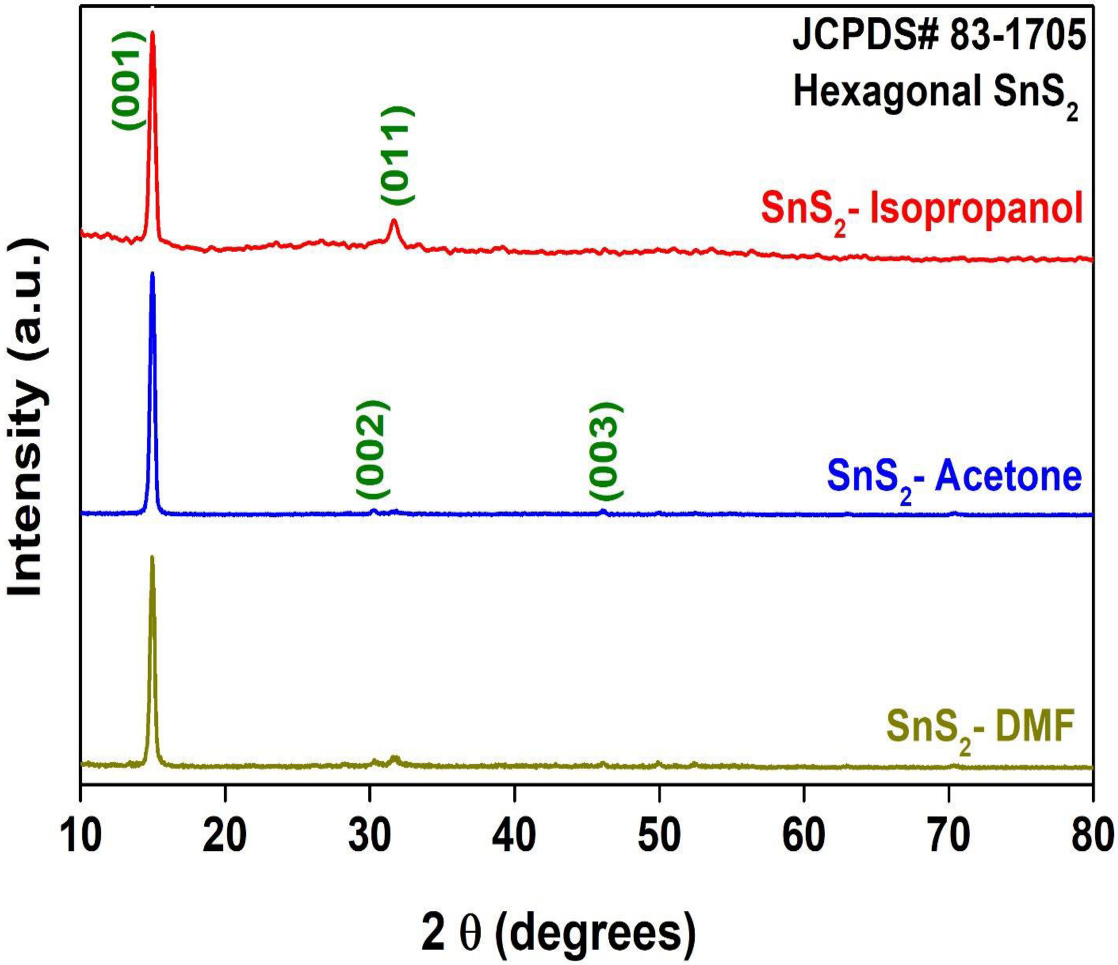

Fig.5.16. GIXRD patterns of SnS_2 NPs synthesized in acetone, isopropanol and DMF by PLAL © 2019, Elsevier

XRD analysis shows that the NPs synthesized are highly crystalline preserving the exact phase of the ablation target. Moreover, purity of the laser generated particles is revealed since no other phases or impurities are detected from the XRD analysis. Synthesis of pure desired particles in the nanometer scale can be attributed at most to the advantage of PLAL method used where the lasing parameters, purity of the target and less ablation time played important roles. Compared to other chemical synthetic approaches which involves a greater number of precursors and hence challenges in controlling the phase of the obtained products, in PLAL it can be achieved easily by adjusting either the target composition or by varying the lasing parameters.

5.2.5 Raman analysis of SnS_2 NPs: effects of liquid medium and laser wavelength

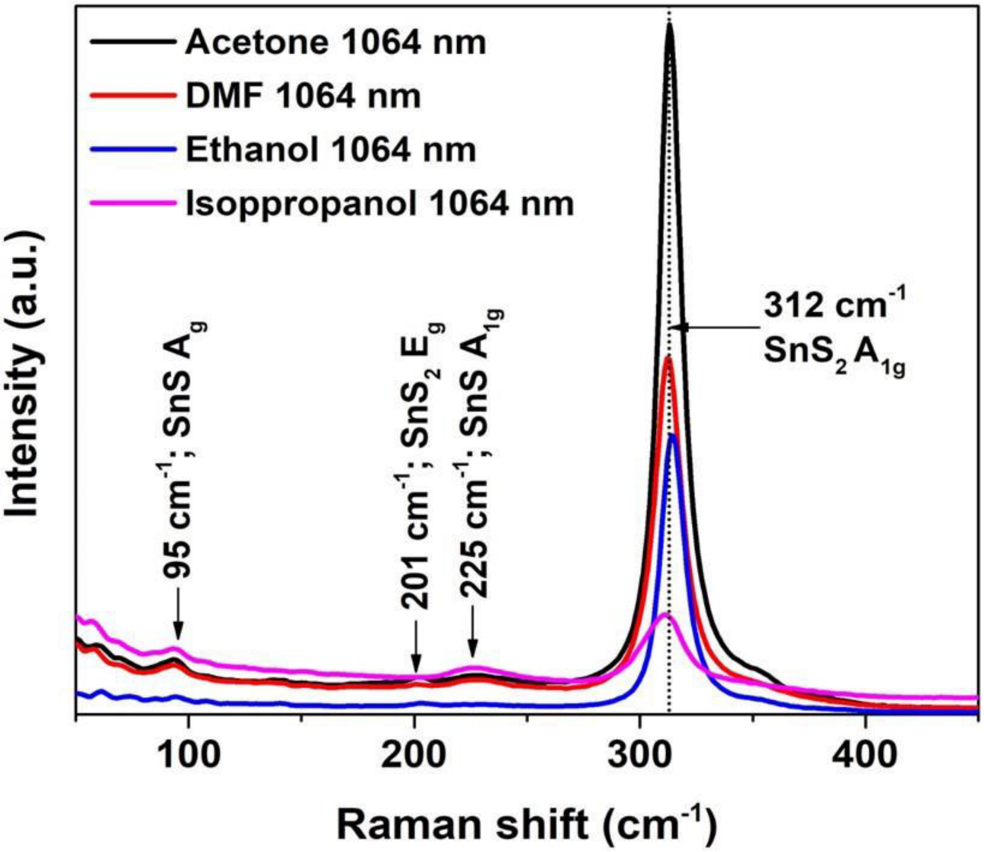

Fig.5.17. Raman spectra of SnS_2 nanoparticles obtained by PLAL using 1064 nm laser output in acetone, isopropanol, ethanol and DMF © 2018, Elsevier

Raman analysis was carried out for detailed information on the phase structure of the NPs synthesized by PLAL. Fig. 5.17 and 5.18 depict the room temperature Raman spectra of SnS_2 nanoparticles produced by 1064 nm and 532 nm laser wavelengths respectively in different liquid media. The strongest peak at 312 cm^{-1} present in all samples is assigned to the A_{1g} vibrational mode of SnS_2[321] confirming the major phase in the samples as SnS_2.

A very weak peak is also observed at 201 cm^{-1} which correlate with the E_g mode of SnS_2[322], but the peak is prominent only when acetone is used as the liquid medium.

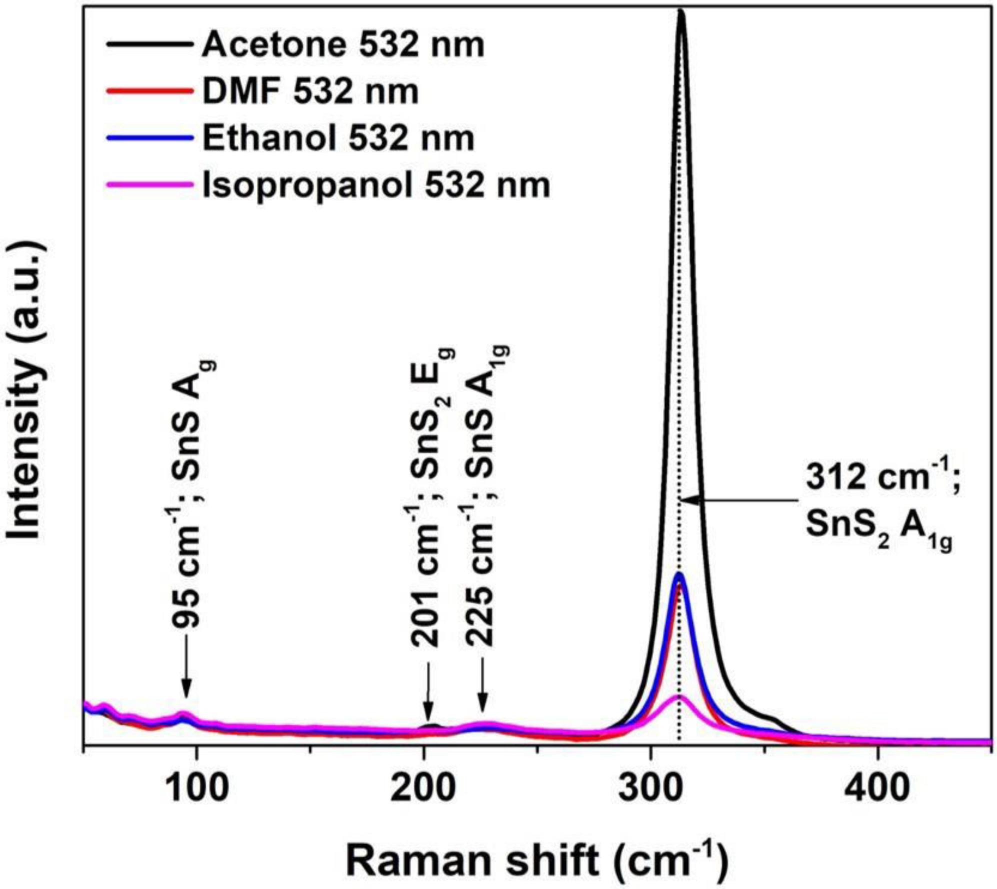

Fig.5.18. Raman spectra of SnS_2 nanoparticles obtained by PLAL using 532 nm laser output in acetone, isopropanol, ethanol and DMF © 2018, Elsevier

In DMF and ethanol the intensity of this peak is relatively very low whereas in isopropanol it is completely absent. This can be attributed to the nanosize effect as reported earlier[323]. Raman analysis confirms that the synthesized SnS_2 particles possess a 2-H polytype structure. In addition to the two SnS_2 peaks, two very weak bands are observed at 95 cm^{-1} and 225 cm^{-1} which correspond to the A_g mode of SnS[324]. Higher intensity of the SnS_2 Raman peaks in acetone is due to the higher concentration of the nanoparticles compared to other liquid media. Raman results indicate that some SnS particles are also formed during the laser ablation of the SnS_2 target. Raman spectrum of the target presented only two peaks corresponding to the SnS_2 phase as shown in fig.5.19.

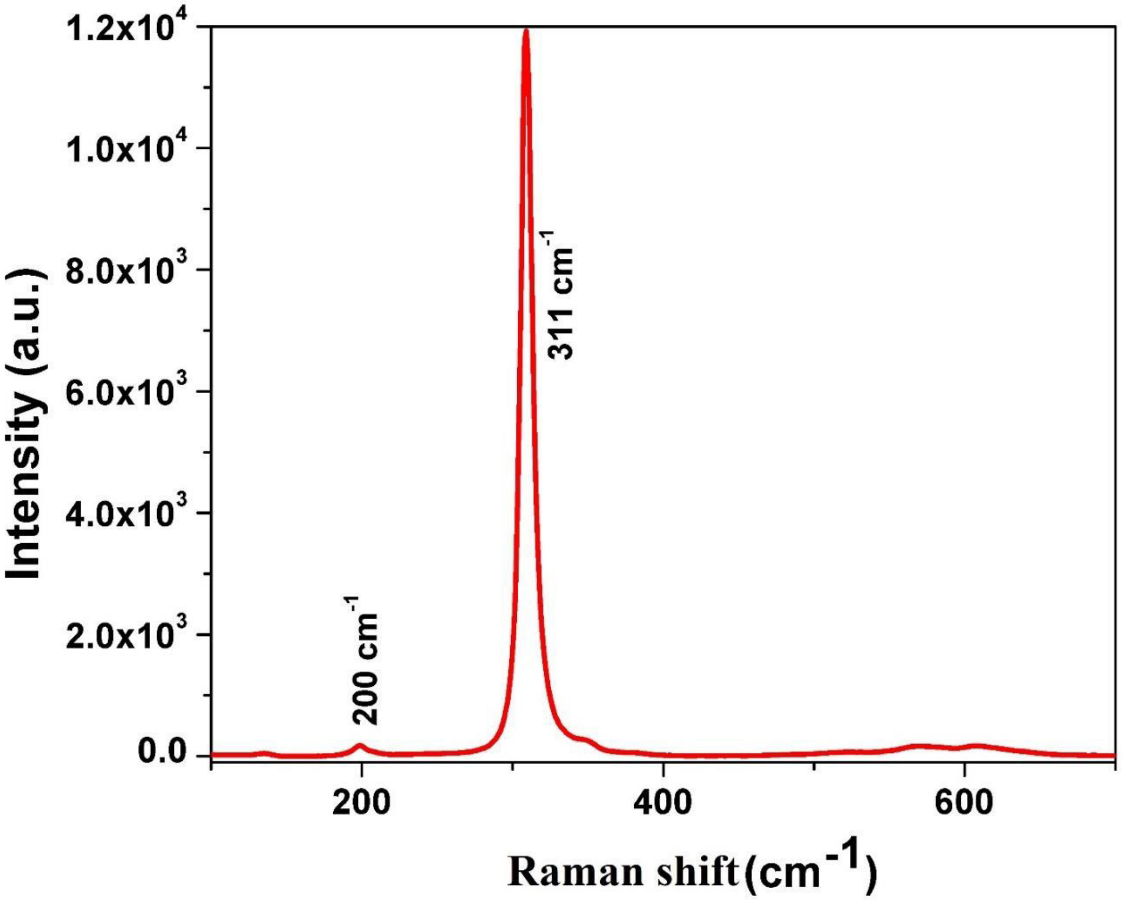

Fig.5.19. Raman spectrum of SnS_2 target used for the laser ablation synthesis of SnS_2 NPs © 2018, Elsevier

Hence it is confirmed that the SnS particles are formed during the ablation process in the plasma probably by depletion of sulfur or by interacting Sn ions with sulfur. However, the intensity of the SnS peaks are negligible in comparison with the peaks corresponding to SnS_2 and the SnS phase is not detected in either XRD or XPS analyses.

5.2.6 Raman analysis of SnS_2 NPs: effect of ablation fluence

Raman spectra of the SnS_2 samples were recorded using an excitation line of 532 nm for detailed information on the crystalline nature of the samples. The SnS_2 NPs possess a major Raman peak located at ~314 cm^{-1} (Fig.5.20) corresponding to the A_{1g} vibrational mode of SnS_2 in all the analyzed samples irrespective of the liquid medium and the laser fluence used. The 2-H polytype structure of the SnS_2 samples prepared by PLAL is revealed by this strong Raman band at 314 cm^{-1}.

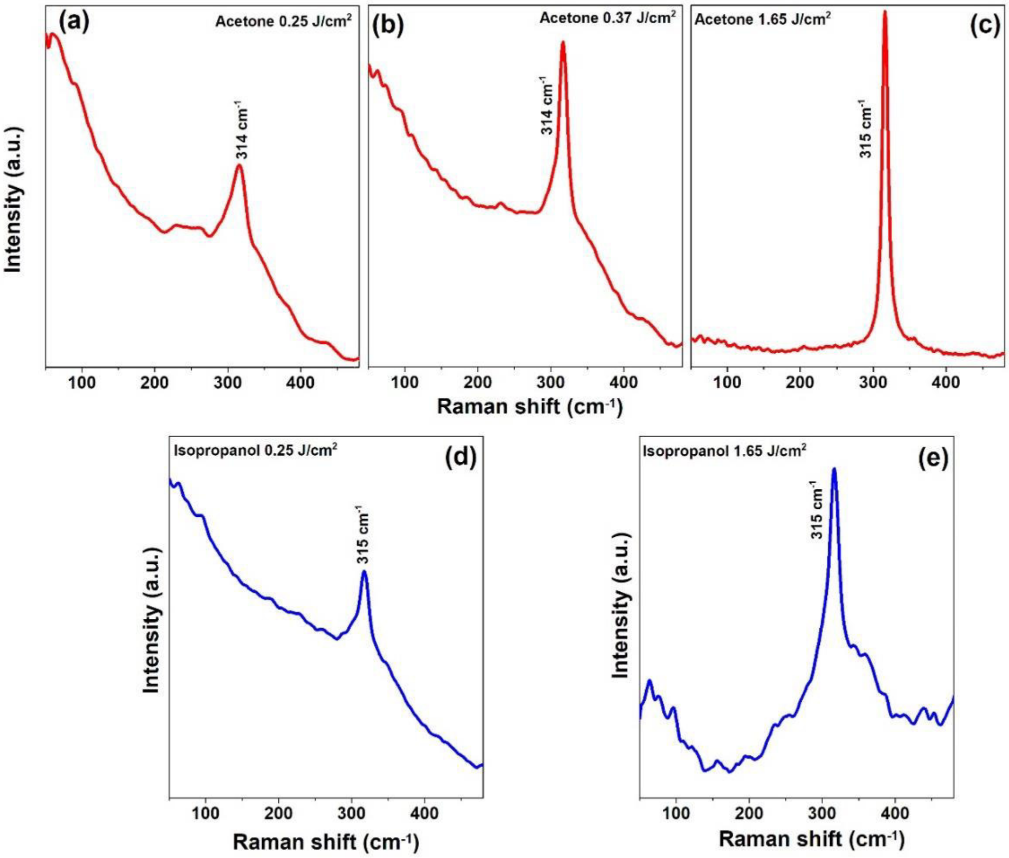

Fig.5.20. Raman spectra of SnS_2 NPs obtained in acetone and isopropanol at different laser fluences © 2019, Elsevier

The 2-H SnS_2 belonging to the D_{3d}^{3} -P$\bar{3}$m1 space group consists three atoms per unit cell. Gou et al. reported synthesis of SnS_2 NPs through a hydrothermal method where the Raman peak observed at 313 cm^{-1} which is close match to the value reported here for the PLAL synthesized SnS_2 particles[325]. SnS_2 nanocrystals obtained through a solvothermal synthetic approach also present an intense Raman band at 311 cm^{-1}. Presence of only one narrow peak with high intensity corresponding to SnS_2 implies high crystallinity of the particles together with the formation of phase pure SnS_2. Moreover, the SnS_2 NPs synthesized by PLAL possess same phase and structure as that of the target used for ablation.

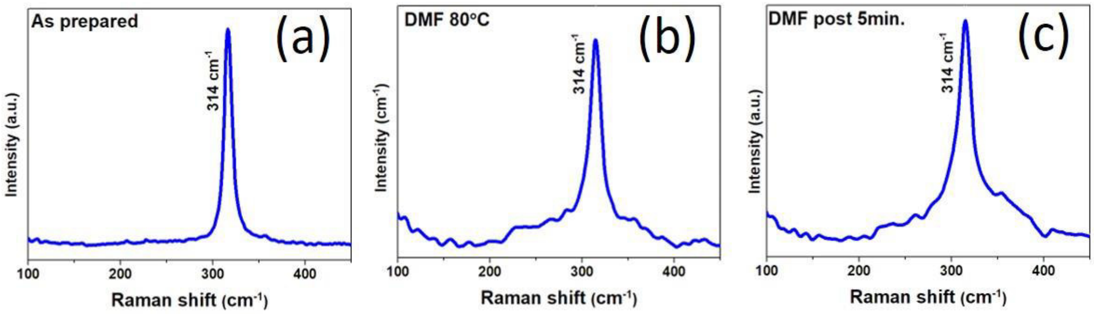

Fig.5.21. Raman spectra of the SnS_2 NPs generated in (a) room temperature DMF, (b) 80 °C preheated DMF (c) sample post irradiated for 5min. © 2019, Elsevier

5.2.7 Raman analysis of SnS_2 NPs: effect of post irradiation and liquid temperature

Raman analysis of the SnS_2 samples generated in room temperature DMF, 80 °C preheated DMF and the sample post irradiated for 5min, all characterize one major peak at 313 cm^{-1} (Fig.5.21) assigned to the A_{1g} vibrational mode of SnS_2. This supports the formation of phase pure SnS_2 nanoparticles in all these three cases.

5.2.8 Elemental composition and chemical states of SnS_2 NPs by XPS analysis

Elemental composition and chemical states of tin and sulfur of the SnS_2 NPs were analyzed by XPS. All survey as well as high resolution scans were corrected with binding energy of adventitious carbon at 284.6 eV in addition to the charge compensation provided by the flood gun in the XPS instrument. Survey spectra of the SnS_2 NPs synthesized by 532 nm and 1064 nm laser ablations in different liquid media are presented in Fig. 5.22 and 5.23. Fig. 5.24. shows the high-resolution scans of Sn3d and S2p of SnS_2 NPs synthesized in acetone, DMF, ethanol and isopropanol by the 1064 nm output of the Nd: YAG laser.

Binding energies obtained for the $Sn3d_{5/2}$ peaks of SnS_2 NPs in acetone, DMF, ethanol and isopropanol are 486.6, 486.8, 486.6 and 486.5 eV respectively. $S2p_{3/2}$ binding energies are 161.8, 161.7, 161.8 and 161.8 eV for the particles obtained in the corresponding liquid media. These binding energy values are very similar and agree well with the reported binding energy values for Sn^{4+} and S^{2-} from SnS_2. Binding energy separation of Sn3d peaks and S2p peaks are also measured and found to be ~8.41 eV and 1.16 eV which are identical with the binding energy separations for Sn and S peaks[326, 327]. Similar kind of results are obtained for the NPs synthesized with the 532 nm output of the laser (Figure. 5.25).

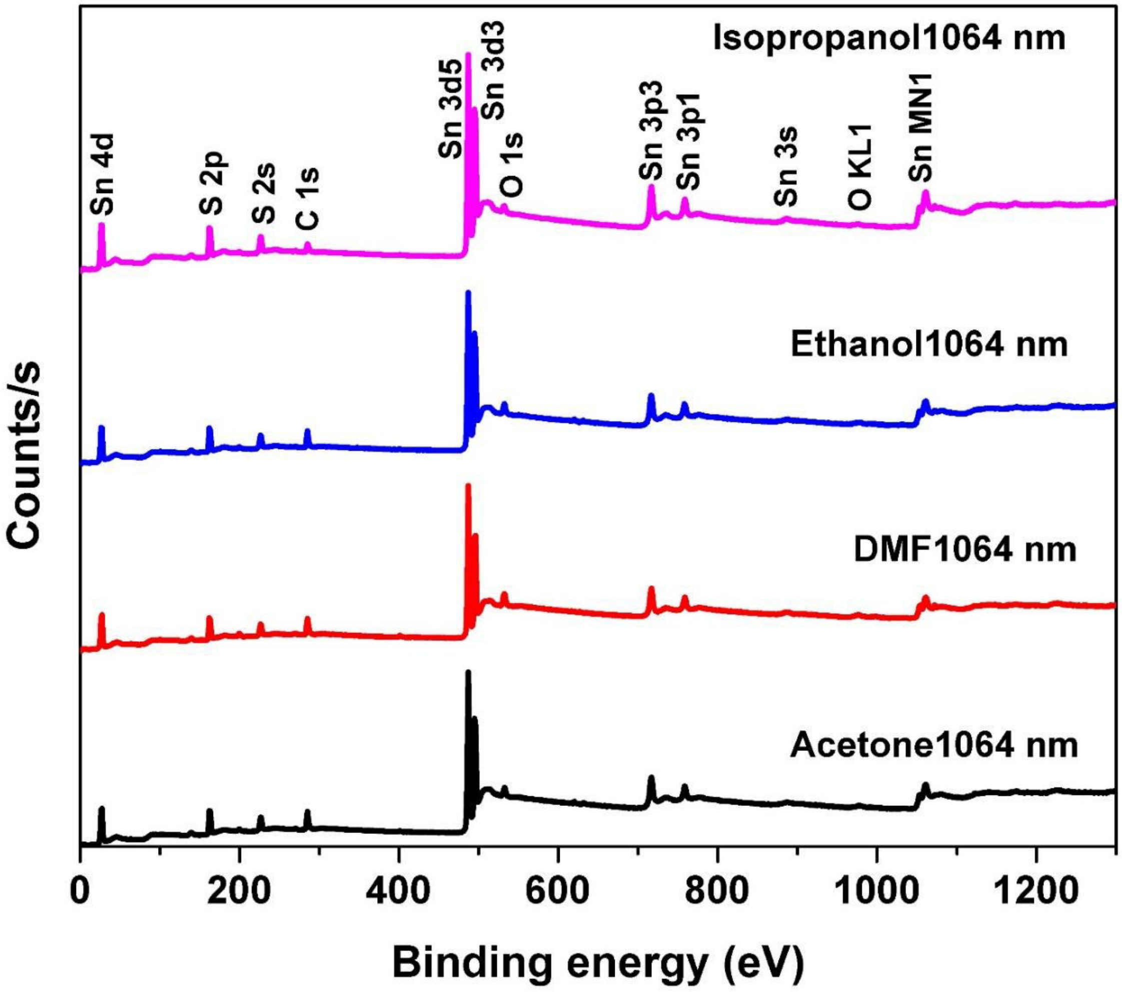

Fig.5.22. XPS survey scans of SnS_2 NPs synthesized by PLAL in acetone, isopropanol, ethanol and DMF using the 1064 nm laser output © 2018, Elsevier

For the nanoparticles synthesized with 532 nm laser, the measured binding energy values of $Sn3d_{5/2}$ are 486.8 eV for acetone, DMF, ethanol and 486.7 eV for SnS_2 in isopropanol. The $S2p_{3/2}$ binding energy is 161.8 eV for SnS_2 particles synthesized in acetone, ethanol and isopropanol whereas it is 161.7 eV for the particles synthesized in DMF. The obtained binding energy values of $Sn3d_{5/2}$ and $S2p_{3/2}$ are in close match not only with the values obtained for the particles synthesized with 1064 nm laser but also with the reported values for Sn and S from SnS_2. SnS_2 target used for the ablation presented similar XPS spectra and binding energy values as shown in fig.5.26. Major peaks obtained in the survey spectrum of the target are from Sn and S.

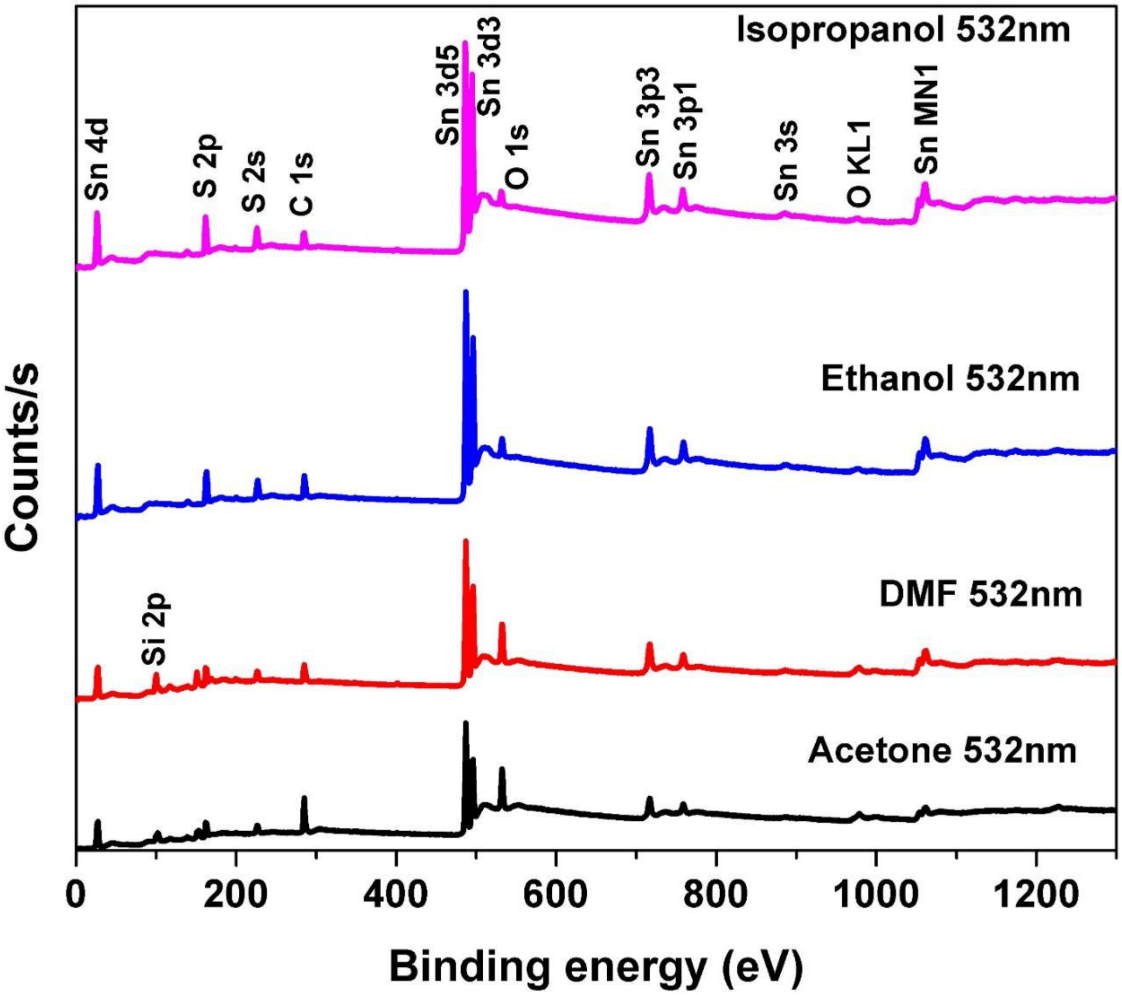

Fig.5.23. XPS survey scans of SnS_2 NPs synthesized by PLAL in acetone, isopropanol, ethanol and DMF using the 532 nm laser output © 2018, Elsevier

In addition to this, oxygen and carbon are also detected which could be attributed to the adventitious oxygen and carbon since the spectrum was collected from surface. $Sn3d_{5/2}$ peak is observed at 486.7 eV and the peak separation between $Sn3d_{5/2}$ and $3d_{3/2}$ is 8.41 eV. $S2p_{3/2}$ peak is observed at 161.66 eV and the binding energy separation between $S2p_{3/2}$ and $S2p_{1/2}$ is 1.19 eV. Binding energy positions of both Sn3d and S2p peaks as well as the separation between coupled peaks are in close agreement with the B.E. values reported for SnS_2. XPS results confirm that the particles synthesized in different liquid media by PLAL are pure SnS_2 without any other impurity phases. Binding energies of $Sn3d_{5/2}$ and $S2p_{3/2}$ of the SnS_2 particles synthesized by both laser wavelengths in all the liquid media are summarized in table 5.4.

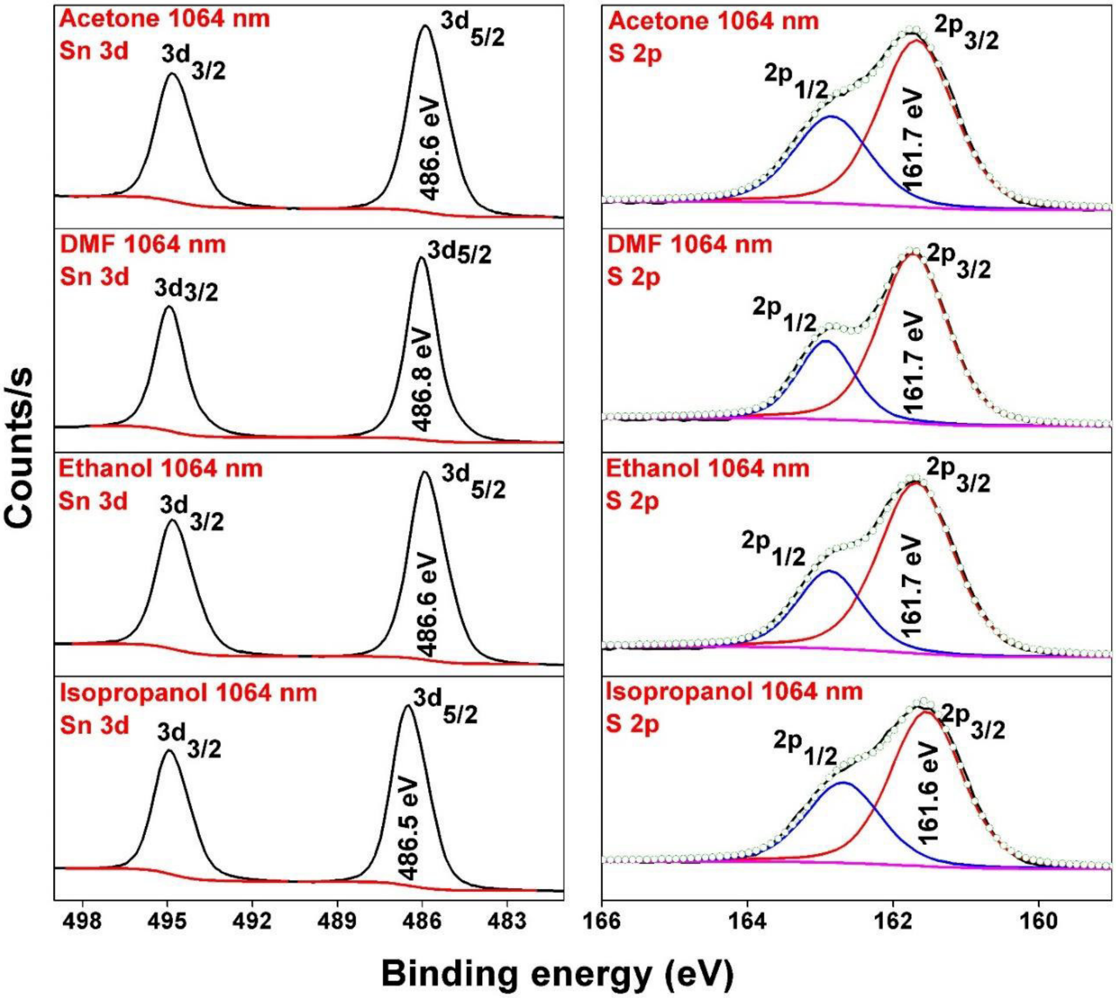

Fig.5.24. XPS high-resolution scans of Sn 3d and S 2p of SnS_2 NPs synthesized in acetone, DMF, ethanol and isopropanol by 1064 nm Nd: YAG pulsed laser. Binding energies of the Sn $3d_{5/2}$ peaks and S $2p_{3/2}$ peaks are marked in the graphs. In S 2p spectra, the solid black line and open circle represent the experimental and fitted data respectively © 2018, Elsevier

No other impurity phases or elements are identified by XPS analysis. This also confirms the products of ablation as pure SnS_2 nanoparticles in their colloidal form. This is one of the advantages of PLAL technique especially when non-reactive ablation is carried out.

Since the laser used was a nanosecond one, upon laser irradiation, the solid target surface transforms into gas phase following melting/thermal evaporation mechanism. The laser induced plasma may contain in addition to SnS_2 species, SnS molecules or Sn and S ions.

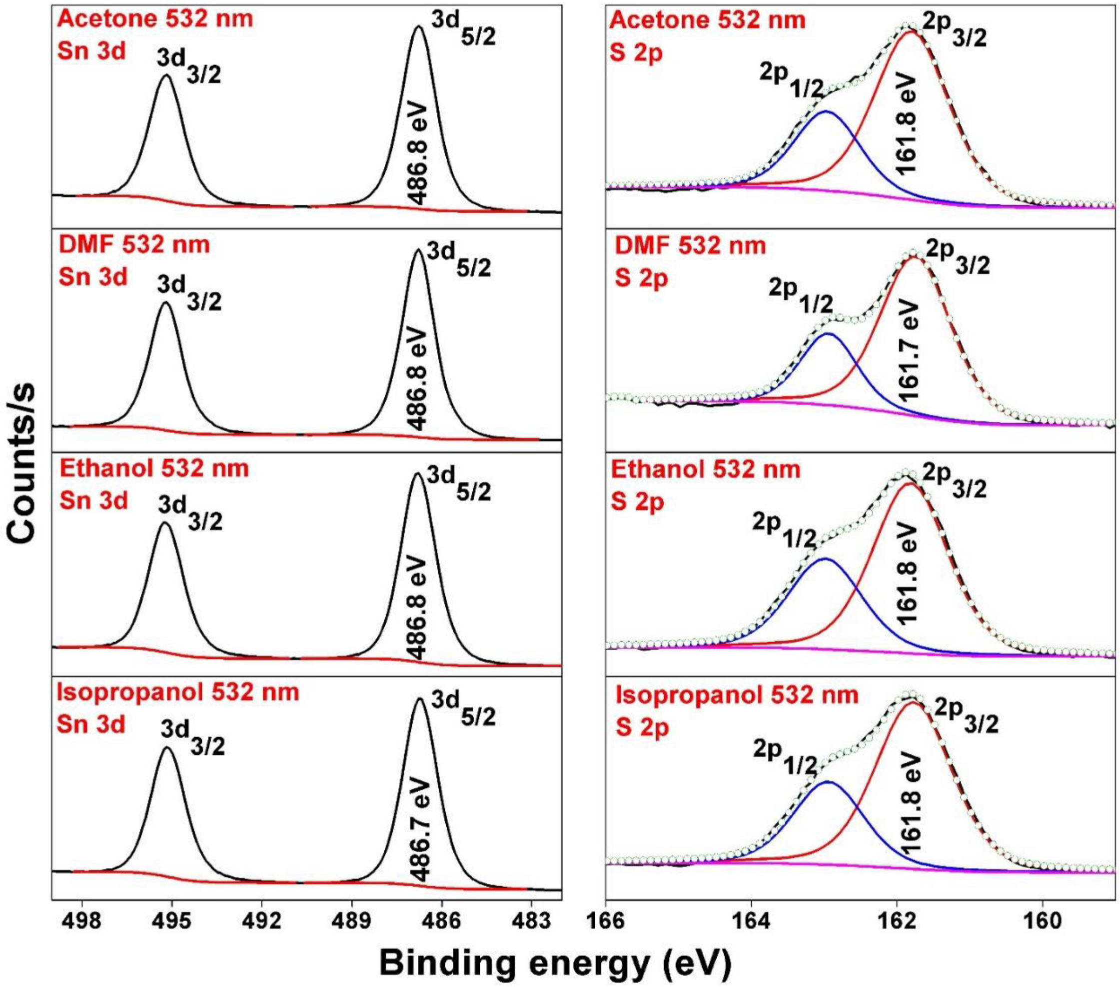

Fig.5.25. XPS high-resolution scans of Sn 3d and S 2p of SnS_2 NPs synthesized in acetone, DMF, ethanol and isopropanol by 1064 nm Nd: YAG pulsed laser. Binding energies of the Sn $3d_{5/2}$ peaks and S $2p_{3/2}$ peaks are marked in the graphs © 2018, Elsevier

Some of the SnS species might react with the S ions inside the plasma generating SnS_2 again, but the non-reacted SnS species resulted in the formation of a very small percentage of SnS particles as identified in the Raman spectra. The generation of nanoparticles from the hot atomic plasma containing SnS_2, SnS, Sn and S is after several steps such as expansion and cooling of plasma, production and expansion of cavitation bubble and its collapse. BEs of the SnS_2 NPs in the present work together with some previously reported values are summarized in table 5.4.

Table.5.4. XPS BEs of Sn 3d$_{5/2}$ and S 2p$_{3/2}$ peaks of SnS$_2$ NPs in the present work and some reported values

Ablation wavelength	**Liquid medium**	**Sn3d$_{5/2}$ (eV)**		**S2p$_{3/2}$ (eV)**	
		Present work	Reported in literature	Present work	Reported in literature
1064 nm 0.95 J/cm^2	Acetone	486.60	486.3[328] 486.6[329]	161.68	161.6[328, 329]
	DMF	486.75		161.73	
	Ethanol	486.60		161.68	
	Isopropanol	486.48		161.54	
532 nm 0.63 J/cm^2	Acetone	486.78		161.80	
	DMF	486.81		161.74	
	Ethanol	486.80		161.82	
	Isopropanol	486.73		161.77	

SnS$_2$ NPs production takes place at the end of these steps when the cavitation bubble shrinks and the nanoparticles are dragged towards the liquid and released into it. Formation of the cavitation bubble also depends on the pressure in the surrounding liquid medium. Sasaki et al. studied the effect of water pressure on the cavitation bubble dynamics during the ablation of Ti target in water. It was observed that as the external pressure was increased, the size and life time of the cavitation bubble decreased and hence a direct impact on the NPs morphology was noticed[330]. Hence in the present study, ablation using different liquid media having different properties and laser parameters (wavelength/photon energy and fluence) might have resulted in the formation of cavitation bubbles having different lifetimes and sizes which resulted in the generation of NPs with various morphologies. However, a detailed study using in-situ techniques such as shadowgraph is needed for deep understanding of the involved mechanisms. In the present study, the XPS analysis confirmed the presence of only SnS$_2$ phase in the NPs and target as identified from the similar binding energies of Sn and S high resolution scans of both.

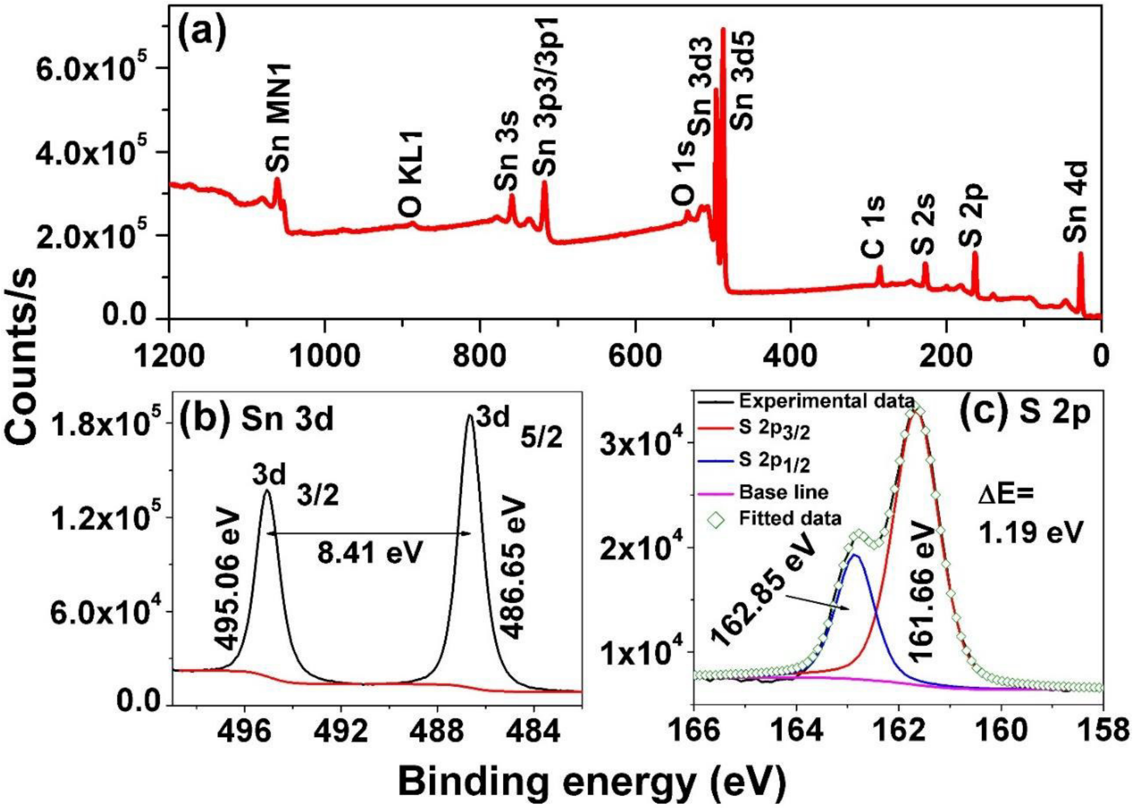

Fig.5.26. (a) XPS survey scan and high-resolution scans of (b) Sn 3d and (c) S 2p of the SnS_2 target © 2018, Elsevier

Composition of the NPs produced by PLAL strongly depends on the target composition unless there is an interaction with the liquid (reactive laser ablation). The materials resistance towards oxidation and redox potentials of the ablated species determines the stoichiometry of the NPs produced by PLAL. When the plasma generation is at a higher rate than the particle clustering time, interaction between the species inside the plasma dominates over the reaction between the plasma species and liquid medium[303, 331]. Semiconducting NPs synthesized from their bulk targets by PLAL found to have the same crystal structure as that of the target material[165, 332] and the ability to conserve the stoichiometry of the target in the whole event of laser ablation is often pointed out elsewhere as a peculiarity of the PLAL method[27]. Based on the basic processes of the plasma plume evolution in a confining liquid, the laser ablation generates cluster formation, nucleation, and crystals growth in the duration of the plasma. The rapid cooling or quenching effect of the confining liquid on the laser-induced plasma enhances the formation of metastable structures generated in the plasma. Formation of the crystalline phases can take place either from the reaction between atomic clusters and ions or from direct nucleation of droplets inside the plasma depending on the thermodynamic states of high pressure, temperature and density[308]. In the present work, nanoparticles having same crystalline structure and chemical states as that of the target could have formed from atomic cluster-ion interaction and/or direct nucleation of SnS_2 from the plasma containing target droplets.

5.2.9 Effect of liquid medium and laser wavelength on the optical properties of SnS_2 NPs

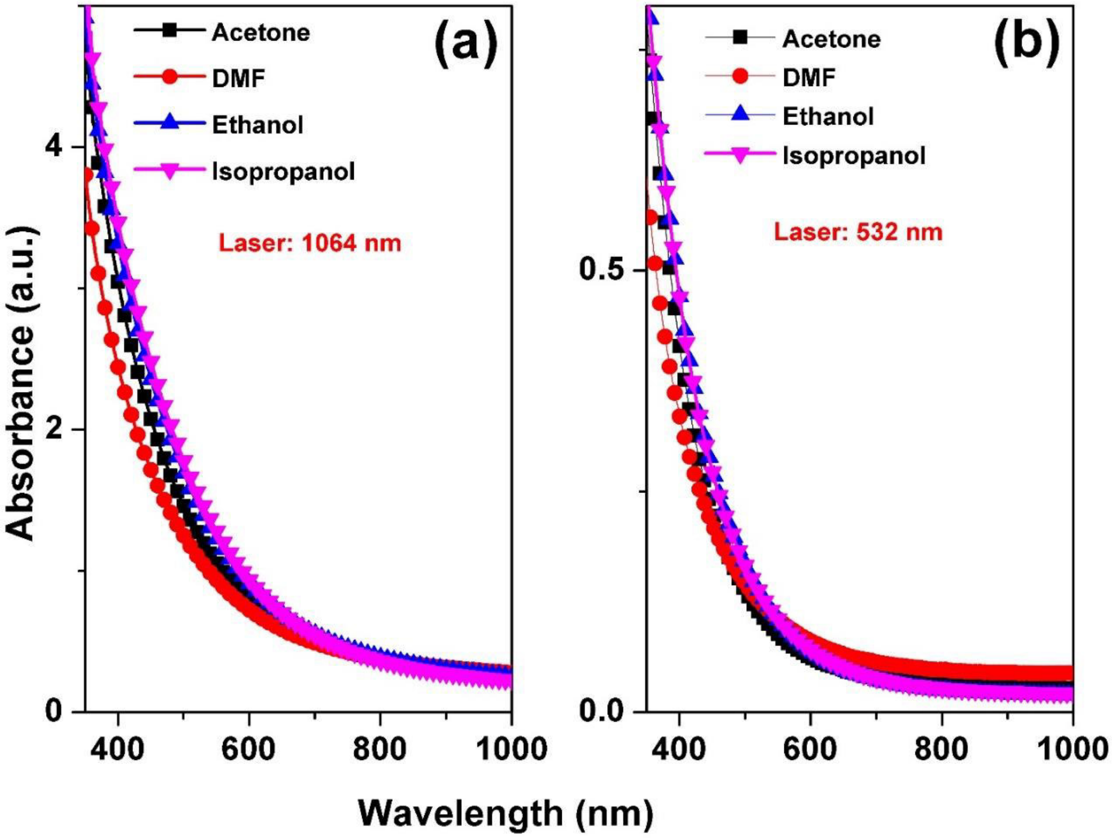

Fig.5.27. Absorption spectra of SnS_2 NPs by 1064 nm (a) and 532 nm (b) laser outputs in different liquid media © 2018, Elsevier

Figure. 5.27 depicts the absorption spectra of SnS_2 NPs by 1064 nm (a) and 532 nm (b) laser outputs in different liquid media. All the SnS_2 nanocolloids exhibited absorption edges around 500-550 nm region. A blue shift is observed for the nanoparticles produced using 532 nm laser output in comparison with that of 1064 nm in the same liquid medium. Beer-Lambert equation was used to calculate the absorption coefficient from the measured absorption spectra of the colloids. Band gaps of the SnS_2 NPs in each liquid media synthesized by different laser wavelengths were estimated using the Tauc plot relations. Optical bandgap of SnS_2 nanocolloids varied with the liquid medium and the laser wavelength (Figure 5.28.)

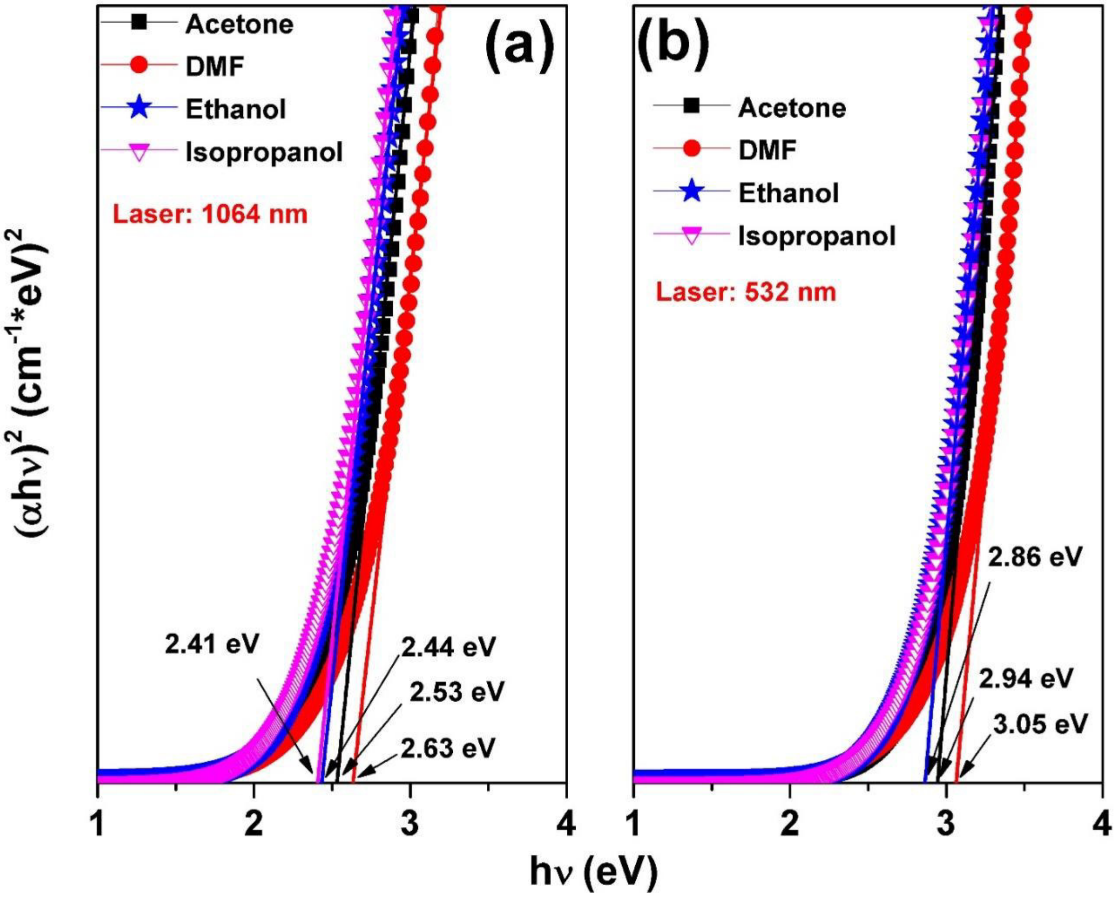

Fig.5.28. Optical band gaps estimated for SnS_2 NPs synthesized by ablating SnS_2 target in different liquid media using (a) 1064 nm and (b) 532 nm Nd: YAG laser outputs © 2018, Elsevier

In all cases, SnS_2 NPs showed an increased band gap compared to the band gap of the bulk SnS_2 (2.2 eV) due to the quantum confinement effect. In addition to this, SnS_2 particles synthesized by 1064 nm laser exhibit lower band gaps compared to that of the particles synthesized by 532 nm laser output. Band gap of the particles are varied from 2.41 eV up to 3.05 eV. The optical bandgaps of all SnS_2 nanocolloids are listed in Table.5.5. When 1064 nm laser was used, the estimated band gaps are 2.41, 2.44, 2.53 and 2.63 eV respectively for isopropanol, ethanol, acetone and DMF. SnS_2 NPs show band gap of 2.86 eV in both ethanol and isopropanol when synthesized by 532 nm laser whereas in acetone and DMF the values are 2.94 eV and 3.05 eV respectively. SnS_2 NPs with larger optical band gaps are generated for the ablation in DMF for both laser wavelengths. Change in the optical absorption behavior and band gaps of SnS_2 particles can be due to the different morphologies obtained when either the liquid medium or the lasing parameters (wavelength and fluence) are changed.

Polarity of the liquid medium is one property that affects the morphology of the nanoparticles synthesized using PLAL. If ablation is carried out in a polar medium, then molecules from the solvent form a thin layer over the charged NPs which will establish an electrical double layer at the solid liquid interface and the particle growth will be terminated. Hence smaller particles are expected when the polarity of the solvent is higher[100]. In the present case, ablation of SnS_2 target in DMF resulted in the formation of NPs having higher band gap. This can be attributed to the relatively smaller size of the particles produced in DMF compared to other solvents due to the higher dipole moment of DMF (3.86D) where the band gap increases with decrease in particle size ascribed to the quantum confinement effects (however, this effect is more significant when the particle size is comparable to the Bohr radius). Acetone has a dipole moment of 2.88D which is lower than DMF and hence the particles synthesized in acetone might be bigger than in DMF. SnS_2 NPs might have similar size in ethanol and isopropanol since the dipole moments of both are similar(1.69D and 1.66D respectively)[144]. For both laser wavelengths, the obtained results are similar where the band gap increased with increase in dipole moment of the solvent used. On the other hand, in all liquid media band gap of the particles were higher for the ablation with 532 nm laser wavelength at fluence 0.63 J/cm^2 compared to the ablation with 1064 nm at 0.95 J/cm^2. When the laser fluence was increased, particles with higher average sizes might have formed compared to the particles synthesized with lower energy fluence. Similar results were previously reported for palladium and platinum NPs synthesized using PLAL by Mendivil et al.[333, 334]. In the present work, however the laser wavelength, polarity, viscosity and refractive index of the solvent might have also played significant roles since each of them contribute differently in determining the final morphology of the NPs. It has been previously reported that above threshold fluence, average NPs size increases with laser fluence. Moreover, longer laser ablation wavelengths are favorable for higher particle sizes. Average particle sizes were estimated for SnS_2 nanoparticles synthesized by 1064 and 532 nm in all the liquid media and the results are included in Table 5.1. Among the four solvents, smallest NPs were generated in DMF which showed higher band gap irrespective of the laser wavelength. Two important parameters that control the particle morphology in PLAL - laser fluence and wavelength - are varied simultaneously, that could affect strongly the evolution stages of SnS_2 nanoparticle formation. Moreover, during the ablation experiment, the non-uniformity of temperature profiles and atomic density inside the plasma plume resulting in generation of NPs having wide size distribution[331]. Difference in band gaps of SnS_2 NPs synthesized by 532 and 1064 nm laser outputs might have originated as combined effects of their size and morphology. As observed in the TEM images, the particles synthesized by 1064 nm laser show definite shapes compared to the irregular shaped particles by 532 nm laser. In addition to the size related quantum confinement, the changes in particle morphologies can also vary the band gaps of SnS_2 NPs dispersed in the solvents.

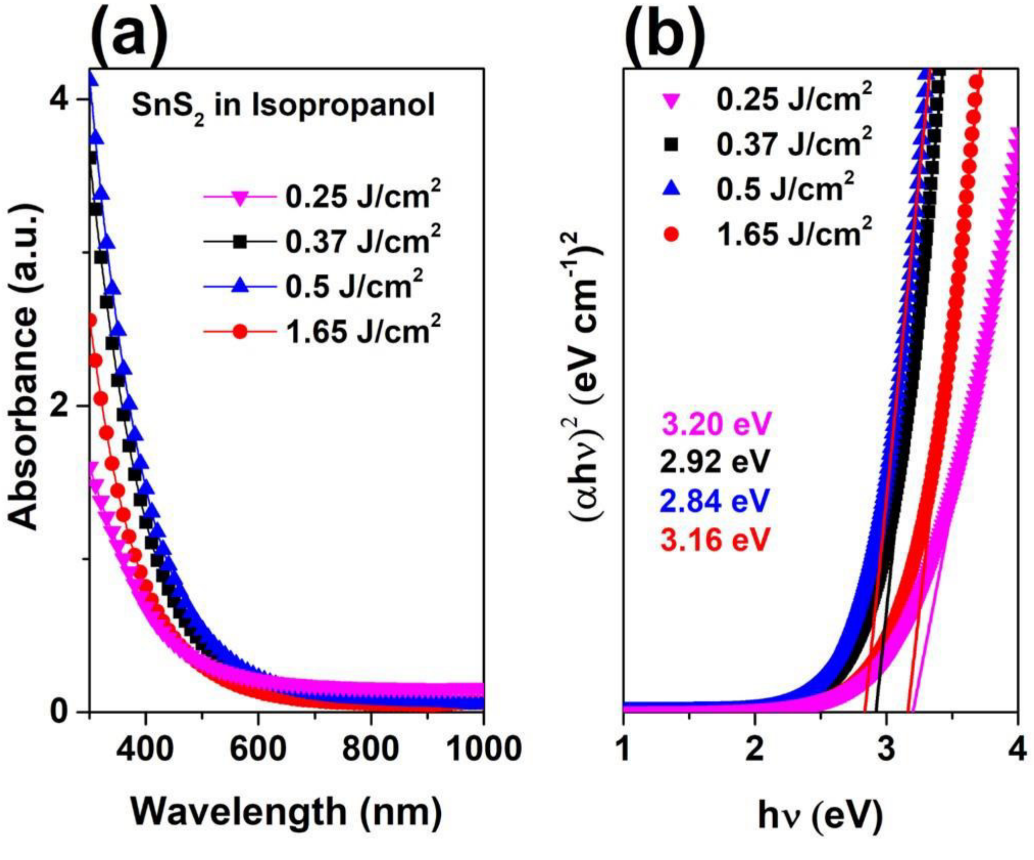

Fig.5.29. (a) Optical absorption and (b) band gap plots of SnS_2 NPs synthesized at varying laser fluence in isopropanol © 2019, Elsevier

5.2.10 Optical properties of SnS_2 NPs: influence of laser fluence

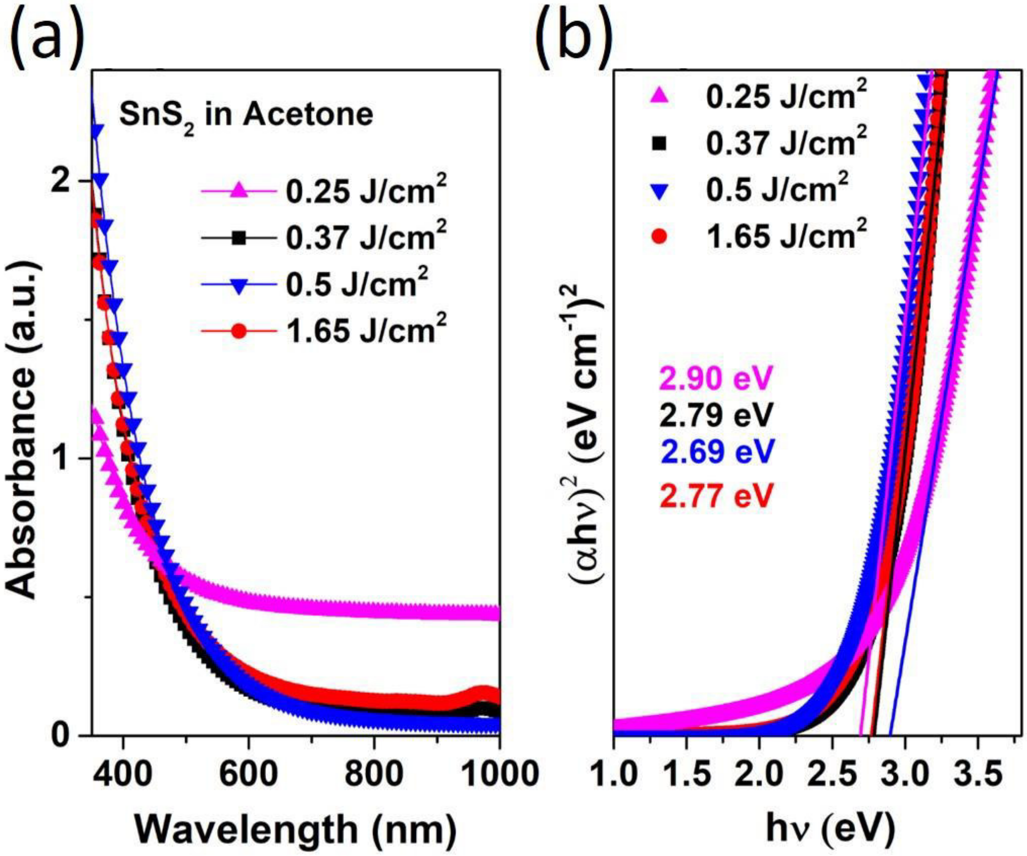

Fig.5.30. (a) Optical absorption and (b) band gap plots of SnS_2 NPs synthesized at varying laser fluence in acetone © 2019, Elsevier

Optical absorption spectra of the SnS_2 NPs synthesized in isopropanol and acetone at varying ablation fluences were recorded. Fig.5.29 (a) and 5.30 (a) depict the optical absorption spectra of the SnS_2 NPs synthesized in acetone and isopropanol at distinct laser fluences. All the samples present similar optical absorption spectra irrespective of the liquid media or laser fluence applied in laser ablation synthesis. Absorption edges of the SnS_2 samples are located around 400-500 nm depending on the laser fluence and solvent where the absorption maximum is towards the UV region. However, a small red shift in the absorption edge is observed when increasing the fluence from 0.25 to 0.5 J/cm^2 in both liquid media. Band gaps of the SnS_2 particles were calculated employing the Tauc plots as seen in Fig.5.29 (b) and 5.30 (b). Estimated band gaps of the SnS_2 NPs in isopropanol are

3.2, 2.92, 2.82 and 3.16 eV respectively for 0.25, 0.5, 0.37 and 1.65 J/cm^2 fluences where the higher bandgaps are for the extreme ends of laser fluences (lowest and highest) used in the present work. Corresponding TEM images showed presence of many smaller nanoparticles and those obtained at 0.5 J/cm^2 are of highest average size showing lowest optical bandgap. In acetone the estimated band gaps of SnS_2 NPs are 2.9, 2.79, 2.69 and 2.77 eV respectively for 0.25, 0.37, 0.5 and 1.65 J/cm^2 fluences. In this case, as the laser fluence increased, the band gap of SnS_2 particles decreased. By comparing the nanoparticles synthesized in acetone and isopropanol at the same laser fluence, the NPs in acetone present lower band gaps compared to that in isopropanol. However, all these nanocolloids show higher optical bandgap compared to the bulk SnS_2 as reported[79]. Band gap changes of the SnS_2 nanoparticles according to the change in fluence or liquid medium can be attributed to the slight differences in NP morphology. The optical bandgap for bulk SnS_2 is 2.2 eV. Band gaps of all the synthesized SnS_2 NPs are shown in table 5.5.

Table.5.5. Band gaps of SnS_2 NPs synthesized in different liquids at various conditions

Laser wavelength (nm)	Liquid medium	Fluence (J/cm^2)	Band gap (eV)
1064	Acetone	0.95	2.53
	Isopropanol		2.41
	Ethanol		2.44
	DMF		2.63
532	Acetone	0.63	2.94
	Isopropanol		2.86
	Ethanol		2.86
	DMF		3.05
532	acetone	0.25	2.90
		0.37	2.79
		0.5	2.69
		1.65	2.77
	Isopropanol	0.25	3.20
		0.37	2.92
		0.5	2.84
		1.65	3.16
532 (100 Hz)	DMF (room temp.)	2.9	2.68
	DMF (80ºC)		3.01

	DMF-post irradiated	0.53	3.11

A blue shift in the absorption edge for the spectra of SnS_2 NPs synthesized by PLAL may be due to the particle size and morphology effects. SnS_2 nanoparticles obtained through PLAL under different conditions exhibit varying size distribution in the range of 7 to 25 nm and nanoparticles having smaller sizes show higher optical band gaps. Peculiarities of the synthesis method, morphology and size distribution might have played significant roles in determining the absorption spectra of the SnS_2 NPs generated by PLAL. Visible light absorption properties and suitable band gap values suggest that the SnS_2 NPs synthesized using PLAL can be used in applications such as photocatalysis, visible light water splitting and solar cells. Non-toxicity, abundance of the constituent elements and unique structure dependent optoelectronic properties of SnS_2 make it widely acceptable for these kinds of applications. On the other hand, PLAL provides a way to tune the optical properties of SnS_2 NPs by varying either the ablation parameters or by changing the liquid medium.

5.2.11 Influence of post irradiation and liquid temperature on the optical properties of SnS_2 NPs

Fig.5.31 (a, b) depicts the absorption spectra and Tauc plots of the SnS_2 NPs synthesized in room temperature DMF, 80 °C pre-heated DMF and SnS_2 NPs after 5min laser post irradiation respectively. The liquid medium temperature is found to play a role in determining the optical band gap of SnS_2 colloids as well. Small shift in the absorption edge is observed when the particles are either prepared in heated DMF solvent or when post irradiated (Fig.5.31a).

However, in general the absorption spectra are similar to the NPs synthesized in isopropanol and acetone using the 10 Hz laser output. Calculated optical band gaps of the SnS_2 particles are 2.68 and 3.08 eV for the NPs obtained in room temperature DMF and preheated DMF solvent respectively. When the particles are post irradiated for 5 minutes using 532 nm green laser, energy band gap increased from 2.68 eV to 3.11 eV(Fig.5.31b). Change in optical band gap with liquid medium temperature can be attributed to the various morphologies of the NPs in heated DMF solution compared to that in room temperature DMF and the one undergone post irradiation.

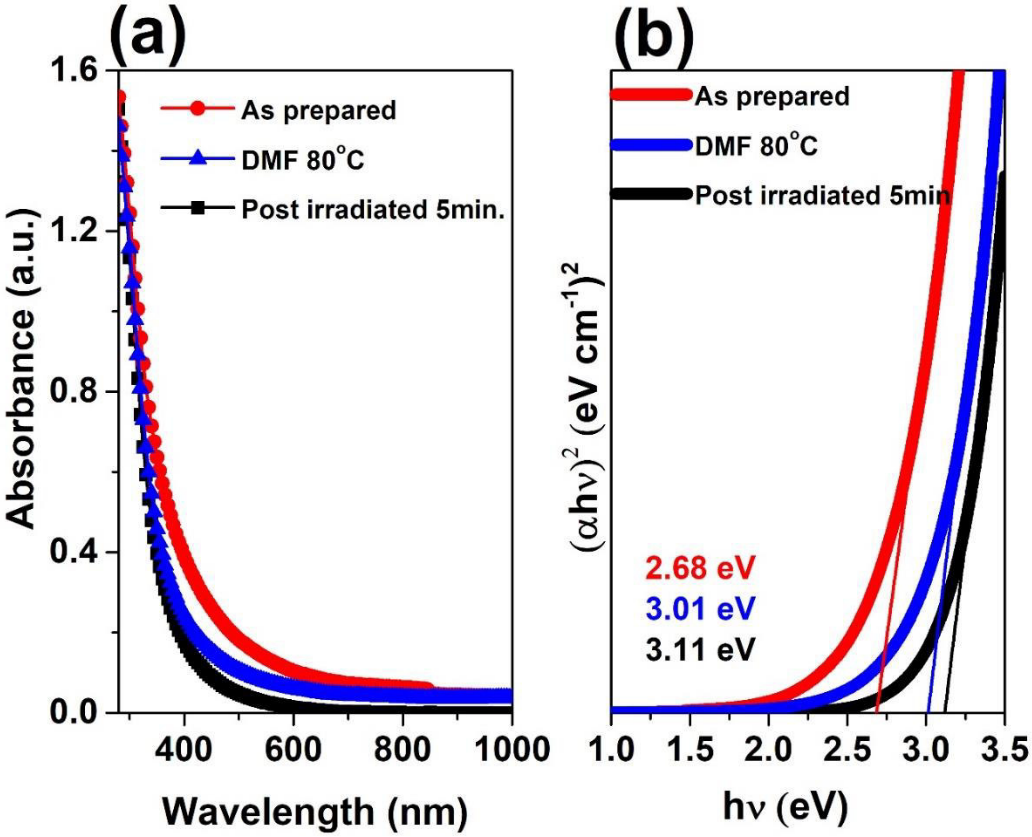

Fig.5.31. (a) UV Visible absorption spectra and (b) Tauc plots of SnS_2 NPs synthesized in room temperature DMF, 80 °C pre-heated DMF and SnS2 particles after 5min laser post irradiation © 2019, Elsevier

5.2.12 Photoluminescence of SnS_2 NPs: effect of solvent and laser wavelength

As an additional optical characterization, photoluminescence (PL) properties of laser generated SnS_2 NPs were measured to identify the emission spectral region. Even though the SnS_2 NPs exhibit similar emission spectra upon changing the liquid medium, different emission properties were noticed as the laser wavelength in the ablation process was changed from 1064 nm to 532 nm. Intensity of the PL peaks were higher in the 1064 nm ablated SnS_2 NPs compared to the 532 nm ablated particles probably due to the higher concentration of the NPs by 1064 nm laser synthesis.

Figure.5.32 depicts the emission spectra in the blue-green wavelength region for SnS_2 NPs synthesized by 532 nm and 1064 nm in different liquid media. A strong photoluminescence peak is observed at 487 nm irrespective of either the liquid medium or laser wavelength used. The SnS_2 particles show another peak at 545 nm with less intensity in addition to the peak at 487 nm only in the case of 1064 nm laser ablation. As the ablation wavelength was varied to 532 nm, the intensity of the peak at 545 nm is diminished but another peak is observed at 462 nm which was absent in 1064 nm laser ablation. Smaller size of SnS_2 nanoparticles obtained by 532 nm ablation could have resulted in this peak emission compared to those obtained by 1064 nm. Photoluminescence studies show that the SnS_2 particles produced by PLAL might have different defect levels according to the laser wavelength used in the ablation process whereas the liquid medium has no noticeable effect.

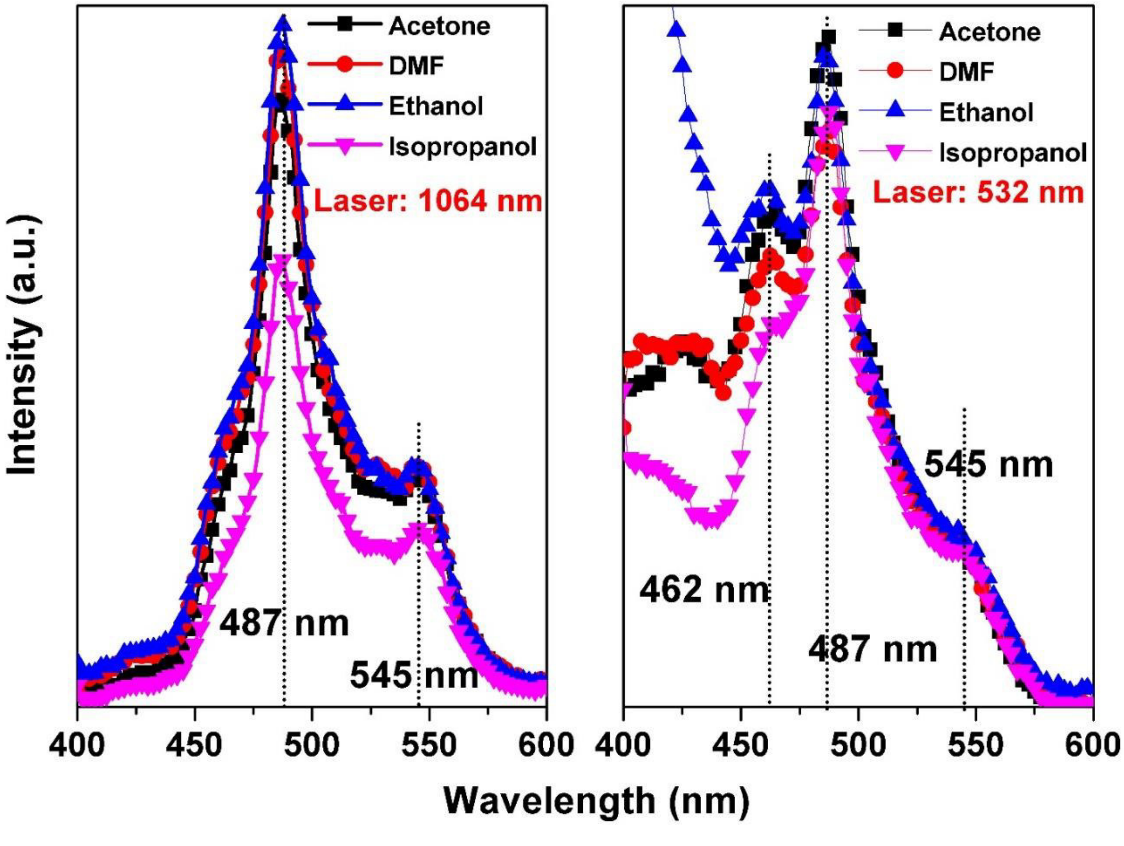

Fig.5.32. Photoluminescence spectra of SnS_2 NPs synthesized in different liquid media using two Nd: YAG laser outputs (532 nm and 1064 nm) © 2018, Elsevier

5.2.13 Photoluminescence of SnS_2 NPs: effect of liquid medium temperature and post irradiation

Emission spectra of the SnS_2 NPs synthesized in DMF were collected by exciting them with 345 nm (Fig.5.33). All the three SnS_2 samples show emission in the visible blue-green region with an emission peak located at 487 nm attributed to the radiative recombination of exciton absorption[335].

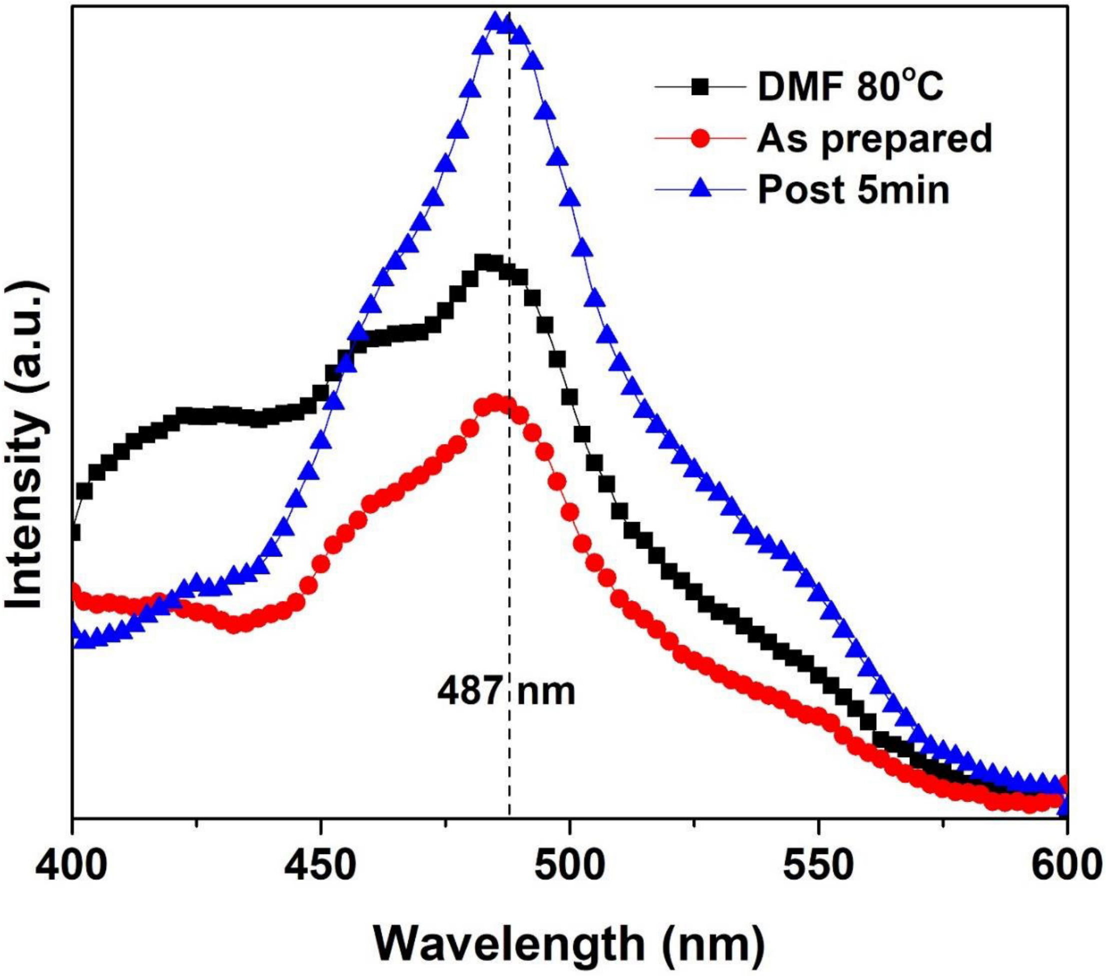

Fig.5.33. Emission spectra of SnS_2 NPs synthesized in room temperature DMF, 80 ºC pre-heated DMF and SnS_2 particles after 5min laser post irradiation. Excitation wavelength: 345 nm © 2019, Elsevier

Most intense and slightly narrow emission is observed for the post irradiated nanoparticles. This supports the smaller particle size and improved crystallinity of SnS_2 NPs obtained by laser post irradiation. SnS_2 NPs synthesized by PLAL in different liquid media by 532 and 1064 nm (as shown in the previous section) also showed similar emission spectra[79, 320].

Photoluminescent peaks at 520, 470 and 490 nm are previously reported for SnS_2 nanoplates where the peak at 520 nm was assigned to radiative recombination of the quantum confined electron-hole pair and the peaks at 470 nm and 490 nm originated from the radiative recombination of exciton absorption[335]. The present study shows that optical properties of the NPs synthesized by PLAL can be tuned by varying the parameters of ablation. However, proper control of various parameters such as laser wavelength, energy fluence, frequency and pulse width together with deep understanding of the ablation mechanism are needed to effectively tune these properties to be beneficial for applications.

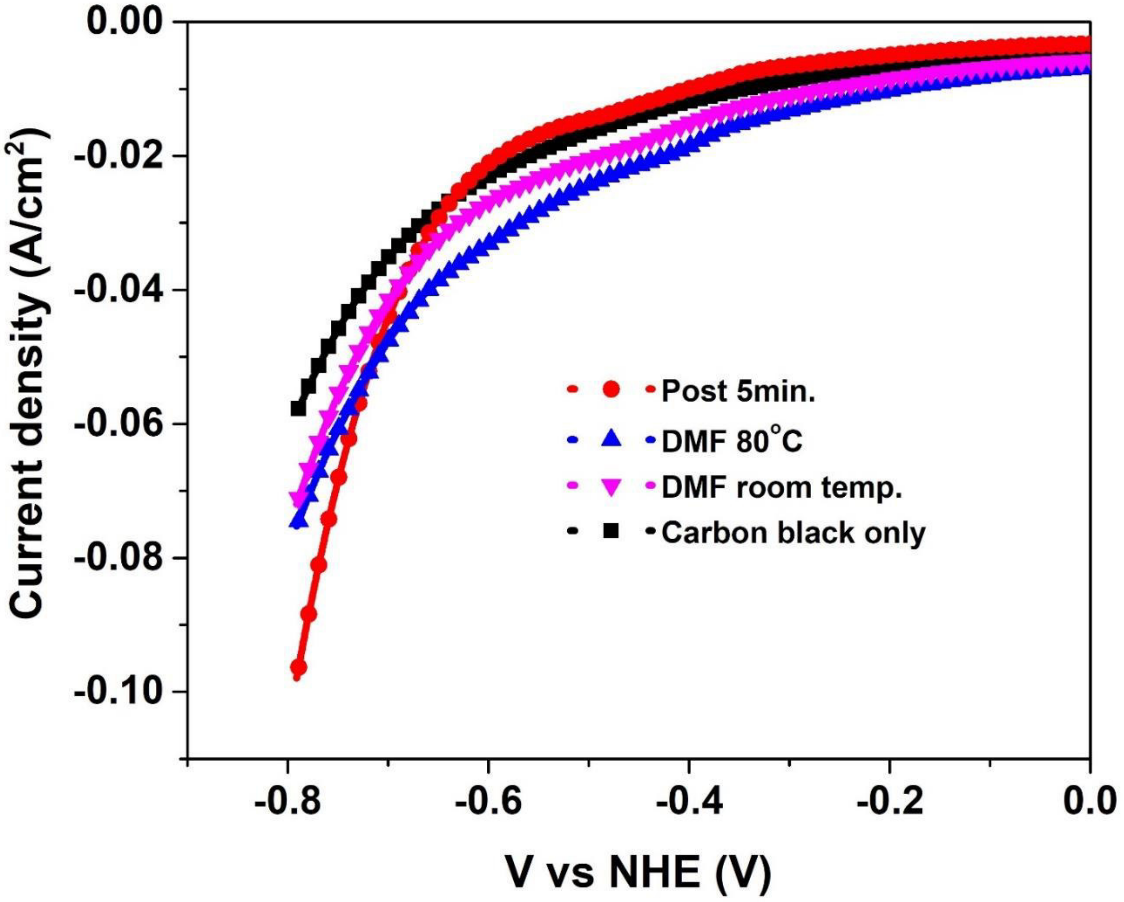

Fig.5.34. HER in 1M H_2SO_4 on SnS_2 NPs synthesized in room temperature DMF, 80 ºC heated DMF and post irradiated SnS_2 for 5min. © 2019, Elsevier

5.2.14 Hydrogen evolution reaction using SnS_2 NPs as catalyst

Electrochemical properties of SnS_2 NPs synthesized in DMF were explored by testing them as electrocatalyst for hydrogen evolution reaction (HER). Laser generated SnS_2 particles were mixed with carbon black and nafion(0.025%) and then dried over glassy carbon electrode which was used as the working electrode in a three-electrode potentiostat. Platinum wire and saturated Ag/AgCl were employed as the counter and reference electrode respectively and 1 M H_2SO_4 was used as the electrolyte. The applied potential was from 250 mV to -1000 mV at a scan speed of 100 mV/s. In each measurement, scanning was done for two consecutive cycles and the data shown are from the second cycle.

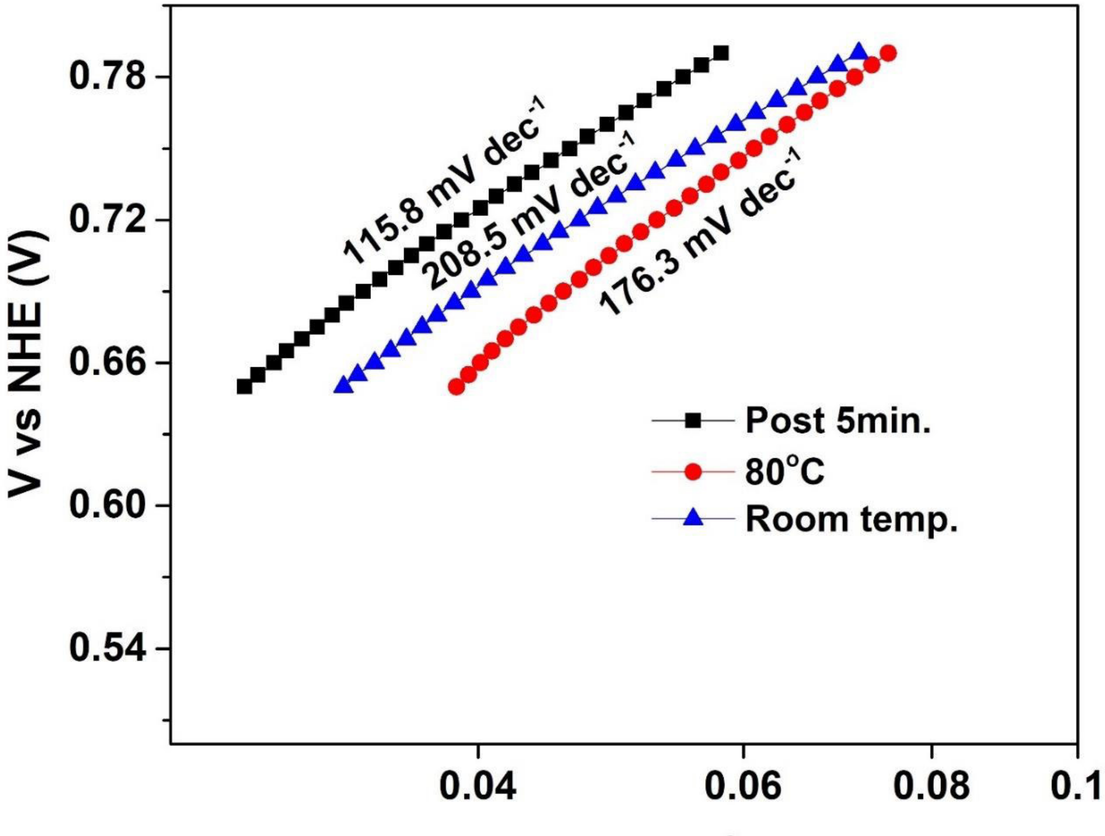

Fig.5.35. Tafel slopes of HER reactions on SnS2 corresponding to the curves in fig.5.34
© 2019, Elsevier

Fig.5.34 shows the HER reaction of SnS_2 NPs synthesized in DMF by PLAL. The current at each potential is enhanced upon modifying the glassy carbon electrode by SnS_2 NPs. Among the samples prepared in room temperature DMF, 80 °C DMF and post irradiated sample, the post irradiated sample shows highest current at a potential of -0.8 V. However, in the post irradiated sample, up to a potential of -0.6 V, the current does not show any significant increase and thereafter increases rapidly. For the samples synthesized in room temperature DMF and 80 °C DMF, the evolution of hydrogen starts at lower potentials.

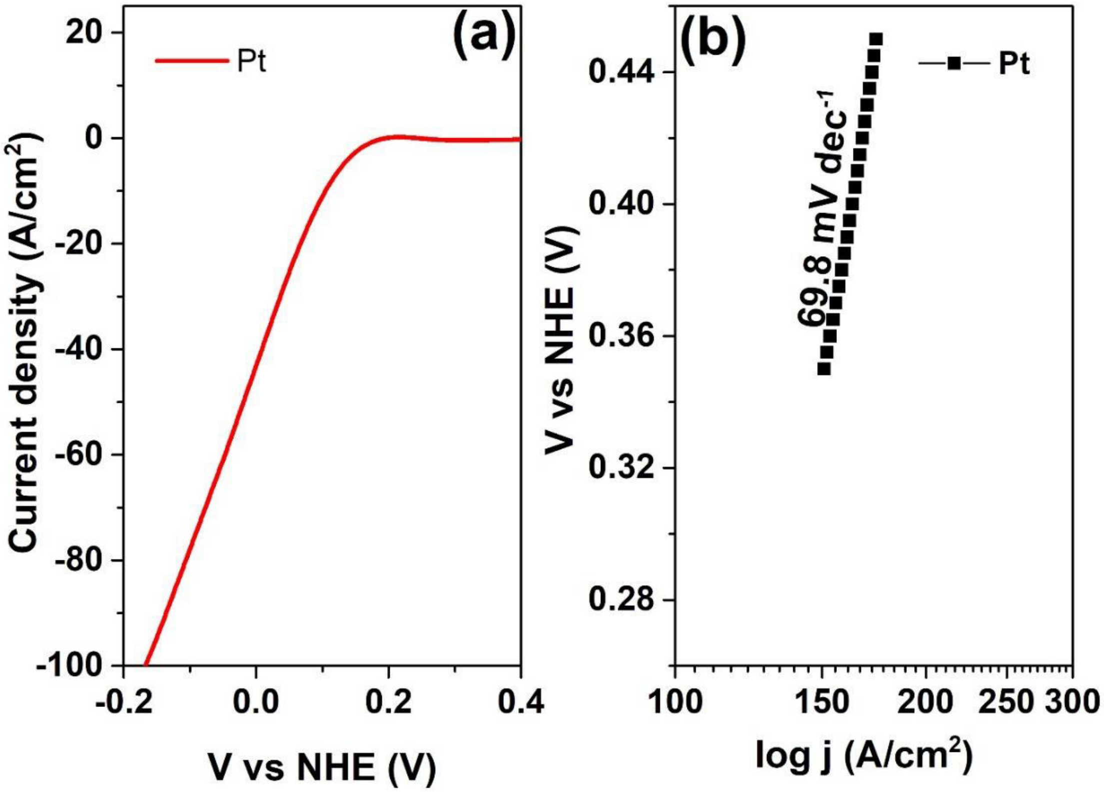

Fig.5.36. HER in 1M H_2SO_4 on Pt electrode and (b) the corresponding Tafel plot © 2019, Elsevier

In acidic media, three different reaction mechanisms are possible for HER as follows[336]

1. $H_3O^+ + e^- \longrightarrow H_{ads} + H_2O$ (Volmer reaction)

2. $H_{ads} + H_3O^+ + e^- \longrightarrow H_2 + H_2O$ (Heyrovsky reaction)

3. $H_{ads} + H_{ads} \longrightarrow H_2$ (Tafel reaction)

The approximate Tafel slopes of the above reaction mechanisms are 120, 40 and 30 mV for Volmer, Heyrovsky and Tafel reactions respectively. The Tafel slopes (Fig.5.34) calculated for the samples are 115.8, 208.5 and 176.3 mV/dec for the post irradiated sample, sample prepared in room temperature DMF and 80 °C heated DMF respectively. Hence in the present work, the HER on SnS_2 NPs synthesized by PLAL follow only the primary discharge step (Volmer reaction) since the Tafel slope values are comparable with that of the Volmer reaction.

A platinum electrode tested under the same conditions exhibited a Tafel slope of 69.8 mV/dec. The HER of Pt electrode and the corresponding Tafel plot are given in fig.5.36. However, Pt is extremely expensive compared to the cost of constituent elements of SnS_2.

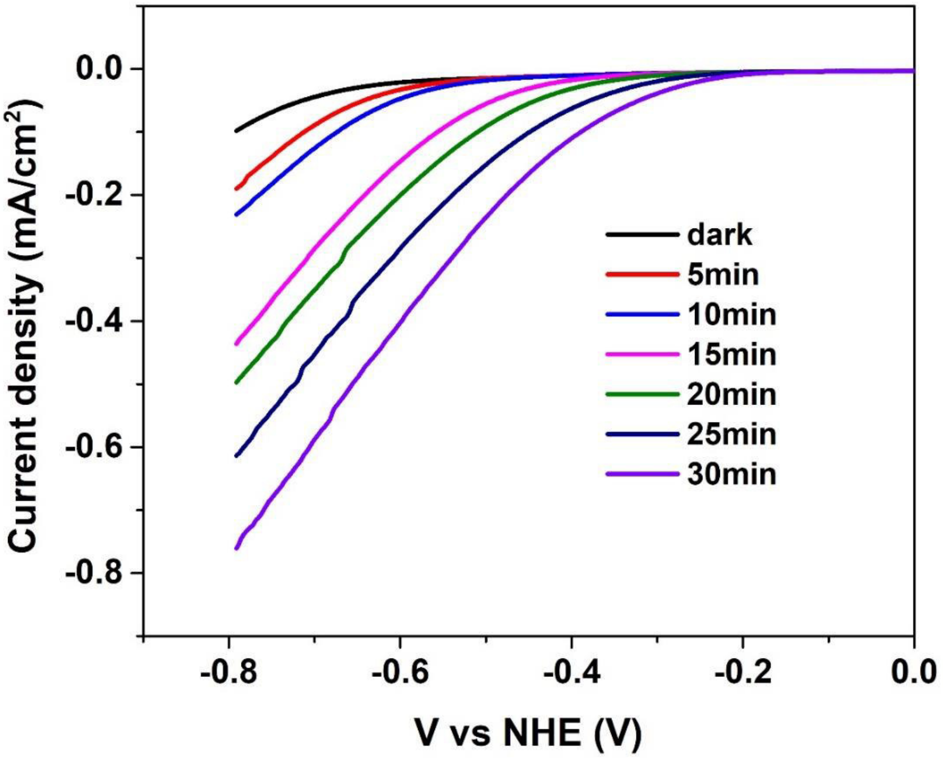

Fig.5.37. HER in 1 M H_2SO_4 for post irradiated SnS_2 NPs for different illumination times using a UV LED lamp © 2019, Elsevier

The reliable HER activity of the SnS_2 NPs could be attributed to the morphology of the particles together with the material properties of SnS_2. Since the NPs are generated in pure solvents without any surfactants, the active particle surface is free from ligands which is advantageous for electrochemical applications. Moreover, varying the nature of liquid medium or ablation parameters, one can get control over the particle morphology and hence on the electrochemical properties of the particles. The glassy carbon electrode modified with SnS_2 NPs were also continuously illuminated using a UV LED lamp and the hydrogen evolution activity was measured each 5 min for a total duration of 30 min. and the corresponding results for the post irradiated SnS_2 sample are graphically presented in fig.5.37.

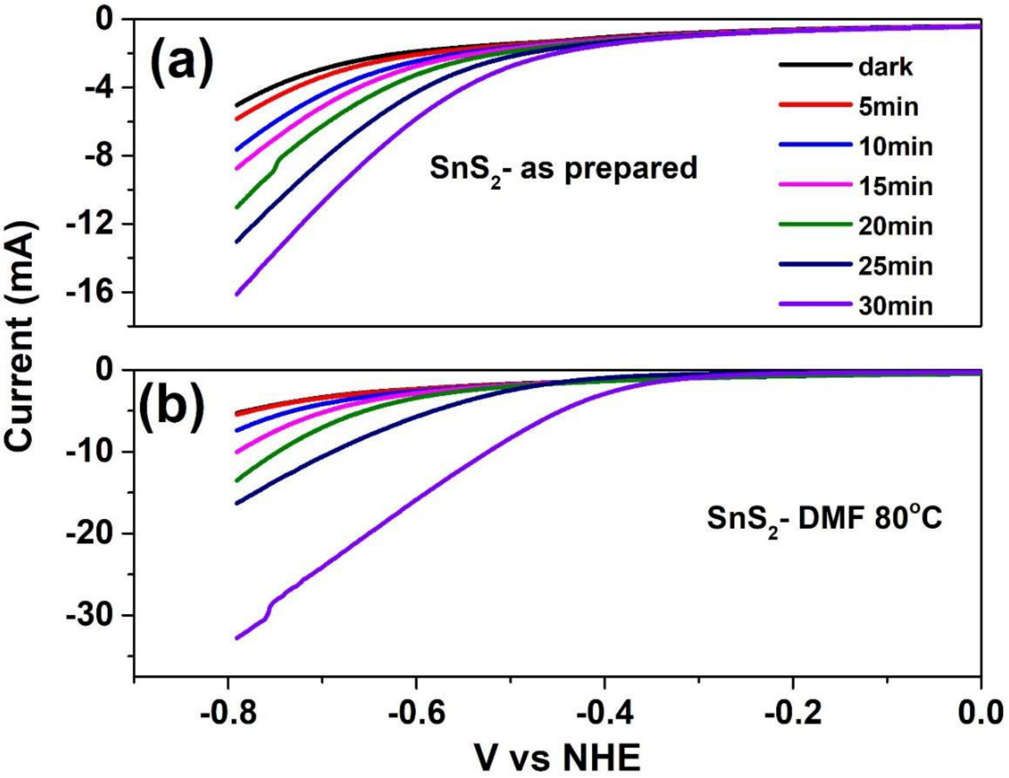

Fig.5.38. HER activity of SnS_2 NPs synthesized in room temperature DMF and heated DMF solvents under different time of UV light illumination © 2019, Elsevier

The measured current at each potential is increased together with a shift of the onset potential towards lower potentials by increasing time of illumination. For example, the current observed at -0.8 V potential for the SnS_2 post irradiated sample without illumination is ~1 mA and increased up to 16.5 mA with 30 min illumination. Both the shift in onset potential and increment in the current implies better HER activity on the SnS_2 NPs upon illumination. More charge carriers are generated by absorbing photons from the incident light which may enhance the electrochemical activity of the SnS_2 NPs based electrodes. Similar increase in the current was observed for the samples synthesized in room temperature and 80 °C heated DMF solvent. The corresponding measurements are included in fig.5.38.

HER activities of layered SnS and SnS_2 obtained through a chemical synthetic approach was reported by Chia et al. In that case, the obtained HER overpotential for SnS_2 was 0.73 V at a current density of 10 mA/cm^2 though for SnS it was 0.88 V suggesting better performance of SnS_2 over SnS and it was attributed to the higher chalcogen-to-metal ratio in SnS_2 compared to SnS[300]. Monodispersed SnS_2 nanosheets having 22 nm thickness also presented better photocatalytic hydrogen generation compared to other studied morphologies and P25-TiO_2[237]. Au-Fe nanoalloys synthesized by PLAL showed enhanced electrocatalytic oxygen evolution owing to the incorporation of high amount of Fe into the Au lattice which was attributed to the peculiarity of the synthesis method[337]. When SnS_2 NPs are synthesized through chemical synthetic ways, although, there is an effective control over the morphology, it leads to production of lots of chemical wastages. Moreover, controlling the exact desired composition through adjusting chemical precursors is another challenging task. In the present work, HER activities of these SnS_2 nanoparticles are mainly dependent on their morphology. The results obtained show that pulsed laser ablation in liquid is an effective way to produce ligand-free SnS_2 NPs without any surfactants or toxic reagents where the morphology can be controlled by adjusting the laser ablation parameters or varying the solvent properties.

5.3 Conclusions

Pulsed laser ablation was successfully used as a facile and fast technique to synthesize SnS_2 nanoparticles by ablating an SnS_2 target in liquids. Nanoparticles were synthesized using two different laser wavelengths and in four different solvents and at various laser fluences. Moreover, the effects of liquid medium temperature and laser post irradiation on the particle morphology were investigated. Morphology and crystal structure were identified by TEM characterization together with SAED and HRTEM analyses. The obtained NPs were predominantly having a spherical particle morphology whereas in some cases they exhibited connected chain like structures without definite boundaries. XRD, XPS and Raman analyses further confirmed the crystal structure, chemical state and crystalline nature of the laser synthesized SnS_2 NPs and proved that they match with the ablation target used. XRD analysis showed that the nanoparticles were having hexagonal crystal structure of SnS_2 whereas XPS analysis confirmed the Sn^{4+} and S^{2-} chemical states of SnS_2. 2-H polytype structure of all the synthesized particles were confirmed by the Raman analysis. As either the liquid medium or the ablation wavelength was varied, the optical band gaps of the SnS_2 NPs were varied from 2.4 eV up to 3.05 eV. Synthesized nanocolloids showed emission in the blue-green region with major peak at 487 nm irrespective of the lasing conditions or liquid medium. Smaller SnS_2 NPs were formed by laser post irradiation as indicated by TEM measurements and high PL intensity. Finally, SnS_2 NPs were effectively used as electrocatalysts for hydrogen evolution reaction where the activity was improved upon illumination of the electrode using an LED light source. The study can pave way to use PLAL as an effective and rapid synthesis technique for SnS_2 NPs in large scale and for their application in electrochemistry.

Chapter 6

Structure, composition, morphology, optoelectronic and electrochemical properties of SnS_2 thin films obtained from laser ablated nanocolloids

6.1 Introduction

In this chapter, deposition and characterization of SnS_2 thin films by spraying laser ablated SnS_2 nanocolloids is demonstrated. SnS_2 NPs were obtained in ethanol and isopropanol by PLAL and the thin films were fabricated by spraying the nanocolloids onto heated substrates. The nanoparticles and thin films were characterized by various techniques for their structure, morphology and chemical states.

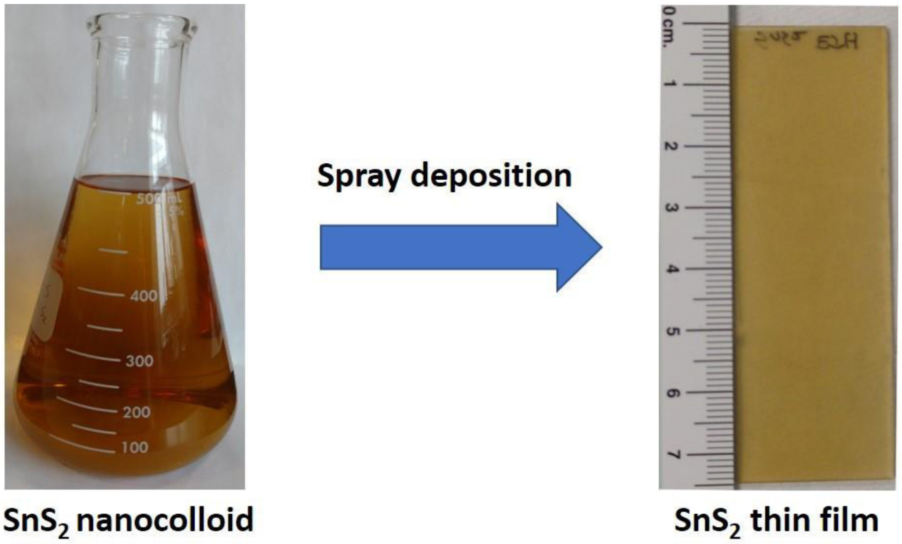

Fig.6.1. Photographs of SnS_2 nanocolloid as well as spray deposited SnS_2 thin film. Adapted with permission [1] © 2018, Wiley

Optical, Opto-electronic and electrochemical properties of such thin films were analyzed in detail by means of UV-Vis spectroscopy, photocurrent measurements and electrochemical characterization respectively. Influence of different post annealing temperature on the above-mentioned properties of SnS_2 thin films was also studied by annealing the films in vacuum. Results demonstrated in this chapter were published in [1]. Photographs of the SnS_2 colloidal suspension and thin film are shown in fig.6.1.

6.2 Structure and properties of SnS_2 thin films

6.2.1 *Particle morphology by TEM*

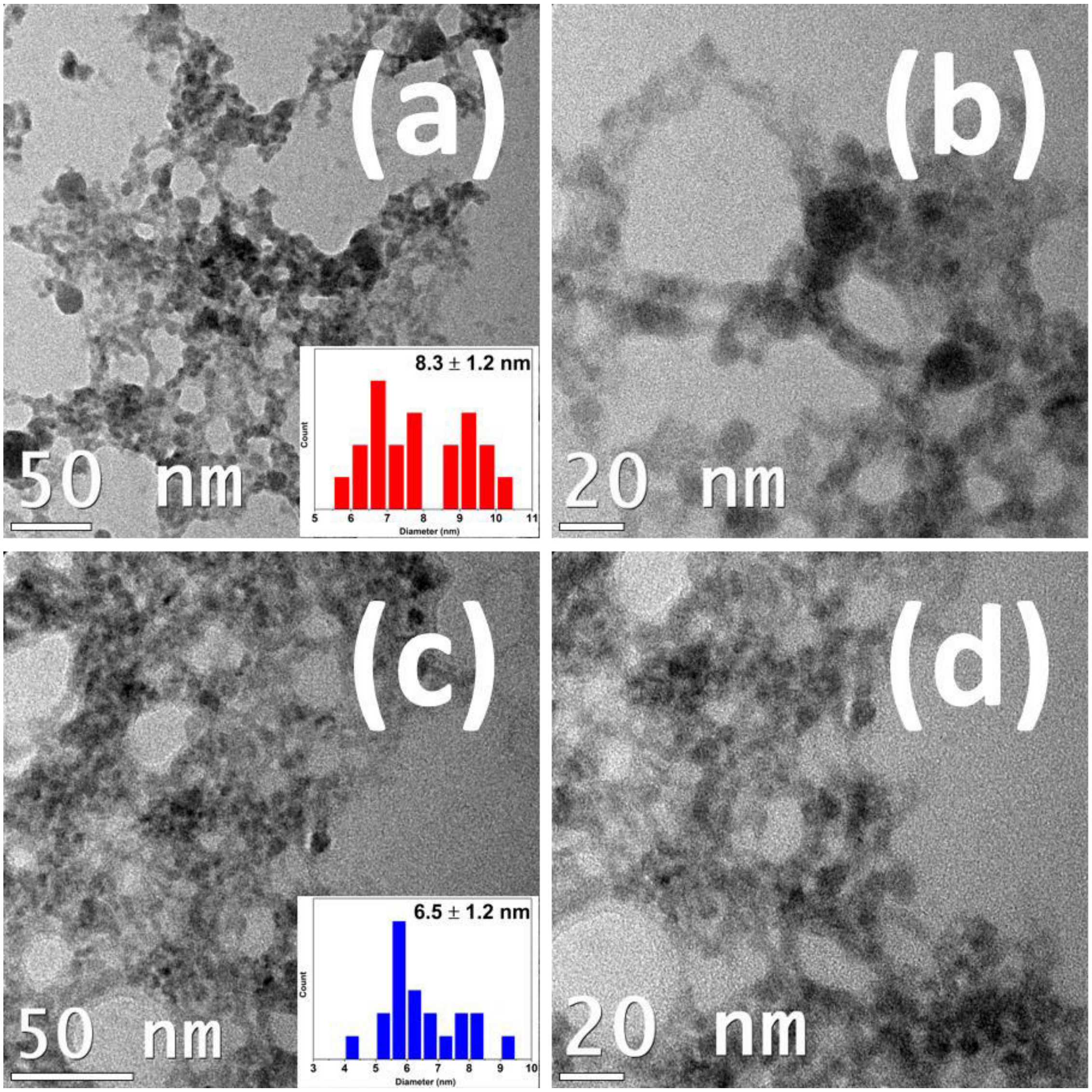

Fig.6.2. TEM micrographs of SnS_2 NPs in (a, b) ethanol and (c, d) isopropanol at two distinct magnifications. The particle size histograms are included in the insets. Adapted with permission [1] © 2018, Wiley

Colloidal SnS_2 nanoparticles were obtained by pulsed laser ablation of the SnS_2 target in ethanol and isopropanol using the 532nm laser output. The as prepared NPs were analyzed by TEM for the particle morphology. TEM micrographs of the SnS_2 NPs obtained in ethanol and isopropanol at two distinct magnifications are presented in fig. 6.2. As seen from the TEM images, the SnS_2 NP morphology is different in ethanol and isopropanol. While in ethanol, slightly interconnected and spherical SnS_2 nanoparticles with well-defined boundaries are formed, nanoparticle chains with less-defined boundaries are formed in isopropanol. SnS_2 NPs have an average size of 8.3 nm with a standard deviation of 1.2 nm (8.3±1.2 nm) in ethanol whereas in isopropanol the average particle size is 6.5±1.2 nm as estimated from the TEM pictures indicating the formation of smaller NPs are in isopropanol in comparison with those generated in ethanol. Different solvent properties such as refractive index, viscosity, dipole moment and density affect the laser induced plasma as well as the life time of the cavitation bubble which may lead to the changes in particle morphologies[61, 100]. In addition to that, the atomic density and temperature gradient in the plasma cannot be controlled during the process and thus results in formation of particles with different sizes and shapes. Further information regarding the role of liquid media in determining the particle morphologies by PLAL can be found in the literature [79, 144, 159, 338-340].

6.2.2 *Thin film crystal structure by XRD*

Crystalline structure and phase of the as prepared and annealed SnS_2 thin films were characterized using X-ray diffraction in the grazing incidence mode (GIXRD). The diffractograms were collected by employing Cu-Kα (λ= 0.154 nm) as the source at an incident angle of 0.3° in 2θ range 10 to 70 degrees. Fig. 6.3 presents the diffractograms of all SnS_2 thin films (as prepared and annealed) deposited from both nanocolloids. All the SnS_2 thin films show a high intensity peak at 2θ= 15.05° which is indexed to the (001) plane of hexagonal crystal structure of SnS_2 in agreement with the JCPDS no. 83-1705 regardless of the liquid medium in PLAL and post annealing temperatures. A small diffraction peak is also observed at 2θ= 32.2° in all the XRD patterns which is assigned to the (011) plane of hexagonal SnS_2 phase. The SnS_2 target used for laser ablation also present similar XRD pattern as shown in the previos chapter and in reference [79]. Grain sizes estimated from the XRD patterns along the (001) plane using the Scherrer equation [341] are 30.8, 31.8, 32 and 29.6 nm for the as prepared, 200, 250 and 300 °C annealed samples respectively synthesized from SnS_2 in isopropanol whereas the corresponding crystallite sizes are 30.1, 31.2, 31.7 and 29.8 nm, for the samples deposited from ethanol. Calculated crystallite sizes for the samples synthesized from SnS_2 in ethanol and isopropanol are very close for each post annealing temperature where the crystallite sizes increase from the as prepared to the 250 °C annealed sample.

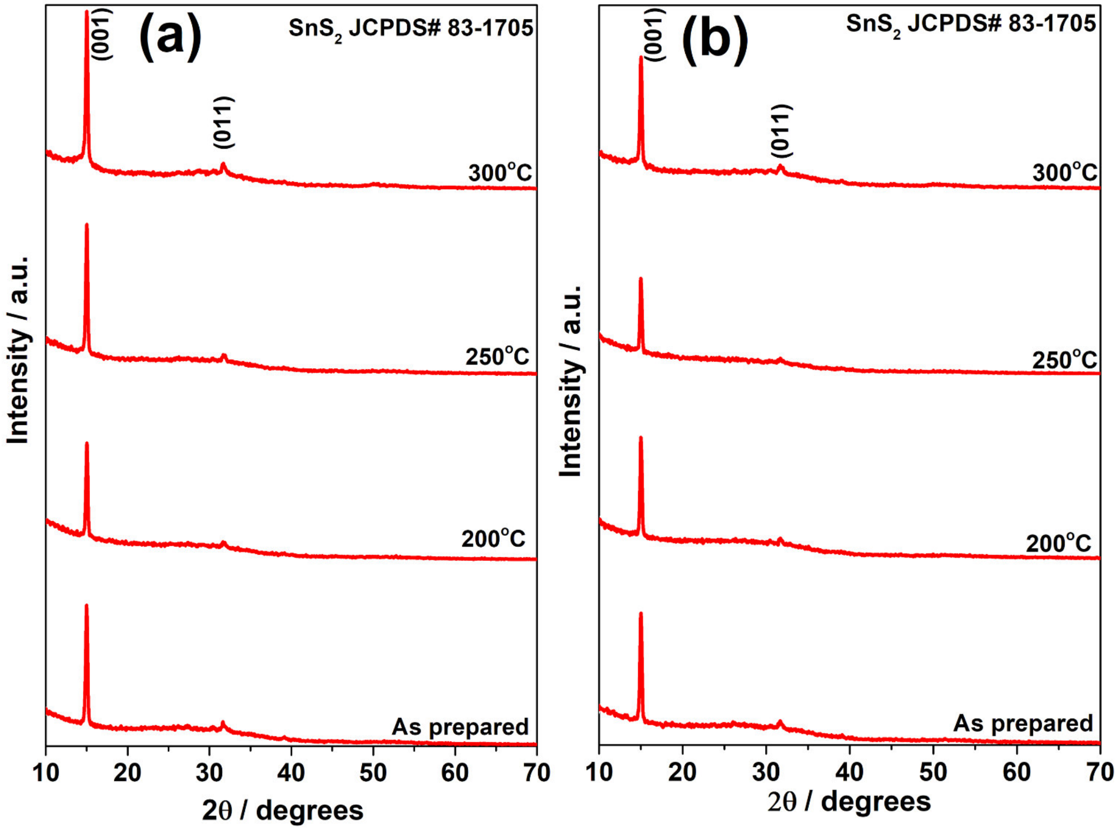

Fig.6.3. GIXRD patterns of the as prepared and annealed SnS_2 thin films synthesized using (a) ethanol and (b) isopropanol as the solvents in PLAL. Adapted with permission [1] © 2018, Wiley

When the thin films were annealed at 300 °C, the grain sizes decreased compared to the as deposited and other annealed samples in both cases (in isopropanol and ethanol) which can be attributed to the formation of SnS phase (identified in Raman spectra as shown in the following section) due to depletion of sulfur from the films. However, it should be noted that, in the present work, crystalline SnS_2 phase is formed without any post annealing treatments to the films as identified from well-defined and intense XRD peaks of the as deposited thin films.

6.2.3 *Raman analysis of SnS_2 thin films*

Raman spectroscopy with an excitation of 532 nm was employed to determine the crystalline nature of the SnS_2 thin films (Fig.6.4). All the SnS_2 thin films are characterized by a strong Raman band located at 314 cm^{-1} corresponding to the A_{1g} vibrational mode of SnS_2 [321] thereby confirming the 2-H polytype structure of these films. This peak is in close match with the Raman spectral analysis of the SnS_2 target as well as SnS_2 NPs as described in the previous chapter. 2H- SnS_2 belongs to the D_{3d}^{3}-P$\bar{3}$m1 space group containing three atoms per unit cell.

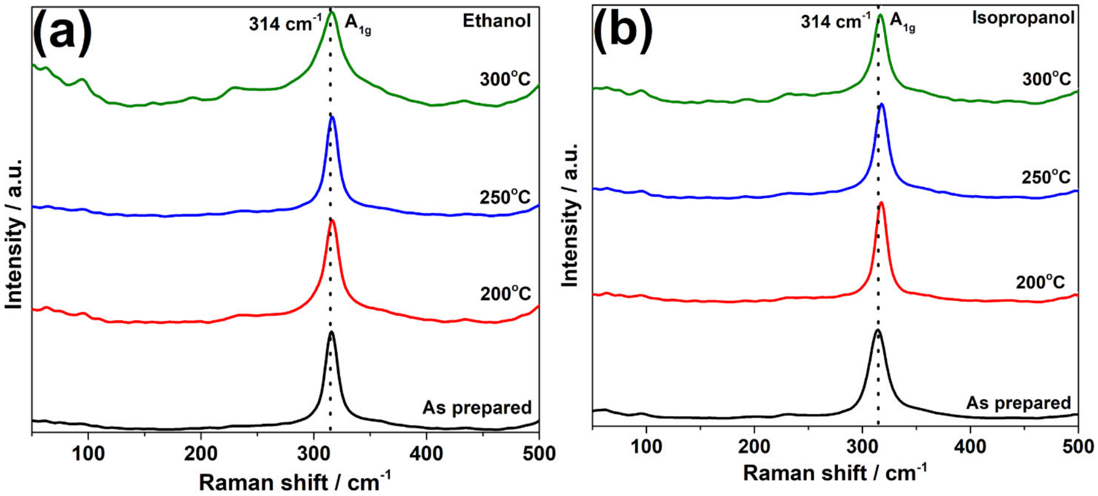

Fig.6.4. Raman spectra of the as prepared and annealed SnS_2 thin films synthesized using (a) ethanol and (b) isopropanol as the solvents in PLAL. Adapted with permission [1] © 2018, Wiley

Among the total nine possible normal vibration modes of SnS_2, three are Raman active belonging to A_{1g} and E_g. [342, 343]. Two weak bands are also present in the 300 °C annealed samples at wavenumbers 95 cm^{-1} and 226 cm^{-1} corresponding to the A_g vibrational mode of SnS phase. In both cases of Raman spectra, the main peak that corresponds to SnS_2 phase at 314 cm^{-1} demonstrate a small peak broadening as well as a minor increase in intensities of the additional peaks because of the SnS phase. This impurity phase might have formed due to the depletion of sulfur from the films when they are annealed at 300 °C. However, the SnS phase is not detected in XRD either due to the amorphous nature or the low content of this phase. In Raman analysis, intensities of the peaks corresponding to SnS phase is very low compared to the SnS_2 phase thereby implying that the synthesized thin films are mainly constituted by the SnS_2 phase.

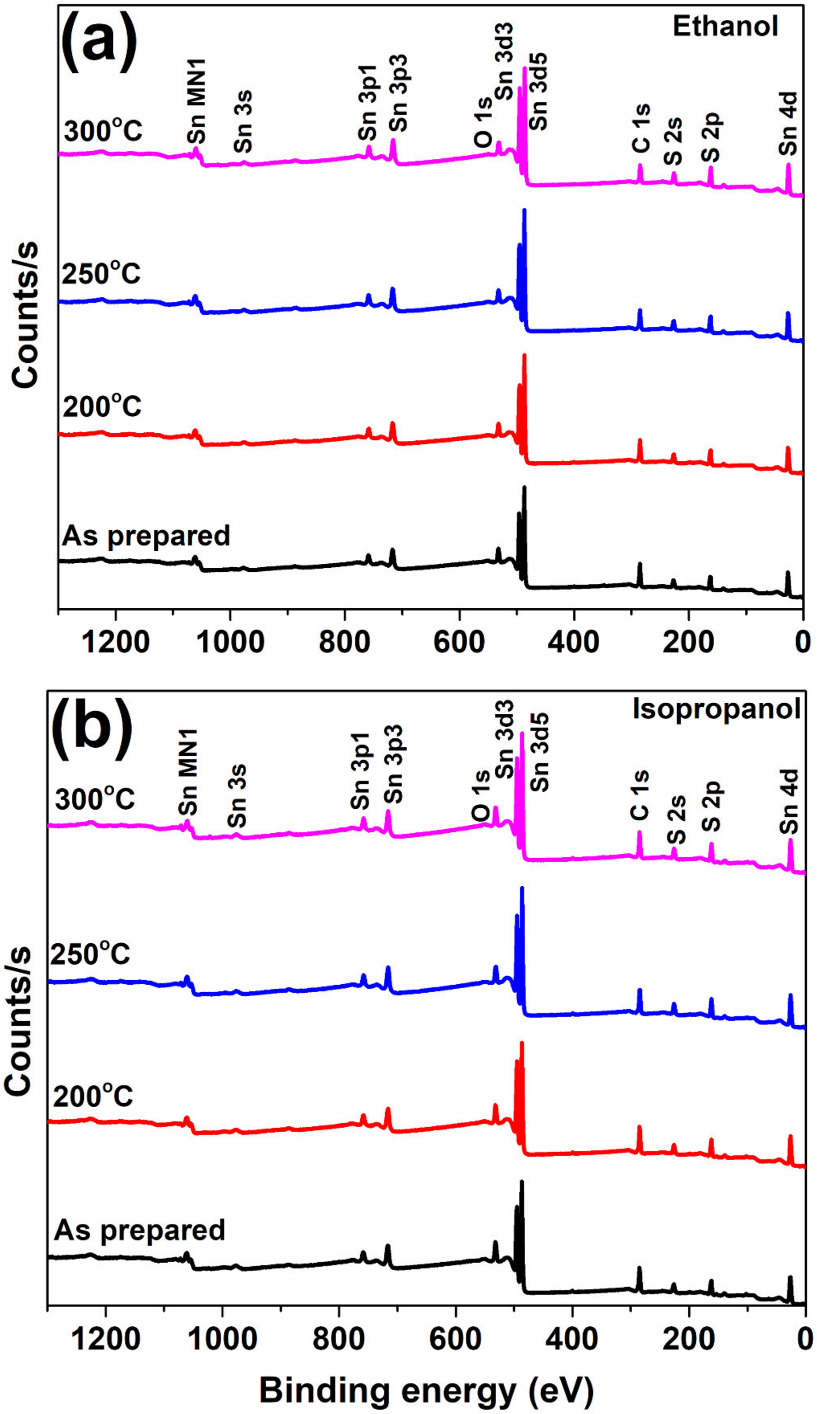

Fig.6.5. XPS survey spectra of as prepared and annealed SnS_2 thin films synthesized using (a) ethanol and (b) isopropanol as the solvents in PLAL. Adapted with permission [1] © 2018, Wiley

This SnS phase could have already formed during the laser ablation since the presence of

SnS as a minor phase was reported in the Raman spectral analysis of SnS_2 nanoparticles itself by PLAL as shown in the previous chapter.

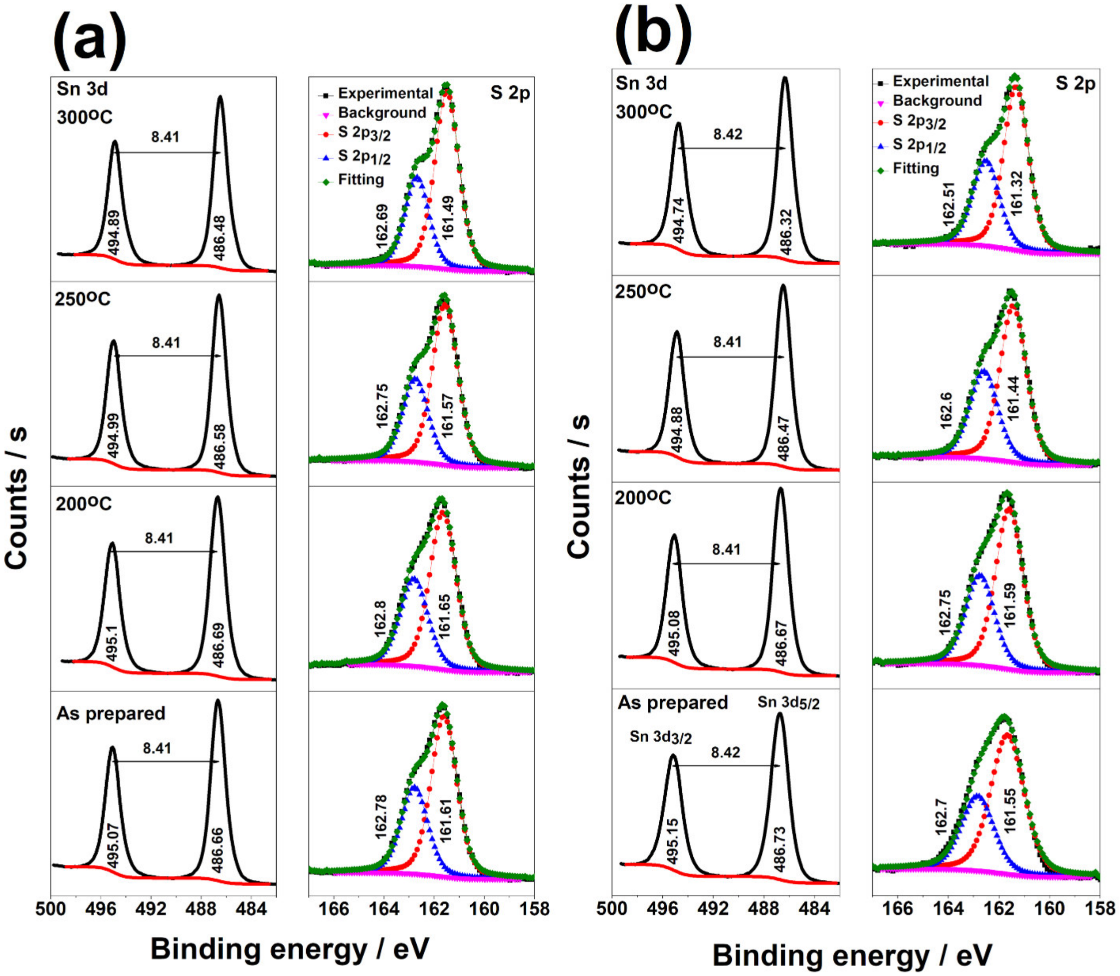

Fig.6.6. High resolution XPS spectra of Sn 3d and S 2p of the SnS_2 thin films synthesized using (a) ethanol and (b) isopropanol as the solvents in PLAL. Adapted with permission [1] © 2018, Wiley

When SnS_2 samples are processed at higher temperatures, the film composition can be altered due to the loss of sulfur content. Moreover, annealing SnS_2 thin films above 300 °C is not favorable for applications in photovoltaics as suggested by Shi et al. They also found that SnS_2 thin films started oxidizing when the annealing temperature was increased to 400 °C [344]. A hybrid SnS@graphene structure for sodium ion battery application was prepared by structural phase transition of hexagonal SnS_2 to orthorhombic SnS by thermal annealing[217].

6.2.4 *XPS analysis of SnS_2 thin films*

Surface of the SnS_2 thin films were characterized by XPS technique for identifying the elemental composition and chemical states of the as deposited and annealed samples. XPS survey scans of the films demonstrated that the samples are elementally free from any contamination (Fig. 6.5). Fig. 6.6 depicts the high-resolution spectra of Sn and S of the SnS_2 thin films. The $Sn3d_{5/2}$ peak possess binding energies (BE) 486.66eV and 486.73 eV for the as prepared SnS_2 thin film in ethanol and isopropanol respectively. Binding energy difference calculated for the splitted Sn3d peaks is 8.4 eV confirming that the peaks belong to tin. For the $S2p_{3/2}$ peak, the BE is varied from 161.61 eV to 161.44 eV according to the liquid medium and annealing temperature. 1.17, 1.15, 1.18 and 1.2 eV are the BE differences of S2p peaks split ($S2p_{3/2}$ and $S2p_{1/2}$) respectively for the as prepared and 200, 250 and 300 °C annealed samples in the case of the films synthesized from SnS_2 in ethanol. For the films deposited from SnS_2 in isopropanol, the BE differences of S2p peaks are 1.15, 1.16, 1.16 and 1.19 eV for as prepared and annealed conditions. These BE differences between $S2p_{3/2}$ and $S2p_{1/2}$ further confirms that the peaks belong to sulfur. BEs of Sn and S agree well with the previously reported BE values for SnS_2 in all the as prepared and annealed SnS_2 thin films deposited from SnS_2 in both liquids. When the annealing temperature is increased from 200 °C to 300 °C, a small decrease in the peak binding energy of $Sn3d_{5/2}$ is noticed (486.48 eV for both solvents) probably due to depletion of some sulfur from the films. Stoichiometry of SnS_2 is slightly altered when more sulfur is depleted, which leads to the variation in the BE compared to the as prepared films. The minor presence of SnS phase in the samples annealed at 300 °C is underlined by the lower $Sn3d_{5/2}$ BEs observed, since the valency of Sn in SnS phase is +2 compared to the +4 valency in SnS_2. The $Sn3d_{5/2}$ and $S2p_{3/2}$ peak BEs of the as prepared SnS_2 samples are summarized in table 6.1.

Table.6.1. BEs of $Sn3d_{5/2}$ and $S2p_{3/2}$ peaks of the as prepared and annealed SnS_2 thin films

Sample	Heat treatment	Sn $3d_{5/2}$ BE (eV)	S $2p_{3/2}$ BE (eV)
SnS_2 (ethanol)	As prepared	486.66	161.61
	200°C	486.69	161.65
	250°C	486.58	161.57
	300°C	486.48	161.49
	As prepared	486.73	161.55

SnS_2 (Isopropanol)	200°C	486.67	161.59
	250°C	486.47	161.44
	300°C	486.32	161.32
Literature value		486.6[329]	161.6[329]

6.2.5 *Morphology of SnS_2 thin films*

Secondary electron images taken by a FESEM were used to identify the SnS_2 thin film morphology. Figure 6.7 presents the FESEM images of the as prepared and annealed SnS_2 thin films deposited from SnS_2 in ethanol.

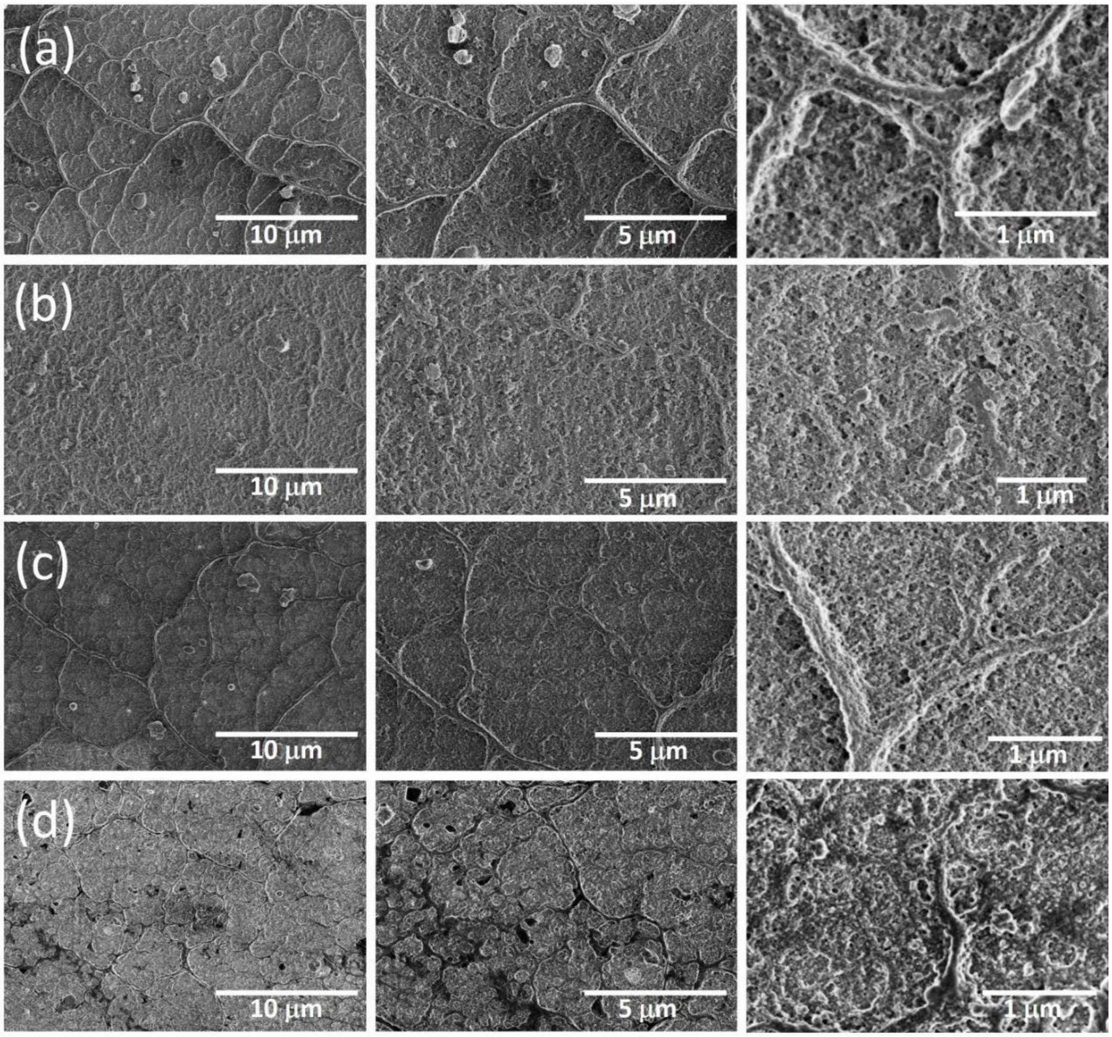

Fig.6.7. SEM images of SnS_2 thin films synthesized from SnS_2 in ethanol (a) as prepared, annealed at (b) 200 °C (c) 250 °C and (d) 300 °C at different magnifications

SnS_2 thin films possess porous, layered surface morphology in ethanol. In isopropanol also the films possess a porous surface morphology similar like in ethanol (fig.6.8). However, small difference in the morphology can be identified as the liquid medium is varied since more porous surface is observed for the thin films deposited using NPs obtained in isopropanol. Different SnS_2 nanoparticle morphologies in ethanol and isopropanol may account for change in surface morphology of the films. Polarity, viscosity, refractive index, heat capacity and density are some important parameters that may affect the final morphology of the nanoparticles synthesized by PLAL[79]. Ethanol and isopropanol are polar protic solvents and smaller NPs are resulted when laser ablation is carried out in polar solvents due to the electrical double layer formation around the generated particles[100].

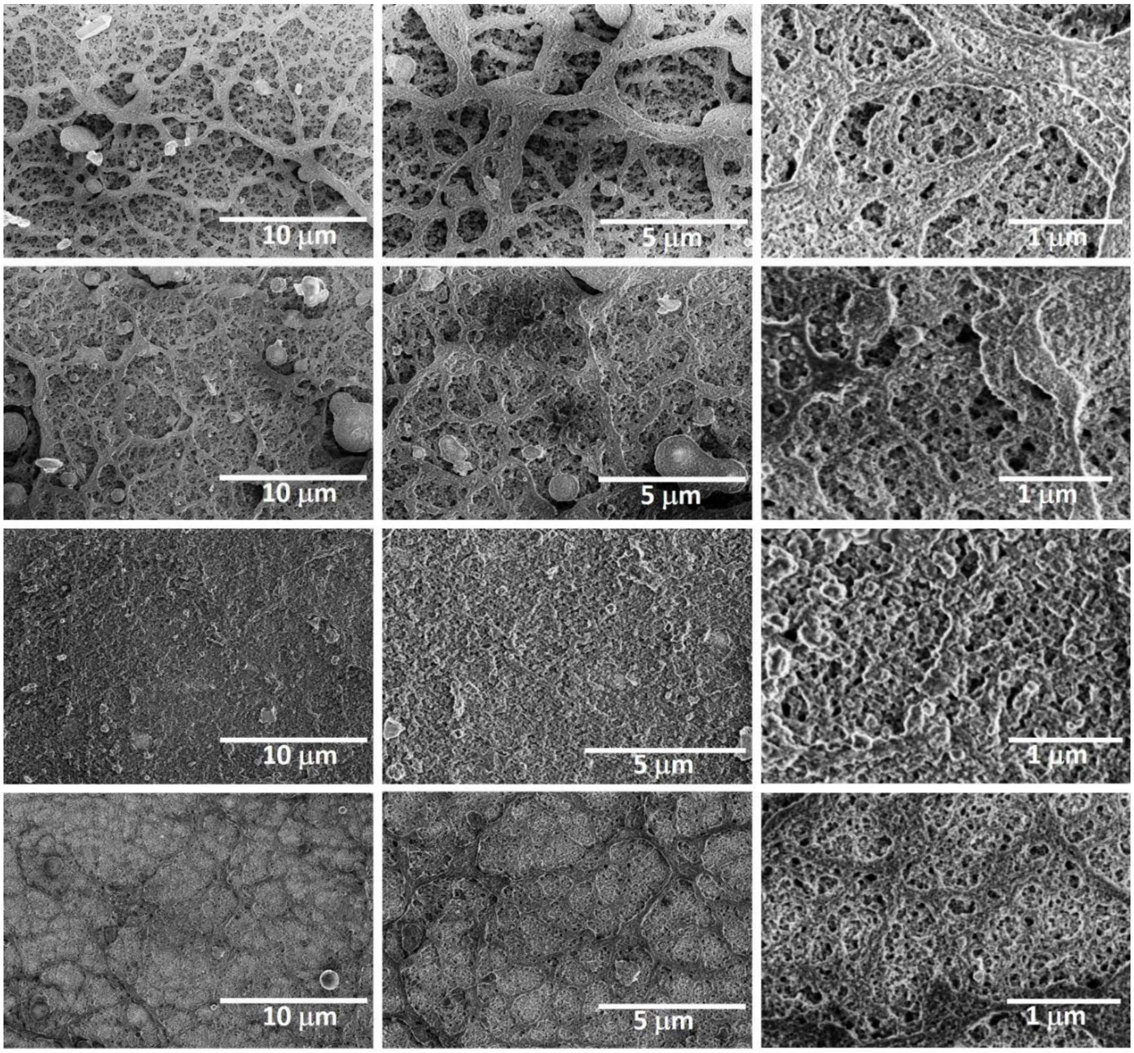

Fig.6.8. SEM images of SnS_2 thin films synthesized from SnS_2 in isopropanol (a) as prepared, annealed at (b) 200 °C (c) 250 °C and (d) 300 °C at different magnifications

Viscosity of the solvents favors the laser induced plasma plume for longer times whereas refractive index of the solvent plays a crucial role on determining the particle morphology since the refractive index is altered dramatically due to the high temperature and vapor pressure[61, 100]. On the other hand, substrate temperature, liquid flow rate and distance between the spray nozzle and the substrate are the most important parameters that determine the thin film morphology when the films are deposited by spray technique. However, when the spray is carried out using two different solvents, the properties such as boiling point and viscosity could also influence the final thin film surface morphology. Viscosity of ethanol is .0011 PaS which differs from that of isopropanol (.0019 PaS)[79] even though the boiling point of the solvents are quite similar. In the present work, the difference in morphologies of the thin films have appeared as a combined effect of the solvent properties while spraying and the different particle sizes in each solvent. Porous kind surface morphology as noticed for the SnS_2 thin films is beneficial for applications such as detectors and energy storage. Morphology of the SnS_2 thin films deposited in the present work differs from the usual morphology obtained for SnS_2 films by conventional techniques such as thermal evaporation and dip coating where the films constitute lots of small grains [323, 344].

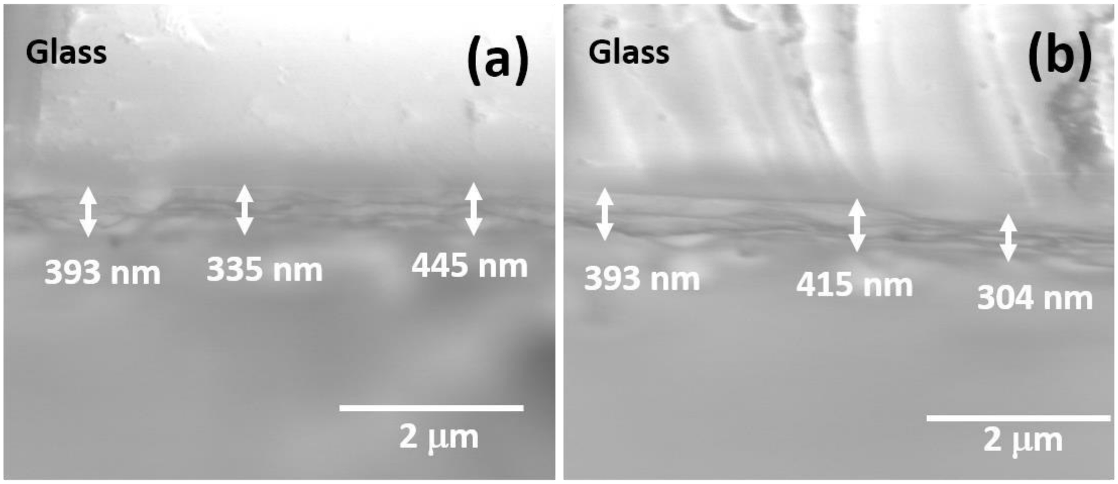

Fig.6.9. Cross-section SEM images of as prepared SnS_2 thin films deposited using (a) ethanol and (b) isopropanol as the solvents in PLAL. Adapted with permission [1] © 2018, Wiley

Enhanced surface area of the films also makes them promising candidates for electrochemical applications. Varying the laser ablation parameters or changing the liquid medium rules the composition and morphology of the generated particles while the substrate temperature, air pressure and rate of liquid flow during spray control interaction between the nanoparticles, adhesion and uniformity of the films on substrate. In the present study, all the parameters of spray deposition were maintained the same for both solvents and hence the morphology changes are primarily due to the SnS_2 nanoparticle morphologies by PLAL. Cross-section SEM images of the as prepared SnS_2 thin films are used to determine average thickness of the films (Fig. 6.9). SnS_2 thin film deposited using ethanol as solvent has an average thickness of 391 nm with standard deviation of 55 nm whereas for the film synthesized using isopropanol, it is 371±59 nm. Higher thickness of the film using ethanol liquid medium might have resulted from the higher average particle size of SnS_2 NPs in ethanol (8.3±1.2 nm) compared to that in isopropanol (6.5±1.2 nm).

Further characterization of the SnS_2 thin film morphology was done using atomic force microscopy (AFM). 2D and 3D AFM images of the as prepared SnS_2 thin films were recorded in contact error mode (figure 6.10) where the morphology difference in the films according to the change of liquid medium in PLAL is clearly seen. While SnS_2-ethanol thin film is constituted by lots of spherical particles, the particles connected each other forming like chains are observed for the films deposited using SnS_2 in isopropanol. However, in both cases, SnS_2 thin films possess a layered surface topography as seen from the AFM height images. Average surface roughness of the as prepared SnS_2 thin films deposited from SnS_2 in ethanol and isopropanol solvents were estimated from the AFM images. The films deposited using ethanol present an average surface roughness of 20.8 nm while the SnS_2-isopropanol films showed surface rougness of 43.6 nm. Three different areas were scanned on each sample and the mean roughness was taken. Hence, the films deposited using ethanol as solvent possess lower average surface roughness compared to the films deposited using isopropanol. Higher surface roughness of the SnS_2-isopropanol thin film can be attributed to the smaller average particle size of SnS_2 in isopropanol together with the solvent properties while spray deposition. The results show that the films synthesized by spraying laser ablated nanocolloids possess high surface roughness which could be attributed to the peculiarity of the combinatorial (PLAL-spray) synthesis method used. Since the thin films are deposited using nanocolloids, highly porous surfaces are formed depending on the morphology of the NPs in the solvents as well as the properties of the solvent. Such highly porous layered morphology is beneficial for electrochemical, charge storage and gas sensing applications.

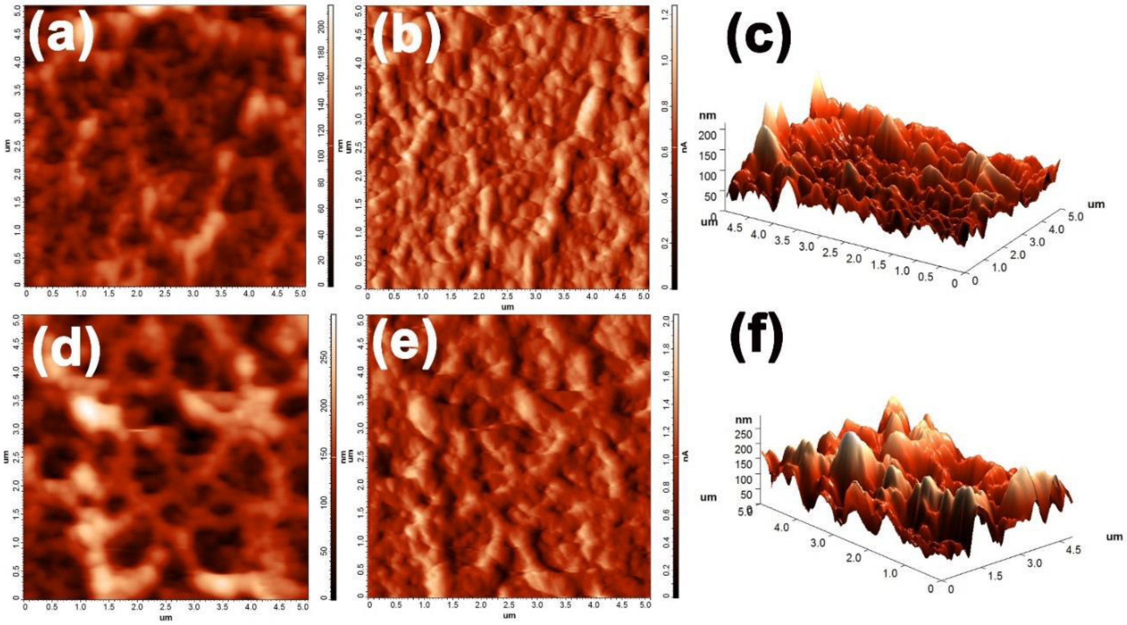

Fig.6.10. AFM (a,d) height, (b,e) DFL and (c,f) 3D images of as prepared SnS_2 thin films deposited from SnS_2 in (a,b,c) ethanol and (d,e,f) isopropanol. Adapted with permission [1] © 2018, Wiley

6.2.6 *Optical properties of SnS_2 thin films*

Absorption spectra of SnS_2 thin films were measured in the visible-NIR range (300-1200 nm). Absorption spectra and corresponding band gap plots of SnS_2 films prepared from ethanol and isopropanol are presented in fig. 6.11 (a-d). Absorption edge of all the SnS_2 films is located at around 500 nm irrespective of the solvent or the temperature used in post vacuum annealing. However, when the films are annealed at 300 °C, a small red shift in the absorption edge is noticed. This small shift could be better understood when comparing the band gaps of the as prepared and annealed SnS_2 thin films as depicted in Fig. 6.11 (b,d). The band gaps were estimated using the Tauc plot[345] relations and average film thicknesses obtained from cross-section SEM analysis. The calculated band gaps are 2.38, 2.37, 2.33 and 2.30 eVs respectively for the as prepared, 200, 250 and 300 °C annealed films for SnS_2 in ethanol whereas in isopropyl alcohol, the corresponding band gaps are

2.49, 2.6, 2.46 and 2.35 eVs for the as prepared and same temperature annealed thin films. The optical band gap is slightly red shifted when the annealing temperature is increased to 300 °C. But for the films synthesized from isopropanol, the band gap of the 200 °C annealed film is higher compared to the as deposited thin film and can be ascribed to slight morphological changes occurred during the vacuum annealing process.

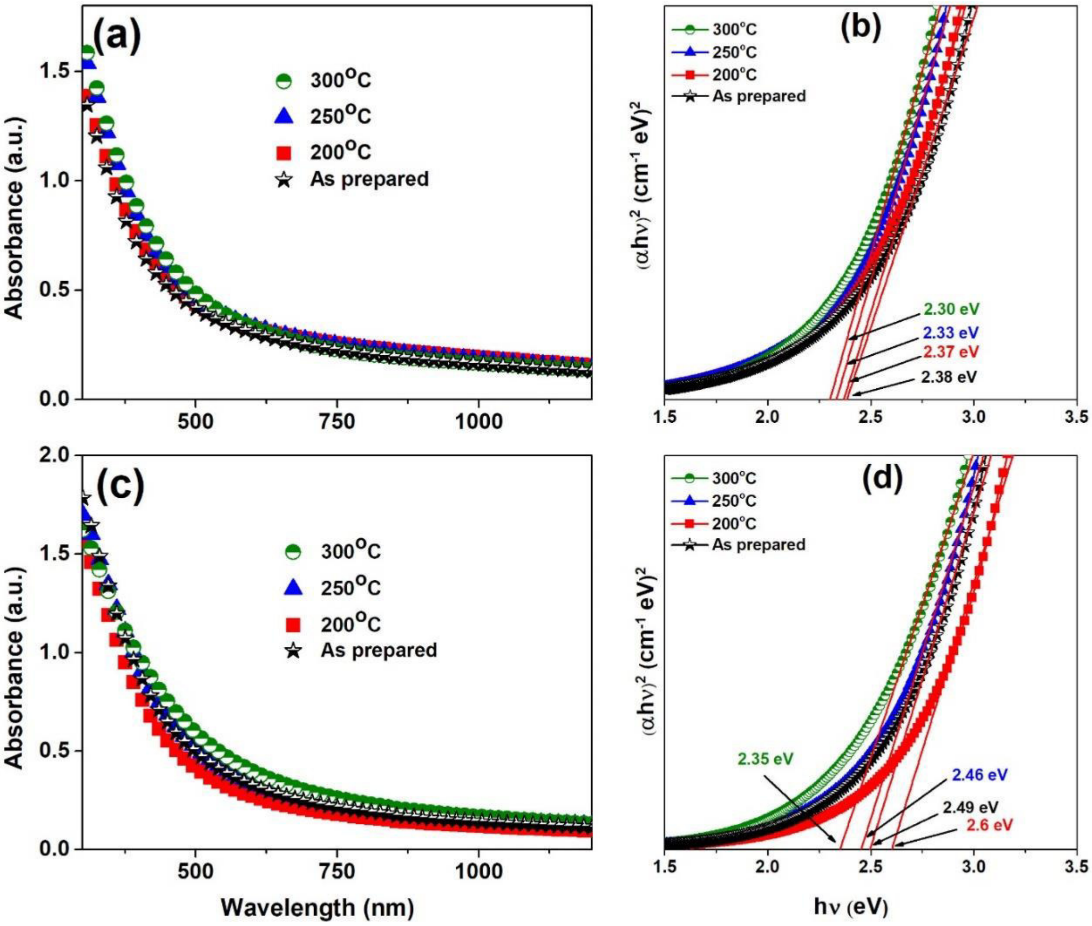

Fig.6.11. Optical absorption spectra and band gap plots of the as prepared and different temperature treated films synthesized using (a) ethanol and (b) isopropanol as the solvents in PLAL. Adapted with permission [1] © 2018, Wiley

On comparing the films deposited from SnS_2 in ethanol and isopropanol, all the films deposited from nanocolloids in isopropyl alcohol present higher band gaps compared to the respective SnS_2 film synthesized from ethanol. Variation in the band gap of SnS_2 according to a change in either the liquid medium or the annealing temperature could be related to the combined effect of small extent of SnS phase (especially at 300 °C annealing temperature) formation and morphological changes of the films. However, the percentage of such a SnS phase is not notable in comparison with the major SnS_2 phase as revealed by XRD, XPS and Raman analyses.

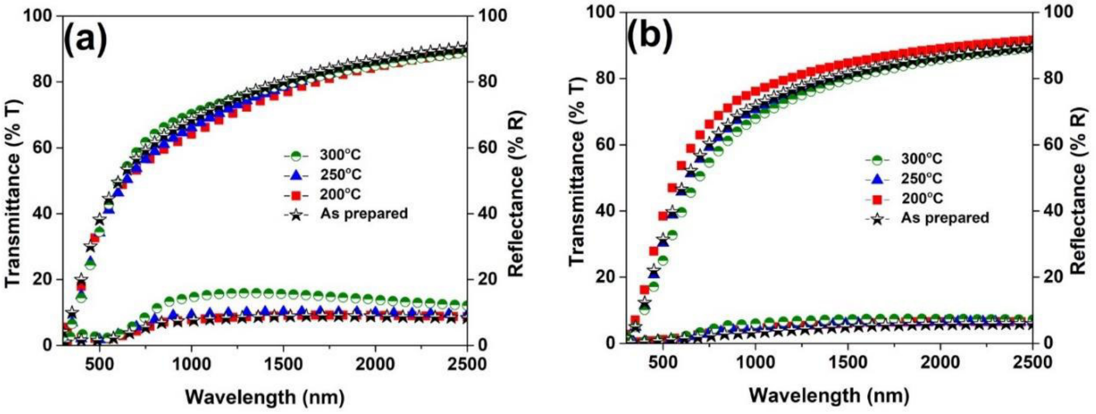

Fig.6.12. Optical transmittance and reflectance spectra for the as prepared and annealed SnS_2 thin films synthesized using (a) ethanol and (b) isopropanol as the solvents in PLAL. Adapted with permission [1] © 2018, Wiley

Hence, the band gap change could be primarily associated with the morphological changes occurred upon varying the liquid medium in PLAL as observed for the SnS thin films as well or with the post annealing temperature. The estimated optical band gap of the SnS_2 thin films deposited by combining PLAL and spray are comparable with literature band gap values as well as with band gap of bulk SnS_2 (2.2 eV)[287, 346]. Optical transmittance and reflectance spectra in the wavelength range of 300 to 2500 nm for the as prepared and annealed SnS_2 thin films synthesized from ethanol and isopropanol are presented in Fig. 6.12 (a, b). The films synthesized from ethanol and isopropanol showed similar optical behavior where all the films exhibit good transmittance in the near infrared (NIR) region which decreases gradually nearing the visible region.

Photoluminescence of the films were measured using excitation line of 345 nm and scanning the emission spectra in 400-600 nm using a PL spectrometer and the corresponding PL spectra are depicted in Fig. 6.13. All the SnS_2 thin films exhibited a strong emission peak centered at 485 nm together with a weak emission peak at 545 nm. For the SnS_2-ethanol films, PL quenching is observed as the annealing temperature was increased. In the case of SnS_2-isopropanol films, the as prepared, 200 and 250 °C annealed films showed similar emission intensities where the intensity was lower for the film processed at 300 °C. Multiple peaks observed in the PL spectra indicate that the films deposited from SnS_2 nanocolloids might have different defect levels. While the emission peak at 485 nm is assigned to radiative recombination of generated electrons at higher excited energy levels upon excitons absorption, the peak at 545 is due to the radiative recombination of quantum confined electron-hole pair with energy lower than the band gap energy of SnS_2 particles.

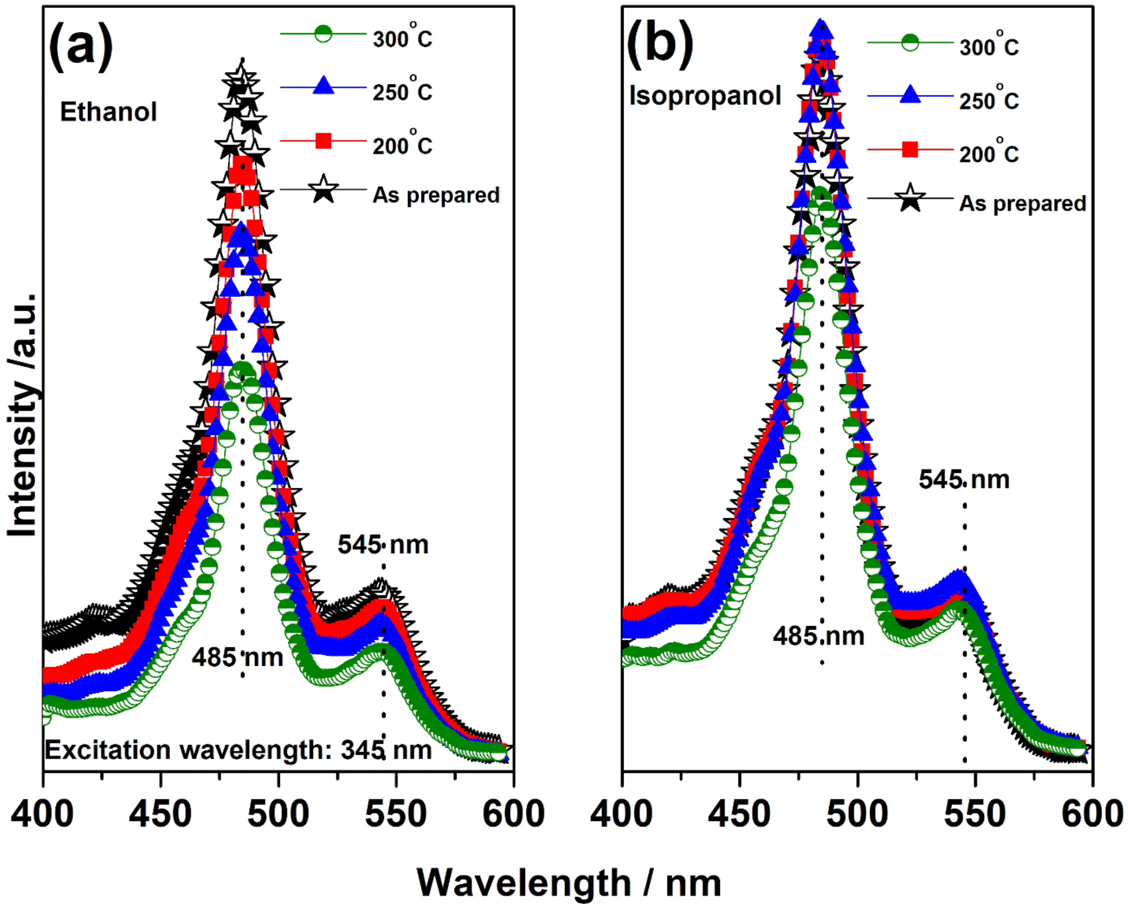

Fig.6.13. Photoluminescence spectra of the as prepared and annealed SnS_2 thin films deposited using (a) ethanol and (b) isopropanol as the solvents in PLAL. Adapted with permission [1] © 2018, Wiley

Similar emission spectra were observed for SnS_2 nanomaterials as reported previously[79, 335, 347]. For the film deposited from SnS_2 in ethanol, the PL quenching occurred at all annealing temperature might be attributed to the slight changes in morphology of the films. Higher PL quenching of the films annealed at 300 °C could be due to the presence of some amorphous SnS phase in the films. The decrease in sulfur content with higher annealing temperature could also be leading to a lower PL intensity as reported [348]. Band gap values and emission peaks of the SnS_2 films are given in table 6.2.

Table.6.2. Band gaps and emission peaks of as prepared and annealed SnS_2 thin films

Sample	Heat treatment	Band gap (eV)	Emission peak (nm)
SnS_2 (ethanol)	As prepared	2.38	485,545
	200°C	2.37	
	250°C	2.33	
	300°C	2.30	
SnS_2 (Isopropanol)	As prepared	2.49	
	200°C	2.6	
	250°C	2.46	
	300°C	2.35	

6.2.7 *Opto-electronic properties of SnS_2 thin films*

I-V curves of all SnS_2 thin films were measured in the voltage range 5-100 V at equal steps of 5V in dark and under illumination from a blue LED (50 W, 450-460 nm) light source (Fig.6.14 a, c). All SnS_2 films show linear I-V curves regardless of the solvent and post annealing temperatures used indicating the ohmic behavior of the films. Even though the as prepared, 200 and 250 °C annealed films, the I-V curves under dark and under light do not show significant variations, for the SnS_2 thin film post annealed at 300 °C, the current increased significantly upon illumination due to the generation of more charge carriers due to the absorption of photons from the incident light by the SnS_2. When the I-V curves of the samples deposited from the two solvents are compared one to another, the films deposited from SnS_2 nanoparticles dispersed in ethanol is more conductive than the films deposited using isopropanol as the PLAL solvent. This is probably due to the more compactness of SnS_2 films in ethanol than in isopropanol as identified from the SEM images which may produce better contact between individual particles. Photoconductivity tests were carried out for the 300 °C annealed SnS_2 thin films by simultaneously applying a bias voltage of 100 V and measuring the current between the painted Ag electrodes on the film surface. Relatively high bias voltage was used since the films were highly resistive and no measurable photoresponse was noticed at lower applied voltages. In addition to this, the as prepared and other temperature processed SnS_2 samples were not at all photoconductive owing to the highly resistive nature of those films. During the measurements, the samples were illuminated using the same LED light source used in the I-V measurements in light to study the photoresponse behavior of these films. The samples were first kept 20 sec. in dark followed by 20 sec. under blue light illumination and finally again 20 sec. in dark.

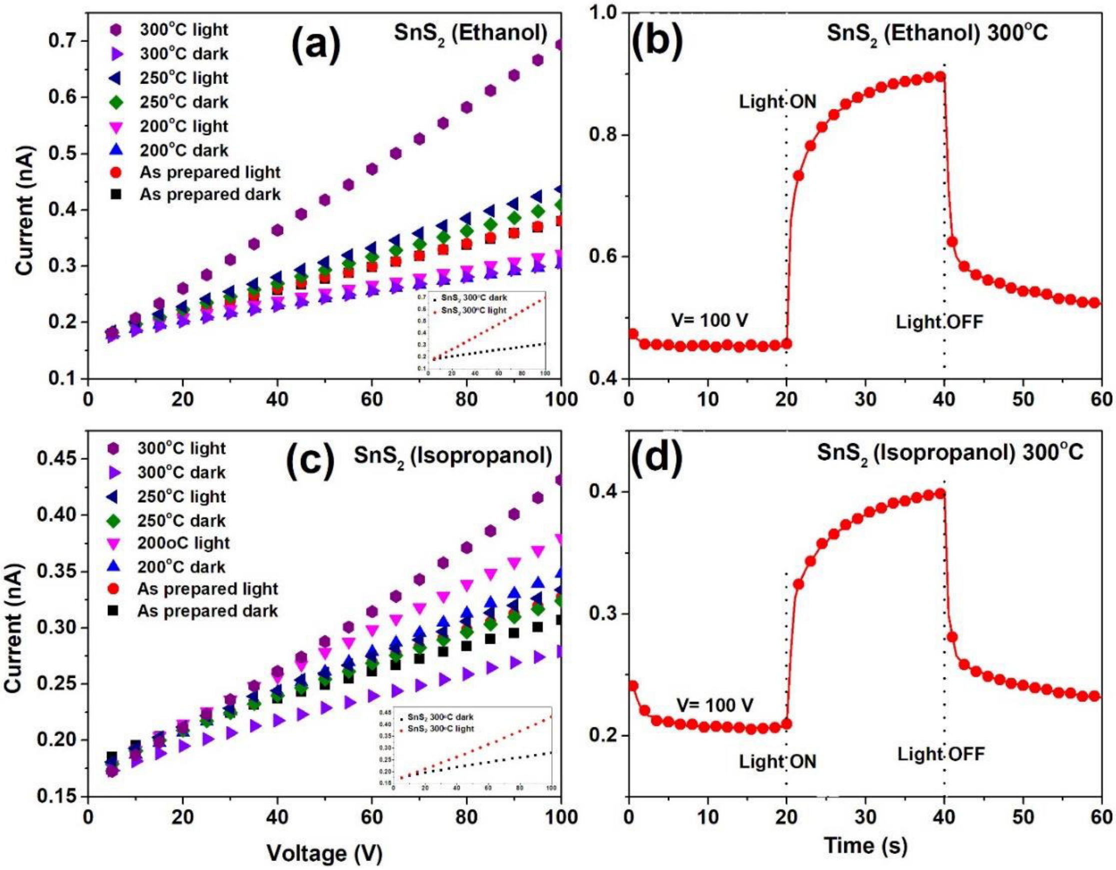

Fig.6.14. I-V curves of the as prepared and annealed SnS_2 thin films synthesized using SnS_2 nanocolloids in (a) ethanol and (c) isopropanol under dark and illumination from a blue LED source. Insets show the I-V curves of the 300 °C annealed samples under dark and light for the corresponding solvents. (b, d) Photoresponse of SnS_2 300 °C annealed sample using the same LED light source. Adapted with permission [1] © 2018, Wiley

The corresponding photoresponse curves of both samples annealed at 300 °C are presented in Fig.6.14 (b, d). Both SnS_2 films (annealed at 300 °C) show good photoresponse as the measured current shows an increase upon illumination by the blue wavelength LED source. Both I-V measurements in dark and light as well as photoresponse support the light assisted electrochemical tests conducted where the 300 °C annealed SnS_2 thin films showed enhanced performance (see the following section).

6.2.8 *Electrochemical properties of SnS_2 thin films*

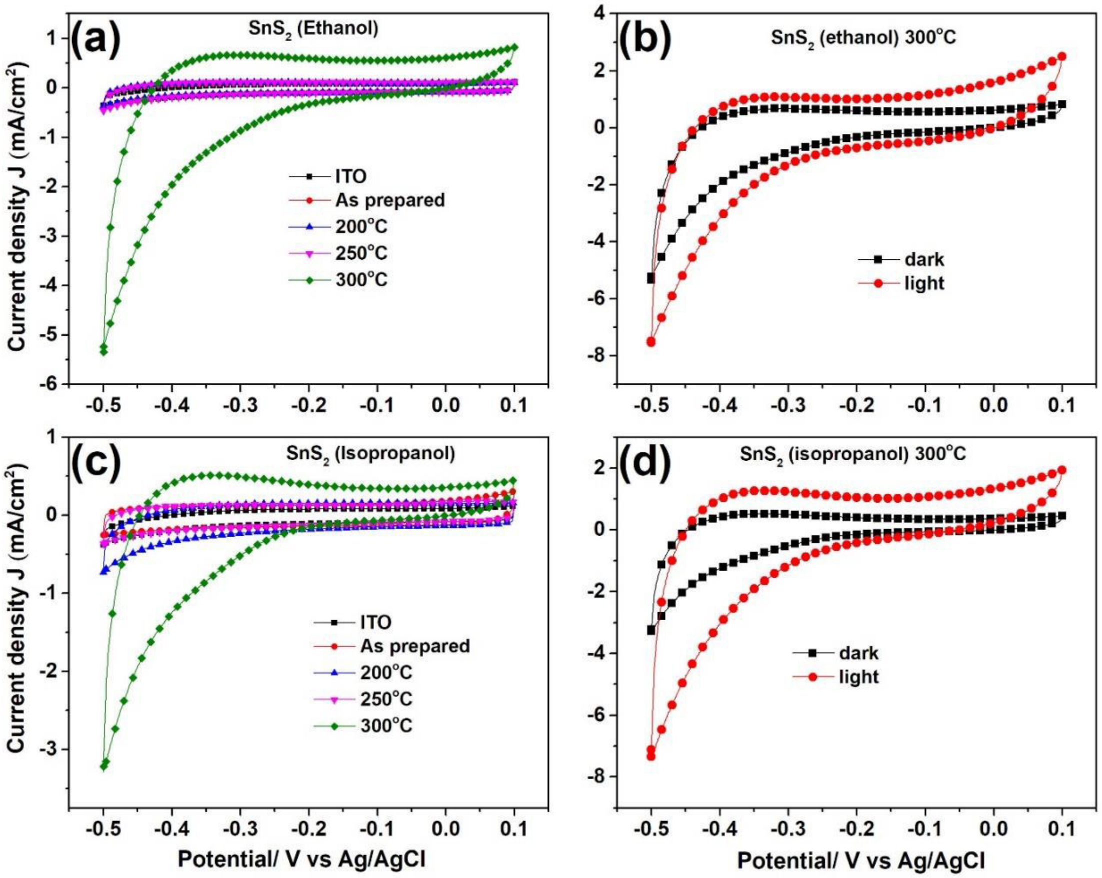

Fig.6.15. Cyclic voltammograms of ITO substrate, as prepared and annealed SnS_2 thin films using (a) ethanol and (b) isopropanol as the solvents in PLAL in 0.1M KCl at a scanning rate of 50 mV/s. Cyclic voltammograms of SnS_2 300 °C annealed thin film electrode. Adapted with permission [1] © 2018, Wiley

Cyclic voltammograms (CVs) were recorded to explore electrochemical properties of the films using the SnS_2 thin films coated on ITO as the working electrodes. All the cyclic voltammograms presented are from the second measured cycle and the scannings were performed after 5 minutes of nitrogen purging to the electrolyte. CVs of all as prepared and annealed SnS_2 thin films in 0.1M KCl at a scanning rate of 50 mV/s as well as the light assisted CVs of 300 °C annealed SnS_2 samples are presented in fig. 6.15. The as prepared, 200 and 250 °C annealed SnS_2 films show a rectangular shaped CV indicating the purely capacitive nature of these thin film electrodes. High surface area of the films originated from the porous surface and layered morphology make the SnS_2 based electrodes more electroactive and thus account for the increased width of the CV curves of SnS_2 thin films in comparison with bare ITO substrate. In both ethanol and isopropanol, the 300 °C annealed SnS_2 thin films show a different electrochemical nature compared to that of the as prepared and other temperature annealed samples. Higher magnitude current density at -0.5V was observed for the SnS_2 films annealed at 300 °C suggesting that these films are suitable for electrolysis reactions. Porous surface morphology of the SnS_2 thin films is beneficial for increasing the surface area as well as for good adhesion of the ions from the electrolyte on the electrode. Photoelectrochemical performance of the 300 °C treated sample was conducted by illuminating the electrode using an LED source (same LED used for photoresponse) and scanning the voltage from -0.5V to 0.1V. The obtained results are presented in Fig. 6.15 (b, d).

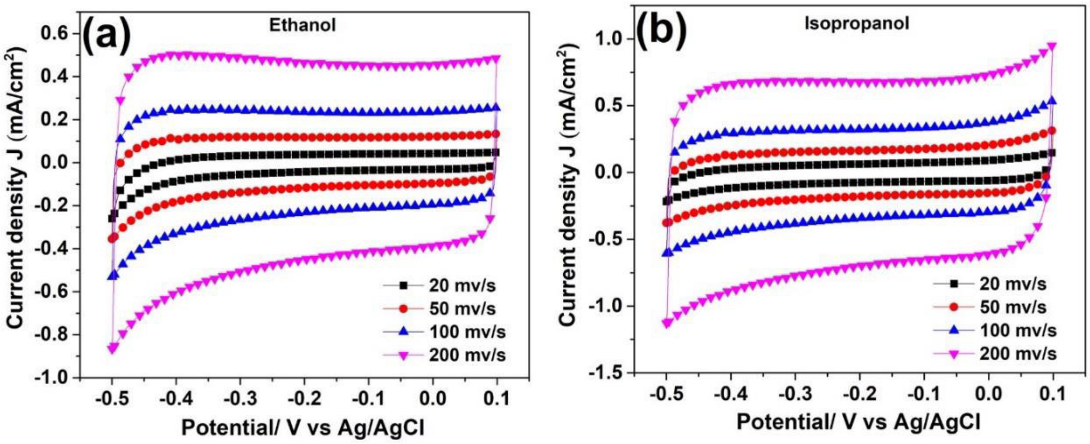

Fig.6.16. Cyclic voltammograms of as prepared SnS_2 thin film electrodes synthesized using (a) ethanol and (b) isopropanol as the solvents in PLAL in 0.1M KCl at different scanning rates viz. 20, 50, 100 and 200 mV/s. Adapted with permission [1] © 2018, Wiley

SnS_2 thin film electrodes show enhanced capacitance upon illumination as compared to that in dark. The current at -0.5 V is shifted towards positive voltage and lowered when the electrodes are illuminated. Improved electrochemical activity of the films while illumination is attributed to the generation of more charge carriers in the electrodes by absorbing photons from the incident light. Minor presence of SnS having p-type conductivity and high absorption coefficient in contrast to the n-type conductivity of SnS_2, can also contribute to the improved electro activity of films upon illumination. Fig. 6.16 shows the CVs of the as prepared SnS_2 thin films at different scan rates from 20 mV/s to 200 mV/s. CV analysis showed that the SnS_2 thin films synthesized by spraying laser ablated SnS_2 nanocolloids are promising candidates in electrochemical applications where the electrochemical activity can be tuned by adjusting the post annealing temperature. Distinct electrochemical behavior of the annealed SnS_2 thin film in dark and in light suggests that these films can be used in photoelectrochemical applications as well. Stability of the SnS_2 thin film electrodes was verified by continuously measuring 50 CV cycles. The corresponding CVs for the as prepared SnS_2 films are presented in Fig. 6.17. The measured

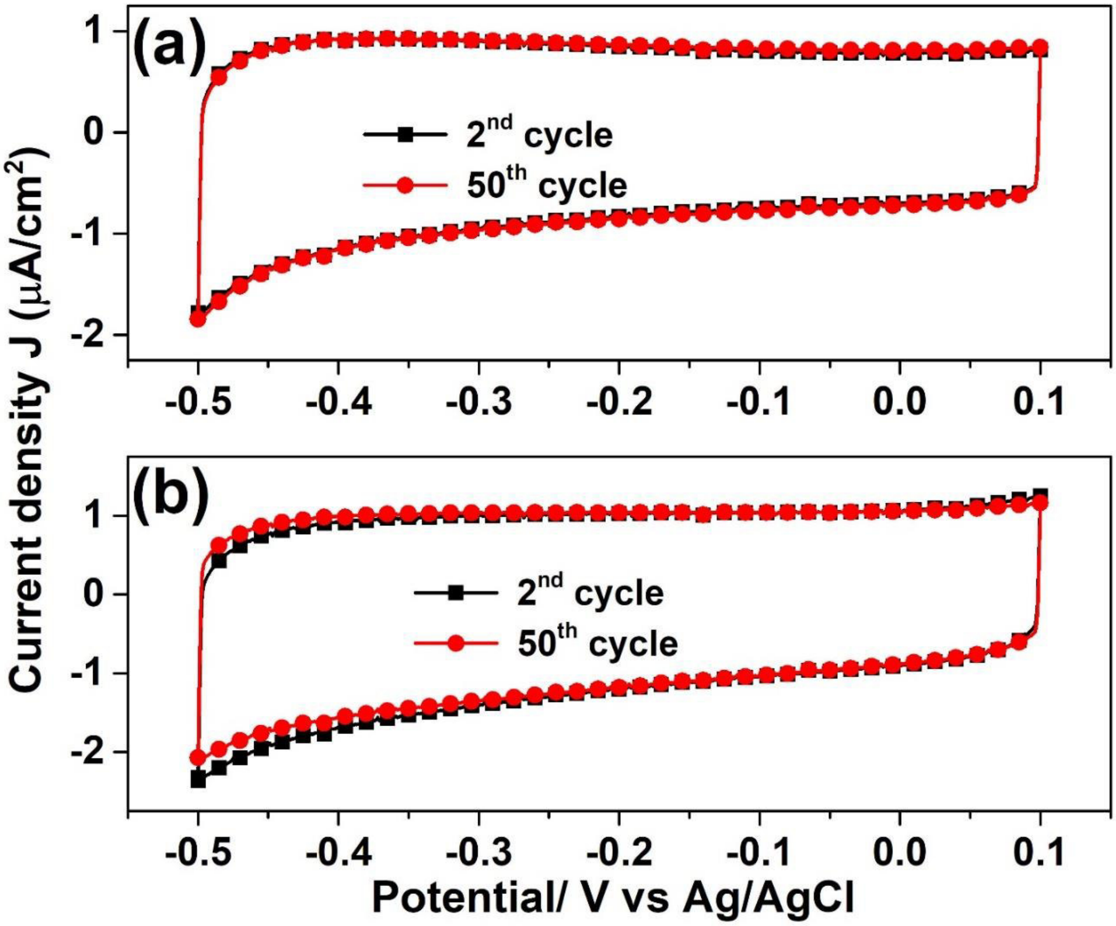

Fig.6.17. Cyclic voltammograms of the as prepared SnS_2 thin films using (a) ethanol and (b) isopropanol as the solvents in PLAL measured for 50 continuous cycles at 50mV/s in 0.1M KCl. Adapted with permission [1] © 2018, Wiley

current at corresponding potential values are almost the same for 2nd and 50th cycles which indicate that the SnS_2 electrodes prepared by spray deposition of laser ablated nanocolloids are stable in the given electrolyte and hence could be a suitable choice for electrochemical applications.

6.3 Conclusions

SnS_2 thin films were deposited by combining PLAL with spray deposition technique. The SnS_2 NPs were obtained in two different solvents of which the effect on thin film morphology was investigated in addition to the influence of post annealing temperatures on the film properties. GIXRD, Raman and XPS analyses were respectively used for confirming the Hexagonal crystal structure, 2-H polytype structure and chemical states of these films. Porous layered surface morphology of the films was identified using FESEM and the morphology found to depend on the liquid medium in PLAL. Depending on the solvent and annealing temperatures, band gap of the films varied from 2.3 eV to 2.6 eV. All the films presented PL emission in the blue-green region. Electrochemical and photoelectrochemical tests showed their electroactive nature and enhancement in the electroactivity upon illumination. I-V measurements conducted in dark and light with photoresponse measurements support the photoelectrochemical tests where the 300 °C annealed SnS_2 thin films showed better performance compared to others.

General conclusions and outlook

This thesis presents synthesis and characterization of nanoparticles of tin monosulfide (SnS) and tin disulfide (SnS_2) by pulsed laser ablation in liquid (PLAL) and their thin films obtained by spray technique from laser ablated nanocolloids. Their applications in opto-electronic, electrochemical and photovoltaic fields are also explored during this thesis work. PLAL was effectively used to synthesize ligand-free SnS and SnS_2 semiconducting nanoparticles. Effects of different laser wavelengths, ablation fluence and nature of liquid media on the morphology, structure and optical properties of the produced NPs were investigated systematically. It was found that, all the lasing parameters such as wavelength, repetition rate, fluence and focusing conditions significantly influence the final NPs morphology in PLAL. Simultaneously, different solvent properties like polarity, viscosity, density, thermal conductivity and heat capacity also play important roles in the formation of the NPs. Hence any change in these parameters may lead to the generation of particles with different morphology or properties or both. This opens a way to tune the desired properties of different nanomaterials synthesized by PLAL simply by adjusting either the lasing parameters or by controlling the solvent properties. For SnS and SnS_2 NPs synthesized by PLAL, the NPs generated at different conditions were of slightly different morphologies and properties. For instance, while spherical SnS_2 NPs with well-defined boundaries were formed by ablation using a 1064 nm, 10 Hz laser, particles with less defined boundaries and interconnected each other were yielded by 532 nm laser ablation. In all cases, the NP morphology was determined by TEM analysis including HRTEM and SAED for the information on the crystal structure. Moreover, the optical band gaps of the NPs were also varied mainly due to the differences in the particle morphology. In addition to the effects of liquid medium and laser wavelength studies conducted on SnS_2 NPs, influences of ablation fluence, liquid medium temperature and laser post irradiation were also studied. Particles with different morphologies were yielded in each case and the morphology change was exploited for hydrogen evolution reaction on such obtained SnS_2 particles thereby exploring the laser synthesized SnS_2 NPs as catalysts for hydrogen production. Furthermore, the HER activity increased upon illuminating the SnS_2 based electrode by a blue LED light source. SnS_2 particles were also photoluminescent in the blue-green region which can be primarily attributed to the synthesis method where extreme plasma conditions and rapid quenching plays important roles.

After preparing the nanocolloidal suspensions, thin films of the same were deposited by spraying the colloids onto heated substrates. Such formed thin films showed totally different surface morphologies compared to the films deposited using other conventional methods. In addition to that, when the thin films are directly formed from the colloidal nanoparticles, they are generally crystalline in the as prepared form itself and the film deposition can be achieved at much lower temperatures depending on the evaporation temperature of the solvent used. SnS thin films obtained in this way were having a layered porous surface morphology and the same crystal structure and phase as that of the NPs. Morphology and properties of the SnS films were also influenced by the liquid medium used in PLAL as the particles were generated in DMF and isopropanol using laser ablation and thin films from both were fabricated. To show the device applicability of thin films obtained by combinatorial PLAL-spray technique, nanocomposite thin films of SnS and reduced graphene oxide were fabricated and incorporated in photovoltaic device as glass/ITO/CdS/Sb_2S_3/SnS(DMF):rGO. The best solar cell consisting an SnS:rGO layer as the absorber showed a maximum photoconversion efficiency of 2.32% in comparison with the highest ever reported 4.4% efficiency of SnS based solar cells. Electrochemical and opto-electronic properties of the films were increased by incorporating rGO into the SnS matrix and a spongy-type porous surface morphology was identified.

SnS_2 thin films were also deposited using laser ablated SnS_2 NPs in ethanol and isopropanol where the structure, morphology, elemental composition and chemical state and optical, opto-electronic and electrochemical properties were analyzed by means of XRD, SEM, XPS, photoresponse measurements and electrochemical tests. The films were having a 2-H polytype structure and layered morphology as identified by Raman and SEM analyses respectively. As either the liquid medium in PLAL or post annealing temperature was varied, the films showed different optical band gaps in the range 2.3 eV to 2.6 eV. The films annealed at $300^{o}C$ showed photoresponse under blue wavelength illumination and hence enhanced electroactivity under the same wavelength illumination.

A different kind of method for thin film deposition and device fabrication was developed by combining PLAL and spray techniques. These films were crystalline with special morphologies and unique properties for different applications including photovoltaics. The method used is relatively green, fast and cost effective. Owing to the features of both PLAL and spray technique, it can produce high quality thin films in large areas including nanocomposites. Since the properties and phase of thin films are predetermined by the composition, morphology and properties of laser generated NPs, the involved thin film formation method is less complicated and therefore can be applied to any similar system. The combinatorial method employed can be easily extended towards other nanocomposites, hybrids and functional nanomaterials and hence underlines the future scope of the thesis work. Such fabricated thin films may find potential applications in various fields such as photodetectors, solar cells, sensors and energy storage keeping cost effectiveness and simplicity of the method as the major advantages.

References

1. Johny, J., et al., *Nanostructured SnS2 Thin Films from Laser Ablated Nanocolloids: Structure, Morphology, Optoelectronic and Electrochemical Properties.* ChemPhysChem, 2018. **19**(21): p. 2902-2914.
2. Johny, J., et al., *Synthesis and Properties of Tin Sulfide Thin Films from Nanocolloids Prepared by Pulsed Laser Ablation in Liquid.* ChemPhysChem, 2017. **18**(9): p. 1061-1068.
3. Bhushan, B., *Springer handbook of nanotechnology*. 2017: Springer.
4. Cao, G., *Nanostructures & nanomaterials: synthesis, properties & applications*. 2004: Imperial college press.
5. Ramsden, J., *Nanotechnology: an introduction (micro and nano technologies).* William Andrew, 2011.
6. Das, B., S. Subramaniam, and M.R. Melloch, *Effects of electron-beam-induced damage on leakage currents in back-gated GaAs/AlGaAs devices.* Semiconductor Science and Technology, 1993. **8**(7): p. 1347.
7. Vieu, C., et al., *Electron beam lithography: resolution limits and applications.* Applied Surface Science, 2000. **164**(1): p. 111-117.
8. Bruus, H., *Introduction to nanotechnology*. 2004: Department of Micro and Nanotechnology, Technical University of Denmark.
9. Watt, F., et al., *Ion beam lithography and nanofabrication: a review.* International Journal of Nanoscience, 2005. **4**(03): p. 269-286.
10. Stulen, R.H. and D.W. Sweeney, *Extreme ultraviolet lithography.* Optics and Photonics News, 1999. **10**(8): p. 34-38.
11. Piner, R.D., et al., *" Dip-pen" nanolithography.* science, 1999. **283**(5402): p. 661-663.
12. Liu, G.-Y., S. Xu, and Y. Qian, *Nanofabrication of self-assembled monolayers using scanning probe lithography.* Accounts of Chemical Research, 2000. **33**(7): p. 457-466.
13. Mackenzie, J.D., *Applications of the sol-gel process.* Journal of Non-Crystalline Solids, 1988. **100**(1-3): p. 162-168.
14. Pierson, H.O., *Handbook of chemical vapor deposition: principles, technology and applications*. 1999: William Andrew.
15. Mattox, D.M., *Handbook of physical vapor deposition (PVD) processing*. 2010: William Andrew.
16. Singh, S.C., et al., *Nanomaterials: processing and characterization with lasers*. 2012: John Wiley & Sons.
17. Chrisey, D.B. and G.K. Hubler, *Pulsed laser deposition of thin films.* 1994.
18. Eason, R., *Pulsed laser deposition of thin films: applications-led growth of functional materials*. 2007: John Wiley & Sons.
19. Sun, X. and H.S. Kwok, *Optical properties of epitaxially grown zinc oxide films on sapphire by pulsed laser deposition.* Journal of applied physics, 1999. **86**(1): p. 408-411.
20. Li, S., S.J. Silvers, and M.S. El-Shall, *Surface Oxidation and Luminescence Properties of Weblike Agglomeration of Silicon Nanocrystals Produced by a Laser*

Vaporization− Controlled Condensation Technique. The Journal of Physical Chemistry B, 1997. **101**(10): p. 1794-1802.

21. Glaspell, G.P., P.W. Jagodzinski, and A. Manivannan, *Formation of cobalt nitrate hydrate, cobalt oxide, and cobalt nanoparticles using laser vaporization controlled condensation.* The Journal of Physical Chemistry B, 2004. **108**(28): p. 9604-9607.
22. Allen, S., *Laser chemical vapor deposition: A technique for selective area deposition.* Journal of Applied Physics, 1981. **52**(11): p. 6501-6505.
23. Baum, T.H. and C.R. Jones, *Laser chemical vapor deposition of gold.* Applied Physics Letters, 1985. **47**(5): p. 538-540.
24. Houle, F., et al., *Laser chemical vapor deposition of copper.* Applied Physics Letters, 1985. **46**(2): p. 204-206.
25. Veintemillas-Verdaguer, S., M. Morales, and C. Serna, *Continuous production of γ-Fe2O3 ultrafine powders by laser pyrolysis.* Materials Letters, 1998. **35**(3-4): p. 227-231.
26. Yang, G., *Laser ablation in liquids: applications in the synthesis of nanocrystals.* Progress in Materials Science, 2007. **52**(4): p. 648-698.
27. Yang, G., *Laser ablation in liquids: principles and applications in the preparation of nanomaterials*. 2012: CRC Press.
28. Lowndes, D.H., et al., *Synthesis of novel thin-film materials by pulsed laser deposition.* Science, 1996. **273**(5277): p. 898-903.
29. Zhong, Z.J., *Optical properties and spectroscopy of nanomaterials*. 2009: World Scientific.
30. Kelly, K.L., et al., *The Optical Properties of Metal Nanoparticles: The Influence of Size, Shape, and Dielectric Environment.* The Journal of Physical Chemistry B, 2003. **107**(3): p. 668-677.
31. Lue, J.T., *Physical properties of nanomaterials.* Encyclopedia of nanoscience and nanotechnology, 2007. **10**(1): p. 1-46.
32. Davis, S., *Biomedical applications of nanotechnology—implications for drug targeting and gene therapy.* Trends in biotechnology, 1997. **15**(6): p. 217-224.
33. Labhasetwar, V. and D.L. Leslie-Pelecky, *Biomedical applications of nanotechnology*. 2007: John Wiley & Sons.
34. Holm, B.A., et al., *Nanotechnology in biomedical applications.* Molecular Crystals and Liquid Crystals, 2002. **374**(1): p. 589-598.
35. Parak, W.J., *WJ Parak, D. Gerion, T. Pellegrino, D. Zanchet, C. Micheel, SC Williams, R. Boudreau, MA Le Gros, CA Larabell, and AP Alivisatos, Nanotechnology 14, R15 (2003).* Nanotechnology, 2003. **14**: p. R15.
36. Tseng, G.Y. and J.C. Ellenbogen, *Toward nanocomputers.* Science, 2001. **294**(5545): p. 1293-1294.
37. Schön, J.H., H. Meng, and Z. Bao, *correction: Self-assembled monolayer organic field-effect transistors.* Nature, 2001. **414**(6862): p. 470.
38. Mahler, G., V. May, and M. Schreiber, *Molecular electronics: properties, Dynamics, and Applications*. 1996: Marcel Dekker.
39. Fan, Z., et al., *ZnO nanowire field-effect transistor and oxygen sensing property.* Applied Physics Letters, 2004. **85**(24): p. 5923-5925.
40. Yang, G., et al., *Single electron tunneling and manipulation of nanoparticles on surfaces at room temperature.* Surface science, 2005. **589**(1-3): p. 129-138.

41. Collier, C.P., et al., *Photochemical Response of Electronically Reconfigurable Molecule-Based Switching Tunnel Junctions.* ChemPhysChem, 2002. **3**(5): p. 458-461.
42. Tans, S.J., A.R. Verschueren, and C. Dekker, *Room-temperature transistor based on a single carbon nanotube.* Nature, 1998. **393**(6680): p. 49.
43. Park, J., et al., *Coulomb blockade and the Kondo effect in single-atom transistors.* Nature, 2002. **417**(6890): p. 722.
44. Hodes, G., I. Howell, and L. Peter, *Nanocrystalline photoelectrochemical cells a new concept in photovoltaic cells.* Journal of the Electrochemical Society, 1992. **139**(11): p. 3136-3140.
45. Minoux, E., et al., *Achieving high-current carbon nanotube emitters.* Nano Letters, 2005. **5**(11): p. 2135-2138.
46. Bhushan, B., *Nanotribology and nanomechanics.* Wear, 2005. **259**(7-12): p. 1507-1531.
47. Porod, W., *Quantum-dot devices and quantum-dot cellular automata.* Journal of the Franklin Institute, 1997. **334**(5-6): p. 1147-1175.
48. Daniel, M.-C. and D. Astruc, *Gold nanoparticles: assembly, supramolecular chemistry, quantum-size-related properties, and applications toward biology, catalysis, and nanotechnology.* Chemical reviews, 2004. **104**(1): p. 293-346.
49. Liu, L., Z. Han, and S. He, *Novel surface plasmon waveguide for high integration.* Optics Express, 2005. **13**(17): p. 6645-6650.
50. Joannopoulos, J.D., P.R. Villeneuve, and S. Fan, *Photonic crystals.* Solid State Communications, 1997. **102**(2-3): p. 165-173.
51. Theodore, H.M., *Stimulated optical radiation in ruby.* Nature, 1960. **187**: p. 493-94.
52. Zeng, H., et al., *Nanomaterials via laser ablation/irradiation in liquid: a review.* Advanced Functional Materials, 2012. **22**(7): p. 1333-1353.
53. Fojtik, A. and A. Henglein, *Laser ablation of films and suspended particles in a solvent: formation of cluster and colloid solutions.* Berichte der Bunsen-Gesellschaft, 1993. **97**(2): p. 252-254.
54. Neddersen, J., G. Chumanov, and T.M. Cotton, *Laser ablation of metals: a new method for preparing SERS active colloids.* Applied Spectroscopy, 1993. **47**(12): p. 1959-1964.
55. Zhang, D., B. Gökce, and S. Barcikowski, *Laser synthesis and processing of colloids: fundamentals and applications.* Chemical reviews, 2017. **117**(5): p. 3990-4103.
56. Barcikowski, S. and G. Compagnini, *Advanced nanoparticle generation and excitation by lasers in liquids.* Physical Chemistry Chemical Physics, 2013. **15**(9): p. 3022-3026.
57. J. Radziemski, L. and D. A. Cremers, *Laser-Induced Plasmas and Applications*. 1989.
58. Sakka, T., et al., *Laser ablation at solid–liquid interfaces: an approach from optical emission spectra.* The Journal of Chemical Physics, 2000. **112**(19): p. 8645-8653.
59. Lam, J., et al., *γ-Al 2 O 3 nanoparticles synthesised by pulsed laser ablation in liquids: a plasma analysis.* Physical Chemistry Chemical Physics, 2014. **16**(3): p. 963-973.

60. Kim, K.K., et al., *Laser ablation dynamics in liquid phase: The effects of magnetic field and electrolyte.* Journal of Applied Physics, 2015. **117**(7): p. 074302.
61. Dell'Aglio, M., et al., *Mechanisms and processes of pulsed laser ablation in liquids during nanoparticle production.* Applied Surface Science, 2015. **348**: p. 4-9.
62. De Giacomo, A., et al., *Plasma processes and emission spectra in laser induced plasmas: A point of view.* Spectrochimica Acta Part B: Atomic Spectroscopy, 2014. **100**: p. 180-188.
63. Casavola, A., et al., *Experimental investigation and modelling of double pulse laser induced plasma spectroscopy under water.* Spectrochimica Acta Part B: Atomic Spectroscopy, 2005. **60**(7): p. 975-985.
64. Petkovšek, R., J. Možina, and G. Močnik, *Optodynamic characterization of the shock waves after laser-induced breakdown in water.* Optics Express, 2005. **13**(11): p. 4107-4112.
65. Vogel, A., S. Busch, and U. Parlitz, *Shock wave emission and cavitation bubble generation by picosecond and nanosecond optical breakdown in water.* The Journal of the Acoustical Society of America, 1996. **100**(1): p. 148-165.
66. Baghdassarian, O., et al., *Spectrum of Luminescence from Laser-Created Bubbles in Water.* Physical Review Letters, 2001. **86**(21): p. 4934-4937.
67. Wolfrum, B., et al., *Shock wave induced interaction of microbubbles and boundaries.* Physics of Fluids, 2003. **15**(10): p. 2916-2922.
68. Noack, J., et al., *Influence of pulse duration on mechanical effects after laser-induced breakdown in water.* Journal of Applied Physics, 1998. **83**(12): p. 7488-7495.
69. Ward, B. and D.C. Emmony, *Direct observation of the pressure developed in a liquid during cavitation-bubble collapse.* Applied Physics Letters, 1991. **59**(18): p. 2228-2230.
70. Kennedy, P.K., D.X. Hammer, and B.A. Rockwell, *Laser-induced breakdown in aqueous media.* Progress in Quantum Electronics, 1997. **21**(3): p. 155-248.
71. Shih, C.-Y., et al., *Atomistic modeling of nanoparticle generation in short pulse laser ablation of thin metal films in water.* Journal of colloid and interface science, 2017. **489**: p. 3-17.
72. Jendrzej, S., et al., *Barrierless growth of precursor-free, ultrafast laser-fragmented noble metal nanoparticles by colloidal atom clusters–A kinetic in situ study.* Journal of colloid and interface science, 2016. **463**: p. 299-307.
73. Ibrahimkutty, S., et al., *A hierarchical view on material formation during pulsed-laser synthesis of nanoparticles in liquid.* Scientific reports, 2015. **5**: p. 16313.
74. Gamaly, E.G., et al., *Ablation of solids by femtosecond lasers: Ablation mechanism and ablation thresholds for metals and dielectrics.* Physics of plasmas, 2002. **9**(3): p. 949-957.
75. Kim, J., et al., *The influence of laser wavelength and fluence on palladium nanoparticles produced by pulsed laser ablation in deionized water.* Solid State Sciences, 2014. **37**: p. 96-102.
76. Tsuji, T., et al., *Preparation of metal colloids by a laser ablation technique in solution: influence of laser wavelength on the ablation efficiency (II).* Journal of Photochemistry and Photobiology A: Chemistry, 2001. **145**(3): p. 201-207.

77. Solati, E., M. Mashayekh, and D. Dorranian, *Effects of laser pulse wavelength and laser fluence on the characteristics of silver nanoparticle generated by laser ablation.* Applied Physics A, 2013. **112**(3): p. 689-694.
78. Giorgetti, E., et al., *Stable gold nanoparticles obtained in pure acetone by laser ablation with different wavelengths.* Journal of Nanoparticle Research, 2012. **14**(1): p. 648.
79. Johny, J., et al., *Facile and fast synthesis of SnS2 nanoparticles by pulsed laser ablation in liquid.* Applied Surface Science, 2018. **435**: p. 1285-1295.
80. García Guillén, G., et al., *Effects of Liquid Medium and Ablation Wavelength on the Properties of Cadmium Sulfide Nanoparticles Formed by Pulsed-Laser Ablation.* ChemPhysChem, 2017. **18**(9): p. 1035-1046.
81. Intartaglia, R., K. Bagga, and F. Brandi, *Study on the productivity of silicon nanoparticles by picosecond laser ablation in water: towards gram per hour yield.* Optics express, 2014. **22**(3): p. 3117-3127.
82. Sajti, C.L., et al., *Ablation efficiency of α-Al 2 O 3 in liquid phase and ambient air by nanosecond laser irradiation.* Applied Physics A, 2010. **100**(1): p. 203-206.
83. Menéndez-Manjón, A., P. Wagener, and S. Barcikowski, *Transfer-matrix method for efficient ablation by pulsed laser ablation and nanoparticle generation in liquids.* The Journal of Physical Chemistry C, 2011. **115**(12): p. 5108-5114.
84. Elsayed, K.A., et al., *Effect of focusing conditions and laser parameters on the fabrication of gold nanoparticles via laser ablation in liquid.* Optics & Laser Technology, 2013. **45**: p. 495-502.
85. Nguyen, T.T.P., R. Tanabe, and Y. Ito, *Influences of focusing conditions on dynamics of laser ablation at a solid–liquid interface.* Applied Physics Express, 2013. **6**(12): p. 122701.
86. Šišková, K., J. Pfleger, and M. Procházka, *Stabilization of Au nanoparticles prepared by laser ablation in chloroform with free-base porphyrin molecules.* Applied Surface Science, 2010. **256**(9): p. 2979-2987.
87. Stasic, J., et al., *Focusing geometry-induced size tailoring of silver nanoparticles obtained by laser ablation in water.* Laser Physics, 2014. **24**(10): p. 106005.
88. Zamiri, R., et al., *The effect of laser repetition rate on the LASiS synthesis of biocompatible silver nanoparticles in aqueous starch solution.* International journal of nanomedicine, 2013. **8**: p. 233.
89. Darroudi, M., et al., *Preparation and characterization of gelatin mediated silver nanoparticles by laser ablation.* Journal of Alloys and Compounds, 2011. **509**(4): p. 1301-1304.
90. Menéndez-Manjón, A. and S. Barcikowski, *Hydrodynamic size distribution of gold nanoparticles controlled by repetition rate during pulsed laser ablation in water.* Applied Surface Science, 2011. **257**(9): p. 4285-4290.
91. Chichkov, B.N., et al., *Femtosecond, picosecond and nanosecond laser ablation of solids.* Applied Physics A, 1996. **63**(2): p. 109-115.
92. Liu, H., et al., *Influence of liquid environments on femtosecond laser ablation of silicon.* Thin Solid Films, 2010. **518**(18): p. 5188-5194.
93. Yan, Z. and D.B. Chrisey, *Pulsed laser ablation in liquid for micro-/nanostructure generation.* Journal of Photochemistry and Photobiology C: Photochemistry Reviews, 2012. **13**(3): p. 204-223.

94. Amendola, V. and M. Meneghetti, *Laser ablation synthesis in solution and size manipulation of noble metal nanoparticles.* Physical chemistry chemical physics, 2009. **11**(20): p. 3805-3821.
95. Asahi, T., T. Sugiyama, and H. Masuhara, *Laser fabrication and spectroscopy of organic nanoparticles.* Accounts of chemical research, 2008. **41**(12): p. 1790-1798.
96. Barcikowski, S., et al., *Handbook of laser synthesis of colloids.* 2016.
97. Zhang, D., et al., *Recent Advances in Surfactant-Free, Surface-Charged, and Defect-Rich Catalysts Developed by Laser Ablation and Processing in Liquids.* ChemNanoMat, 2017. **3**(8): p. 512-533.
98. Liu, P., et al., *From nanocrystal synthesis to functional nanostructure fabrication: laser ablation in liquid.* Physical Chemistry Chemical Physics, 2010. **12**(16): p. 3942-3952.
99. Sasaki, T., Y. Shimizu, and N. Koshizaki, *Preparation of metal oxide-based nanomaterials using nanosecond pulsed laser ablation in liquids.* Journal of Photochemistry and Photobiology A: Chemistry, 2006. **182**(3): p. 335-341.
100. Rao, S.V., G.K. Podagatlapalli, and S. Hamad, *Ultrafast Laser Ablation in Liquids for Nanomaterials and Applications.* Journal of Nanoscience and Nanotechnology, 2014. **14**(2): p. 1364-1388.
101. Tymoczko, A., et al., *How the crystal structure and phase segregation of Au–Fe alloy nanoparticles are ruled by the molar fraction and size.* Nanoscale, 2018. **10**(35): p. 16434-16437.
102. Zhang, K., et al., *Preparation, characterization, and fluorescence properties of well-dispersed core–shell CdS/carbon nanoparticles.* Journal of materials science, 2011. **46**(21): p. 6975.
103. Santagata, A., et al., *Carbon-based nanostructures obtained in water by ultrashort laser pulses.* The Journal of Physical Chemistry C, 2011. **115**(12): p. 5160-5164.
104. De Giacomo, A., et al., *Laser ablation of graphite in water in a range of pressure from 1 to 146 atm using single and double pulse techniques for the production of carbon nanostructures.* The Journal of Physical Chemistry C, 2011. **115**(12): p. 5123-5130.
105. Taylor, U., et al., *Influence of gold, silver and gold–silver alloy nanoparticles on germ cell function and embryo development.* Beilstein journal of nanotechnology, 2015. **6**(1): p. 651-664.
106. Walter, J.G., et al., *Laser ablation-based one-step generation and bio-functionalization of gold nanoparticles conjugated with aptamers.* Journal of nanobiotechnology, 2010. **8**(1): p. 21.
107. Mutisya, S., et al., *Comparison of in situ and ex situ bioconjugation of Au nanoparticles generated by laser ablation.* Applied Surface Science, 2013. **264**: p. 27-30.
108. Joshi, D. and R. Soni, *Synthesis of gold and silver nanoparticle S-ovalbumin protein conjugates by in situ conjugation process.* Journal of Nanoparticle Research, 2015. **17**(5): p. 210.
109. Petersen, S., J. Jakobi, and S. Barcikowski, *In situ bioconjugation—novel laser based approach to pure nanoparticle-conjugates.* Applied Surface Science, 2009. **255**(10): p. 5435-5438.

110. Kőrösi, L., et al., *Ultrasmall, ligand-free Ag nanoparticles with high antibacterial activity prepared by pulsed laser ablation in liquid.* Journal of Chemistry, 2016. **2016**.
111. Longano, D., et al., *Analytical characterization of laser-generated copper nanoparticles for antibacterial composite food packaging.* Analytical and bioanalytical chemistry, 2012. **403**(4): p. 1179-1186.
112. Zimbone, M., et al., *Photocatalytical and antibacterial activity of TiO2 nanoparticles obtained by laser ablation in water.* Applied Catalysis B: Environmental, 2015. **165**: p. 487-494.
113. Hamad, A., et al., *Generation of silver titania nanoparticles from an Ag–Ti alloy via picosecond laser ablation and their antibacterial activities.* Rsc Advances, 2015. **5**(89): p. 72981-72994.
114. Zhang, J. and C.Q. Lan, *Nickel and cobalt nanoparticles produced by laser ablation of solids in organic solution.* Materials Letters, 2008. **62**(10-11): p. 1521-1524.
115. Amendola, V., P. Riello, and M. Meneghetti, *Magnetic Nanoparticles of Iron Carbide, Iron Oxide, Iron@Iron Oxide, and Metal Iron Synthesized by Laser Ablation in Organic Solvents.* The Journal of Physical Chemistry C, 2011. **115**(12): p. 5140-5146.
116. Franzel, L., et al., *Synthesis of magnetic nanoparticles by pulsed laser ablation.* Applied Surface Science, 2012. **261**: p. 332-336.
117. Swiatkowska-Warkocka, Z., et al., *Pulsed laser irradiation of colloidal nanoparticles: a new synthesis route for the production of non-equilibrium bimetallic alloy submicrometer spheres.* RSC Advances, 2013. **3**(1): p. 79-83.
118. Bertorelle, F., et al., *Efficient AuFeOx Nanoclusters of Laser-Ablated Nanoparticles in Water for Cells Guiding and Surface-Enhanced Resonance Raman Scattering Imaging.* The Journal of Physical Chemistry C, 2014. **118**(26): p. 14534-14541.
119. Nakamura, T., Z. Yuan, and S. Adachi, *High-yield preparation of blue-emitting colloidal Si nanocrystals by selective laser ablation of porous silicon in liquid.* Nanotechnology, 2014. **25**(27): p. 275602.
120. Singh, S., et al., *Optical properties of selenium quantum dots produced with laser irradiation of water suspended Se nanoparticles.* The Journal of Physical Chemistry C, 2010. **114**(41): p. 17374-17384.
121. Vadavalli, S., et al., *Optical properties of germanium nanoparticles synthesized by pulsed laser ablation in acetone.* Frontiers in Physics, 2014. **2**: p. 57.
122. Gondal, M., Q. Drmosh, and T.A. Saleh, *Preparation and characterization of SnO2 nanoparticles using high power pulsed laser.* Applied Surface Science, 2010. **256**(23): p. 7067-7070.
123. Usui, H., et al., *Photoluminescence of ZnO nanoparticles prepared by laser ablation in different surfactant solutions.* The Journal of Physical Chemistry B, 2005. **109**(1): p. 120-124.
124. Singh, S., R. Swarnkar, and R. Gopal, *Synthesis of titanium dioxide nanomaterial by pulsed laser ablation in water.* Journal of nanoscience and nanotechnology, 2009. **9**(9): p. 5367-5371.
125. Lalayan, A., *Formation of colloidal GaAs and CdS quantum dots by laser ablation in liquid media.* Applied surface science, 2005. **248**(1-4): p. 209-212.

126. Yang, J., et al., *A top–down strategy towards monodisperse colloidal lead sulphide quantum dots.* Nature communications, 2013. **4**: p. 1695.
127. Dong, W., et al., *The effect of the Au loading on the liquid-phase aerobic oxidation of ethanol over Au/TiO2 catalysts prepared by pulsed laser ablation.* Journal of Catalysis, 2015. **330**: p. 497-506.
128. Wu, S., et al., *Highly Dispersed Ultrafine Pt Nanoparticles on Reduced Graphene Oxide Nanosheets: In Situ Sacrificial Template Synthesis and Superior Electrocatalytic Performance for Methanol Oxidation.* ACS Applied Materials & Interfaces, 2015. **7**(41): p. 22935-22940.
129. Zhang, J., et al., *Gold nanoparticle decorated ceria nanotubes with significantly high catalytic activity for the reduction of nitrophenol and mechanism study.* Applied Catalysis B: Environmental, 2013. **132-133**: p. 107-115.
130. Blakemore, J.D., et al., *Co3O4 Nanoparticle Water-Oxidation Catalysts Made by Pulsed-Laser Ablation in Liquids.* ACS Catalysis, 2013. **3**(11): p. 2497-2500.
131. Guo, W. and B. Liu, *Liquid-Phase Pulsed Laser Ablation and Electrophoretic Deposition for Chalcopyrite Thin-Film Solar Cell Application.* ACS Applied Materials & Interfaces, 2012. **4**(12): p. 7036-7042.
132. Zeng, H., et al., *Composition/structural evolution and optical properties of ZnO/Zn nanoparticles by laser ablation in liquid media.* The Journal of Physical Chemistry B, 2005. **109**(39): p. 18260-18266.
133. Fazio, E., et al., *ZnO nanostructures produced by laser ablation in water: Optical and structural properties.* Applied Surface Science, 2013. **272**: p. 30-35.
134. Guillén, G.G., et al., *Structure and morphologies of ZnO nanoparticles synthesized by pulsed laser ablation in liquid: Effects of temperature and energy fluence.* Materials Chemistry and Physics, 2015. **162**: p. 561-570.
135. Ishikawa, Y., et al., *Preparation of zinc oxide nanorods using pulsed laser ablation in water media at high temperature.* Journal of Colloid and Interface Science, 2006. **300**(2): p. 612-615.
136. Liang, C., et al., *Synthesis, characterization, and phase stability of ultrafine TiO 2 nanoparticles by pulsed laser ablation in liquid media.* Journal of materials research, 2004. **19**(5): p. 1551-1557.
137. Nikolov, A., et al., *Synthesis and characterization of TiOx nanoparticles prepared by pulsed-laser ablation of Ti target in water.* Applied Surface Science, 2009. **255**(10): p. 5351-5354.
138. Zimbone, M., et al., *Photocatalytical activity of amorphous hydrogenated TiO2 obtained by pulsed laser ablation in liquid.* Materials Science in Semiconductor Processing, 2016. **42**: p. 28-31.
139. Zuñiga-Ibarra, V.A., et al., *Synthesis and characterization of black TiO2 nanoparticles by pulsed laser irradiation in liquid.* Applied Surface Science, 2019. **483**: p. 156-164.
140. Zhang, H., et al., *Single phase Mn3O4 nanoparticles obtained by pulsed laser ablation in liquid and their application in rapid removal of trace pentachlorophenol.* The Journal of Physical Chemistry C, 2010. **114**(29): p. 12524-12528.

141. Gondal, M., T.A. Saleh, and Q. Drmosh, *Synthesis of nickel oxide nanoparticles using pulsed laser ablation in liquids and their optical characterization.* Applied Surface Science, 2012. **258**(18): p. 6982-6986.
142. Kumar, B. and R.K. Thareja, *Synthesis of aluminum oxide nanoparticles using laser ablation in liquid.* physica status solidi c, 2010. **7**(5): p. 1409-1412.
143. Singh, M.K., M.C. Mathpal, and A. Agarwal, *Optical properties of SnO2 quantum dots synthesized by laser ablation in liquid.* Chemical Physics Letters, 2012. **536**: p. 87-91.
144. Guillen, G.G., et al., *Tin sulfide nanoparticles by pulsed laser ablation in liquid.* Journal of Materials Science: Materials in Electronics, 2016. **27**(7): p. 6859-6871.
145. Darwish, A.M., et al., *Synthesis of Nano-Cadmium Sulfide by Pulsed Laser Ablation in Liquid Environment.* Spectroscopy Letters, 2015. **48**(9): p. 638-645.
146. Lalayan, A.A., *Formation of colloidal GaAs and CdS quantum dots by laser ablation in liquid media.* Applied Surface Science, 2005. **248**(1): p. 209-212.
147. Wu, H., et al., *Biocompatible inorganic fullerene-like molybdenum disulfide nanoparticles produced by pulsed laser ablation in water.* ACS nano, 2011. **5**(2): p. 1276-1281.
148. Compagnini, G., et al., *Monitoring the formation of inorganic fullerene-like MoS2 nanostructures by laser ablation in liquid environments.* Applied Surface Science, 2012. **258**(15): p. 5672-5676.
149. Oztas, T., et al., *Synthesis of colloidal 2D/3D MoS2 nanostructures by pulsed laser ablation in an organic liquid environment.* The Journal of Physical Chemistry C, 2014. **118**(51): p. 30120-30126.
150. Wu, X., et al., *Inorganic fullerene-like molybdenum selenide with good biocompatibility synthesized by laser ablation in liquids.* Nanotechnology, 2018. **29**(29): p. 295604.
151. Garza, D., et al., *Nanoparticles of antimony sulfide by pulsed laser ablation in liquid media.* Journal of materials science, 2013. **48**(18): p. 6445-6453.
152. Sun, R.-D. and T. Tsuji, *Preparation of antimony sulfide semiconductor nanoparticles by pulsed laser ablation in liquid.* Applied Surface Science, 2015. **348**: p. 38-44.
153. Shaji, S., et al., *Copper antimony sulfide nanoparticles by pulsed laser ablation in liquid and their thin film for photovoltaic application.* Applied Surface Science, 2019. **476**: p. 94-106.
154. Mendivil, M., et al., *CuInGaSe2 nanoparticles by pulsed laser ablation in liquid medium.* Materials Research Bulletin, 2015. **72**: p. 106-115.
155. Rioux, D., et al., *Silicon nanoparticles produced by femtosecond laser ablation in water as novel contamination-free photosensitizers.* J Biomed Opt, 2009. **14**(2): p. 021010.
156. Kuzmin, P.G., et al., *Silicon Nanoparticles Produced by Femtosecond Laser Ablation in Ethanol: Size Control, Structural Characterization, and Optical Properties.* The Journal of Physical Chemistry C, 2010. **114**(36): p. 15266-15273.
157. Abderrafi, K., et al., *Silicon Nanocrystals Produced by Nanosecond Laser Ablation in an Organic Liquid.* The Journal of Physical Chemistry C, 2011. **115**(12): p. 5147-5151.

158. Yang, S., et al., *Optical Study of Redox Behavior of Silicon Nanoparticles Induced by Laser Ablation in Liquid.* The Journal of Physical Chemistry C, 2009. **113**(16): p. 6480-6484.
159. Yang, S., et al., *Size and Structure Control of Si Nanoparticles by Laser Ablation in Different Liquid Media and Further Centrifugation Classification.* The Journal of Physical Chemistry C, 2009. **113**(44): p. 19091-19095.
160. Umezu, I., et al., *Synthesis of photoluminescent colloidal silicon nanoparticles by pulsed laser ablation in liquids.* Journal of Physics: Conference Series, 2007. **59**: p. 392-395.
161. Perminov, P.A., et al., *Silicon nanoparticles formation by means of laser ablation in liquid media.* Bulletin of the Russian Academy of Sciences: Physics, 2010. **74**(1): p. 93-95.
162. Perminov, P.A., et al., *Creation of silicon nanocrystals using the laser ablation in liquid.* Laser Physics, 2011. **21**(4): p. 801.
163. Švrček, V. and M. Kondo, *Blue luminescent silicon nanocrystals prepared by short pulsed laser ablation in liquid media.* Applied Surface Science, 2009. **255**(24): p. 9643-9646.
164. Vadavalli, S., et al., *Optical properties of germanium nanoparticles synthesized by pulsed laser ablation in acetone.* Frontiers in Physics, 2014. **2**(57).
165. Semaltianos, N.G., et al., *CdTe nanoparticles synthesized by laser ablation.* Applied Physics Letters, 2009. **95**(3): p. 033302.
166. Jacob, J., et al., *Synthesis and Properties of Tin Sulfide Thin Films from Nanocolloids Prepared by Pulsed Laser Ablation in Liquid.* ChemPhysChem, 2017. **18**(9): p. 1061-1068.
167. Johny, J., et al., *Nanostructured SnS2 Thin Films from Laser Ablated Nanocolloids: Structure, Morphology, Optoelectronic and Electrochemical Properties.* ChemPhysChem. **0**(0).
168. Koteeswara Reddy, N., M. Devika, and E. Gopal, *Review on tin (II) sulfide (SnS) material: synthesis, properties, and applications.* Critical Reviews in Solid State and Materials Sciences, 2015. **40**(6): p. 359-398.
169. Wiley, J., W. Buckel, and R. Schmidt, *Infrared reflectivity and Raman scattering in GeS.* Physical Review B, 1976. **13**(6): p. 2489.
170. Chandrasekhar, H., et al., *Infrared and Raman spectra of the IV-VI compounds SnS and SnSe.* Physical Review B, 1977. **15**(4): p. 2177.
171. Zhu, H., et al., *Two-dimensional SnS nanosheets fabricated by a novel hydrothermal method.* Journal of materials science, 2005. **40**(3): p. 591-595.
172. Ghazali, A., et al., *Cathodic electrodeposition of SnS in the presence of EDTA in aqueous media.* Solar energy materials and solar cells, 1998. **55**(3): p. 237-249.
173. Nasirov, V. and K.A. Adgezalova, *Stabilization of low-temperature SnS by rare-earth doping*. Inorganic materials, 2001. **37**(11): p. 1099-1100.
174. Ettema, A., et al., *Electronic structure of SnS deduced from photoelectron spectra and band-structure calculations.* Physical Review B, 1992. **46**(12): p. 7363.
175. Barrow, R., G. Drummond, and H. Rowlinson, *The Absorption Spectrum of SnS Vapour in the Ultra-Violet and Schumann Regions.* Proceedings of the Physical Society. Section A, 1953. **66**(10): p. 885.

176. Sharon, M. and K. Basavaswaran, *Photoelectrochemical behaviour of tin monosulphide.* Solar cells, 1988. **25**(2): p. 97-107.
177. Anderson John, S., M.C. Morton, and D. Rivett Albert Cherbury, *The electrical conductivity of stannous sulphide.* Proceedings of the Royal Society of London. Series A. Mathematical and Physical Sciences, 1945. **184**(996): p. 83-101.
178. Nassary, M.M., *Temperature dependence of the electrical conductivity, Hall effect and thermoelectric power of SnS single crystals.* Journal of Alloys and Compounds, 2005. **398**(1): p. 21-25.
179. Ristov, M., et al., *Chemical deposition of TIN(II) sulphide thin films.* Thin Solid Films, 1989. **173**(1): p. 53-58.
180. Ghosh, B., et al., *Fabrication and optical properties of SnS thin films by SILAR method.* Applied Surface Science, 2008. **254**(20): p. 6436-6440.
181. Gonzalez, J.M. and I.I. Oleynik, *Layer-dependent properties of ${\mathbf{SnS}}_{2}$ and ${\mathbf{SnSe}}_{2}$ two-dimensional materials.* Physical Review B, 2016. **94**(12): p. 125443.
182. Pałosz, B. and E. Salje, *Lattice parameters and spontaneous strain in AX2 polytypes: CdI2, PbI2 SnS2 and SnSe2.* Journal of Applied Crystallography, 1989. **22**(6): p. 622-623.
183. Tao, Y., et al., *Flexible photodetector from ultraviolet to near infrared based on a SnS2 nanosheet microsphere film.* Journal of Materials Chemistry C, 2015. **3**(6): p. 1347-1353.
184. Patil, S. and R. Tredgold, *Electrical and photoconductive properties of SnS2 crystals.* Journal of Physics D: Applied Physics, 1971. **4**(5): p. 718.
185. Qu, B., et al., *Layered SnS2-Reduced Graphene Oxide Composite – A High-Capacity, High-Rate, and Long-Cycle Life Sodium-Ion Battery Anode Material.* Advanced Materials, 2014. **26**(23): p. 3854-3859.
186. Madelung, O., *Semiconductors: data handbook.* 2012: Springer Science & Business Media.
187. Amalraj, L., C. Sanjeeviraja, and M. Jayachandran, *Spray pyrolysised tin disulphide thin film and characterisation.* Journal of Crystal Growth, 2002. **234**(4): p. 683-689.
188. Julien, C., et al., *Optical and electrical characterizations of SnSe, SnS2 and SnSe2 single crystals.* Materials Science and Engineering: B, 1992. **15**(1): p. 70-72.
189. Tanusevski, A., *Optical and photoelectric properties of SnS thin films prepared by chemical bath deposition.* Semiconductor Science and Technology, 2003. **18**(6): p. 501.
190. Turan, E., et al., *Structural and optical properties of SnS semiconductor films produced by chemical bath deposition.* Journal of Physics D: Applied Physics, 2009. **42**(24): p. 245408.
191. Guneri, E., et al., *Effect of deposition time on structural, electrical, and optical properties of SnS thin films deposited by chemical bath deposition.* Applied Surface Science, 2010. **257**(4): p. 1189-1195.
192. Gao, C., H. Shen, and L. Sun, *Preparation and properties of zinc blende and orthorhombic SnS films by chemical bath deposition.* Applied Surface Science, 2011. **257**(15): p. 6750-6755.

193. Ray, S.C., M.K. Karanjai, and D. DasGupta, *Structure and photoconductive properties of dip-deposited SnS and SnS2 thin films and their conversion to tin dioxide by annealing in air.* Thin Solid Films, 1999. **350**(1-2): p. 72-78.
194. Su, G., et al., *Chemical vapor deposition of thin crystals of layered semiconductor SnS2 for fast photodetection application.* Nano letters, 2014. **15**(1): p. 506-513.
195. Price, L.S., et al., *Atmospheric pressure chemical vapor deposition of tin sulfides (SnS, Sn2S3, and SnS2) on glass.* Chemistry of materials, 1999. **11**(7): p. 1792-1799.
196. Thangaraju, B. and P. Kaliannan, *Spray pyrolytic deposition and characterization of SnS and SnS2 thin films.* Journal of Physics D: Applied Physics, 2000. **33**(9): p. 1054.
197. Seo, W., et al., *Thickness-dependent structure and properties of SnS2 thin films prepared by atomic layer deposition.* Japanese Journal of Applied Physics, 2017. **56**(3): p. 031201.
198. Sinsermsuksakul, P., et al., *Atomic layer deposition of tin monosulfide thin films.* Advanced Energy Materials, 2011. **1**(6): p. 1116-1125.
199. Chaki, S.H., et al., *Wet chemical synthesis and characterization of SnS 2 nanoparticles.* Applied Nanoscience, 2013. **3**(3): p. 189-195.
200. Sohila, S., et al., *Synthesis and characterization of SnS nanosheets through simple chemical route.* Materials Letters, 2011. **65**(8): p. 1148-1150.
201. Kiruthigaa, G., et al., *Synthesis and spectroscopic analysis of undoped and Zn doped SnS2 nanostructure by solid state reaction method.* Materials Science in Semiconductor Processing, 2014. **26**: p. 533-539.
202. Im, H.S., et al., *Facile phase and composition tuned synthesis of tin chalcogenide nanocrystals.* RSC Advances, 2013. **3**(26): p. 10349-10354.
203. Sinsermsuksakul, P., et al., *Overcoming efficiency limitations of SnS-based solar cells.* Advanced Energy Materials, 2014. **4**(15): p. 1400496.
204. Steinmann, V., et al., *3.88% efficient tin sulfide solar cells using congruent thermal evaporation.* Advanced Materials, 2014. **26**(44): p. 7488-7492.
205. Burton, L.A. and A. Walsh, *Band alignment in SnS thin-film solar cells: Possible origin of the low conversion efficiency.* Applied Physics Letters, 2013. **102**(13): p. 132111.
206. Schneikart, A., et al., *Efficiency limitations of thermally evaporated thin-film SnS solar cells.* Journal of Physics D: Applied Physics, 2013. **46**(30): p. 305109.
207. Sinsermsuksakul, P., et al., *Enhancing the efficiency of SnS solar cells via band-offset engineering with a zinc oxysulfide buffer layer.* Applied Physics Letters, 2013. **102**(5): p. 053901.
208. Sugiyama, M., et al., *Band offset of SnS solar cell structure measured by X-ray photoelectron spectroscopy.* Thin Solid Films, 2011. **519**(21): p. 7429-7431.
209. Lu, F., et al., *Gas-dependent photoresponse of SnS nanoparticles-based photodetectors.* Journal of Materials Chemistry C, 2015. **3**(6): p. 1397-1402.
210. Deng, Z., et al., *Solution synthesis of ultrathin single-crystalline SnS nanoribbons for photodetectors via phase transition and surface processing.* ACS nano, 2012. **6**(7): p. 6197-6207.

211. Wang, J., et al., *Growth of Large-Size SnS Thin Crystals Driven by Oriented Attachment and Applications to Gas Sensors and Photodetectors.* ACS Applied Materials & Interfaces, 2016. **8**(15): p. 9545-9551.
212. Mahdi, M.S., et al., *A highly sensitive flexible SnS thin film photodetector in the ultraviolet to near infrared prepared by chemical bath deposition.* RSC Advances, 2016. **6**(116): p. 114980-114988.
213. Tang, P., et al., *Nanoparticulate SnS as an efficient photocatalyst under visible-light irradiation.* Materials letters, 2011. **65**(3): p. 450-452.
214. Xie, Q., et al., *Sn 4+ self-doped hollow cubic SnS as an efficient visible-light photocatalyst for Cr (vi) reduction and detoxification of cyanide.* Journal of Materials Chemistry A, 2017. **5**(13): p. 6299-6309.
215. Subramanian, B., C. Sanjeeviraja, and M. Jayachandran, *Cathodic electrodeposition and analysis of SnS films for photoelectrochemical cells.* Materials Chemistry and Physics, 2001. **71**(1): p. 40-46.
216. Chao, J., et al., *Tin sulfide nanoribbons as high performance photoelectrochemical cells, flexible photodetectors and visible-light-driven photocatalysts.* RSC Advances, 2013. **3**(8): p. 2746-2753.
217. Zhou, T., et al., *Enhanced sodium-ion battery performance by structural phase transition from two-dimensional hexagonal-SnS2 to orthorhombic-SnS.* Acs Nano, 2014. **8**(8): p. 8323-8333.
218. Zheng, Y., et al., *Boosted Charge Transfer in SnS/SnO2 Heterostructures: Toward High Rate Capability for Sodium-Ion Batteries.* Angewandte Chemie International Edition, 2016. **55**(10): p. 3408-3413.
219. Xiong, X., et al., *SnS nanoparticles electrostatically anchored on three-dimensional N-doped graphene as an active and durable anode for sodium-ion batteries.* Energy & Environmental Science, 2017. **10**(8): p. 1757-1763.
220. Xia, J., et al., *Large-Scale Growth of Two-Dimensional SnS2 Crystals Driven by Screw Dislocations and Application to Photodetectors.* Advanced Functional Materials, 2015. **25**(27): p. 4255-4261.
221. Tao, Y., et al., *Flexible photodetector from ultraviolet to near infrared based on a SnS 2 nanosheet microsphere film.* Journal of Materials Chemistry C, 2015. **3**(6): p. 1347-1353.
222. Zhang, Y.C., et al., *Size-tunable hydrothermal synthesis of SnS2 nanocrystals with high performance in visible light-driven photocatalytic reduction of aqueous Cr (VI).* Environmental science & technology, 2011. **45**(21): p. 9324-9331.
223. Li, X., J. Zhu, and H. Li, *Comparative study on the mechanism in photocatalytic degradation of different-type organic dyes on SnS2 and CdS.* Applied Catalysis B: Environmental, 2012. **123**: p. 174-181.
224. Zhang, Z., et al., *Ultrathin hexagonal SnS2 nanosheets coupled with g-C3N4 nanosheets as 2D/2D heterojunction photocatalysts toward high photocatalytic activity.* Applied Catalysis B: Environmental, 2015. **163**: p. 298-305.
225. Lei, Y., et al., *Facile synthesis and assemblies of flowerlike SnS2 and In3+-doped SnS2: hierarchical structures and their enhanced photocatalytic property.* The Journal of Physical Chemistry C, 2009. **113**(4): p. 1280-1285.

226. Zhang, Y.C., et al., *Novel synthesis and high visible light photocatalytic activity of SnS2 nanoflakes from SnCl2· 2H2O and S powders.* Applied Catalysis B: Environmental, 2010. **95**(1-2): p. 153-159.
227. Seo, J.w., et al., *Two-dimensional SnS2 nanoplates with extraordinary high discharge capacity for lithium ion batteries.* Advanced Materials, 2008. **20**(22): p. 4269-4273.
228. Kim, T.-J., et al., *Novel SnS2-nanosheet anodes for lithium-ion batteries.* Journal of Power Sources, 2007. **167**(2): p. 529-535.
229. Luo, B., et al., *Two dimensional graphene–SnS 2 hybrids with superior rate capability for lithium ion storage.* Energy & Environmental Science, 2012. **5**(1): p. 5226-5230.
230. Chang, K., et al., *Few-layer SnS2/graphene hybrid with exceptional electrochemical performance as lithium-ion battery anode.* Journal of Power Sources, 2012. **201**: p. 259-266.
231. Tan, F., et al., *Preparation of SnS 2 colloidal quantum dots and their application in organic/inorganic hybrid solar cells.* Nanoscale research letters, 2011. **6**(1): p. 298.
232. Bai, Y., et al., *Scalable low-cost SnS2 nanosheets as counter electrode building blocks for dye-sensitized solar cells.* Chemistry–A European Journal, 2014. **20**(28): p. 8670-8676.
233. Cui, X., et al., *High-performance dye-sensitized solar cells based on Ag-doped SnS 2 counter electrodes.* Journal of Materials Chemistry A, 2016. **4**(5): p. 1908-1914.
234. Yang, B., et al., *SnS2 as low-cost counter-electrode materials for dye-sensitized solar cells.* Materials Letters, 2014. **133**: p. 197-199.
235. Fakhri, A. and S. Behrouz, *Assessment of SnS2 nanoparticles properties for photocatalytic and antibacterial applications.* Solar Energy, 2015. **117**: p. 187-191.
236. Gupta, R. and F. Yakuphanoglu, *Photoconductive Schottky diode based on Al/p-Si/SnS2/Ag for optical sensor applications.* Solar Energy, 2012. **86**(5): p. 1539-1545.
237. Yu, J., et al., *Monodisperse SnS2 Nanosheets for High-Performance Photocatalytic Hydrogen Generation.* ACS Applied Materials & Interfaces, 2014. **6**(24): p. 22370-22377.
238. Zeng, Y., et al., *Application of flower-like SnS 2 nanoparticles for direct electrochemistry of hemoglobin and its electrocatalysis.* Analytical Methods, 2014. **6**(2): p. 404-409.
239. Parveen, N., et al., *Facile synthesis of SnS2 nanostructures with different morphologies for high-performance supercapacitor applications.* ACS Omega, 2018. **3**(2): p. 1581-1588.
240. Lee, D., M.F. Rubner, and R.E. Cohen, *All-nanoparticle thin-film coatings.* Nano letters, 2006. **6**(10): p. 2305-2312.
241. Schulz, D.L., et al., *CdTe thin films from nanoparticle precursors by spray deposition.* Chemistry of materials, 1997. **9**(4): p. 889-900.
242. Pehnt, M., et al., *Nanoparticle precursor route to low-temperature spray deposition of CdTe thin films.* Applied physics letters, 1995. **67**(15): p. 2176-2178.

243. Wang, W., et al., *Spray Deposition of Au/TiO 2 Composite Thin Films Using Preformed Nanoparticles*, in *Nanotechnology in Construction 3*. 2009, Springer. p. 395-401.
244. Sharma, S., et al., *Spin-coated ZnO thin films using ZnO nano-colloid.* Journal of electronic materials, 2006. **35**(6): p. 1237-1240.
245. Toolan, D.T., et al., *On the mechanisms of colloidal self-assembly during spin-coating.* Soft Matter, 2014. **10**(44): p. 8804-8812.
246. Patil, P.S., *Versatility of chemical spray pyrolysis technique.* Materials Chemistry and physics, 1999. **59**(3): p. 185-198.
247. Marcano, D.C., et al., *Improved Synthesis of Graphene Oxide.* ACS Nano, 2010. **4**(8): p. 4806-4814.
248. Williams, D.B. and C.B. Carter, *The transmission electron microscope*, in *Transmission electron microscopy*. 1996, Springer. p. 3-17.
249. Kaufmann, E.N., *Characterization of Materials, 2 Volume Set.* Characterization of Materials, 2 Volume Set, by Elton N. Kaufmann (Editor), pp. 1392. ISBN 0-471-26882-8. Wiley-VCH, January 2003., 2003: p. 1392.
250. Watts, J.F. and J. Wolstenholme, *An introduction to surface analysis by XPS and AES.* An Introduction to Surface Analysis by XPS and AES, by John F. Watts, John Wolstenholme, pp. 224. ISBN 0-470-84713-1. Wiley-VCH, May 2003., 2003: p. 224.
251. Vinayakumar, V., et al., *CuSbS2 thin films by rapid thermal processing of Sb2S3-Cu stack layers for photovoltaic application.* Solar Energy Materials and Solar Cells, 2017. **164**: p. 19-27.
252. Sohila, S., et al., *Optical and Raman scattering studies on SnS nanoparticles.* Journal of Alloys and Compounds, 2011. **509**(19): p. 5843-5847.
253. Koteswara Reddy, N. and K.T. Ramakrishna Reddy, *Growth of polycrystalline SnS films by spray pyrolysis.* Thin Solid Films, 1998. **325**(1): p. 4-6.
254. Hartman, K., et al., *SnS thin-films by RF sputtering at room temperature.* Thin Solid Films, 2011. **519**(21): p. 7421-7424.
255. Ichimura, M., et al., *Electrochemical deposition of SnS thin films.* Thin Solid Films, 2000. **361**: p. 98-101.
256. Moulder, J.F. and J. Chastain, *Handbook of X-ray Photoelectron Spectroscopy: A Reference Book of Standard Spectra for Identification and Interpretation of XPS Data*. 1992: Physical Electronics Division, Perkin-Elmer Corporation.
257. Cheng, S. and G. Conibeer, *Physical properties of very thin SnS films deposited by thermal evaporation.* Thin Solid Films, 2011. **520**(2): p. 837-841.
258. Mathews, N.R., et al., *Tin sulfide thin films by pulse electrodeposition: structural, morphological, and optical properties.* Journal of the electrochemical society, 2010. **157**(3): p. H337-H341.
259. Zhang, H., et al., *Synthesis and photosensitivity of SnS nanobelts.* Journal of Alloys and Compounds, 2012. **513**: p. 1-5.
260. El-Nahass, M.M., et al., *Optical properties of thermally evaporated SnS thin films.* Optical Materials, 2002. **20**(3): p. 159-170.
261. Reddy, N.K. and K.T.R. Reddy, *SnS films for photovoltaic applications: Physical investigations on sprayed SnxSy films.* Physica B: Condensed Matter, 2005. **368**(1–4): p. 25-31.

262. Nair, M.T.S. and P.K. Nair, *Simplified chemical deposition technique for good quality SnS thin films.* Semiconductor Science and Technology, 1991. **6**(2): p. 132.

263. Ramakrishna Reddy, K.T., N. Koteswara Reddy, and R.W. Miles, *Photovoltaic properties of SnS based solar cells.* Solar Energy Materials and Solar Cells, 2006. **90**(18–19): p. 3041-3046.

264. Sinsermsuksakul, P., et al., *Overcoming Efficiency Limitations of SnS-Based Solar Cells.* Advanced Energy Materials, 2014. **4**(15): p. 1400496-n/a.

265. Patel, M. and A. Ray, *Evaluation of Back Contact in Spray Deposited SnS Thin Film Solar Cells by Impedance Analysis.* ACS Applied Materials & Interfaces, 2014. **6**(13): p. 10099-10106.

266. Li, Y., et al., *Nanoscale SnS with and without carbon-coatings as an anode material for lithium ion batteries.* Electrochimica Acta, 2006. **52**(3): p. 1383-1389.

267. Steinmann, V., et al., *3.88% Efficient Tin Sulfide Solar Cells using Congruent Thermal Evaporation.* Advanced Materials, 2014. **26**(44): p. 7488-7492.

268. Muthuvinayagama, A. and B. Viswanathanb, *Hydrothermal synthesis and LPG sensing ability of SnS nanomaterial.* Indian Journal of Chemistry, 2015. **54**: p. 155-160.

269. Gaiardo, A., et al., *Metal Sulfides as Sensing Materials for Chemoresistive Gas Sensors.* Sensors, 2016. **16**(3): p. 296.

270. Yue, G., et al., *Characterization and Optical Properties of the Single Crystalline SnS Nanowire Arrays.* Nanoscale Research Letters, 2009. **4**(4): p. 359.

271. Liu, Y., D. Hou, and G. Wang, *Synthesis and characterization of SnS nanowires in cetyltrimethylammoniumbromide (CTAB) aqueous solution.* Chemical Physics Letters, 2003. **379**(1–2): p. 67-73.

272. Ning, J., et al., *Facile synthesis of iv-vi SnS nanocrystals with shape and size control: Nanoparticles, nanoflowers and amorphous nanosheets.* Nanoscale, 2010. **2**(9): p. 1699-1703.

273. Lu, J., et al., *Flexible SnS nanobelts: Facile synthesis, formation mechanism and application in Li-ion batteries.* Nano Research, 2013. **6**(1): p. 55-64.

274. Falkovsky, L.A., *Optical properties of graphene.* Journal of Physics: Conference Series, 2008. **129**(1): p. 012004.

275. Novoselov, K.S., et al., *Electric Field Effect in Atomically Thin Carbon Films.* Science, 2004. **306**(5696): p. 666-669.

276. Ovid'ko, I., *Mechanical properties of graphene.* Rev. Adv. Mater. Sci, 2013. **34**: p. 1-11.

277. Hummers, W.S. and R.E. Offeman, *Preparation of Graphitic Oxide.* Journal of the American Chemical Society, 1958. **80**(6): p. 1339-1339.

278. Guerrero-Bermea, C., et al., *Two-dimensional and three-dimensional hybrid assemblies based on graphene oxide and other layered structures: A carbon science perspective.* Carbon, 2017. **125**(Supplement C): p. 437-453.

279. Yang, B., et al., *Nanocomposite of Tin Sulfide Nanoparticles with Reduced Graphene Oxide in High-Efficiency Dye-Sensitized Solar Cells.* ACS Applied Materials & Interfaces, 2015. **7**(1): p. 137-143.

280. Chen, S., et al., *Graphene Oxide−MnO2 Nanocomposites for Supercapacitors.* ACS Nano, 2010. **4**(5): p. 2822-2830.

281. Williams, G., B. Seger, and P.V. Kamat, *TiO2-Graphene Nanocomposites. UV-Assisted Photocatalytic Reduction of Graphene Oxide.* ACS Nano, 2008. **2**(7): p. 1487-1491.
282. Zhang, J., et al., *Noble Metal-Free Reduced Graphene Oxide-ZnxCd1–xS Nanocomposite with Enhanced Solar Photocatalytic H2-Production Performance.* Nano Letters, 2012. **12**(9): p. 4584-4589.
283. Liu, X., et al., *Microwave-assisted synthesis of CdS-reduced graphene oxide composites for photocatalytic reduction of Cr(vi).* Chemical Communications, 2011. **47**(43): p. 11984-11986.
284. Yang, B., et al., *Structural Phase Transition from Tin (IV) Sulfide to Tin (II) Sulfide and the enhanced Performance by Introducing Graphene in Dye-sensitized Solar Cells.* Electrochimica Acta, 2015. **176**(Supplement C): p. 797-803.
285. Xu, L., et al., *Interfacial Interactions of Semiconductor with Graphene and Reduced Graphene Oxide: CeO2 as a Case Study.* ACS Applied Materials & Interfaces, 2014. **6**(22): p. 20350-20357.
286. Chabot, V., et al., *A review of graphene and graphene oxide sponge: material synthesis and applications to energy and the environment.* Energy & Environmental Science, 2014. **7**(5): p. 1564-1596.
287. Thangaraju, B. and P. Kaliannan, *Spray pyrolytic deposition and characterization of SnS and SnS 2 thin films.* Journal of Physics D: Applied Physics, 2000. **33**(9): p. 1054.
288. Schneikart, A., et al., *Efficiency limitations of thermally evaporated thin-film SnS solar cells.* Journal of Physics D: Applied Physics, 2013. **46**(30): p. 305109.
289. Johny, J., et al., *Tin sulfide: Reduced graphene oxide nanocomposites for photovoltaic and electrochemical applications.* Solar Energy Materials and Solar Cells, 2019. **189**: p. 53-62.
290. Yang, D., et al., *Chemical analysis of graphene oxide films after heat and chemical treatments by X-ray photoelectron and Micro-Raman spectroscopy.* Carbon, 2009. **47**(1): p. 145-152.
291. Johny, J., et al., *Synthesis and Properties of Tin Sulfide Thin Films from Nanocolloids Prepared by Pulsed Laser Ablation in Liquid.* ChemPhysChem, 2017: p. n/a-n/a.
292. Reddy, T.S. and M.C.S. Kumar, *Co-evaporated SnS thin films for visible light photodetector applications.* RSC Advances, 2016. **6**(98): p. 95680-95692.
293. Gupta, Y. and P. Arun, *Suitability of SnS thin films for photovoltaic application due to the existence of persistent photocurrent.* physica status solidi (b), 2016. **253**(3): p. 509-514.
294. Velasco-Soto, M., et al., *Selective band gap manipulation of graphene oxide by its reduction with mild reagents.* Carbon, 2015. **93**: p. 967-973.
295. Jayalakshmi, M., M. Mohan Rao, and B.M. Choudary, *Identifying nano SnS as a new electrode material for electrochemical capacitors in aqueous solutions.* Electrochemistry Communications, 2004. **6**(11): p. 1119-1122.
296. Li, Y., H. Xie, and J. Tu, *Nanostructured SnS/carbon composite for supercapacitor.* Materials Letters, 2009. **63**(21): p. 1785-1787.

297. Chauhan, H., et al., *Synthesis of surfactant-free SnS nanorods by a solvothermal route with better electrochemical properties towards supercapacitor applications.* RSC Advances, 2015. **5**(22): p. 17228-17235.
298. Dubal, D.P., S.H. Lee, and W.B. Kim, *Sponge-like β-Ni(OH)2 nanoparticles: synthesis, characterization and electrochemical properties.* Journal of Materials Science, 2012. **47**(8): p. 3817-3821.
299. Eftekhari, A., *Electrocatalysts for hydrogen evolution reaction.* International Journal of Hydrogen Energy, 2017. **42**(16): p. 11053-11077.
300. Chia, X., et al., *Layered SnS versus SnS2: Valence and Structural Implications on Electrochemistry and Clean Energy Electrocatalysis.* The Journal of Physical Chemistry C, 2016. **120**(42): p. 24098-24111.
301. Johny, J., et al., *SnS2 nanoparticles by liquid phase laser ablation: Effects of laser fluence, temperature and post irradiation on morphology and hydrogen evolution reaction.* Applied Surface Science, 2019. **470**: p. 276-288.
302. Zhang, D., B. Gökce, and S. Barcikowski, *Laser Synthesis and Processing of Colloids: Fundamentals and Applications.* Chemical Reviews, 2017. **117**(5): p. 3990-4103.
303. Zeng, H., et al., *Nanomaterials via Laser Ablation/Irradiation in Liquid: A Review.* Advanced Functional Materials, 2012. **22**(7): p. 1333-1353.
304. Kim, J., et al., *The influence of laser wavelength and fluence on palladium nanoparticles produced by pulsed laser ablation in deionized water.* Solid State Sciences, 2014. **37**(Supplement C): p. 96-102.
305. Kim, H.J., I.C. Bang, and J. Onoe, *Characteristic stability of bare Au-water nanofluids fabricated by pulsed laser ablation in liquids.* Optics and Lasers in Engineering, 2009. **47**(5): p. 532-538.
306. Werner, D., et al., *Examination of Silver Nanoparticle Fabrication by Pulsed-Laser Ablation of Flakes in Primary Alcohols.* The Journal of Physical Chemistry C, 2008. **112**(5): p. 1321-1329.
307. Tsuji, T., et al., *Preparation of silver nanoparticles by laser ablation in polyvinylpyrrolidone solutions.* Applied Surface Science, 2008. **254**(16): p. 5224-5230.
308. Yang, G.W., *Laser ablation in liquids: Applications in the synthesis of nanocrystals.* Progress in Materials Science, 2007. **52**(4): p. 648-698.
309. Caricato, A.P., A. Luches, and M. Martino, *Laser Fabrication of Nanoparticles*, in *Handbook of Nanoparticles*, M. Aliofkhazraei, Editor. 2016, Springer International Publishing: Cham. p. 407-428.
310. Rehbock, C., et al., *Current state of laser synthesis of metal and alloy nanoparticles as ligand-free reference materials for nano-toxicological assays.* Beilstein journal of nanotechnology, 2014. **5**: p. 1523.
311. Amendola, V. and M. Meneghetti, *Controlled size manipulation of free gold nanoparticles by laser irradiation and their facile bioconjugation.* Journal of Materials Chemistry, 2007. **17**(44): p. 4705-4710.
312. Mafuné, F., et al., *Formation and Size Control of Silver Nanoparticles by Laser Ablation in Aqueous Solution.* The Journal of Physical Chemistry B, 2000. **104**(39): p. 9111-9117.

313. Brito-Silva, A.M., et al., *Laser Ablated Silver Nanoparticles with Nearly the Same Size in Different Carrier Media.* Journal of Nanomaterials, 2010. **2010**: p. 7.
314. Guillén, G.G., et al., *Effects of ablation energy and post-irradiation on the structure and properties of titanium dioxide nanomaterials.* Applied Surface Science, 2017. **405**: p. 183-194.
315. Takeuchi, Y., T. Ida, and K. Kimura, *Colloidal Stability of Gold Nanoparticles in 2-Propanol under Laser Irradiation.* The Journal of Physical Chemistry B, 1997. **101**(8): p. 1322-1327.
316. Werner, D., et al., *Femtosecond Laser-Induced Size Reduction of Aqueous Gold Nanoparticles: In Situ and Pump−Probe Spectroscopy Investigations Revealing Coulomb Explosion.* The Journal of Physical Chemistry C, 2011. **115**(17): p. 8503-8512.
317. Akinori, T., et al., *Size Reduction of Silver Particles in Aqueous Solution by Laser Irradiation.* Japanese Journal of Applied Physics, 1996. **35**(6B): p. L781.
318. Bae, C.H., S.H. Nam, and S.M. Park, *Formation of silver nanoparticles by laser ablation of a silver target in NaCl solution.* Applied Surface Science, 2002. **197-198**: p. 628-634.
319. Guillén, G.G., et al., *Structure and morphologies of ZnO nanoparticles synthesized by pulsed laser ablation in liquid: Effects of temperature and energy fluence.* Materials Chemistry and Physics, 2015. **162**: p. 561-570.
320. Shaji, S., et al., *Nanostructured SnS2 thin films from laser ablated nanocolloids: structure, morphology, optoelectronic and electrochemical properties.* ChemPhysChem. **0**(ja).
321. Kiruthigaa, G., et al., *Solid state synthesis and spectral investigations of nanostructure SnS2.* Spectrochimica Acta Part A: Molecular and Biomolecular Spectroscopy, 2014. **129**: p. 415-420.
322. Burton, L.A., et al., *Electronic and optical properties of single crystal SnS2: an earth-abundant disulfide photocatalyst.* Journal of Materials Chemistry A, 2016. **4**(4): p. 1312-1318.
323. Panda, S.K., et al., *Optical properties of nanocrystalline SnS2 thin films.* Materials Research Bulletin, 2007. **42**(3): p. 576-583.
324. Xia, J., et al., *Physical vapor deposition synthesis of two-dimensional orthorhombic SnS flakes with strong angle/temperature-dependent Raman responses.* Nanoscale, 2016. **8**(4): p. 2063-2070.
325. Gou, X.-L., J. Chen, and P.-W. Shen, *Synthesis, characterization and application of SnSx (x=1, 2) nanoparticles.* Materials Chemistry and Physics, 2005. **93**(2): p. 557-566.
326. Moulder, J.F., J. Chastain, and R. King, *Handbook of X-ray photoelectron spectroscopy: a reference book of standard spectra for identification and interpretation of XPS data; Physical Electronics: Eden Prairie, MN, 1995.* There is no corresponding record for this reference, 2000.
327. Yang, F., et al., *Improving the photo-degradation activity of SnS2 under visible light by TiO2 (rutile).* Materials Letters, 2013. **99**: p. 24-27.
328. Dashairya, L., et al., *SnS2/RGO based nanocomposite for efficient photocatalytic degradation of toxic industrial dyes under visible-light irradiation.* Journal of Alloys and Compounds, 2019. **774**: p. 625-636.

329. Ham, G., et al., *Engineering the crystallinity of tin disulfide deposited at low temperatures.* RSC Advances, 2016. **6**(59): p. 54069-54075.
330. Koichi, S., et al., *Effect of Pressurization on the Dynamics of a Cavitation Bubble Induced by Liquid-Phase Laser Ablation.* Applied Physics Express, 2009. **2**(4): p. 046501.
331. Caricato, A., A. Luches, and M. Martino, *Laser fabrication of nanoparticles.* Handbook Of Nanoparticles, 2016: p. 407-428.
332. Semaltianos, N.G., et al., *II–VI semiconductor nanoparticles synthesized by laser ablation.* Applied Physics A, 2008. **94**(3): p. 641.
333. Mendivil, M.I., et al., *Synthesis and properties of palladium nanoparticles by pulsed laser ablation in liquid.* Applied Surface Science, 2015. **348**: p. 45-53.
334. Mendivil Palma, M.I., et al., *Synthesis and properties of platinum nanoparticles by pulsed laser ablation in liquid.* Journal of Nanomaterials, 2016. **2016**.
335. Du, Y., et al., *A facile, relative green, and inexpensive synthetic approach toward large-scale production of SnS2 nanoplates for high-performance lithium-ion batteries.* Nanoscale, 2013. **5**(4): p. 1456-1459.
336. Li, Y., et al., *MoS2 Nanoparticles Grown on Graphene: An Advanced Catalyst for the Hydrogen Evolution Reaction.* Journal of the American Chemical Society, 2011. **133**(19): p. 7296-7299.
337. Vassalini, I., et al., *Enhanced Electrocatalytic Oxygen Evolution in Au–Fe Nanoalloys.* Angewandte Chemie International Edition, 2017. **56**(23): p. 6589-6593.
338. Ganeev, R.A., et al., *Characterization of optical and nonlinear optical properties of silver nanoparticles prepared by laser ablation in various liquids.* Optics Communications, 2004. **240**(4): p. 437-448.
339. Garza, D., et al., *Nanoparticles of antimony sulfide by pulsed laser ablation in liquid media.* Journal of Materials Science, 2013. **48**(18): p. 6445-6453.
340. García Guillén, G., et al., *Effects of Liquid Medium and Ablation Wavelength on the Properties of Cadmium Sulfide Nanoparticles Formed by Pulsed-Laser Ablation.* ChemPhysChem, 2017. **18**(9): p. 1035-1046.
341. Klug, H.P. and L.E. Alexander, *X-ray diffraction procedures: for polycrystalline and amorphous materials.* X-Ray Diffraction Procedures: For Polycrystalline and Amorphous Materials, 2nd Edition, by Harold P. Klug, Leroy E. Alexander, pp. 992. ISBN 0-471-49369-4. Wiley-VCH, May 1974., 1974: p. 992.
342. Smith, A.J., P.E. Meek, and W.Y. Liang, *Raman scattering studies of SnS 2 and SnSe 2.* Journal of Physics C: Solid State Physics, 1977. **10**(8): p. 1321.
343. Wang, C., et al., *Raman scattering, far infrared spectrum and photoluminescence of SnS2 nanocrystallites.* Chemical Physics Letters, 2002. **357**(5): p. 371-375.
344. Shi, C., et al., *Influence of annealing on characteristics of tin disulfide thin films by vacuum thermal evaporation.* Thin Solid Films, 2012. **520**(15): p. 4898-4901.
345. Tauc, J., *Optical properties and electronic structure of amorphous Ge and Si.* Materials Research Bulletin, 1968. **3**(1): p. 37-46.
346. Deshpande, N.G., et al., *Growth and characterization of tin disulfide (SnS2) thin film deposited by successive ionic layer adsorption and reaction (SILAR) technique.* Journal of Alloys and Compounds, 2007. **436**(1): p. 421-426.

347. Tan, F., et al., *Preparation of SnS2 colloidal quantum dots and their application in organic/inorganic hybrid solar cells.* Nanoscale Research Letters, 2011. **6**(1): p. 298.

348. Arulanantham, A., et al., *Effect of sulfur concentration on the properties of tin disulfide thin films by nebulizer spray pyrolysis technique.* Journal of Materials Science: Materials in Electronics, 2017. **28**(24): p. 18675-18685.

List of figures

List of tables

List of publications

1. **Johny, J.**, Guzman, S. S., Krishnan, B., Martinez, J. A. A., Avellaneda, D. A., & Shaji, S. (**2019**). SnS2 nanoparticles by liquid phase laser ablation: Effects of laser fluence, temperature and post irradiation on morphology and hydrogen evolution reaction. *Applied Surface Science*, *470*, 276-288
2. **Johny, J.**, Sepulveda-Guzman, S., Krishnan, B., Avellaneda, D. A., Martinez, J. A., Anantharaman, M. R., & Shaji, S. (**2019**). Tin sulfide: Reduced graphene oxide nanocomposites for photovoltaic and electrochemical applications. *Solar Energy Materials and Solar Cells*, *189*, 53-62
3. **Johny, J.**, Sepulveda-Guzman, S., Krishnan, B., Avellaneda, D., & Shaji, S. (**2018**). Facile and fast synthesis of SnS2 nanoparticles by pulsed laser ablation in liquid. *Applied Surface Science*, *435*, 1285-1295
4. **Johny, J.**, Sepulveda Guzman, S., Krishnan, B., Avellaneda Avellaneda, D., & Shaji, S. (**2018**). Nanostructured SnS2 thin films from laser ablated nanocolloids: structure, morphology, optoelectronic and electrochemical properties. *ChemPhysChem*, *19*(21), 2902-2914
5. **Johny, J.**, Sepulveda-Guzman, S., Krishnan, B., Avellaneda, D. A., Aguilar Martinez, J. A., & Shaji, S. (**2017**). Synthesis and properties of tin sulfide thin films from nanocolloids prepared by pulsed laser ablation in liquid. *ChemPhysChem*, *18*(9), 1061-1068
6. I.C. Novoa-De León, **J. Johny**, S. Vázquez-Rodríguez, N. García-Gómez, S. Carranza-Bernal, I. Mendivil, S. Shaji, S. Sepúlveda-Guzmán (**2019**). Tuning the luminescence of nitrogen-doped graphene quantum dots synthesized by pulsed laser ablation in liquid and their use as a selective photoluminescence on–off–on probe for ascorbic acid detection, *Carbon*, *150*, 455-464
7. Safeera, T. A., **Johny, J.**, Shaji, S., Nien, Y. T., & Anila, E. I. (**2019**). Impact of activator incorporation on red emitting rods of ZnGa2O4: Cr3+ phosphor. *Materials Science and Engineering: C*, *94*, 1037-1043

8. V.A. Zuñiga-Ibarra, S. Shaji, B. Krishnan, **J. Johny**, S. Sharma Kanakkillam, D.A. Avellaneda, J.A. Aguilar Martinez, T.K. Das Roy, N.A. Ramos-Delgado, (**2019**). Synthesis and characterization of black TiO2 nanoparticles by pulsed laser irradiation in liquid. *Applied Surface Science*.
9. V. N. Archana, Manoj Mani, **Johny J.**, S. Vinayasree, P. Mohanan, Marco A. Garza-Navarro, Sadasivan Shaji, & M. R. Anantharaman (**2019**). On the microwave absorption of magnetic nanofluids based on barium hexaferrite in the S and X bands prepared by pulsed laser ablation in liquid. *AIP Advances*, *9*(3), 035035.
10. Archana, V. N., **Johny, J.**, Garza-Navarro, M. A., Shaji, S., Thomas, S., & Anantharaman, M. R. (**2018**). Synthesis of surfactant free stable nanofluids based on barium hexaferrite by pulsed laser ablation in liquid. *RSC Advances*, *8*(34), 19261-19271
11. Shaji, S., Vinayakumar, V., Krishnan, B., **Johny, J.**, Kanakkillam, S. S., Herrera, J.M.Flores Herrera, S.Sepulveda Guzman, D.A.Avellaneda, G.A.Castillo Rodriguez, & J.A.Aguilar Martinez (**2019**). Copper antimony sulfide nanoparticles by pulsed laser ablation in liquid and their thin film for photovoltaic application. *Applied Surface Science*, *476*, 94-106
12. Howson, M. P., Wynne, B. P., Mercado-Solis, R. D., Leduc-Lezama, L. A., **Jonny, J.**, & Shaji, S. (**2016**). An Analysis of the Quenching Performance of a Copper Nanofluid Prepared Using Laser Ablation. *Journal of Thermal Science and Engineering Applications*, *8*(4), 044501